

**LONG-TERM MATRIC SUCTION MEASUREMENTS
IN HIGHWAY SUBGRADES**

A Thesis

Submitted to the College of Graduate Studies and Research

in Partial Fulfillment of the Requirements

for the Degree of Master of Science

in the Department of Civil Engineering

University of Saskatchewan

Saskatoon, Canada

By

Quan Nguyen

© Copyright Q. Nguyen, May 2006 All Rights Reserved

COPYRIGHT

The author has agreed that the library, University of Saskatchewan, may make this thesis freely available for inspection. Moreover, the author has agreed that permission for extensive copying of this thesis for scholarly purposes may be granted by the professor or professors who supervised the thesis work recorded herein or in their absence, by the Head of the Department or the Dean of the College in which recognition will be given to the author of this thesis and to the University of Saskatchewan in any use of the material in this thesis. Copying or publication of any other use of this thesis for financial gain without approval by the University of Saskatchewan and the author's written permission is prohibited.

Requests for permission to copy or to make any other use of material in this thesis in whole or in part should be addressed to:

Head of the Department of Civil Engineering
University of Saskatchewan
Saskatoon, Canada
57 Campus Drive
S7N 5A9

ABSTRACT

The performance of Thin Membrane Surface (TMS) highways is largely controlled by the strength of the subgrade soil which in turn is a function of the soil suction (Fredlund and Morgenstern, 1977). Thermal conductivity suction sensors can be used to indirectly measure *in situ* matric suction.

Thirty two (32) thermal conductivity sensors were installed under Thin Membrane Surface (TMS) in two highway locations; namely, Bethune and Torquay, Saskatchewan, in September 2000. The sensors were installed beneath the pavement, shoulder and side-slope to monitor matric suction and temperature changes with time. The monitoring system at Bethune was damaged after two years of operation. The thermal conductivity sensors at Torquay all appear to have been working well and data are still being collected.

Other attempts had been made in the past to use thermal conductivity sensors for field suction measurement, but all were terminated within a short period of time due to limitations associated with the equipment. The long-term suction measurement at the Torquay site is unique and provides valuable field data.

This research project presents and interprets the long-term matric suction measurements made between the years 2000 to 2005 at the Torquay site and from 2000 to 2002 at the Bethune site. To help in the interpretation of the data, a site investigation was undertaken along with a laboratory testing program that included the measurement of Soil-Water Characteristic Curves (SWCC). As well, a limited laboratory study was undertaken on several new thermal conductivity matric suction sensors.

The matric suction readings in the field showed a direct relationship to rainfall and regional evaporation conditions at the test sites. At the Bethune and Torquay test sites, the changes in matric suctions appeared to be mainly due to the movement of moisture through the edge of the road. Relatively constant equilibrium suctions were encountered under the driving-lanes. Conversely, matric suctions under the side-slopes were found to vary considerably with time and depth. Matric suctions under the driving-lanes ranged from 20 to 60 kPa throughout the years. Matric suctions on the side-slopes changed from 100 to 1500 kPa over the years.

The greatest variation of soil suctions occurred in the month of April from location to location in the subgrade. The soil suctions became less variable in June while larger variations again occurred from July to October.

The matric suction measurements obtained from the thermal conductivity sensors showed a general agreement with the values estimated using the soil-water characteristic curves, SWCC, measured in the laboratory.

ACKNOWLEDGEMENTS

The author would like to take this opportunity to express his sincere thanks and gratitude to his supervisors, Drs. Del Fredlund and Lal Samarasekera for their assistance, guidance and words of encouragement during the formation of this thesis

I am grateful to the funding provided by Saskatchewan Highways and Transportation, Government of Saskatchewan, Regina, and Natural Sciences and Engineering Research Council of Canada, Ottawa.

A special thank goes to Mr. Brent Marjerison for the help of providing the field data and helping me in numerous other ways. The field data are a unique collection and made the research project possible.

I would like to extend my gratitude to my committee members, Drs. Dennis Pufahl, Chris Hawkes, Jian Peng and external examiner Mr. Allan Widger for their comments and advice during the research program.

The author would also like to extend his thanks to Mr. Alex Kozlow for his instruction and assistance in the completion of the laboratory testing program. The generous assistance of departmental staff and fellow graduate students is acknowledged.

The author would also like to express his thanks to his wife Oanh, who provided much support and encouragement through out the course of this project.

TABLE OF CONTENTS

COPYRIGHT	i
ABSTRACT	ii
ACKNOWLEDGEMENTS	iv
TABLE OF CONTENTS	v
LIST OF TABLES	ix
LIST OF FIGURES	x
CHAPTER 1	
INTRODUCTION AND FIELD STUDIES	1
1.1 Background	1
1.2 Objectives and scope of thesis	3
1.3 Methodology	4
1.4 Thesis layout	4
1.5 Field studies analyzed	6
CHAPTER 2	
LITERATURE REVIEW	14
2.1 Suction theory and typical soil suction profiles	14
2.2 Field suction measurement, thermal conductivity sensor and history of <i>in situ</i> sensor installations	18
2.3 Measurement difficulties associated with thermal conductivity sensor	31
CHAPTER 3	
RESEARCH PROGRAM	48
3.1 Overview of the research program	48
3.2 Site investigation	51
3.4.1 Staff and equipment	51
3.4.2 Purpose and scope of site investigation	52
3.4.3 Drilling operations	52
3.4.4 Geological conditions	52
3.4.5 Groundwater condition	53

3.4.6	Subsurface soil conditions at Bethune	53
3.4.7	Subsurface soil conditions at Torquay	54
3.3	Collection of weather data	54

CHAPTER 4

VERIFICATION OF EQUATIONS FOR SUCTION CALCULATIONS AND SUCTION ANALYSIS

4.1	Equations for temperature correction	57
4.1.1	Correction method for ambient temperature presented by Shuai et al. (2002)	57
4.1.2	Correction method for ambient temperature presented by Nichol et al. (2003)	58
4.2	Validity of the calibration equations	61
4.3	Equations for sensor hysteresis correction	63
4.3.1	Feng and Fredlund's fitting equations	63
4.3.2	Shuai's practical fitting equations	66
4.3.3	Fitting equations regarding bending point of voltage output	69
4.4	The field data reduction	72
4.5	Analysis of in situ suction data	72
4.5.1	Assumptions for the hysteresis correction and procedural analyses	72
4.5.2	Determination of $V_{bending}$	74
4.5.3	Determination of the location of the current point on the hysteresis curves	74
4.5.4	Selection of the current suction	77

CHAPTER 5

PRESENTATION OF LABORATORY TEST RESULTS AND *IN SITU* SUCTIONS CALCULATED ON THE MAIN HYSTERESIS LOOP WITH NO TEMPERATURE CORRECTION

5.1	Laboratory test results	82
5.2	Temperature and rainfall data	84
5.2.1	Temperature comparison between sensor and thermister	84
5.3	Presentation of <i>in situ</i> uncorrected matric suction	86
5.3.1	Background of <i>in situ</i> uncorrected matric suction	86
5.3.2	Vertical grid-line under driving-lane at the Torquay site	87
5.3.3	Vertical grid-line under shoulder at the Torquay site	90

5.3.4	Vertical grid-line under side-slope at the Torquay site	92
-------	---	----

CHAPTER 6

PRESENTATION AND DISCUSSION OF <i>IN SITU</i> CORRECTED MATRIC SUCTIONS		96
6.1	Comparison of corrected suctions and uncorrected suctions	97
6.1.1	The effect of temperature correction on suction measurement	97
6.1.2	The effect of the hysteresis correction on field suction measurement	100
6.2	The first equilibrium of sensor with surrounding soil	101
6.3	Suctions along vertical depth versus time	103
6.3.1	Vertical grid-line under driving-lane at the Torquay site	103
6.3.2	Vertical grid-line under driving-lane at the Bethune site	108
6.3.3	Vertical grid-line under shoulder at the Torquay site	110
6.3.4	Vertical grid-line under side-slope at the Torquay site	113
6.3.5	Vertical grid-line under side-slope at the Bethune site	117
6.4	Suctions along horizontal grid-line versus time	120
6.4.1	Horizontal grid-line along top sensors at the Torquay site	120
6.4.2	Horizontal grid-line along top sensors at the Bethune site	122
6.4.3	Horizontal grid-line along middle-depth sensors at the Torquay site	124
6.4.4	Horizontal grid-line along bottom sensors at the Torquay site	126
6.4.5	Horizontal grid-line along bottom sensors at the Bethune site	129
6.5	Contour maps of suction	132
6.5.1	Contour maps of suctions at the Torquay site	132
6.5.2	Contour maps of suction at the Bethune site	134
6.6	Suction presentation with small time scales	136
6.6.1	Sensor response to rainfall	136
6.6.2	Noise levels of the thermal conductivity sensors	139
6.7	Suction variations with temperature and time	141
6.7.1	Suction measurement during freezing	141
6.7.2	Suction measurement with variation of ambient temperature	142
6.7.3	Suction and temperature change cycle	144

CHAPTER 7

INTERPRETATION OF MEASURED *IN SITU* MATRIC SUCTIONS 146

7.1 Interpretation of the matric suction patterns with respect to the climatic conditions 146

7.1.1 Matric suction interpretation on the vertical grid-lines 147

7.1.2 Matric suction interpretation on the horizontal grid-lines 152

7.1.3 Matric suction interpretation on contour map 159

7.1.4 Possible explanations for low matric suctions under the side-slope at the Torquay site in 2004 160

7.1.5 Effects of thawing on the drop of matric suction during “spring break-up” 163

7.2 *In situ* matric suctions in conjunction with SWCC and water content 163

7.3 Noise levels of the thermal conductivity sensors 166

7.4 Response time of the thermal conductivity sensors with rainfall 167

7.5 Malfunction and possible erratic readings and of the sensors 168

7.6 General discussion of the field suction measurements at the Bethune and Torquay site 170

CHAPTER 8

CONCLUSIONS AND RECOMMENDATIONS FOR FUTURE RESEARCH 171

8.1 Conclusions 171

8.2 Recommendation for future research 173

LIST OF REFERENCES 175

Appendix A: A study on new thermal conductivity sensors

Appendix B: Presentation of in situ matric suctions

Appendix C: Site investigation and laboratory test results

LIST OF TABLES

Table 2.1 Techniques for in situ measurement of matric suction	19
Table 2.2 Orders of magnitude of the thermal conductivity	22
Table 2.3 Thermal conductivity values for soils	22
Table 2.4 Technical specification	27
Table 2.5 The properties of the three ceramics used for hysteresis studies	35
Table 3.1 Location of weather stations and the sites	56
Table 5.1 Temperatures recorded by the thermister and the thermal conductivity sensor at 0.3 m depth	85
Table 7.1 Comparison between sensors suctions and estimated matric suctions from SWCC	165

LIST OF FIGURES

Figure 1.1 A map with field sites of Bethune and Torquay	7
Figure 1.2 The TMS highway at the site of north Bethune, Saskatchewan	8
Figure 1.3 Installation layout of sensors on a highway cross-section	9
Figure 1.4 Schematic illustration of wiring connection of the system	9
Figure 1.5 DAS in place	11
Figure 1.6 Solar panels at the site of north Bethune, Saskatchewan	11
Figure 1.7 Custom sensor insertion tool	12
Figure 1.8 Sensor installation on site	12
Figure 2.1 A typical soil matric suction profile	16
Figure 2.2 Suction profiles in a highway subgrade	17
Figure 2.3 Variations in matric suction with rainfall and time obtained from tensiometers	18
Figure 2.4 Variation of soil suction with time measured using tensiometers and thermal conductivity sensors	20
Figure 2.5 Cross-section of a thermal conductivity sensor	23
Figure 2.6 Calibration curves for two AGWA-II sensors	25
Figure 2.7 The University of Saskatchewan thermal conductivity sensor	26
Figure 2.8 Heating curves for U of S thermal conductivity sensor before and after improvement	27
Figure 2.9 Field suction data from one sensor	30
Figure 2.10 A hysteresis process and scanning curves	31
Figure 2.11 Schematic illustration of the “Ink-bottle” effect	33
Figure 2.12 Soil-water hysteresis curves for a one-pore size system	33
Figure 2.13 Definitions of hysteretic Soil-Water Characteristic Curves	34
Figure 2.14 Laboratory hysteresis curves for Thermal Conductivity Sensor #1	36
Figure 2.15 Maximum possible relative error of suction measurement due to hysteresis	37
Figure 2.16 Typical calibration curve for a U of S thermal conductivity sensor	39
Figure 2.17 Test results for temperature corrections using Equation 2.8	41
Figure 2.18 Correction factor for ambient soil temperature	42
Figure 2.19 Set up for thermal conductivity sensor in a freezing test	45
Figure 2.20 Test results from the bottom sensor in a freezing environment	45

Figure 2.21 Effect of freeze-thaw cycles on sensor readings	47
Figure 3.1 General outline of the research program	49
Figure 3.2 Outline for the study to verify the equations for matric suction calculations	49
Figure 3.3 Outline of the procedural analysis of suction from the field data	50
Figure 3.4 Layout for the presentation of the matric suction data	51
Figure 3.5 Location map of Torquay and the vicinities	55
Figure 3.6 Location map of Bethune and the vicinities	55
Figure 4.1 Graphical notations for the applied calibration equation	61
Figure 4.2 Measured and fitted data for sensor B5-16, Bethune	62
Figure 4.3 Measured and fitted data for sensor T2-7, Torquay	62
Figure 4.4 Graphical notations for Equation 2.6	64
Figure 4.5 Graphical notations for Equation 2.7	64
Figure 4.6 Comparison of drying scanning curves for Sensor	65
Figure 4.7 Comparison of wetting scanning curves for Sensor 2	65
Figure 4.8 Estimated wetting scanning curves using Equation 4.5 for Sensor 2	67
Figure 4.9 Estimated drying scanning curves using Equation 4.6 for Sensor 1	67
Figure 4.10 Wetting scanning curves using Equation 4.5 with different ratios of V_{out}/V_{limit}	68
Figure 4.11 Drying scanning curves using Equation 4.6 with different ratios of V_{out}/V_{limit}	69
Figure 4.12 Graphical notations for Equation 4.7	70
Figure 4.13 Graphical notations for Equation 4.8	71
Figure 4.14 Estimated wetting scanning curves using Equation 4.7 for Sensor 2	71
Figure 4.15 Estimated drying scanning curves using Equation 4.8 for Sensor 1	72
Figure 4.16 Diagram showing possible hysteresis positions of a voltage output from a thermal conductivity sensor	75
Figure 4.17 Suction with hysteresis correction using $V_{bending}$ for a shallow-depth sensor (T1-1 at 0.3 m depth, Torquay)	79
Figure 4.18 Suction with hysteresis correction using $V_{bending}$ for a middle-depth (0.8m) sensor (T1-2 at 0.8 m depth, Torquay)	79
Figure 4.19 Suction with hysteresis correction using $V_{bending}$ for a bottom-depth sensor (T1-5 at 2.2 m depth, Torquay)	80
Figure 4.20 Suction with hysteresis correction using V_{limit} for a shallow-depth sensor at Torquay (T1-1)	81

Figure 4.21 Suction with hysteresis correction using Vlimit for a bottom-depth sensor at Torquay (T1-5)	81
Figure 5.1 Pre-consolidation pressures, water contents (w/c) and Atterberg limits with depth at the Bethune site and Torquay site	83
Figure 5.2 Soil-water characteristic curve of sample T5-1 (at a depth of 0.10 to 0.25 m) at the Torquay site	84
Figure 5.3 The air temperatures at the Torquay site from 2001 to 2005	85
Figure 5.4 The 14-day moving average of rainfall at the Torquay site	86
Figure 5.5 In situ uncorrected suctions along vertical grid-line under driving-lane at the Torquay site	88
Figure 5.6 In situ uncorrected suctions at Sensor T1-1 in 2002 and 2003 at the Torquay site	88
Figure 5.7 In situ uncorrected suctions at Sensor T1-2 in 2002 and 2003 at the Torquay site	89
Figure 5.8 In situ uncorrected suctions at Sensor T1-5 in 2002 and 2003 at the Torquay site	89
Figure 5.9 In situ uncorrected suctions along vertical grid-line under shoulder at the Torquay site	90
Figure 5.10 In situ uncorrected suctions at Sensor T3-10 in 2002 and 2003 at the Torquay site	91
Figure 5.11 In situ uncorrected suctions at Sensor T3-11 in 2002 and 2003 at the Torquay site	91
Figure 5.12 In situ uncorrected suctions at Sensor T3-12 in 2002 and 2003 at the Torquay site	92
Figure 5.13 In situ uncorrected suctions along vertical grid-line under side-slope at the Torquay site	93
Figure 5.14 In situ uncorrected suctions at Sensor T4-13 in 2002 and 2003 at the Torquay site	93
Figure 5.15 In situ uncorrected suctions at Sensor T4-14 in 2002 and 2003 at the Torquay site	94
Figure 5.16 In situ uncorrected suctions at Sensor T4-15 in 2002 and 2003 at the Torquay site	94
Figure 6.1 Suctions with and without temperature correction at Sensor T1-5	98
Figure 6.2 Suctions with and without temperature correction at Sensor T1-1	99
Figure 6.3 Suctions with and without temperature correction at Sensor T4-13	99
Figure 6.4 Suctions with and without hysteresis correction at Sensor T2-9	100
Figure 6.5 Suctions with and without hysteresis correction at Sensor B1-1	101

Figure 6.6 Suctions before reaching equilibrium at the Torquay site	102
Figure 6.7 Suctions before reaching equilibrium at the Bethune site	103
Figure 6.8 Suctions along vertical grid-line under the driving-lane at the Torquay site	104
Figure 6.9 Five-year average suctions along vertical grid-line under the driving-lane at the Torquay site	105
Figure 6.10 Five-year average suctions versus depth along vertical grid-line under the driving-lane at the Torquay site	106
Figure 6.11 Suctions at Sensor T1-1 for years 2001 to 2005 at the Torquay site	106
Figure 6.12 Suctions at Sensor T1-2 for years 2001 to 2005 at the Torquay site	107
Figure 6.13 Suctions at Sensor T1-5 for years 2001 to 2005 at the Torquay site	107
Figure 6.14 Suctions along vertical grid-line under the driving-lane at the Bethune site	108
Figure 6.15 Two-year average suctions along vertical grid-line under the driving-lane at the Bethune site	109
Figure 6.16 Two-year average suctions versus depth along vertical grid-line under the driving-lane at the Bethune site	109
Figure 6.17 Suctions along vertical grid-line under the shoulder at the Torquay site	111
Figure 6.18 Five-year average suctions along vertical grid-line under the shoulder at the Torquay site	111
Figure 6.19 Five-year average suctions versus depth along vertical grid-line under the shoulder at the Torquay site	112
Figure 6.20 Suctions at Sensor T3-10 for years 2001 to 2005 at the Torquay site	112
Figure 6.21 Suctions at Sensor T3-12 for years 2001 to 2005 at the Torquay site	113
Figure 6.22 Suctions along vertical grid-line under the side-slope at the Torquay site	114
Figure 6.23 Five-year average suctions along vertical grid-line under the side-slope at the Torquay site	114
Figure 6.24 Five-year average suctions versus depth along vertical grid-line under the side-slope at the Torquay site	115
Figure 6.25 Suctions at Sensor T4-13 for years 2001 to 2005 at the Torquay site	115
Figure 6.26 Suctions at Sensor T4-14 for years 2001 to 2005 at the Torquay site	116
Figure 6.27 Suctions at Sensor T4-15 for years 2001 to 2005 at the Torquay site	116
Figure 6.28 Summary of suctions along the three vertical grid-lines: under the driving-lane, under the shoulder and under the side-slope for years 2001 to 2005 at the Torquay site	117

Figure 6.29 Suctions along vertical grid-line under the side-slope at the Bethune site	118
Figure 6.30 Two-year average suctions along vertical grid-line under the side-slope at the Bethune site	118
Figure 6.31 Suctions at Sensor B4-13 for years 2001 to 2002 at the Bethune site	119
Figure 6.32 Suctions at Sensor B4-14 for years 2001 to 2002 at the Bethune site	119
Figure 6.33 Summary of suctions along the three vertical grid-lines: under the driving-lane, under the shoulder and under the side-slope for years 2001 to 2002 at the Bethune site	120
Figure 6.34 Suctions along horizontal top sensors at the Torquay site	121
Figure 6.35 Five-year average suctions versus time along horizontal top sensors at the Torquay site	121
Figure 6.36 Five-year average-monthly suctions along top sensors versus distance from the centerline of highway at the Torquay site	122
Figure 6.37 Suctions along horizontal top sensors at the Bethune site	123
Figure 6.38 Two-year average suctions versus time along horizontal top sensors at the Bethune site	123
Figure 6.39 Two-year average suctions at top sensors versus distance from the centerline of highway at the Bethune site	124
Figure 6.40 Suctions along horizontal middle-depth sensors at the Torquay site	125
Figure 6.41 Five-year average suctions versus time along horizontal middle-depth sensors at the Torquay site	125
Figure 6.42 Five-year average suctions at middle-depth sensors versus distance from the centerline of highway at the Torquay site	126
Figure 6.43 Suctions along horizontal bottom sensors at the Torquay site	127
Figure 6.44 Five-year average suctions versus time along horizontal bottom sensors at the Torquay site	127
Figure 6.45 Five-year average suctions at bottom sensors versus distance from the centerline of highway at the Torquay site	128
Figure 6.46 Summary of suctions at horizontal grid-lines for years 2001 to 2005 at the Torquay site	129
Figure 6.47 Suctions along horizontal middle-depth sensors at the Bethune site	130
Figure 6.48 Two-year average suctions versus time along horizontal bottom sensors at the Bethune site	130
Figure 6.49 Two-year average suctions at middle-depth sensors versus distance from the centerline of the highway at the Bethune site	131

Figure 6.50 Summary of suctions along different horizontal grid-lines for years 2001 to 2002 at the Bethune site	132
Figure 6.51 Contour map of average suction in April at the Torquay site	133
Figure 6.52 Contour map of average suction in July at the Torquay site	133
Figure 6.53 Contour map of average suction in September at the Torquay site	134
Figure 6.54 Contour map of average suction in May at the Bethune site	135
Figure 6.55 Contour map of average suction in July at the Bethune site	135
Figure 6.56 Contour map of suctions in September at the Bethune site	136
Figure 6.57 Response of suction to rainfall at Sensor T3-10 in May, 2004 and 2005	137
Figure 6.58 Response of suction to rainfall at Sensor T3-10 in June 2004	137
Figure 6.59 Response of suction to rainfall at Sensor T3-10 in October 2004	138
Figure 6.60 Response of suction to rainfall at Sensor T3-10 in October 2005	138
Figure 6.61 Response of suction at Sensor T3-11 in July 2004 and 2005.	139
Figure 6.62 Response of suction at Sensor T3-10 (0.3 m deep under the shoulder) to rainfall and temperature in November.	140
Figure 6.63 Response of suction at Sensor T1-5 (2.2 m deep under the driving-lane) with rainfall and temperature in December 2003 and 2004	140
Figure 6.64 Response of suction at Sensor T2-6 at temperatures less than zero in April 2001 and 2002.	141
Figure 6.65 Response of suction at Sensor T2-7 at temperatures less than zero in April of 2001 to 2005 at the Torquay site.	142
Figure 6.66 Suction and temperature versus time at Sensor T1-1 in September of 2002 to 2004 at the Torquay site	143
Figure 6.67 Suction and temperature versus time at Sensor T1-1 in October of 2001 to 2004 at the Torquay site	143
Figure 6.68 Suction and temperature cycles at sensors T1-1 and T1-2 at the Torquay site	144
Figure 6.69 Suction and temperature cycles at sensors B1-1 and B1-2 at the Bethune site	145
Figure 7.1 Variations in suction with rainfall and time along vertical grid-line under the driving-lane at the Torquay site	147
Figure 7.2 Average matric suctions over 5 years (2001 to 2005) and 5-year average rainfall versus time, under the driving-lane at the Torquay site	148
Figure 7.3 Variations in suction with rainfall and time along a vertical grid-line under the shoulder at the Torquay site	149

Figure 7.4 Average matric suctions over 5 years (2001-2005) and 5-year average rainfall versus time, under the shoulder at the Torquay site	150
Figure 7.5 Variations in suction with rainfall and time along a vertical grid-line under the side-slope at the Torquay site	151
Figure 7.6 Average matric suctions over 5 years (2001-2005) and 5-year average rainfall versus time under the side-slope at the Torquay site	151
Figure 7.7 Variations in suction with rainfall and time along horizontal top sensors at the Torquay site	153
Figure 7.8 Average matric suctions over 5 years (2001-2005) and 5-year average rainfall versus time, along horizontal top sensors at the Torquay site	153
Figure 7.9 Variations in suction with rainfall and time in June and July 2005, along horizontal top sensors at the Torquay site	154
Figure 7.10 Matric suctions versus time and rainfall in June and July 2002, along horizontal top sensors at the Bethune site	154
Figure 7.11 Variations in suction with rainfall and time along horizontal middle-depth sensors at the Torquay site	155
Figure 7.12 Average matric suctions over 5 years (2001-2005) and 5-year average rainfall versus time along horizontal middle-depth sensors at the Torquay site	156
Figure 7.13 Variations in suction with rainfall and time along horizontal middle-depth sensors at the Bethune site	156
Figure 7.14 Variations in suction with rainfall and time along horizontal bottom sensors at the Torquay site	157
Figure 7.15 Variations in suction with rainfall and time along horizontal bottom sensors at the Bethune site	158
Figure 7.16 Average matric suctions over 5 years (2001-2005) and 5-year average rainfall versus time, along horizontal bottom-depth sensors at the Torquay site	158
Figure 7.17 Contour map of five-year average matric suctions in October at the Torquay site	159
Figure 7.18 Variations in suction with rainfall and time under the side-slope at the Torquay site	160
Figure 7.19 Variations in suction with rainfall and time at Sensor T4-13, from May to September at the Torquay site	161
Figure 7.20 Variations in suction with rainfall and time at Sensor T4-14, from May to September at the Torquay site	161
Figure 7.21 Variations in suction with rainfall and time under side slope at the Bethune site	162
Figure 7.22 Effects of thawing on matric suction measurement during “spring break-up” at Sensor T2-7 (0.8 m deep) under the driving-lane at the Torquay site	163

Figure 7.23 Soil-water characteristic curve for soil at depths of 0.10 to 0.25 m at the Torquay site	164
Figure 7.24 Matric suctions at the sensors closest to the borehole at the Torquay site in September 2004	165
Figure 7.25 Matric suction versus temperature in October 2001 at Sensor T1-5	166
Figure 7.26 Matric suctions versus temperature in November 2001 at Sensor T1-1	167
Figure 7.27 Correlation between a rainfall event and matric suctions at Sensor B4-14, at depth of 1.1 m under the side-slope	168
Figure 7.28 Non-recoverable erratic readings of Sensor B3-12 from January 1, 2002	169
Figure 7.29 Recoverable readings at Sensor B5-16 from August 2, 2001	169

CHAPTER 1

INTRODUCTION AND FIELD STUDIES

1.1 Background

The strength of a soil depends on effective stresses as reflected in total stresses and negative pore-water pressures. The magnitude of the negative pore-water pressure is referred to as soil matric suction. Soil matric suction is an important factor in determining the shear strength of an unsaturated soil. Matric suction can be measured using thermal conductivity sensors. These sensors have proven to be a promising means of measuring field suctions.

The roadways in the province of Saskatchewan, Canada experience harsh weather conditions with the daily low air temperatures falling below 0°C for about six months of a year followed by warm summer months of 22° C average daily high temperature. In the winter, the soil freezes and has a high bearing capacity. When thawing occurs in spring followed by precipitation in summer, the pore-water pressures increase and thus decrease the shear strength of the soil. A re-distribution of pore-water pressures occurs following spring and summer.

During spring break-up, excess pore-water may be trapped within the soil from time to time because the frozen soil immediately under the thawed area does not allow the water to drain downwards. The excess water may not be able to drain laterally because the soil in the shoulders of the road is usually still frozen. The increase in pore-water pressures in the soil reduces the matric suction and the bearing capacity of the highway subgrade.

The pavement structures of most secondary roads can be characterized as “Thin Membrane Surfaces”, (TMS). The subgrades of these low volume roads in Saskatchewan, Canada are usually composed of unsaturated soils. TMS roads consist of a layer of 3-10 cm cold mix asphalt concrete overlying a 1-2 m fill compacted from the native soils. The secondary roads were originally designed and constructed for low volume traffic. However, due to demographic shifts, the rail lines have been abandoned and these roads are now being used to haul various agricultural commodities. It is therefore necessary to study the seasonal changes in the strength of highway subgrades which depend on the distribution of the matric suction in the soil.

In September 2000, Saskatchewan Highways and Transportation (SHT), Government of Saskatchewan, installed sixteen thermal conductivity sensors at each of two locations in Southern Saskatchewan; namely, Bethune and Torquay, to monitor *in situ* matric suctions under the roadways Marjerison (2001). These sensors recorded and retrieved both soil temperature and matric suction data. The data acquisition was performed on site and controlled from the SHT office in Saskatoon. Unfortunately, the monitoring work at Bethune was terminated as of 30 September 2002 due to flooding after two years in operation. However, the sensors at the Torquay site have all been working well and the data are still being collected.

Other attempts had been made in the past to use thermal conductivity sensors for measurement of soil matric suction in highway subgrades. However, due to limitations in the equipment and technical difficulties, the matric suction measurements were terminated within a short time. Further details related to past attempts to measure soil suctions are described in the literature review found in Chapter 2. The long term suction measurement program at the Torquay site is unique and provides a valuable and a large volume of the field data set for researchers.

Tan (2004) studied the temperature changes recorded from the thermal conductivity sensors at the Bethune and Torquay sites. The temperature variations can be combined with soil suction measurements to show the cyclic changes in soil strength under the highway subgrades.

This thesis presents and interprets the long-term soil suction measurements made using the thermal conductivity sensors between the years 2000 to 2005 at Bethune and Torquay, Saskatchewan.

1.2 Objectives and scope of thesis

Objectives

The objectives of this thesis are:

1. to analyze and present the measured suction data of highway subgrade over the past five years,
2. to apply necessary corrections to the data and interpret the matric suctions with respect to the rainfall,
3. to carry out field investigations and a laboratory testing program in order to better understand soil conditions at both the sites, thus aiding in the interpretation, and
4. to discuss the role of the thermal conductivity sensor in the long term measurement of matric suction.

Scope of thesis

The collected soil suction measurements used in this study are the data from Bethune and Torquay. The laboratory test program was carried out at the geotechnical research laboratory of the University of Saskatchewan.

This research project is not intended to compare or verify the data collected from other sites.

Future Research

Based on the results of this thesis, it is anticipated that the soil suctions below thin membrane highway pavements at Bethune and Torquay can be predicted using numerical modeling techniques and the results can be compared with the measured values.

1.3 Methodology

The methodology used in this thesis is as follows.

1. The field data including temperatures and voltage outputs were obtained, calculated and corrected to provide the best possible values for *in situ* matric suction. These soil suction data were then presented versus time, depth from the ground surface and distance from the highway centerline as well as plotted on contour maps. The trends of the matric suction changes were interpreted using rainfall and temperature data collected from Environment Canada;
2. A field investigation including drilling, sampling and site description was carried out to characterize the encountered soil conditions at both the sites;
3. A laboratory testing program composed of determining the soil-water characteristic curves and associated geotechnical properties was conducted to better understand the geotechnical conditions of the sites. The field investigation and laboratory testing programs supported the interpretation of the suction data; and
4. A study of the performance of the thermal conductivity suction sensors consisted of calibrating and evaluating several new thermal conductivity sensors. This part of the study allowed for a better understanding of the collected field data.

1.4 Thesis layout

The thesis consists of seven chapters. A brief description of each chapter is given below.

Chapter 1: Introduction

Chapter 1 introduces the main objectives of the thesis along with background information related to the thesis and information on previous field studies related to the two sites of interest to this research.

Chapter 2: Literature Review

Chapter 2 reviews the relevant literature related to soil suction theory and typical soil suction profiles, thermal conductivity sensor background and the history of *in situ* installation of the thermal conductivity sensor and the measurement of soil suction. Measurement difficulties associated with the use of thermal conductivity sensors including the effects of changes in ambient temperature, hysteresis and freeze-thaw cycle are discussed in this chapter.

Chapter 3: Research Program

Chapter 3 provides the overview of the research program that was implemented to analyze, present and interpret the suction data from the field measurements. The procedural outlines for equation verification, matric suction analysis and the presentation of soil suction data are included in this chapter. The field investigation and the collection of the air temperatures and rainfall data are also presented in this chapter.

Chapter 4: Verification of Equations for Suction Calculations and Suction Analysis

Chapter 4 verifies the calibration equations as well as the equations for ambient temperature and hysteresis corrections. This chapter describes the assumptions and procedural analysis to convert the voltage outputs from the thermal conductivity sensors to matric suction values.

Chapter 5: Presentation of Laboratory Test Results and *In situ* Suctions Calculated Using the Main Hysteresis Loop with No Temperature Correction

Chapter 5 presents the *in situ* uncorrected soil suctions. The laboratory test results and weather data are also given in this chapter.

Chapter 6: Presentation of *in situ* corrected soil suctions

Chapter 6 presents the *in situ* soil suctions on vertical and horizontal grid-lines. The vertical grid-lines show the trend of matric suction changes with depth. The horizontal grid-lines present the mechanism of suction changes with distance from the highway centerlines. The monthly-average matric suctions in the highway subgrades are plotted on contour maps. To investigate the sensor response to a rainfall event, the matric suctions are presented in small time scales (i.e., daily data). The temperatures of

surrounding soil are shown along with the matric suctions to demonstrate the effects of the freeze-thaw cycle and the ambient temperature on the suction measurement using thermal conductivity sensors.

Chapter 7: Interpretation and Discussion of Matric Suction Distribution

Chapter 7 interprets the long-term data with time and with respect to micro-climatic conditions and the limitations of the thermal conductivity sensors.

Chapter 8: Conclusions and Recommendations for Future Research

Chapter 8 summarizes and discusses the results obtained from the research.

1.5 Field studies analyzed

The following section provides background information on the two test sites and on the previous studies related to the sites.

Site location

The sensor installation sites were chosen because these locations had temperature thermistors previously installed in the subgrades of TMS. In addition, the two sites, among the four originally tentative sites (i.e., Bethune, Torquay, Bengough and Consul) in Southern Saskatchewan, met the criteria of maximum sunshine so that the sites would experience thawing at the earliest possible time. The SHT determined the matric suction sensors would be 5.0 m distant from the existing thermistor installation at the sites. This would ensure sufficient distance to prevent any damage to the thermistor installation, but would also be sufficiently close together to consider the site conditions to be essentially the same (Marjerison, 2001).

The locations of the two sites are as follows:

- Site 1: 3.5 km north of Bethune on highway No 354, and
- Site 2: 8.6 km south of Torquay on highway No 350.

The map showing the site locations can be seen in Figure 1.1 and a picture of the TMS highway at Bethune is presented in Figure 1.2.



Figure 1.1 A map with field sites of Bethune and Torquay



Figure 1.2 The TMS highway at the site of north Bethune, Saskatchewan

Schematic installation of the sensor

Sixteen sensors were installed each test site. The sensors were placed beneath the pavement, shoulder and side-slope to monitor suction changes resulting from micro-climatic changes within the subgrade. The installation layout of the sensors on a highway cross-section is shown in Figure 1.3. The sensors at the Torquay site are denoted by a prefix T (e.g. T1-1) and with a prefix B (e.g. B1-1) for the sensors at the Bethune site.

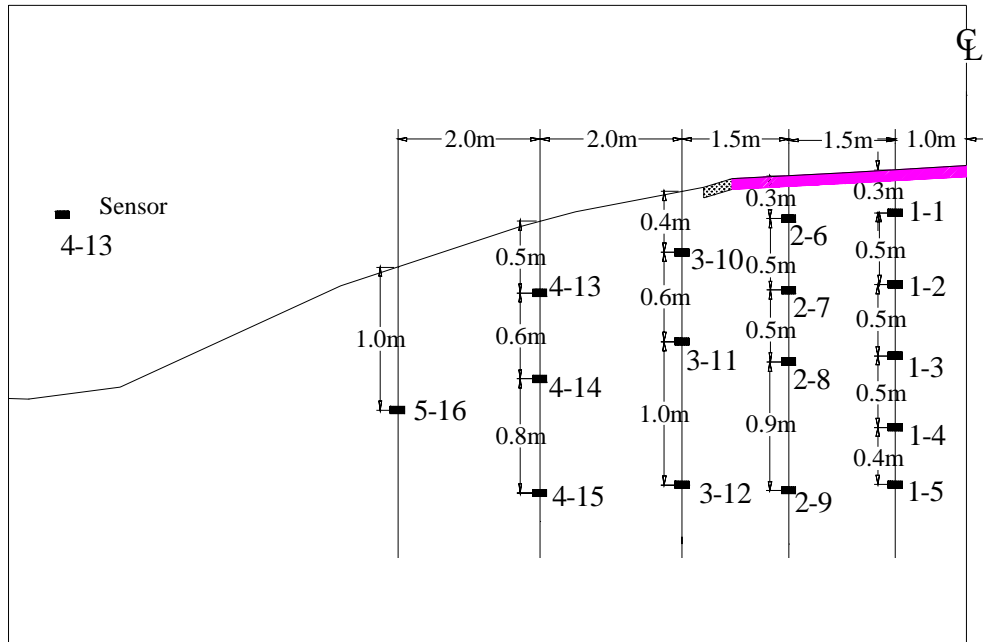


Figure 1.3 Installation layout of sensors on a highway cross-section (modified from Marjerison 2001)

Equipment

The main components of the field measurement system and the schematic connections are presented in Figure 1.4.

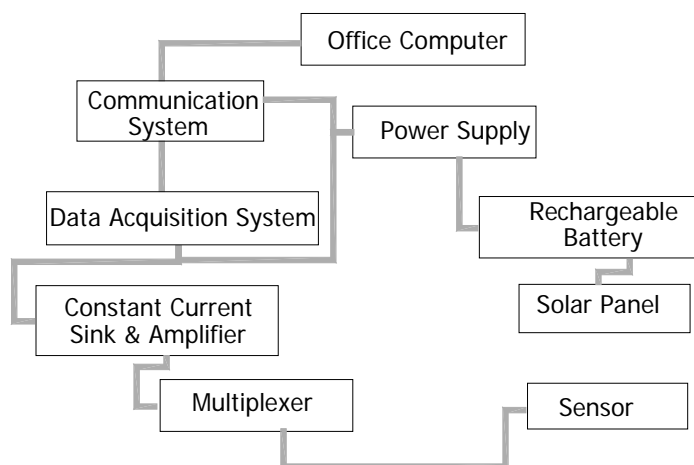


Figure 1.4 Schematic illustration of wiring connection of the system

The sensors were manufactured at the University of Saskatchewan and called the University of Saskatchewan thermal conductivity sensors. These sensors are connected to the multiplexer. The multiplexer of the system monitors and controls the various sensor readings. The multiplexer is positioned between the sensors and the constant current sink and amplifier. Relays are utilized to switch between desired sensor signals.

In Figure 1.4, the constant current sink and amplifier are used to ensure precision of the heating voltage by maintaining a 200 mA current for the heater resistor. The constant current sink and amplifier compensates for varying lengths of extension wires. Temperature changes of the surrounding environment leading to changes in heating resistance are also minimized by the constant current sink and amplifier. The output signals from the sensors are amplified, isolated and filtered through the constant current sink and amplifier then stored in the datalogger.

The datalogger, CR10X, can hold 60,000 data values for the *in situ* measurement. The datalogger supplies real-time information at designated intervals and reduces data saving storage space and minimizing the post processing work on the data. The datalogger is connected to the computer through either telephone line or cellular phone and a modem. The function of the cellular phone package is to send and receive signals while the modem transfers data files. The software for the CR10X is able to observe a poor electrical connection and retransmit incorrectly received blocks of data. A picture of the data logger is shown in Figure 1.5.



Figure 1.5 Data acquisition system in place (Marjerison 2001)

A continuous power supply for long durations is important for the datalogger; therefore, a solar power was set up as an option of providing power. A picture of the solar panels is presented in Figure 1.6.



Figure 1.6 Solar panels at the site of north Bethune, Saskatchewan

Field sensor installation

The first step towards the sensor installation was to excavate a 2.4 m-depth trench using a backhoe. An electric drill was then used to make holes to house the sensors. The sensors were inserted into the holes using a special tool called Custom Built Insertion Tool (Figure 1.7). Once the drilling for the holes was completed, compressed air was used to remove any loose debris from the sensor hole. After the installation of the sensors was completed (Figure 1.8), a tamping dowel was used to backfill and compact soil around the lead wires.



Figure 1.7 Custom sensor insertion tool (Marjerison 2001)



Figure 1.8 Sensor installation on site (Marjerison 2001)

The functioning of the system was verified by connecting the installed sensor to the multiplexer and recording a sensor reading. The results were compared to the calibration curve to determine whether the system was functioning properly. The system was deemed satisfactory if readings matched with dry condition in the laboratory.

The field sensor installation was connected to the data acquisition system, DAS. Soil matric suction readings and temperatures were continuously monitored and controlled at remote locations over a long time period.

Analysis of field temperature data

Tan (2004) obtained the field data from September 2000 until July 2002 to analyze the changes in temperature at both test sites. The temperature changes were presented with time and position on the highway cross-section. An uncoupled two-dimensional heat transfer numerical simulation was conducted to compare with the field readings and to predict the temperature changes during freezing. As a result, a soil freezing profile was proposed that was useful to explain the interruption of suction readings from the sensors during winter months.

Tan (2004) also concluded that there was a time lag for deeper sensors to reach peak temperatures. The same trends of temperature change for the sensors were observed in the same horizontal plane. The fluctuations of temperature happened with the same cycle, frequency and amplitude each year. However, the temperatures were more variable with time at shallower depths than at greater depths. In addition, the shallowest sensors provided more fluctuations in the readings of temperature than the deeper sensors. This assisted in understanding the mechanism of change in matric suctions. In light of these results, Tan (2004) suggested that the freezing profiles could possibly be used to improve the implementation of road bans limiting loads caused by vehicular traffic.

CHAPTER 2

LITERATURE REVIEW

Relevant literature related to the theory of soil suction and typical suction profiles are mentioned to clarify practical applications in this thesis. The background of thermal conductivity suction sensors is also summarized to help understand the collected field data. Some difficulties associated with the suction sensor measurements are briefly discussed.

2.1 Suction theory and typical soil suction profiles

Suction theory

Soil suction is related to the free energy of the soil-water (Edlefsen and Anderson, 1943). The soil suction evaluated in terms of the relative humidity, is referred to as the total suction. Total suction consists of two components; namely matric suction and osmotic suction as defined by Aitchison (1965) as follows:

“Matric suction (capillary component): The equivalent suction derived from the measurement of the partial pressure of the water vapor, relative to the partial water vapor on the soil-water, to which a solution identical in composition with the soil-water must be subjected in order to be in equilibrium with the soil-water.”

“Osmotic suction (solute component): The negative gauge pressure to which a pool of pure water must be subjected in order to be in equilibrium with a pool containing a solution identical in composition to the soil-water.”

Total suction is equal to the sum of matric and osmotic suctions.

In addition to the three independent phases: solid, liquid and air that are ascribed to soil, a fourth phase has been postulated as being of importance in understanding the behaviour of unsaturated soils. Fredlund and Morgenstern (1977) considered the air water interface as the fourth and independent phase. Padday (1969) referred to the air-water face as the “contractile skin” in the surface chemistry literature. Hence, an element of an unsaturated soil can be studied as a mixture with two phases (solid and contractile skin) coming to equilibrium under applied external stresses and another two (air and water) flowing under applied external stress. As a result, the contractile skin provides an isotropic stress to the pore-water pressure. Unsaturated soils possess negative pore-water pressures which create tension at all air-water interfaces inside a soil. The surface tension associated with the contractile skin of an unsaturated soil pulls solid particles together providing additional strength to the soil. The difference between the pore-air pressure (u_a) and negative pore-water pressure (u_w) in unsaturated soils is greater than zero and is referred to as soil matric suction. Soil matric suction is an important stress state variable in unsaturated soil mechanics.

In most geotechnical engineering practice, the changes in osmotic suction are insignificant and can be simulated in laboratory testing (Fredlund and Rahardjo, 1993). Therefore, total suction can generally be replaced by matric suction in solving geotechnical engineering problems.

Typical soil suction profile

Maximum changes of suction can be observed near the ground surface. The evapotranspiration from vegetation leads to the removal of water from the soil, resulting in an increase in the matric suction. When the water table is close to the ground surface the matric suction may possibly be higher than when the water table is deeper (Figure 2.1).

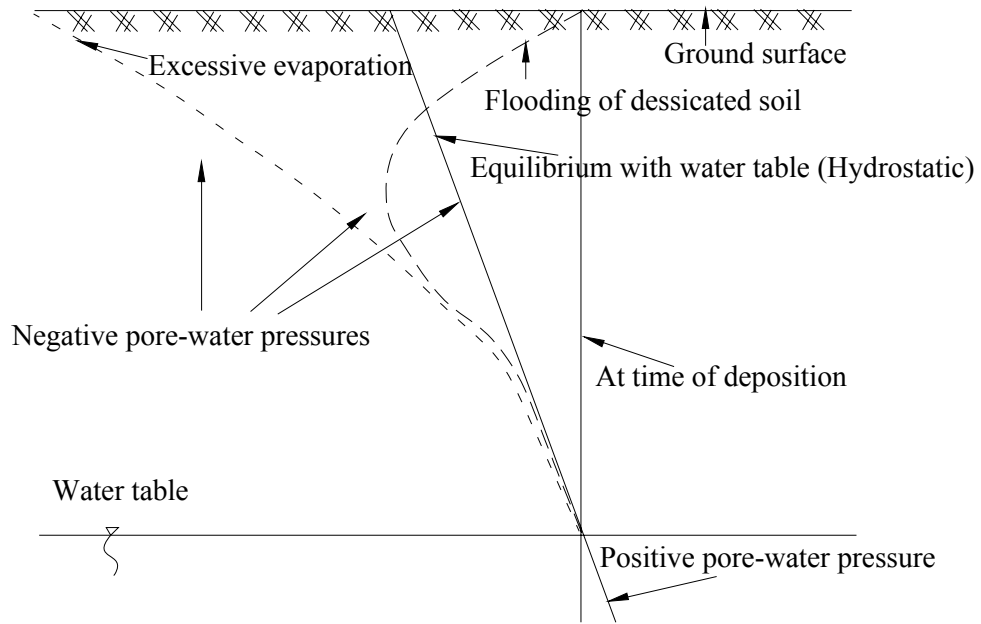


Figure 2.1 A typical soil matric suction profile (Fredlund and Rahardjo, 1993)

Aitchison and Holmes (1961) reported soil suction results in subgrade soil for a site in Southern Australia. Basic preliminary data showed a sharp distinction between uncovered and covered soil as shown in Figure 2.2. The suction profile beneath the pavement centerline was shown to be stable with environmental changes. The variation in suction with depth is somewhat more pronounced for uncovered soils. The soil suction profile below an uncovered ground surface may be strongly influenced by environmental changes.

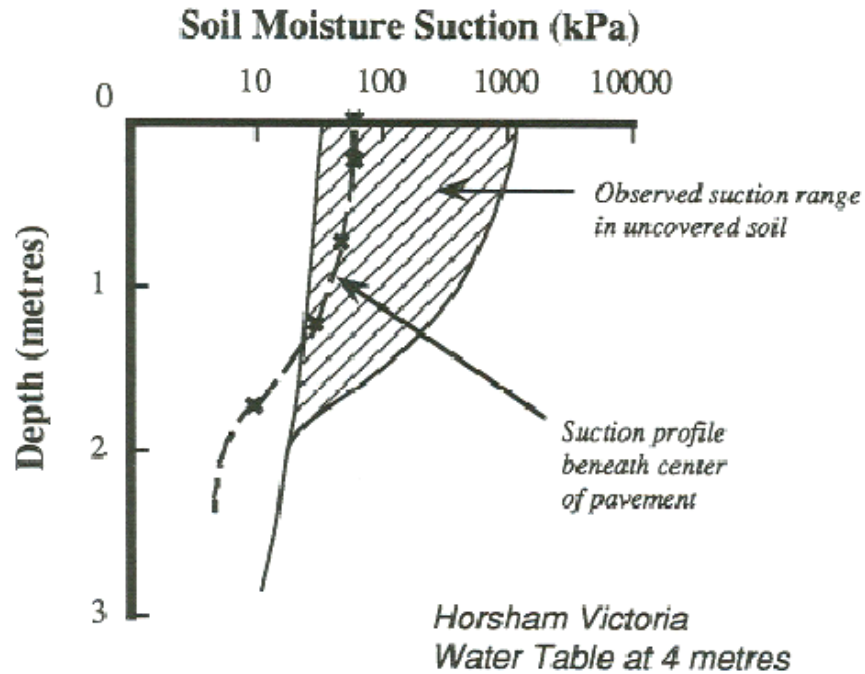


Figure 2.2 Suction profiles in a highway subgrade (Aitchison and Holmes 1961)

Blight (1980) presented several factors influencing soil suction profile. These factors are ground surface conditions, environmental conditions, vegetation, water-table position and permeability of the soil profile.

Rahardjo et al. (2001) used tensiometers to measure suction in soils under a slope in Singapore (Figure 2.3). The purpose of the study was to better understand environment-induced slope failure. It was concluded that the changes in suction responding to rainfall, infiltration and evapotranspiration processes are variable in space and time and are largely influenced by dynamic climatic conditions, soil properties and vegetation.

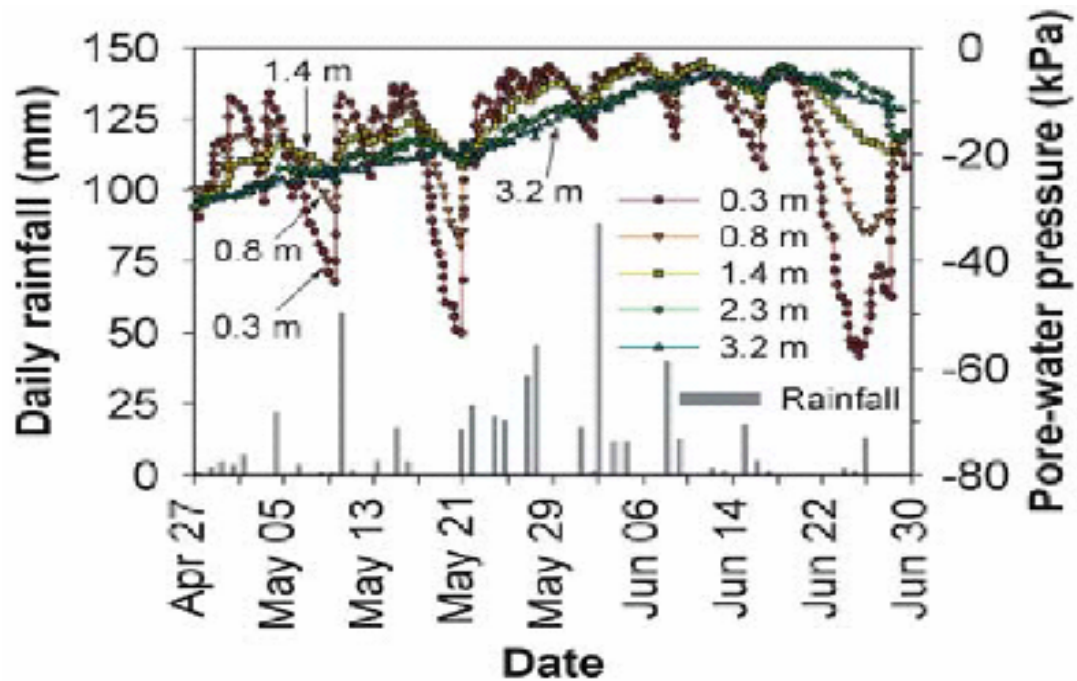


Figure 2.3 Variations in matric suction with rainfall and time obtained from tensiometers (Rahardjo et al. 2001)

2.2 Field suction measurement, thermal conductivity sensor and history of *in situ* sensor installations

Obtaining suction measurements in the field is a challenging task for researchers and practicing engineers due to various limitations of the equipment, laborious procedures, and the cost of currently available devices. Most common methods of *in situ* suction measurements include filter papers, tensiometers, and thermal conductivity sensors. The method of suction measurement, component of suction measured, range of suctions, and constraints associated with these methods are summarized in Table 2.1. The information provided in Table 2.1 points out the limitations associated with each method. Thermal conductivity sensors are highly promising for field applications due to low maintenance costs, durability, reasonable accuracy of measurements, ability to automate data acquisition, for being unaffected by salinity and soil type, and reasonable cost (Lee 1984). Previous testing on the sensors has shown that the suction sensors are accurate in measuring soil suction between 5 kPa and 1500 kPa with a coefficient of

variation less than $\pm 5\%$ (Fredlund et al. 2000). No other soil suction measuring device has been shown to have this accuracy over the entire suction range. The applied suctions used in calibrating the sensors are the most reliable means available for the evaluation of the suction sensors. Fredlund et al. (2000) installed a University of Saskatchewan sensor into a soil specimen in the laboratory to measure soil suctions. The results presented in Figure 2.4 shows that good agreement was obtained between the soil suction measured by thermal conductivity sensors and by tensiometer in the low suction range.

Table 2.1 Techniques for *in situ* measurement of matric suction (Fredlund and Rahardjo 1993)

Device	Method (Property Measured)	Suction measured	Range (kPa)	Principal constraints
Filter paper (in-contact)	Indirect (Water content)	Matric	Entire range	Automation of the procedure is impossible.
Standard tensiometer	Direct	Matric	0 to 90	Requires daily maintenance. Temperature fluctuations affect readings. Slow to equilibrate in highly plastic soils.
Porous block (Gypsum, nylon, fiberglass)	Indirect (Electrical resistance)	Matric	30 to 3000	Observations need to be corrected for temperature. Blocks are subject to hysteresis. Response to suction can be slow.
Heat dissipation sensors	Indirect (Thermal conductivity)	Matric	0 to 10,000 \pm	High failure rate. Fragile.
Osmotic cell	Indirect (Osmotic pressure of solutions)	Osmotic	Unknown	Unknown.

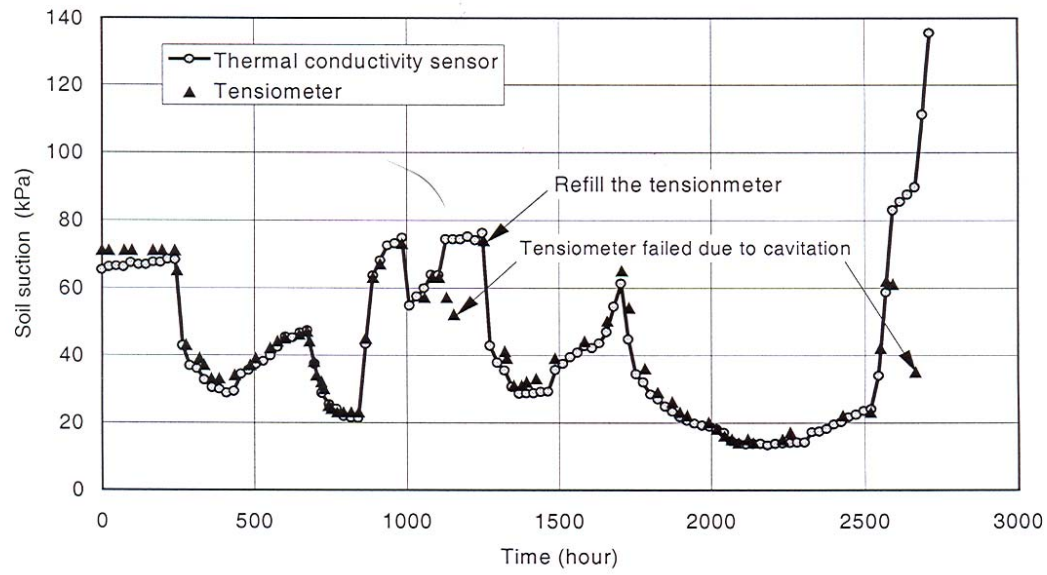


Figure 2.4 Variation of soil suction with time measured using tensiometers and thermal conductivity sensors (Fredlund et al. 2000)

To understand the operation of thermal conductivity sensors, some thermal properties of materials involved are reviewed.

Thermal properties of material

The important thermal properties of a material are: thermal conductivity (λ), specific heat capacity (C_p) and thermal diffusivity (D). Simple definitions and typical values are as follows:

Thermal conductivity is an ability of a substance to conduct heat. The thermal conductivity can be expressed in $W/m^{\circ}C$ and given the symbol λ .

The specific heat capacity of a substance is the heat capacity per unit of mass, measured in joules per kilogram per degree Celsius $C_p(J/^{\circ}Ckg)$.

The thermal diffusivity is a measure of transient heat flow and is defined as the thermal conductivity divided by the product of specific heat and density. When dynamic processes are involved, the change of temperature versus time is known at the boundary conditions and is controlled by both thermal conductivity and heat capacity:

$$D = 1 / \rho * C_p \quad (2.2)$$

The formula for the heat flux is:

$$f = \lambda * \Delta T \quad (2.3)$$

Thermal conductivity should be noted as a property that presents a semi static condition when the temperature gradient is assumed to be constant. Once the temperature starts changing other parameters enter the equation. This partly explains why it is difficult to measure thermal conductivity. Ideally thermal conductivities should be measured under steady state conditions. This is not easy because it requires a carefully planned laboratory experiment and time to come to equilibrium.

There are a number of techniques that can be used to measure thermal conductivity. The “steady-state” techniques perform a measurement when the material that is studied is in equilibrium, making the process of signal analysis easy (i.e., steady state implies constant signals). The disadvantage is that it takes a long time to reach the required equilibrium. The “non-steady-state” techniques perform a measurement during the process of heating up. The advantage is that measurements can be made more quickly.

Typical values of thermal conductivities for materials and soils are tabulated in Tables 2.2 and 2.3.

Table 2.2 Orders of magnitude of the thermal conductivity (from Hukseflux 2005)

	Thermal conductivity at 20° C W/mK	Density at 20° C Kg/m ³	Volumetric heat capacity at 20° C 10 ⁶ J/m ³	Thermal diffusivity at 20° C 10 ⁻⁸ m ² /s
Air	0.025	1.29	0.001	1938
Water	0.6	1000	4.180	14
Ice	2.1	917	2.017	104
Plastic insulation materials	0.03	50	0.100	30

Table 2.3 Thermal conductivity values for soils (from Hukseflux 2005)

Saturated soil	0.6 to 4 W/mK
Sand perfectly dry	0.15 to 0.25 W/mK
Sand saturated	2 to 4 W/mK
Clay dry to moist	0.15 to 1.8 W/mK
Clay saturated	0.6 to 2.5 W/mK

Theory of thermal conductivity sensor operation

Thermal conductivity sensors indirectly measure the soil matric suction by measuring the thermal conductivity of a standard ceramic sensor. A thermal conductivity soil suction sensor consists of a cylindrical porous tip containing a miniature heater and a temperature-sensing element (Phene et al. 1971). Figure 2.5 shows the structure of a thermal conductivity sensor developed at the University of Saskatchewan (Shuai et al. 1998). The porous tip is a specially designed and manufactured ceramic with an appropriate pore-size distribution corresponding to the range of soil suctions to be measured. The heater at the centre of the ceramic tip converts electrical energy to thermal energy. The temperature sensor (i.e., IC in Fig 2.5) measures the temperature rise with respect to time in terms of output voltage. Water can move in and out of the sensor ceramic (altering the degree of saturation of the sensor

and hence its thermal conductivity) allowing the sensor to come into equilibrium with the surrounding soil.

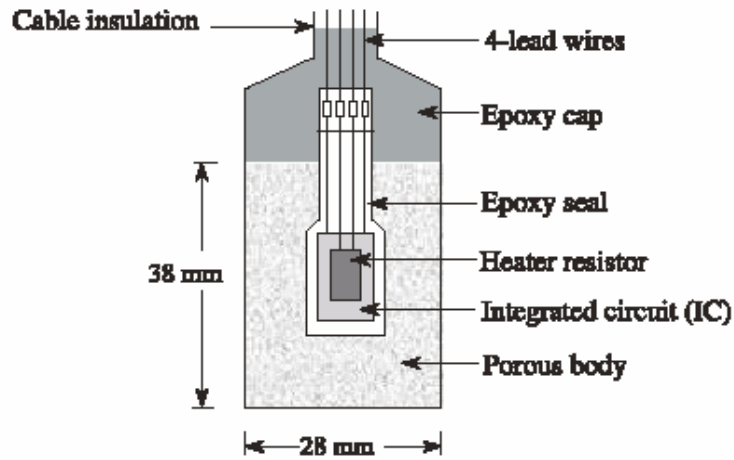


Figure 2.5 Cross-section of a thermal conductivity sensor (Shuai et al. 1998)

For a sensor made of porous material, the thermal conductivity of the sensor depends on the proportion of the material that is pore space as well as the proportion that is filled with water. Phene (1970) concluded that the thermal conductivity of the sensor increases exponentially with water content. The wetter the sensor, the greater the thermal conductivity, the more heat that is dissipated, and the lower the temperature rises. The sensor precision for suction measurements is based on the ratio of the conductivity of the sensor when it is dry to that when the sensor is saturated. Therefore, this ratio should be as large as possible. The thermal conductivity of the sensor is an important factor when choosing suitable materials for sensor matrices. Another important factor when developing sensor is the distribution of pore space. Some large pores are necessary so that the sensor can desaturate under low suctions. From these two considerations a suitable ceramic can be selected for a sensor. The sensor is heated using a heat pulse and the temperature rise is measured. The heating pulse must entirely be contained within the sensor so that the thermal properties of the surrounding soil do not come into consideration. However, it is desirable to keep the size of the sensor as small as possible to reduce the time for a sensor to come to equilibrium. If the minimum radius of the porous block is determined, the diameter must be sufficient to store the heat pulse of the sensor when it is dry. The temperature is measured by the sensing

element after a specific time interval and its magnitude is inversely proportional to the water content of the porous block. For some types of the sensor, temperature rise can also be expressed as a voltage output. A laboratory calibration curve between sensor output (temperature rise) and matric suction must be developed in order to later measure the matric suction in the soil.

Suction sensor development

Extensive studies have been done on the use of heat dissipation of a porous medium as an index of the amount of water present. In one of the earliest studies, Shaw and Baver (1939) installed the temperature sensor-heater directly into a soil. In this case, separate calibrations had to be made for different soils.

Richards (1955) developed an electro-thermal element for measuring water content in porous media. With this element, a resistance thermometer was wrapped with a small heating coil. The element was put into a porous cup and coated with ceramic cement. Richards recommended the ceramic cup have an air entry value less than 10kPa.

Bloodworth and Page (1957) used a nonlinear thermistor temperature sensor to measure temperature change. A separate calibration or a correction curve was required at different temperatures.

Phene et al. (1970) built a thermal conductivity sensor based on a Germanium P-N Diode as a temperature sensor. The heating coil was made up using copper wire sealed by 40-gauge Teflon. The sensing unit was mounted in a porous block. The optimum dimensions of the porous block were calculated on the basis of a theoretical analysis. The block must be large enough to contain the heat pulse during the heating process. The dimensions must be calculated in order to prevent heat dissipation to the surrounding soils. However, the porous block should be as small as possible to reduce the time for the sensor to come to equilibrium with surrounding soils and calibration time as well. The higher the ratio of thermal conductivity and diffusivity, the higher the precision with which the water content can be measured. Research was conducted on

the pore size distribution of material to make up porous blocks by Phene et al. (1970). It was found that the ceramic tip showed a linear correlation between sensor output and suction values and provided a stable solid matrix.

Moisture Control System Inc. manufactured the MCS 6000 thermal conductivity sensor in the mid-1970's. The design and construction procedures were the same as proposed by Phene et al., (1971). It was assumed that the calibration curve was linear from 0 kPa to 300 kPa. When the suction was more than 300 kPa, its values were empirically extrapolated. Therefore, the calibration procedure could be implemented using 1-point calibration. The MCS 6000 sensor was used both in the laboratory and in the field (Lee and Fredlund 1984). The usage for *in situ* measurements was accepted and proved to be a promising device since the thermal conductivity sensor had a relatively low sensitivity to ambient temperature and salinity changes (Lee and Fredlund 1984). The data obtained from the sensor showed close agreement with tensiometer and neutron probe data.

In 1981, Agwatronics Inc. Merced, CA started manufacturing the AGWA thermal conductivity sensors with a design and style proposed by Phene et al. (1970). The sensors were then improved and upgraded to AGWA-II in 1984. But the sensors proved to have some problems with the electronics and the porous block which could be easily damaged. Figure 2.6 shows typical calibration curves for two AGWA-II sensors.

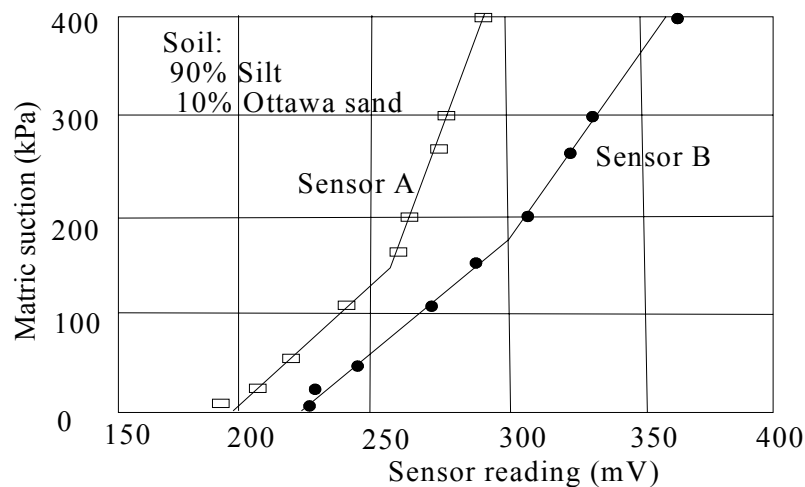


Figure 2.6 Calibration curves for two AGWA-II sensors (Fredlund and Rahardjo 1993)

Later in the 1980's, the sensor was further improved. In 1992 the Center for Irrigation Technology (CIT) of California State University, Fresno (Solomon and Jorgensen 1993) installed AGWA-III soil moisture sensors from Agwatronics midway between the drip-lines to control the irrigation. The sensors were utilized to prevent any irrigation until the soil suction exceeded 20 centibars. The sensor and control system is designed to apply only as little water as is needed to maintain high quality turf. Those sensors proved to function quite well on this project.

In 1997, the University of Saskatchewan developed a thermal conductivity sensor for laboratory testing and field monitoring. A picture of the University of Saskatchewan sensor can be seen in Figure 2.7. There are some characteristics of the sensor design that are superior over other earlier sensors (Fredlund et al. 2000). The ceramic tip was made with high porosity (greater than 60%) and a wide variety of pore sizes (from 0.05 mm to less than 0.0001 mm) so that it could be used to measure a wide range of suctions from 5 kPa to 1500 kPa. Moreover, the relationship between water content and the logarithm of soil suction was nearly linear between 5 and 500 kPa (Fredlund et al. 2000). The University of Saskatchewan (U of S) sensor's electronics were improved using an advanced integrated circuitry for the temperature sensing device. Amplification, isolation and filtering, which are signal conditionings, were applied to make the sensor function better in terms of resolution and accuracy. Figure 2.8 shows temperature change with time due to a heat pulse before and after improvement.

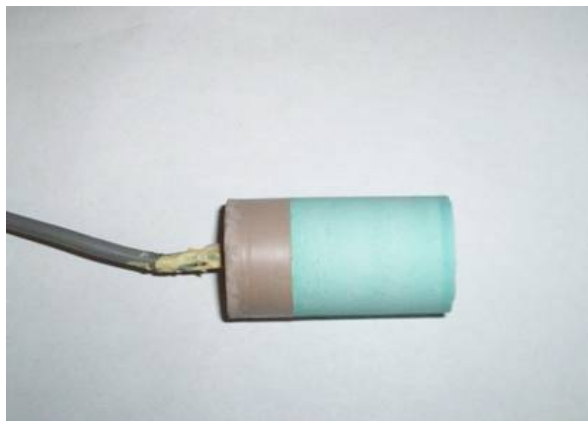


Figure 2.7 The University of Saskatchewan thermal conductivity sensor

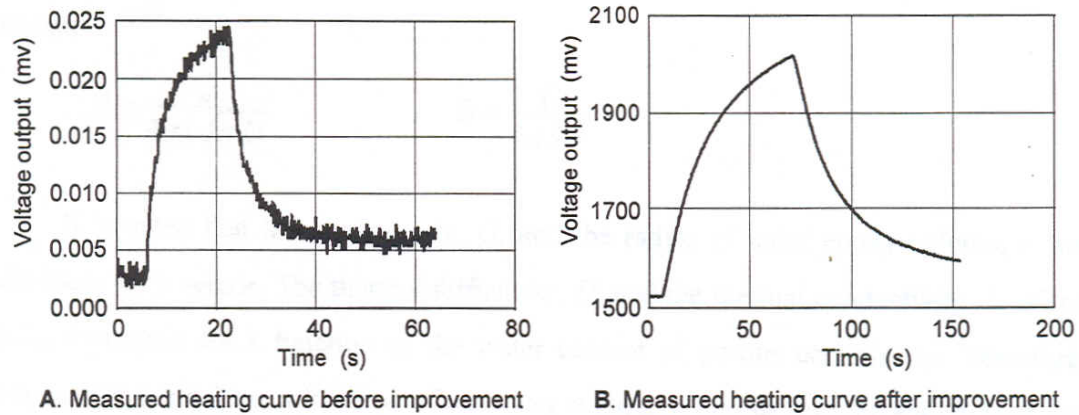


Figure 2.8 Heating curves for U of S thermal conductivity sensor before and after improvement (Shuai et al. 1998)

The main technical specifications for the U of S sensor are tabulated in Table 2.4. There were some drawbacks with the sensors; one was a possible failure of the sensor in moist environments due to ceramic cracking and the other was the sensitivity of the reading to ambient temperature and length of the cables.

Table 2.4 Technical specification (Fredlund et al. 2000)

Measurement parameters	Suction and temperature
Measurement range	Suction from 5 to 1500 kPa Temperature -40°C to 110°C
Accuracy	±5% for suction measurements ±0.5°C for temperature measurement
Resolution	0.33mV
Soil types	Suitable for all soil types
Protection	Suitable for long-term burial
Temperature	0 to 40°C for suction measurement
Power supply	12V ~ 15V DC, 250mA
Size	Diameter: 28mm, Length: 38 mm
Cable length	Standard: 8m, Maximum: 100 m

History of *in situ* sensor installations

van der Raadt et al. (1987) installed the AGWA-II sensors at highways subgrades in western Canada to determine the reliability of the sensor for the measurement of *in situ* matric suction. This research also presented the evaluation of several different methods of measuring subgrade suction. The research concluded that utilization of the thermal conductivity sensor was the most preferable means for measuring soil suction when compared to other forms of available soil suction measurement. The research also showed that the AGWA-II sensor produced interpretable results and could be compatible with a Data Acquisition System (DAS) for collecting data at remote locations.

Khogali et al. (1991) installed twelve AGWA-II sensors in a primary highway in the province of Alberta, Canada. These sensors were instrumented at depths between 0.15 m and 1.15 m in the subgrade of Highway 16 west of Edmonton. Attention had to be paid to prevent the fragile ceramic sensors from being damaged and to ensure good soil-to-sensor contact. The results confirmed the AGWA-II thermal conductivity sensors were promising and potential devices for field matric suction measurements.

Fredlund et al. (1992) carried out *in situ* measurements of soil suction on a railway embankment in Manitoba, Canada using eighteen sensors. The work was done in conjunction with some remedial design of damaged sections of the railway embankment. The eighteen sensors were distributed over four different locations. Two sensors had been broken before the measurement, one during calibration and the other during installation. This required the improvements of the weak material used for the porous ceramic tips as well as great care during calibration and installation. Matric suction readings were collected from September of 1989 to November of 1990. Later, six sensors malfunctioned due to broken or cracked sensor tips or as the breakdown of electronics in the sensor tip due to penetration of water into the heat sensor device. The data collected during the research indicated that the sensors performed satisfactorily in the field. The matric suctions were interpretable with time. This study revealed that there were still further improvements necessary for the sensor tips and the sensor

electronics. For example, it was determined that a stronger ceramic consisting of a wide range of pore sizes was required to eliminate some of the problems associated with the existing sensors. The integrated circuit needed to be improved for future applications.

Loi et al. (1992) used sensors to measure suction on a full-scale track in an indoor controlled environment operated by Saskatchewan Highways and Transportation, Regina, Canada. These tests were used to examine the performance of the thermal conductivity sensors under field conditions. The work consisted of the installation of several sensors at various locations and depths under a pavement structure. The test results indicated that the thermal conductivity sensors produced long-term stable and reliable matric suction readings as long as the sensors were not subjected to long-term positive pore-water pressures. This was due mainly to the alteration of the sensor tip characteristics. Other observed problems resulted from poor backfilling of the sensor holes which provided an avenue for water flow along the sensor leads to the sensors. The vertical installation boreholes for the sensors exaggerated this problem. Desiccation cracking of the subgrade was attributed to the reason for the rapid inflow of water to the sensors. The research conducted also found negative matric suction readings in certain cases during the testing and this resulted in further testing to determine the reasons for such readings. During the research the sensor tips also exhibited deterioration leading to the need for the development of a more durable ceramic for the sensor tip.

Szafron and Fredlund (1992) utilized thermal conductivity sensors and a DAS to monitor matric suction in the subgrade of a gravel road in Saskatoon, Canada. Twenty four thermal conductivity sensors made by Agwatronics Inc. were calibrated in 1990. Fourteen sensors broke during calibration, handling and installation due to overheating of the ceramic tip during the manufacturing process. The remaining ten sensors were sacrificed due to their poor, unreliable quality. These sensors were installed at Site I and the integrity of the sensors and then the accuracy of readings recorded from Site I were later questioned. In May 1991, fourteen new sensors were installed at Site II, approximately 25 m west of Site I. Matric suction measurements from one of these sensors are shown in Figure 2.9. The research concluded that the matric suction below

the shoulder and side-slope of the road was lower than that beneath the traveled portion. The reason given to explain the results was that the shoulder and side slope are exposed to not only rainfall but runoff from the road surface. This runoff was a result of the compaction of the travelled portion of the roadway which made it less permeable. This is also an explanation for failures occurring on shoulders and edges of covered and uncovered roads. The research also pointed out that the suction profile is not constant and is a function of local climatic conditions. Some sensors showed erratic readings. Equipment problems such as poor contact in the relays of the data acquisition system and poor soil-sensor contact could explain irregular behaviors. The suction measurements carried out by Szafron (1991) were terminated after six months of operation due to damage of the data acquisition system.

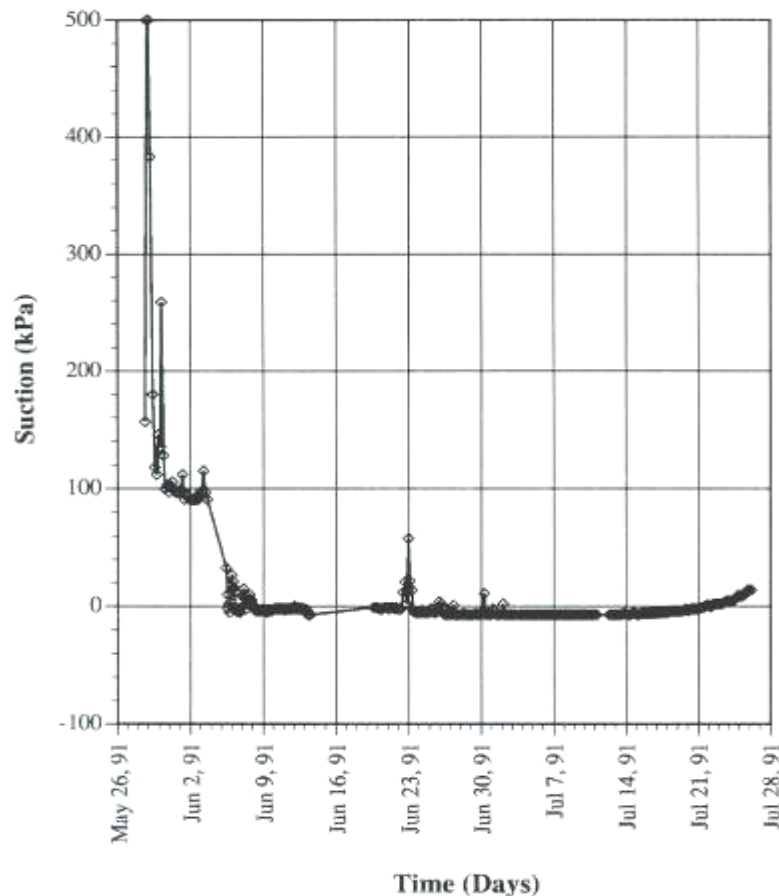


Figure 2.9 Field suction data from one sensor (Szafron 1991)

2.3 Measurement difficulties associated with thermal conductivity sensor

The main factors associated with the accuracy of thermal conductivity sensor measurements described in the literature are due to hysteresis, changes in ambient temperature and freeze-thaw cycles.

Hysteresis in the ceramic

The relationship between the water content of the ceramic and matric suction is hysteretic. For example, the water content at a given soil suction for the wetting path is smaller than that for the drying path. This phenomenon can be represented through the relationship between independent and dependent variables as shown in Figure 2.10. If a process is implemented from A to B, a certain set of independent values along ADB (Figure 2.10) is established. Conversely, if the process is vice versa, (i.e., from B to A), a set of values along BCA is recorded. The changes along the path from B to A (i.e., BCA) are different from the path from A to B (i.e., ADB). The term “hysteresis” describes all phenomena of this type. When a porous medium imbibes or drains immiscible fluids driven by capillary pressures the flow can exhibit hysteresis depending on the direction of flow prior to the point at which a measurement is made. This flow hysteresis caused by capillary pressures is referred to as the capillary hysteresis

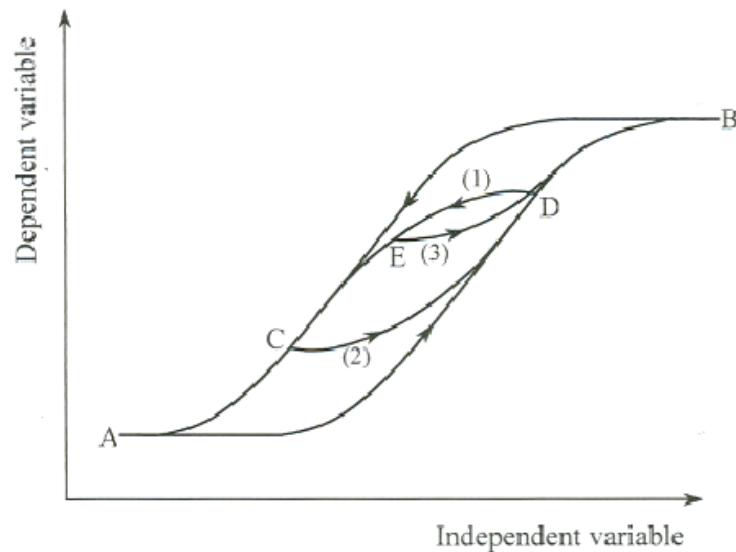


Figure 2.10 A hysteresis process and scanning curves (Feng 1999)

Factors that cause hysteresis in soils include the following (Klausner, 1991):

1. Irregularities in the cross-sections of the void passages or the “ink-bottle” effect.
2. The effect of the contact angle which is greater in an advancing meniscus than in a receding meniscus.
3. Entrapped air or a vacuum condition in advancing or receding menisci and the corresponding soil suction.
4. Thixotropic regain or aging due to wetting and drying history of the soil.

The process of hysteresis can be simplified as shown in Figure 2.11. Two identical capillary tubes with irregular cross sections have different diameters (i.e., $D_1 < D_2$). Each tube diameter corresponds to a certain suction value describing the state of the tube (i.e., dry or saturated), (i.e., $\psi = T_s/D$, where: T_s is surface tension of water). Suppose ψ_1 and ψ_2 are two suction values for two tube diameters, D_1 and D_2 , respectively ($\psi_2 < \psi_1$ because $D_1 < D_2$). The height of the water column represents the magnitude of the soil suction value (i.e., $h = \psi/(\rho_w g)$, where: ρ_w is density of water, g is gravitational acceleration). If two tubes are initially saturated, the tubes will be spontaneously drained when the suction exceeds ψ_1 . Conversely, if two tubes are dry, the tubes will be saturated spontaneously when the suction decreases below ψ_2 . The drying processes depend on the narrow radii of the connecting channel while the wetting processes depend on the maximum diameter of the large tube. The wetting and drying processes of a one-tube two-size system can be simply illustrated in Figure 2-12.

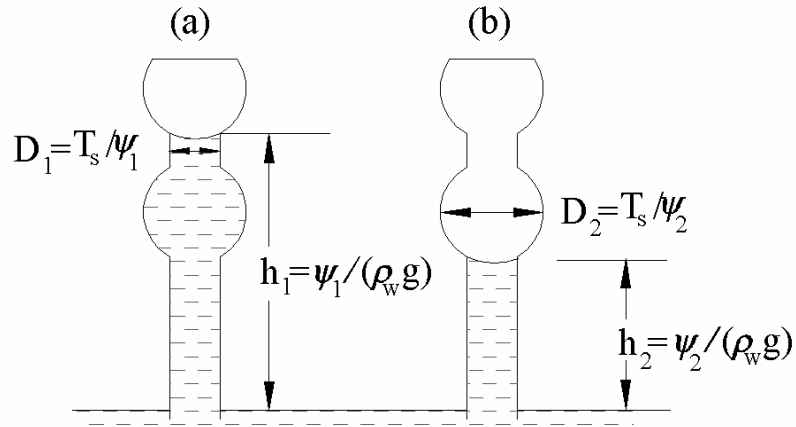


Figure 2.11 Schematic illustration of the “Ink-bottle” effect: (a) the drying process and (b) the wetting process (Hillel, 1980)

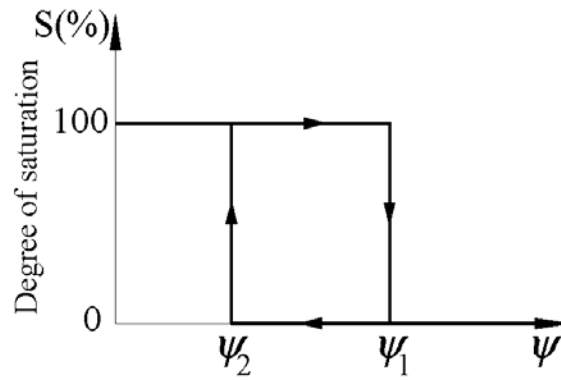


Figure 2.12 Soil-water hysteresis curves for a one-pore size system (Pham, 2002)

The capillary pressure function of a porous medium is defined as the relationship between the content of the wetting fluid and the capillary pressure in the porous medium.

The definitions for different curves showing capillary hysteresis of the matrix in Figure 2.13 are as follows:

1. initial drying curve (starting at saturated water content, θ_s),
2. main drying curve (boundary drying curve, or primary drying curve),

3. main wetting curve (boundary wetting curve, or primary wetting curve),
4. drying scanning curve (primary drying scanning curve),
5. wetting scanning curve (primary wetting scanning curve),
6. second order wetting scanning curve, and
7. third order drying scanning curve.

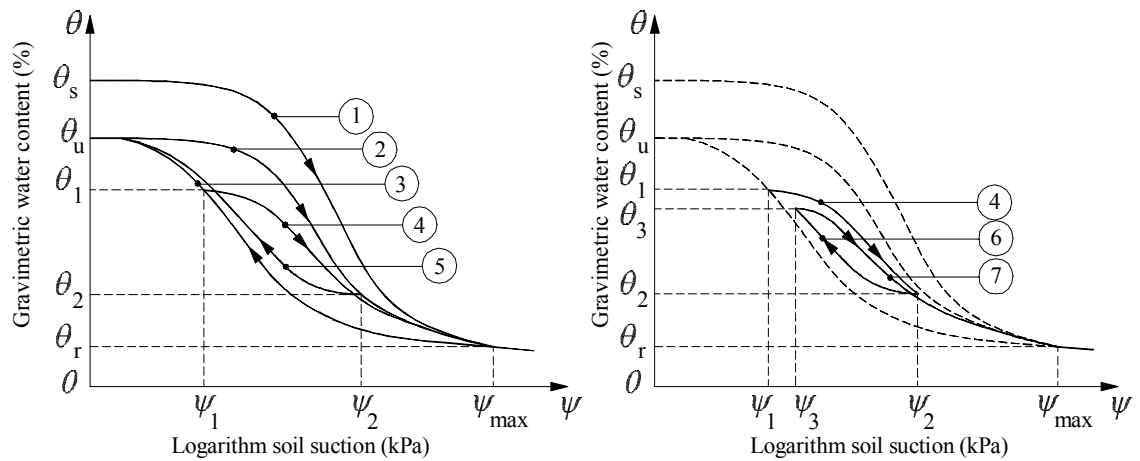


Figure 2.13 Definitions of hysteretic Soil-Water Characteristic Curves (Pham, 2002)

The two main hysteresis curves (i.e., main drying curve and main wetting curve) are referred to as the main hysteresis loop.

The entrapment of air generally occurs during the first drying (i.e., the initial drying curve starts at saturation, θ_s) and the first wetting processes of the soil (Figure 2-13). For most porous media there is no further entrapped air during the second drying and wetting processes. The initial drying curve is a relatively unique curve and is mainly applied for calibration of the ceramic sensor.

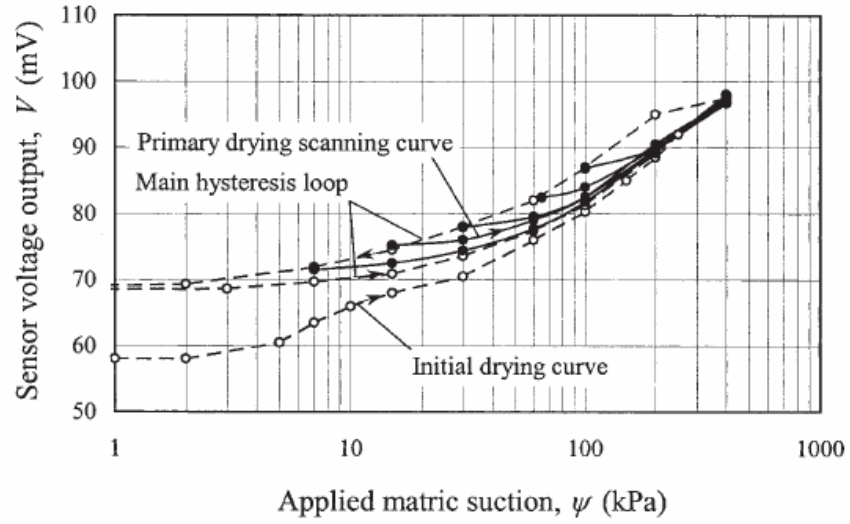
Effects of sensor ceramic hysteresis

Feng (1999) investigated the properties of capillary hysteresis of the sensor ceramic and its effects on the measurement of matric suction. Feng (1999) carried out two groups of laboratory tests. One group measured the relationship between water content and matric suction of three ceramic specimens and the other measured the function between sensor output and matric suction for six U of S sensors. The basic properties of the ceramics used in Feng's (1999) studies are tabulated in Table 2.5.

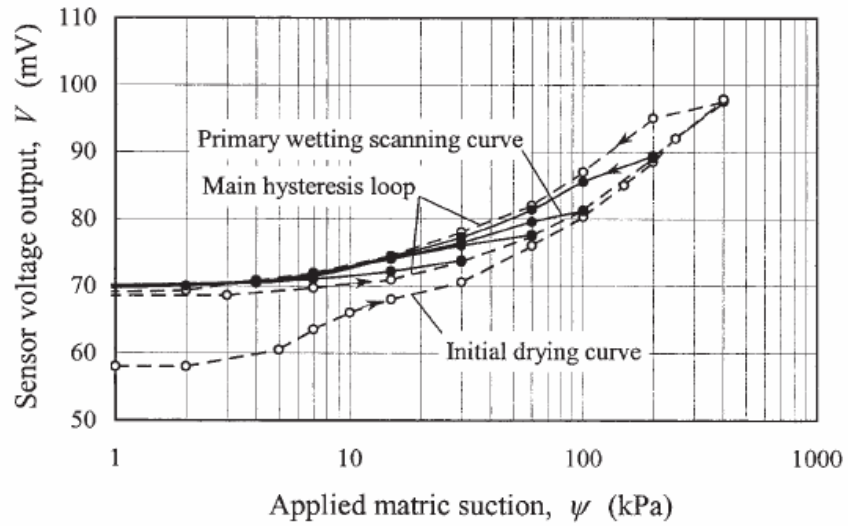
Table 2.5 The properties of the three ceramics used for hysteresis studies (after Feng, 1999)

No.	Dry density γ_d (g/cm ³)	Void ratio e	Porosity n (%)	Diameter (mm)	Height (mm)
1	0.814	1.56	60.9	28.5	38.4
2	0.836	1.52	60.3	28.4	38.3
3	0.824	1.53	60.5	28.4	38.5

Similar hysteresis curves were measured for three ceramic blocks and for the six suction sensors. Figure 2.14 shows the test results for Sensor-1. As can be seen in Figure 2.14, the main hysteresis loop is above the initial drying curve for the output voltage versus applied matric suction (i.e., $V-\psi$) relationship for the suction sensors. The results from the test program showed that even though the hysteresis loop is relatively thin in comparison with other coarse-grained materials such as silty sand; the capillary hysteresis effects are not negligible. Feng (1999) estimated the maximum possible relative error of suction measurement caused by the capillary hysteresis was from 24% to 50% (as defined by equation 2.4) for the thermal conductivity sensors. However, the hysteresis loop for the new ceramic tip is stable and reproducible. In the other words, the wetting and drying curves for a ceramic tip do not change with time.



(a) Primary drying scanning curves



(b) Primary wetting scanning curves

Figure 2.14 Laboratory hysteresis curves for Thermal Conductivity Sensor #1 (Feng et al. 2002)

The equation for calculating the maximum possible relative error caused by hysteresis is as follows (Feng 1999):

$$\varepsilon_{max} = \frac{\delta\psi_{max}}{\psi_w} = \frac{\psi_d - \psi_w}{\psi_w} \quad (2.4)$$

where: ε_{max} : maximum relative error; $\delta\psi_{max}$: maximum absolute error; ψ_w : suction measured based on the wetting curve; ψ_d : suction measured based on the drying curve.

As presented in Figure 2.15 possible relative errors tend to increase with decreasing suction when the suction is less than 100 kPa.

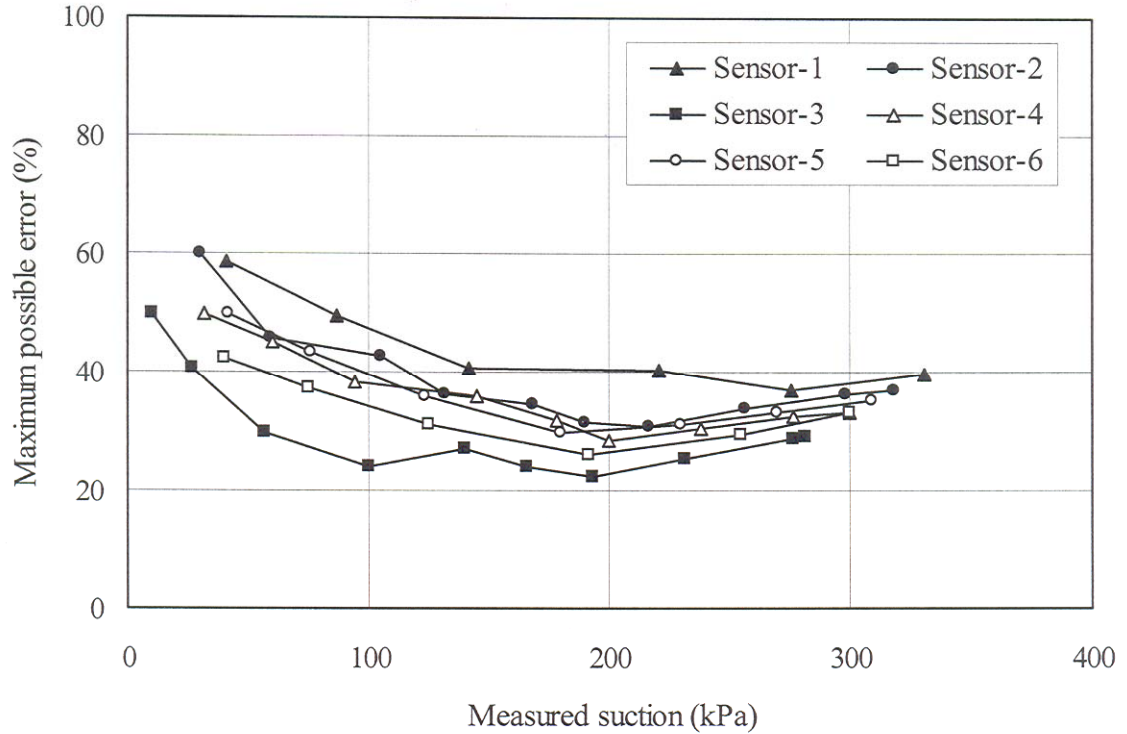


Figure 2.15 Maximum possible relative error of suction measurement due to hysteresis (Feng et al. 2002)

Four models for simulating the capillary hysteresis for ceramic materials were investigated in the research by Feng (1999). The models were:

1. Néel-Everett Independent Domain Model,
2. Mualem Independent Domain Model,
3. Parlange Model, and

4. Nimmo Model.

Studying the laboratory data from both the sensors and the ceramics, Feng (1999) showed most of the available models failed to predict hysteresis for the thermal conductivity sensor. Only could the Néel-Everett independent domain model produce close hysteresis curves for the ceramic. Although the Parlange model reasonably predicted the hysteresis effect of the ceramic, this model had been shown to be theoretically defective. In addition, the existing models required a large amount of measured data to make the predictions. The capillary hysteresis properties were found consistent from sensor to sensor and from ceramic to ceramic in the experimental data.

Fitting equations for estimating the hysteresis properties of the sensor ceramic

On the basis of the results obtained from the laboratory test program and for purposes of practical use, Feng (1999) recommended that curve fitting equations be used to fit the measured main drying curve and to predict the main wetting curve and the primary scanning curves. Generally, the calibration curves obtained in the laboratory test program show a non-linear relationship between voltage output and suction. Feng and Fredlund (1999) proposed the following non-linear fitting equation for the calibration curve as follows:

$$\psi = \left(\frac{b(\Delta V - a)}{c - \Delta V} \right)^d \quad (2.5)$$

where:

ΔV = change in voltage before and after heating of sensor

Ψ = matric suction

a = parameter designating the output voltage under saturated conditions,

c = parameter designating the output voltage under dry conditions,

d = parameter designating the slope of the calibration curve, and

b = parameter related to the inflection point on the calibration curve.

A typical calibration curve listing the corresponding parameter values is shown in Figure 2.16. From equation 2.5 the soil suction can be calculated from the output voltage of the sensor. Using equation 2.5, the calibration process is simplified and the time required for sensor calibration can be greatly reduced.

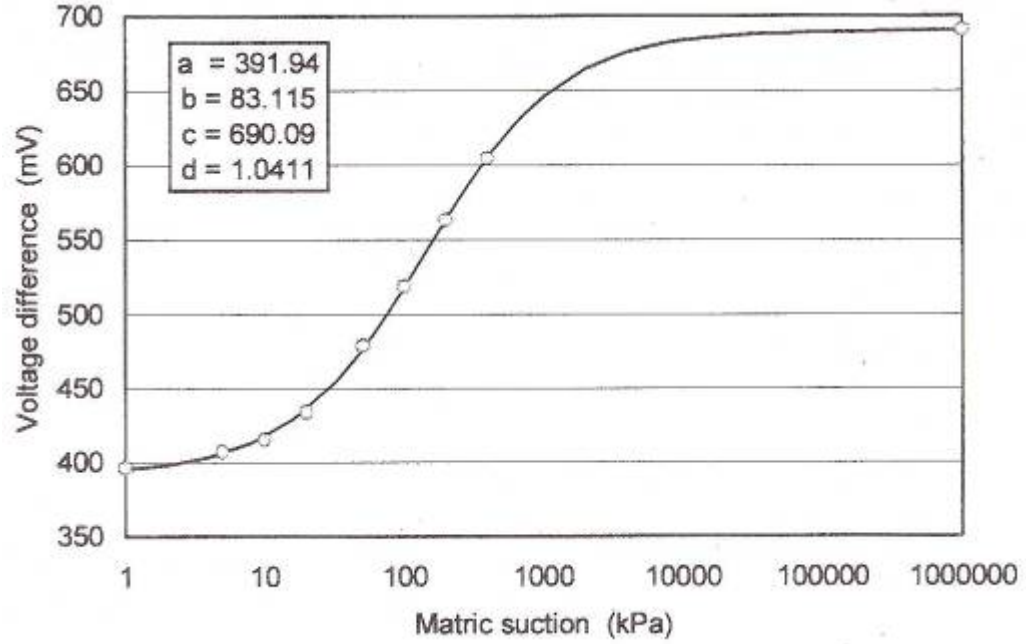


Figure 2.16 Typical calibration curve for a U of S thermal conductivity sensor
(Fredlund et al. 2000)

The equations used to fit the scanning curves are as follows (Feng and Fredlund 2002):

$$\text{From drying to wetting: } V_w(\psi, \psi_l) = V_w - \left(\frac{\psi}{\psi_l} \right)^{1.8} (V_w - V_d) \quad (2.6)$$

$$\text{From wetting to drying: } V_d(\psi, \psi_l) = V_d + \left(\frac{\psi_l}{\psi} \right)^{1.8} (V_w - V_d) \quad (2.7)$$

where:

$V_{d(w)}(\psi, \psi_1)$ = output voltage at suction ψ on the drying (wetting) scanning curve that starts at a suction value ψ_1 ;

ψ_1 = suction at which the scanning curve starts

V_w = output voltages at suction ψ on the main wetting curve

V_d = output voltages at suction ψ on the main drying curve

1.8 = an empirical parameter that controls the degree of curvature of the scanning curves and is the only unknown parameter in the equations.

Temperature correction for the thermal conductivity sensor

The influence of ambient temperature was proposed by Shuai et al. (2002) as follows:

$$\Delta T(t, T_0) = \Delta T(t, T_1) \frac{0.0014T_1 + 0.5743}{0.6065} \quad (2.8)$$

where

$\Delta T(t, T_0)$: the rise in sensor core temperature that was measured at the ambient temperature (T_0) during calibration at time t , and

$\Delta T(t, T_1)$: the field measured sensor core temperature rise (T_1) at an ambient temperature at time t .

The testing results by Shuai et al. (2002) show reasonable temperature corrections when using equation 2.8 (Figure 2.17). This test program included three sensors placed in a thermally-controlled box. The controlled temperatures in the box were gradually decreased from 20° C to 4° C and then increased again in steps while the applied suction was kept constant. Three tests were implemented with three applied suctions of 10, 50 and 200 kPa.

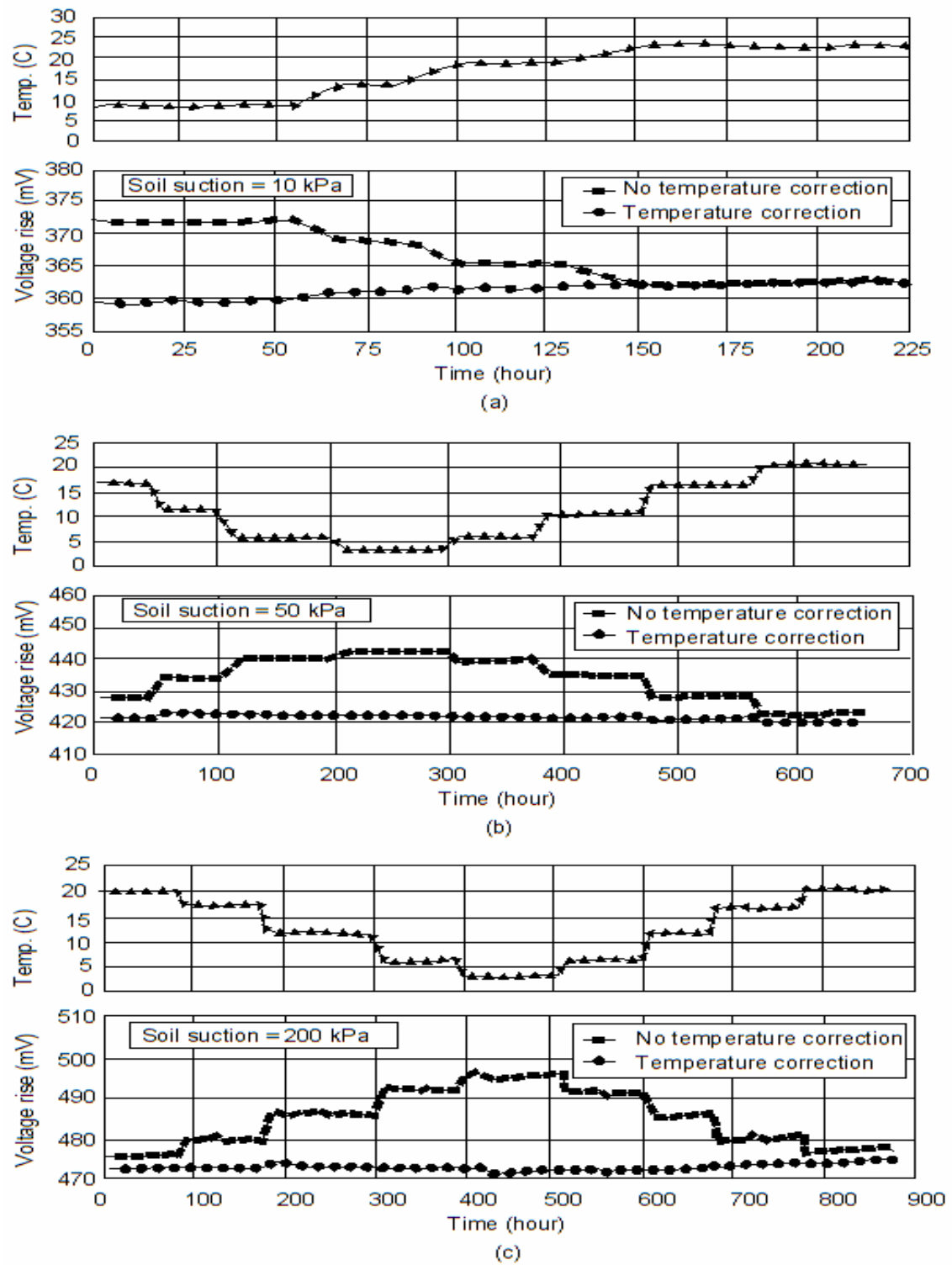


Figure 2.17 Test results for temperature corrections using Equation 2.8 (Shuai et al., 2002)

Nichol et al. (2003) suggested that the thermal conductivity of a sensor λ_{sensor} is a function of both temperature and matric suction from theoretical standpoint,

$$\lambda_{\text{sensor}}(T, \psi) = \lambda_{\text{dry_sensor}} + F(\psi)\lambda_w(T) \quad (2.9)$$

where:

$F(\psi)$ = the fractional contribution to the total thermal conductivity from the water phase,

$\lambda_w(T)$ = thermal conductivity of water: $-8 \times 10^{-6}(T_1)^2 + 0.002(T_1) + 0.5607$ and

$\lambda_{\text{dry_sensor}}$ = thermal conductivity of the dry sensor, $0.15 \text{ Wm}^{-1}\text{K}^{-1}$ (Shuai et al. 2002).

The correction factors using equation 2.9 can be interpolated from the diagram on Figure 2.18

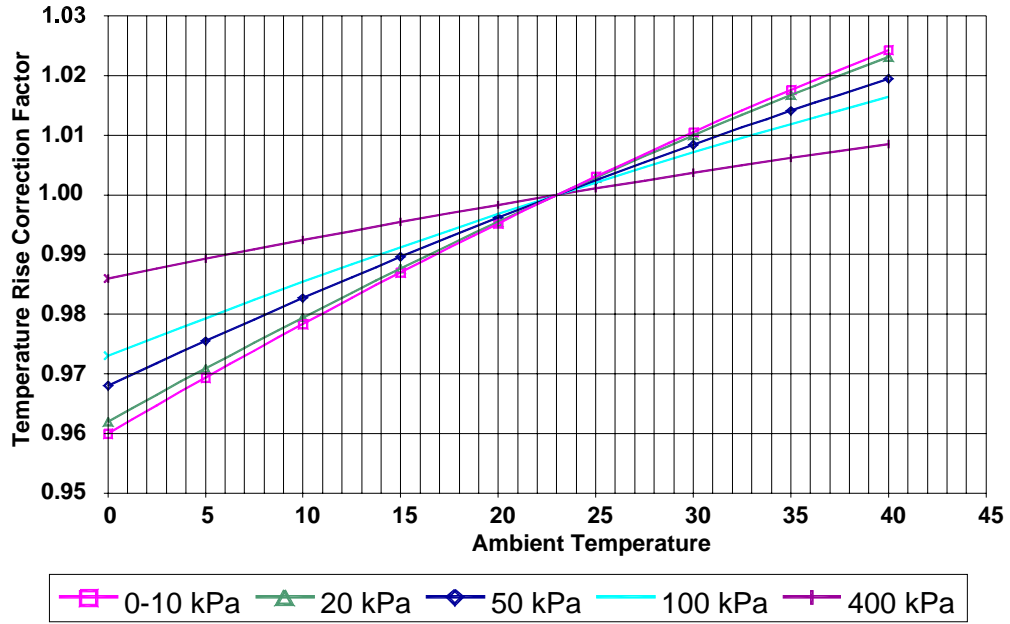


Figure 2.18 Correction factor for ambient soil temperature (Nichol et al., 2003)

Tan et al (2002) concluded that the method proposed by Shuai et al. (2002) has a maximum difference of 26 % when compared to the results from the method by Nichol et al. (2003). This issue needs to be addressed through future research.

Sensor measurements in a freezing environment

When temperatures fall to 0° C, part of the soil-water freezes producing ice in the soil. Water usually moves from the unfrozen zone to the frozen zone through a thin partially frozen fringe and as a result the frozen zone penetrates to a greater depth. The suction acts as a force tending to move water upwards.

Williams (1982) described the change of suction in a frozen soil by the following relation:

$$d(-u_w) = -\frac{L}{T_f v_w} dT_f \quad (2.10)$$

where:

L = latent heat of fusion, which is the heat liberated when water turns to ice or the heat absorbed when ice turns to water (i.e., 333kJ/kg)

T_f = normal freezing temperature in Kelvin (i.e., 273.15°K)

dT_f = freezing point depression either in degrees Celsius or Kelvin

u_w = pore-water pressure

v_w = specific volume of water [i.e., $1/\rho_w$ where ρ_w is the water density (1,000 kg/m³)]

As expressed in the equation 2.10, soil suction in a freezing environment increases proportionally with the freezing temperature decrease dT_f .

Water in a porous medium does not all freeze at a single temperature and the freezing characteristics of the pore-water vary depending on several factors. In general, the smaller the particles, the greater the amount of unfrozen water present at any temperature below freezing. For some clayey soils, at 0° C, the unfrozen gravimetric water content is around 1 to 2 %. When the temperature is less than -2° C, most soils have a negligible amount of unfrozen water (Anderson and Morgenstern 1973).

However, as freezing proceeds, the remaining water becomes more and more difficult to turn to ice. The thermal conductivity of ice is some 3 to 4 times higher than that of purified water. During freezing it is expected that the thermal conductivity of the suction sensor increases.

The higher rise of temperature showing a lower thermal conductivity in the soil corresponds to a lower water content. Therefore, a high temperature difference reading from the sensor indicates a high suction of soil, and vice versa. For a partially frozen soil or frozen soil, the temperature increase is expected to be low, leading to higher interpolated suctions from the standard calibration, as compared to that of unfrozen soil. The difference is because of the presence of ice with high thermal conductivity.

Lee (1983) used MCS 6000 thermal conductivity sensors to measure suction of an *in situ* glacial till. The results indicated that suction variations followed consistently the variations of temperature and when the temperature decreased below 0° C the sensors were not able to record data. van der Raadt et al. (1988) installed AGWA-II thermal conductivity sensors under railway subgrade. The data, from the AGWA-II sensors, showed an increase in suction when the temperatures went down below 0° C. This was believed to be due to a significant amount of unfrozen water. Some suction values were registered during freezing.

Fredlund et al. (1991) carried out a laboratory test program to evaluate the suitability of the thermal conductivity sensor for suction measurements in a freezing environment. A temperature of -22° C was applied at the top of the soil column that was insulated along the sides of the column as shown in Figure 2.19. Three sensors were inserted in the soil column at different depths. Thermocouples were installed next to those sensors to measure temperature. All the sensors seemed to give similar responses. When the temperature fell to the freezing point, the suction dropped sharply. As the freezing proceeded, the suction rose again to almost the same values as before freezing. When temperature increased from below freezing to the freezing point, the same behavior was also observed and a big drop of suction was recorded. After thawing, three

sensors showed the suction values ranging from 0 to 40 kPa as can be seen in Figure 2.20.

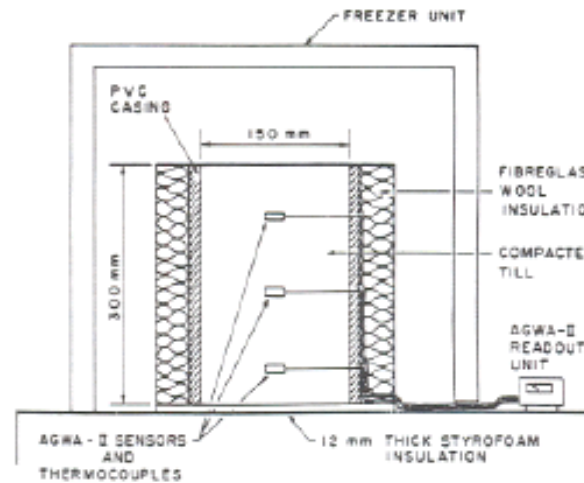


Figure 2.19 Set up for thermal conductivity sensor in a freezing test (Fredlund et al. 1991)

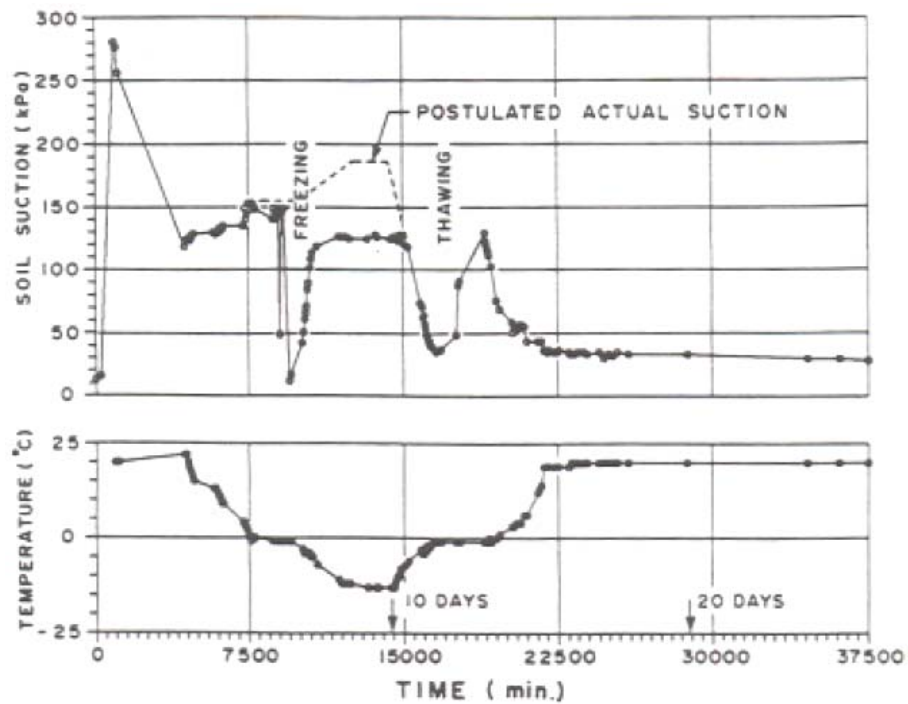


Figure 2.20 Test results from the bottom sensor in a freezing environment (Fredlund et al. 1991)

Fredlund et al. (1991) explained the latent heat of fusion was released at constant temperature during freezing. The water in the porous block does not all freeze simultaneously, rather it freezes gradually. Hence, the temperature rise by the heat pulse in a freezing environment is smaller than that in an unfrozen environment. This is attributed to the tendency of water to maintain the constant temperature during phase change. The reduction in the temperature difference by the heat pulse could lead to the interpretation of the drop in suction during phase change according to the calibration curve. As the temperature continued to be lowered, the majority of water in the ceramic block became frozen and the temperature rise was dependent upon the proportions of ice, unfrozen water and air bubbles. The rise of suction in a frozen state was believed to be the result of a high volume of air bubbles in the sensor (Fredlund et al. 2001). The latent heat of fusion is absorbed at a constant temperature during thawing. The tendency to maintain the constant temperature during phase change would again lower the temperature rise generated by a heat pulse. As a result, the suctions interpreted from the standard calibration reduced sharply when temperatures rose from minus values to 0° C.

Shuai et al. (2002) also conducted tests to investigate the effect of the freeze-thaw actions on the function of the U of S sensor. A pressure cell with three thermal conductivity sensors embedded inside was insulated in a temperature controlled chamber. The suction was kept constant while the temperature inside the chamber was lowered from 20° C to below 0° C. When the sensor became entirely frozen the temperature was increased again to above 20° C. The above procedure was repeated twice. The voltage output from the sensor and temperature measurements with respect to time are shown in Figure 2.21. All three sensors responded in a similar manner and showed the same trend as observed by Fredlund et al. (1991). As the temperature decreased from positive to negative values, the voltage differences dropped dramatically to approximately zero. As freezing proceeded, the voltage differences remained from zero to the original reading before freezing. A distinct drop of suction was observed during phase change including thawing and freezing. This could be attributed to the effect of latent heat of fusion on the thermal conductivity measurements. On the other hand, when freezing proceeds, the ratio of different phases in the sensor changes leading to high thermal conductivity of the sensor due to higher proportion of ice. Therefore, the

readings of thermal conductivity sensor are difficult to interpret and convert to suction in a freezing environment. Moreover, it might be anticipated that the ceramic block could possibly be fractured in a freezing state if there is high water content in the sensor.

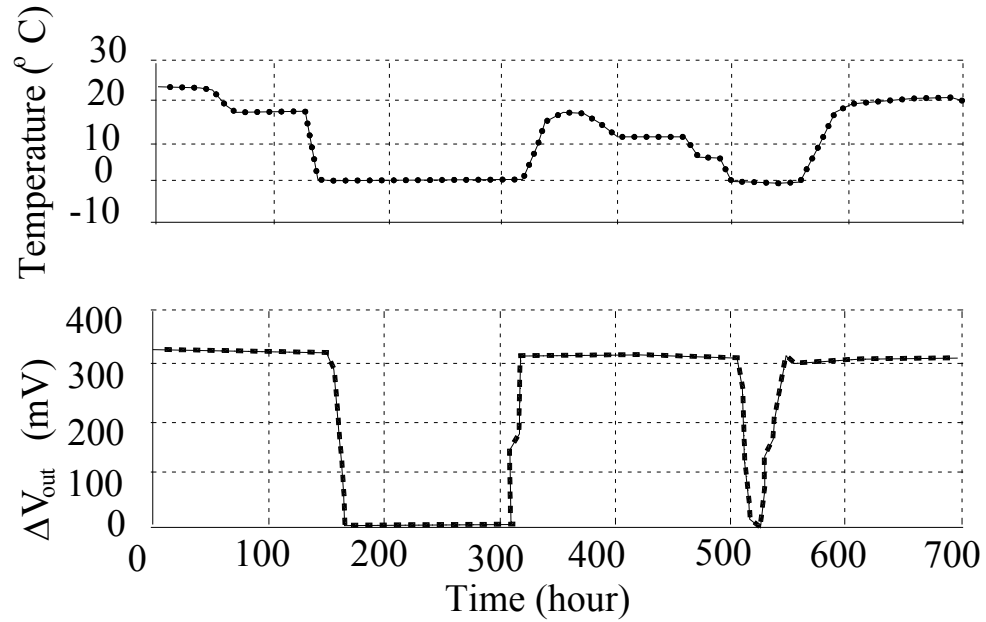


Figure 2.21 Effect of freeze-thaw cycles on sensor readings (Shuai et al., 2002)

CHAPTER 3

RESEARCH PROGRAM

This chapter describes the research program that was implemented to analyze, present and interpret the suction data from the field measurements.

3.1 Overview of the research program

The research program included the following tasks:

1. verification of the equations for matric suction calculations,
2. analyses of the matric suctions,
3. presentation of the laboratory testing results, rainfall and matric suction data,
4. interpretation of the matric suction readings,
5. site investigation and laboratory testing program,
6. collection of the weather data, and
7. studies on the new sensor.

The layout of the research program is graphically presented in Figure 3.1.

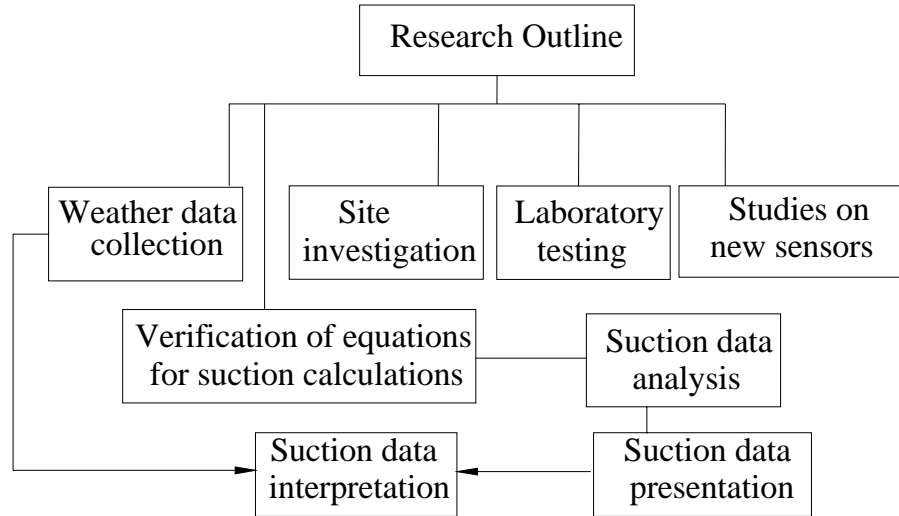


Figure 3.1 General outline of the research program

The outline for the verification of the equations for calculating matric suctions is presented in Figure 3.2. After reviewing the calibration curve equations, the temperature and hysteresis corrections for the thermal conductivity sensor were discussed in light of the laboratory testing study carried out by Feng (1999) and Shuai et al. (2002). Two approaches for temperature corrections that were developed by Shuai et al. (2002) and Nichol et al. (2003) were reviewed. The fitting equations by Feng (1999) were clarified with the respect to the hysteresis correction. Feng's (1999) fitting equations were extended for hysteresis corrections applied to the field data.

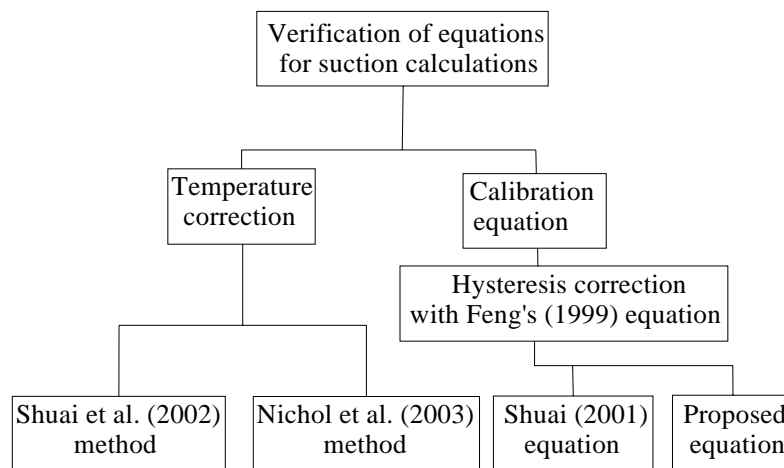


Figure 3.2 Outline for the study to verify the equations for matric suction calculations

The procedure for analyzing matric suction results is summarized in Figure 3.3. The field data were first reduced into a standard form for the analytical purposes. The temperature correction converted the field voltage outputs to the equivalent voltage outputs under laboratory conditions. To correct the matric suctions for hysteresis effects assumptions of matric suction specific times of the year (i.e., after being installed and after “spring break-up”) were made. These assumptions were to locate a matric suction on a specific hysteresis branch at a time. Further details of these assumptions can be found in section 4.5 (Chapter 4). The noise level of the thermal conductivity sensor and other related factors were also taken into consideration in the assumptions. $V_{bending}$ was determined using these assumptions to calculate the hysteresis correction. Different matric suction values can be calculated on different hysteresis branches; therefore the determination of a matric suction corresponding to a specific hysteresis branch was necessary. The calculations of the hysteresis corrections were performed on the basis of these determinations. After calculating the hysteresis correction, the selection of suction was made with regards to the accuracy of the scanning curves and the main calibration loop.

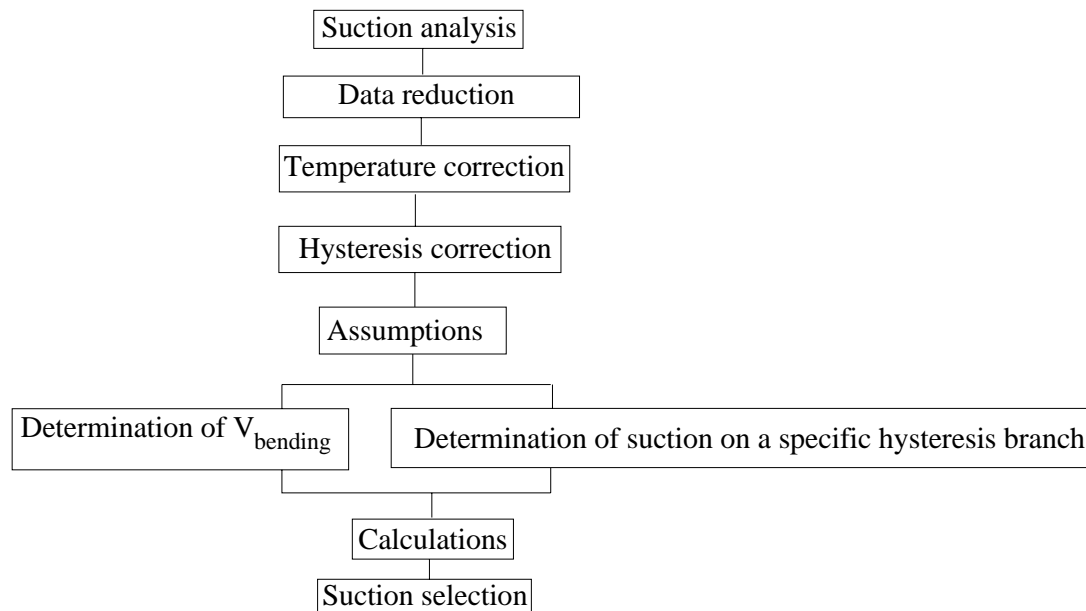


Figure 3.3 Outline of the procedural analysis of suction from the field data

Figure 3.4 gives the general view of the data presentation conducted in this study.

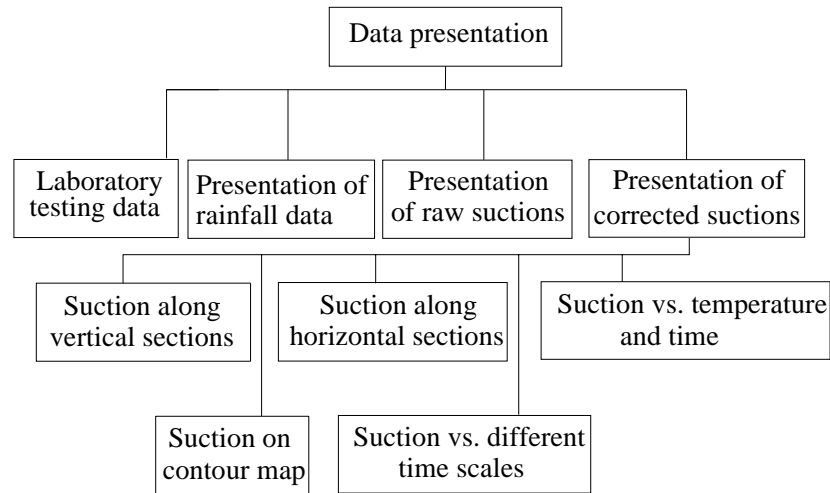


Figure 3.4 Layout for the presentation of the matric suction data

The matric suctions were then interpreted with regard to the collected rainfall information.

The studies on the new sensors were conducted in order to better understand the collected field data. The details of these sensor studies can be found in Appendix A.

3.2 Site investigation

Geotechnical characterization of the sites was carried out in September 2004. The site work at Bethune was implemented on 13th September 2004 and at Torquay on 14th September 2004. One borehole of approximately ten (10) feet depth was drilled at each site. The elevations of the top of each borehole were determined based on the assumed datum provided by Saskatchewan Highways and Transportation, Government of Saskatchewan.

3.4.1 Staff and equipment

The site investigation team included a drilling crew of three people from Saskatchewan Highways and Transportation. The boreholes were made using a truck

mounted, heavy auger drill rig. Drilling was carried out using a hydraulic rotary combined with air-percussion equipment. Soil samples were obtained using 91-mm (outside diameter) Shelby-tube samplers lined with stainless steel rings. Sampling was conducted continuously and separate small samples were collected for water content tests.

3.4.2 Purpose and scope of site investigation

The purpose of this investigation is to explore and evaluate the subsurface soil conditions at the site and to collect soil samples for the laboratory testing program. Eighteen (18) undisturbed samples and eighteen (18) water content samples were collected at each site. The scope of this study includes the following items:

1. A review of available geological data pertinent to the project site.
2. A field study consisting of an exploratory boring program to formulate a description of the subsurface conditions.
3. Reporting of findings regarding the geotechnical aspects of the project site.

Site location plans are shown in Appendix C.

3.4.3 Drilling operations

Rotary drilling was implemented and the drilling auger was 150 mm in diameter. The soil sample recovery on the entire length of the borehole was approximately 70% on average. Sample losses were observed when rocks were encountered.

3.4.4 Geological conditions

The Quaternary sediments, also called glacial drift, vary from zero in thickness to hundreds of meters through out southern Saskatchewan. The drift has been subdivided into various till units and intertill units indicating that several glacial and interglacial periods have affected southern Saskatchewan (Saskatchewan Industry and Resources, 2005).

The relief at Bethune was separated by different glacial streams in the past but the streams are now inactive. On the other hand, the Torquay site is relatively flat with an assumed (local) level of about +500 m. The surficial geology at Bethune consists of a morainal deposit eroded by glacial melt water (Saskatchewan Industry and Resources, 2005). Bethune is located just north of a glacial melt water area containing the Arm River. The subgrade at Bethune is a compacted clay till and was constructed prior to 1972. Glacial sediments at Torquay are placed on a morainal plain deposit and the subgrade is constructed with a compacted clay till. Torquay is also located north of a glacial melt water channel (Saskatchewan Industry and Resources, 2005).

3.4.5 Groundwater condition

The deep aquifers in southern Saskatchewan are recharged by water filtering down through the overlying materials. Although recharge may be slow, it is relatively consistent resulting in fairly stable ground water levels. An observation conducted at a well in Saskatchewan's Estevan Valley showed a maximum water level fluctuation of less than 15 centimeters from 1965 until a major groundwater production project led to a decline in water levels in 1988. As a result of this project, major drawdowns occurred and reached 45 meters within the well field and less than 20 meters at distances of up to 20 kilometers (Shaheen, 2005). This exploitation terminated in 1994; however, recovery is slow due to the low rate of recharge to the aquifer. Recharge rates are now estimated at 1 to 3 millimeters per year (Shaheen, 2005).

At the time of investigation no groundwater was recorded.

3.4.6 Subsurface soil conditions at Bethune

A fill overlain with a pavement of 8 to 10 cm mixture of asphalt consists of a hard, grey glacial till interbedded with some small sand lenses to a depth of 2.0 m. Underlying that layer is a hard, brown-grey to mottled sandy clay till (glacial origin) from 2.0 to 3.3 m (bottom of the borehole). Some rocks from 5 to 10 cm in diameter were encountered throughout the entire length of the borehole.

3.4.7 Subsurface soil conditions at Torquay

A fill overlain with a 10 cm asphalt pavement consists of a hard, brown-mottled glacial till, interbedded with some small sand lenses to a depth of 1.1 m. Underlying this layer is a hard, brown-grey to mottled sandy clay till (glacial origin) from 1.1 to 3.3 m (bottom of the borehole). Some rocks from 5 to 10 cm in diameter were encountered throughout the depth of the borehole.

Further details on the soil conditions at the sites are contained in the borehole logs in Appendix C.

3.3 Collection of weather data

Weather data available from Environment Canada were used to assist in the interpretation of the soil matric suction results at the two sites. No weather stations were in existence at the sites. Some neighbouring locations were recommended by Environment Canada. For Torquay, the surrounding weather stations are at Benson, Estevan, Macoun, Midale, and Weyburn. The closest weather stations at Bethune are Buffalo Pound Lake, Duval, and Holdfast. As can be seen in Figure 3.5, Macoun is the closest station to Torquay; however, the temperatures are not monitored at Macoun. Therefore, the data at Estevan were chosen. Likewise, the station at Buffalo Pound Lake was selected to provide weather data for Bethune (Figure 3.6). The weather stations are approximately 20-25 km from the sites. The coordinates of the stations and the sites are tabulated in Table 3.1.

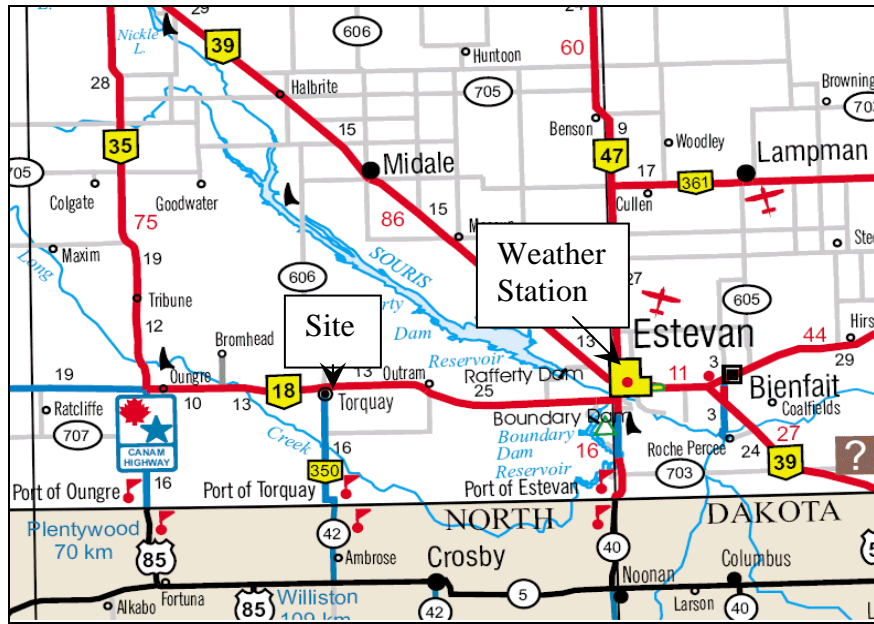


Figure 3.5 Location map of Torquay and the vicinities

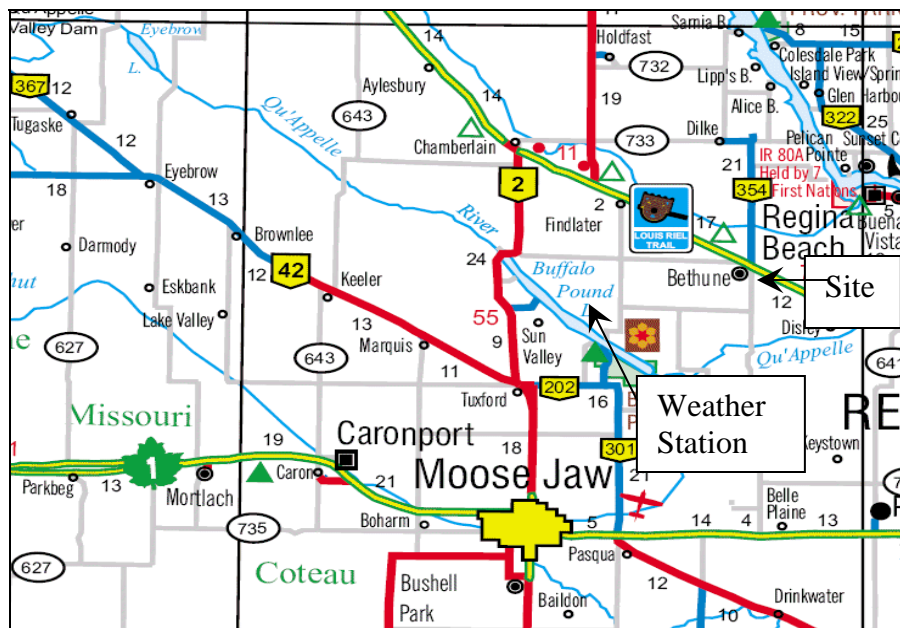


Figure 3.6 Location map of Bethune and the vicinities

Table 3.1 Location of weather stations and the sites (after Environment Canada, 2005)

	Latitude	Longitude	Elevation
Torquay	49° 4' N	103° 30' W	586.70 m
Estevan	49° 13' N	102° 58' W	580.60 m
Bethune	50° 34' N	105° 10' W	579.00 m
Buffalo Pound Lake	50° 33' N	105° 22' W	588.00 m

The focus was on two weather parameters, namely temperature in degrees Celsius and rainfall in “mm”.

The discussions in this chapter provide explanations for the data presentation and data interpretation in Chapters 5; 6 and 7.

CHAPTER 4

VERIFICATION OF EQUATIONS FOR SUCTION CALCULATIONS AND SUCTION ANALYSIS

This chapter reviews the equations to be used for matric suction calculations in terms of accuracy and conditions of application.

4.1 Equations for temperature correction

Two methods proposed by Shuai et al. (2002) and Nichol et al. (2003) for ambient temperature correction to the sensor reading are reviewed in this section.

4.1.1 Correction method for ambient temperature presented by Shuai et al. (2002)

Shuai et al. (2002) proposed the following correction for the ambient temperature as follows:

$$\Delta T(t, T_0) = \frac{0.0014T_1 + 0.5743}{0.6065} \Delta T(t, T_1) \quad (2.8)$$

where: $\Delta T(t, T_0)$ = the rise in sensor core temperature that was measured at the ambient temperature during calibration (T_0) at time t and $\Delta T(t, T_1)$ = the field measured sensor core temperature rise at an ambient temperature (T_1) at time t .

Shuai et al. (2002) assumed that thermal conductivity of sensor is mainly controlled by the water in the sensor. It was assumed that all variations in of the thermal conductivity sensor caused by environmental changes are directly related to the change of

water thermal conductivity. The thermal conductivity of water at 23° C is 0.6065 W/mK and the linear function $0.0014t + 0.5743$ presents the relation of thermal conductivity of water with temperature.

4.1.2 Correction method for ambient temperature presented by Nichol et al. (2003)

Xing and Fredlund (1994), using an analytical solution, approximated the theoretical temperature $T(t,r)$ at the center of a sphere for large values of time by performing the inverse Laplace transform of the radial heat conduction equation as follows:

$$T(t,r) = \frac{Q}{4\pi\lambda} \left[1 - \frac{r}{\sqrt{\pi Dt}} + \frac{r^3}{4\sqrt{\pi} (Dt)^{3/2}} \times \left(2 - \frac{4}{3} \rho c \frac{D}{\lambda} \right) - \dots \right] \quad (4.1)$$

where:

Q = the heating rate (W)

r = the radius of the heating element core (m)

λ = thermal conductivity (W.m⁻¹.K⁻¹)

D = thermal diffusivity (m².s⁻¹)

ρ = the density (kg/m³)

c = the specific heat capacity (J/kg.K)

Choosing the first two terms, the temperature at the center of the sphere for large values of time can be approximated by:

$$T(t,r) = A - B(1/\sqrt{t}) \quad (4.2)$$

where:

$$A = Q/4\pi\lambda r$$

$$B = Q/(4\lambda\sqrt{\pi D})$$

A and B can be determined by the measuring of temperature at two different times and then by plotting ΔT versus $1/\sqrt{t}$. For large values of t (i.e., $t > 60$ s) Equation 4.2 gives a good approximation to the actual temperature. If c and ρ at the inner center of the thermal conductivity sensor are known, the first three terms of Equation 4.2 can be used to better approximate the temperature.

Based on Equation 4.2, Nichol et al. (2003) derived the following temperature correction equation:

$$\Delta T(t, T_0) = \Delta T(t, T_1) \left[\frac{\lambda_{sensor}(T_1)}{\lambda_{sensor}(T_0)} \right] \left(\frac{1 - \frac{c^n}{\sqrt{D(T_0)}}}{1 - \frac{c^n}{\sqrt{D(T_1)}}} \right) \quad (4.3)$$

$$\text{where: } c^n = \frac{r}{\sqrt{\pi t}}$$

In Equation 4.3 the second term represents the correction pertaining to thermal conductivity change and the third term is related to diffusivity change. Due to the unavailability of experimental results of the temperature effect on diffusivity, Nichol et al. (2003) used the water diffusivity change instead of the sensor diffusivity. The magnitude of the third term in Equation (4.3) varies from 1.000002 to 0.999999 over the range of ambient temperatures. Therefore, this term can be set to a value of unity.

To more accurately represent the thermal conductivity of the sensor, a function of thermal conductivity for the dry ceramic, the sensor water content and the interconnectedness of the water phase can be taken into account. As a result, an improved equation was proposed for the thermal conductivity λ_{sensor} as a function of both temperature and matric suction (Nichol et al. 2003):

$$\lambda_{sensor}(T, \psi) = \lambda_{dry_sensor} + F(\psi) \lambda_w(T) \quad (2.9)$$

$F(\psi)$ = the fractional contribution to the total thermal conductivity from the water phase which is hysteretic.

The value for the thermal conductivity of water $\lambda_w(T)$ is obtained using data from CRC Press (1994):

$$\lambda_w(T) = -8 \times 10^{-6}(T_I)^2 + 0.002(T_I) + 0.5607 \quad (4.4)$$

The correction can be determined by measuring the thermal conductivity of the dry sensor, $\lambda_{\text{dry_sensor}}$, and then by measuring $\lambda(T_0, \psi)$, A , B and $\Delta T(t, T_0)$. Nichol et al. (2003) estimated the function, $F(\psi)$ based on thermal conductivity as a function of suction $\lambda(\psi)$ from Shuai et al. (1998) and the equation for thermal conductivity, $\lambda(\psi)$ from Reece (1996).

The Nichol et al.'s (2003) method appears to be theoretically more rational than Shuai et al.'s (2002) method since the effects of both matric suction and temperature are taken into account. However, Nichol et al.'s (2003) used many unverified assumptions, such as:

1. spherical solution of temperature instead of a cylindrical sensor,
2. empirical heating rate,
3. estimated heater element radius, and
4. unverified thermal conductivity of dry sensor.

In addition, the plot of correction values, as shown in Figure 2.18 (Chapter 2) can only be applied for the drying curve. The temperature correction method proposed by Nichol et al (2003) would yield more accurate suction values if more required parameters were obtained from laboratory calibration measurements.

The method developed by Shuai et al. (2002) was developed along with a supporting laboratory testing program and shows good agreement between the estimated values and the test data as illustrated in Figure 2.17. For the above-mentioned reasons,

the temperature corrections to be applied in this research were derived from the Shuai et al.'s (2002) equation.

4.2 Validity of the calibration equations

The equation for sensor calibration was proposed by Feng and Fredlund (1999):

$$\psi = \left(\frac{b(\Delta V - a)}{c - \Delta V} \right)^d \quad (2.5)$$

where: ΔV = change in voltage prior to and after heating of sensor; ψ = matric suction; a = parameter designating the output voltage under saturated conditions; c = parameter designating the output voltage under dry conditions; d = parameter designating the slope of the calibration curve, and b = parameter related to the inflection point on the calibration curve. Figure 4.1 gives the graphical notations for Equation 2.5.

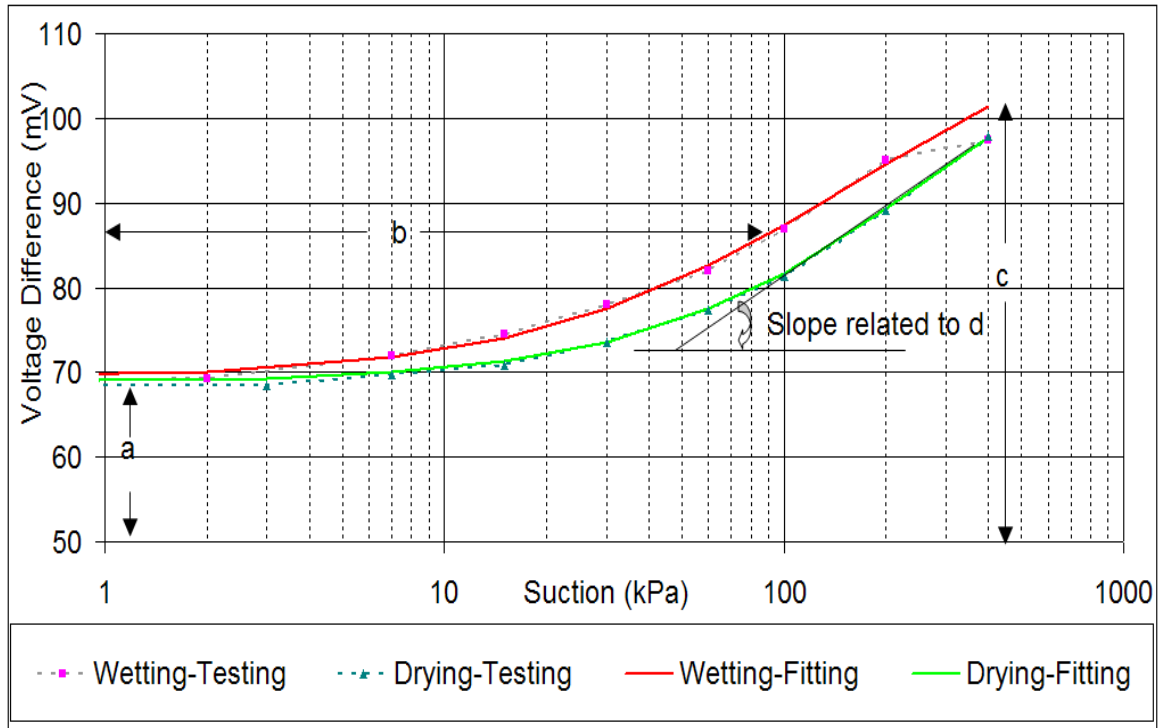


Figure 4.1 Graphical notations for the applied calibration equation

The calibration Equation 2.5 matches well with most of the sensors installed at Torquay and Bethune. Out of the sixteen sensors installed at Bethune there was only one sensor which does not fit well with the test data. That sensor is sensor B2-7 with ID of S-9-9. At Torquay, there are 11 sensor fitting calibration curves that fit well with the data from laboratory experiments. Some sensors were difficult to fit with Equation 4.7 such as sensor T1-4 (ID: S6-119) and sensor T2-7 (ID: S-6-116). During the calibration process eight points on the drying branch were measured in order to build up the fitting curves. Figures 4.2 and 4.3 show the fitting calibration curves for two representative sensors that were installed at Bethune and Torquay.

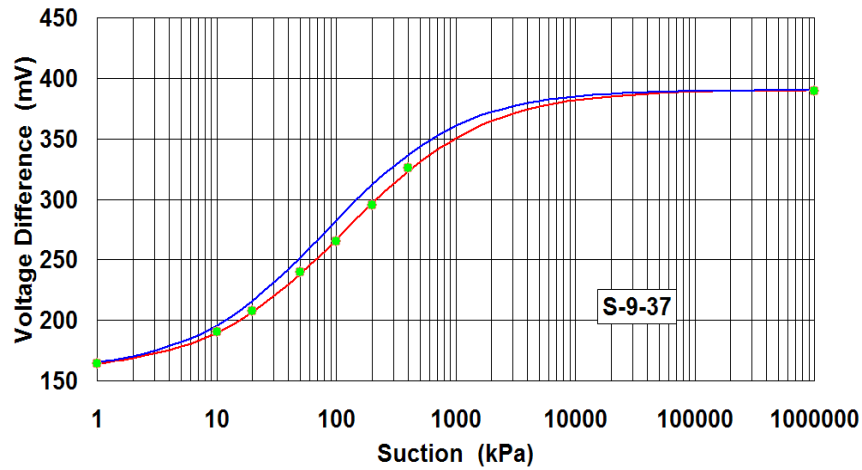


Figure 4.2 Measured and fitted data for sensor B5-16, Bethune (Marjerison 2001)

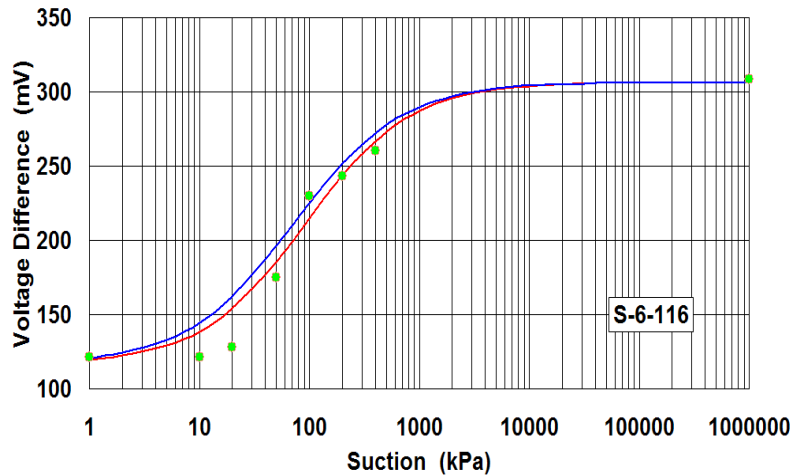


Figure 4.3 Measured and fitted data for sensor T2-7, Torquay (Marjerison 2001)

In general, Equation 2.5 provided a reasonable estimation of the calibration curves and saved a significant amount of the laboratory work.

4.3 Equations for sensor hysteresis correction

In this section, the equations for hysteresis correction are reviewed and extended for field data.

4.3.1 Feng and Fredlund's fitting equations

Feng and Fredlund (2002) proposed the following equations to present the scanning curves:

$$\text{From drying to wetting: } V_w(\psi, \psi_1) = V_w - \left(\frac{\psi}{\psi_1} \right)^{1.8} (V_w - V_d) \quad (2.6)$$

$$\text{From wetting to drying: } V_d(\psi, \psi_1) = V_d + \left(\frac{\psi_1}{\psi} \right)^{1.8} (V_w - V_d) \quad (2.7)$$

where: $V_{d(w)}(\psi, \psi_1)$ = output voltage at suction ψ on the drying (wetting) scanning curve that starts at a suction value ψ_1 ; ψ_1 = suction at which the scanning curve starts; V_w = output voltages at suction ψ on the main wetting curve; V_d = output voltages at suction ψ on the main drying curve; 1.8 = an empirical parameter that controls the degree of curvature of the scanning curves and is the only unknown parameter in the equations.

The diagrams showing the notations are presented in Figures 4.4 and 4.5.

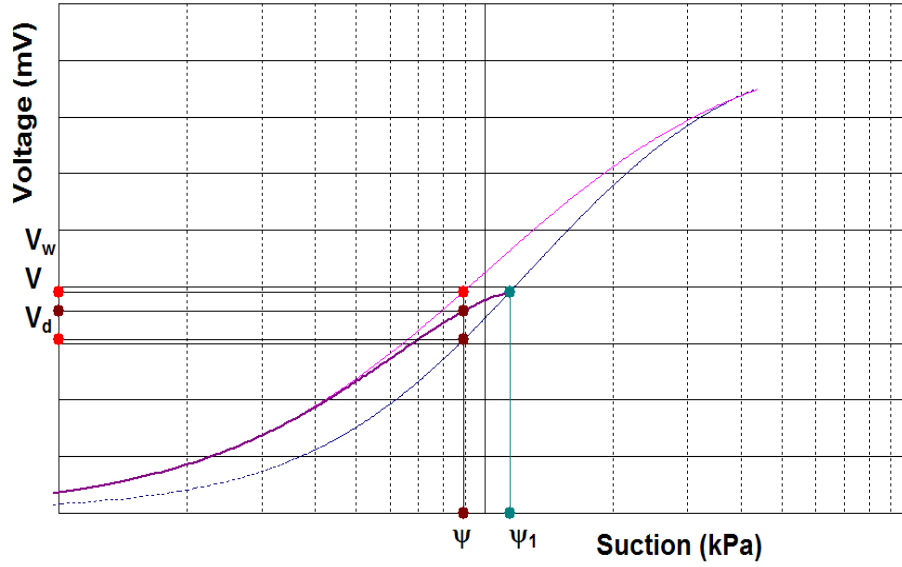


Figure 4.4 Graphical notations for Equation 2.6

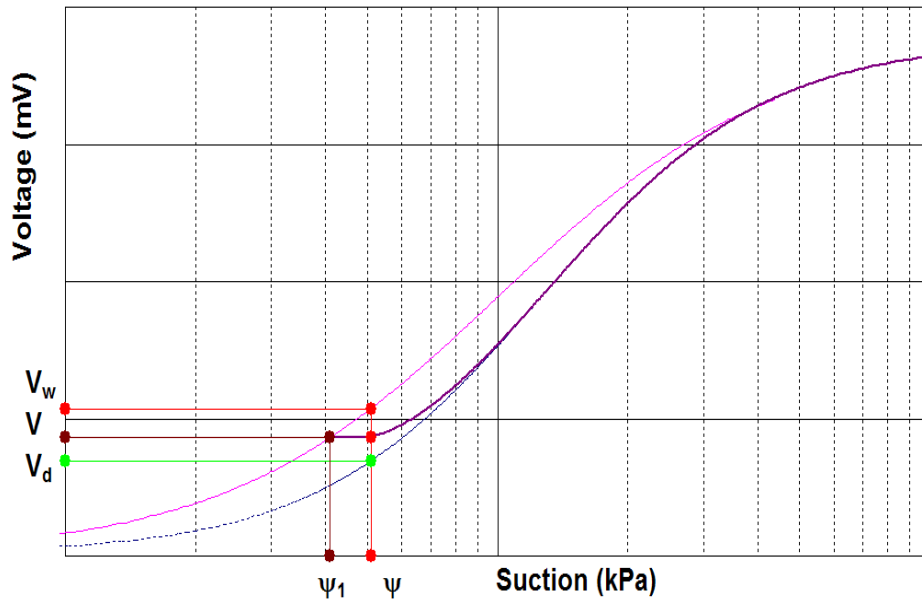


Figure 4.5 Graphical notations for Equation 2.7

The verification of Equations 2.6 and 2.7 used Feng's (1999) experimental results for Sensor 1 and Sensor 2. From the experimental results, the calculations for Equations 2.6 and 2.7 were made to produce scanning curves for Sensor 1 and Sensor 2 as shown in Figures 4.6 and 4.7.

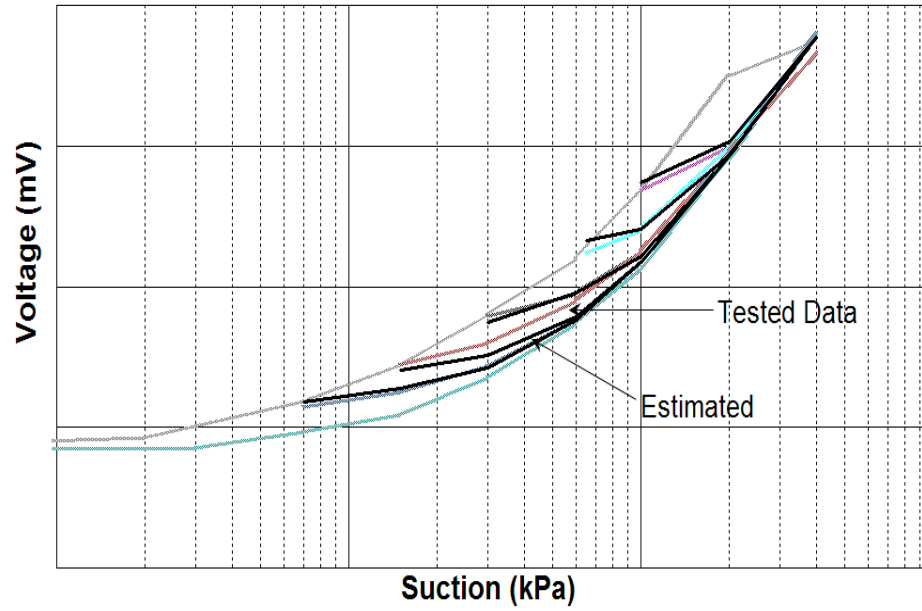


Figure 4.6 Comparison of drying scanning curves for Sensor 1 (redrawn from Feng's 1999 data)

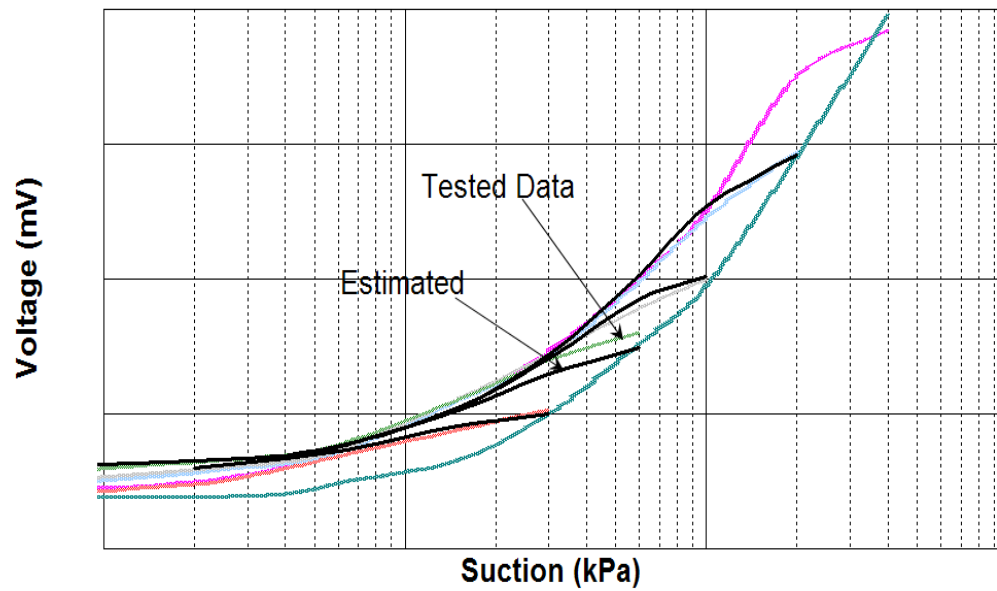


Figure 4.7 Comparison of wetting scanning curves for Sensor 2 (redrawn from Feng's 1999 data)

As can be seen in Figures 4.6 and 4.7, the curves predicted using Equations 2.6 and 2.7 are close to the measured curves. The errors between the predicted results and the

measured results are less than 10 %. Therefore, the fitting equations can provide reasonable estimations. However, these equations can only be used for primary scanning curves (definitions of the scanning curves are shown in Figure 2.13) since no experimental data are available for secondary curves or higher than that (e.g. tertiary curves). For a surface soil under consecutive micro-climatic changes the trend of moving between high-order scanning curves may dominate. Moreover, if Equations 2.6 and 2.7 are applied for high-order scanning curves it will be difficult to determine ψ_l (i.e., the value at which a scanning curve shifts from drying to wetting or vice versa).

4.3.2 Shuai's practical fitting equations

Shuai (2001, personal communication) proposed the following fitting equations for the scanning curves:

Matric suction on wetting scanning curve:

$$\psi_{d-w} = \psi_{wet} + \left(\frac{V_{out}}{V_{limit}} \right)^{103} (\psi_{dry} - \psi_{wet}) \quad (4.5)$$

Matric suction on drying scanning curve:

$$\psi_{w-d} = \psi_{dry} - \left(\frac{V_{limit}}{V_{out}} \right)^{103} (\psi_{dry} - \psi_{wet}) \quad (4.6)$$

where: Ψ_{dry} = matric suction measured based on the sensor drying curve; Ψ_{wet} = matric suction measured based on the sensor wetting curve; V_{out} = change in voltage prior to and after heating of the sensor; 103 = empirical parameter controlling the degree of curvature of the scanning curves; V_{limit} = the starting point of the scanning curves. V_{limit} can be determined as $V_{previous}$ in scanning curves or V_{out} in the main loop.

The laboratory test results by Feng (1999) were used to verify Equations 4.5 and 4.6. The comparisons were graphically presented in Figures 4.8 and 4.9. The fitting equations provided reasonable predictions for the hysteresis effect of the sensors.

Moreover, the parameters in Equations 4.5 and 4.6 can be easily determined from the field data.

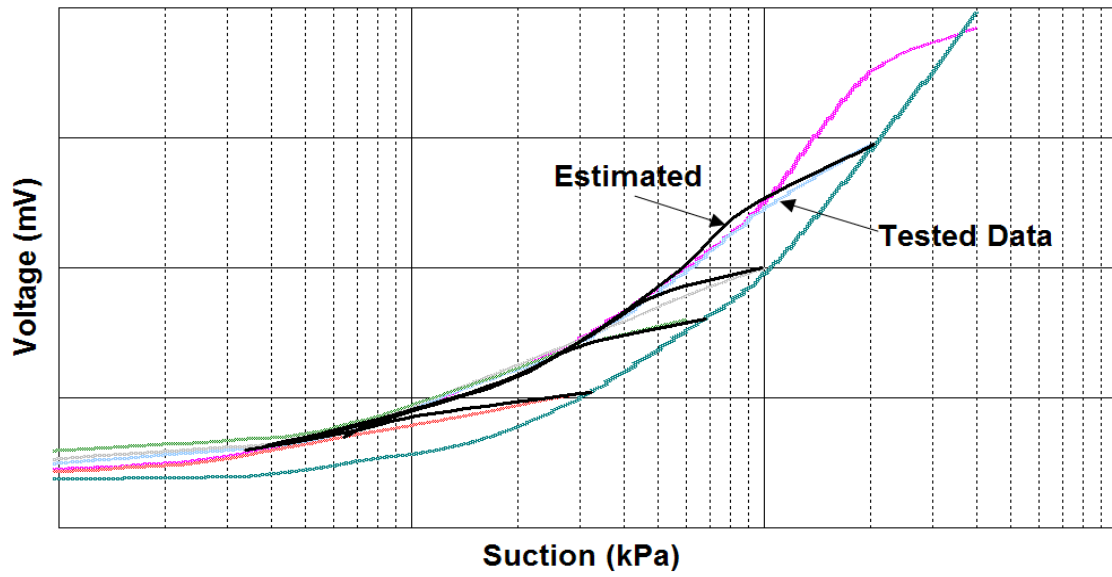


Figure 4.8 Estimated wetting scanning curves using Equation 4.5 for Sensor 2

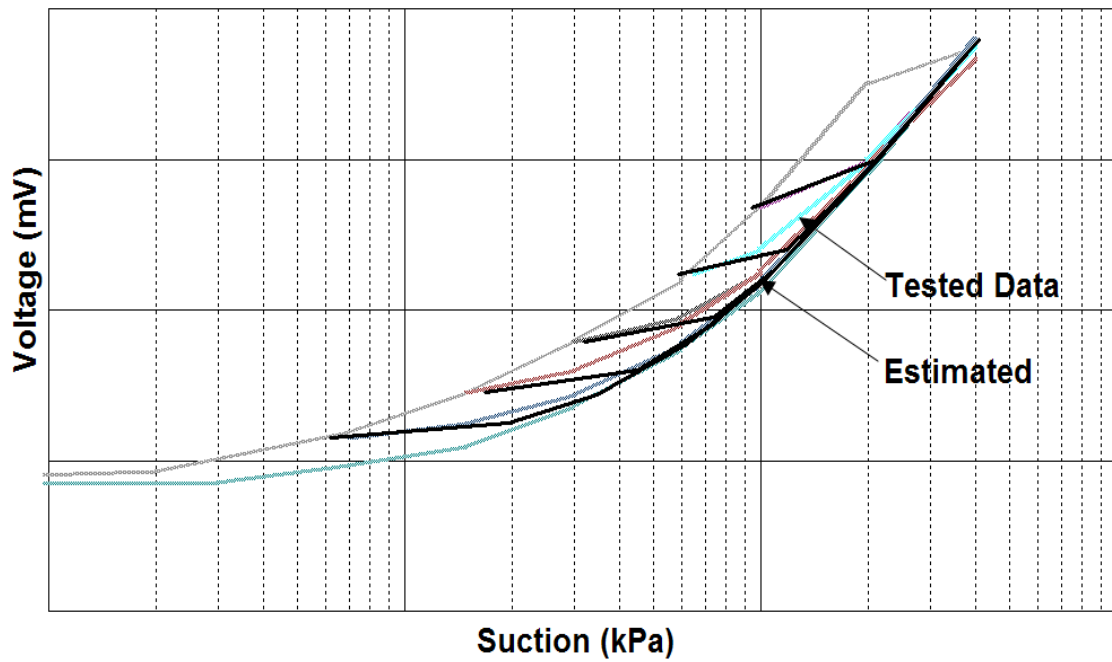


Figure 4.9 Estimated drying scanning curves using Equation 4.6 for Sensor 1

The ratio V_{out}/V_{limit} and V_{limit}/V_{out} in Equations 4.10 and 4.11 have both a numerator and a denominator that continuously vary (i.e., continuous changes of both V_{limit} and V_{out}) while moving on the scanning curves. Therefore, these equations need to be verified with different random data. Some series of data were randomly generated to check the workability of the equations. Two trends of increasing voltage outputs from small to bigger ratios of V_{out}/V_{limit} (or vice versa) were applied to evaluate the differences in the obtained curves. The calculated curves are presented in Figures 4.10 and 4.11. Curve Scan-1 has the lower ratio and curve Scan-2 has the higher ratio. When the ratio is increased the scanning curves shift closer to the other branch of main loop. Thus, different curves of different horizontal locations of the inflection point (relative to main loop) can be generated from Equations 4.4 and 4.5. The horizontal locations of the scanning curves are dependent on the magnitude of the ratio V_{out}/V_{limit} . For this reason, the accuracy of the equations may be questionable in the case of high fluctuations in the voltage readings. However, the derived scanning curves are stable and reproducible.

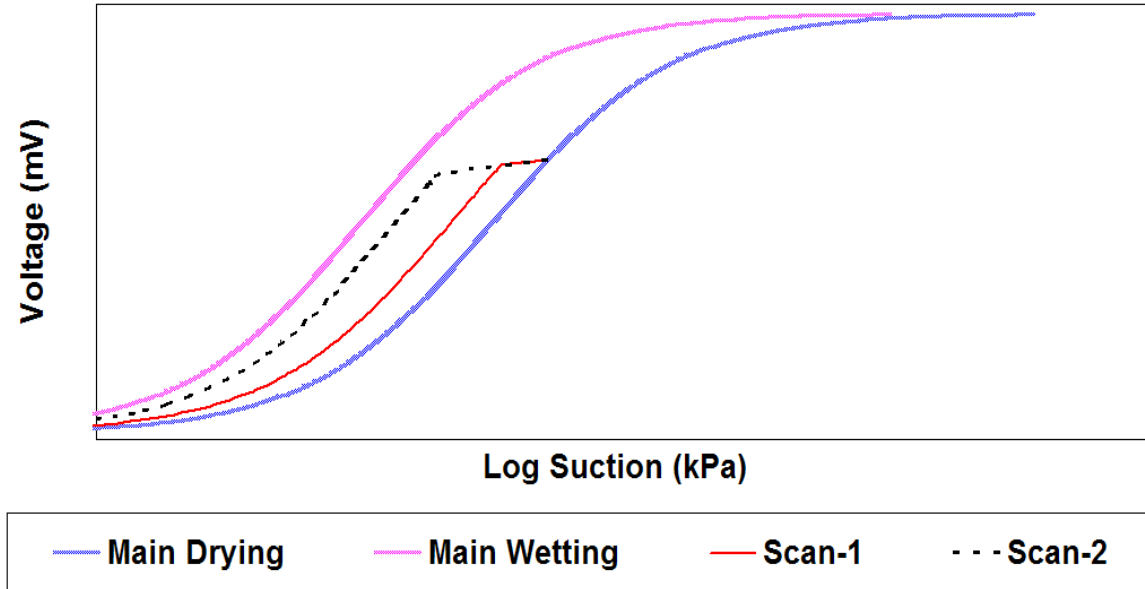


Figure 4.10 Wetting scanning curves using Equation 4.5 with different ratios of V_{out}/V_{limit}

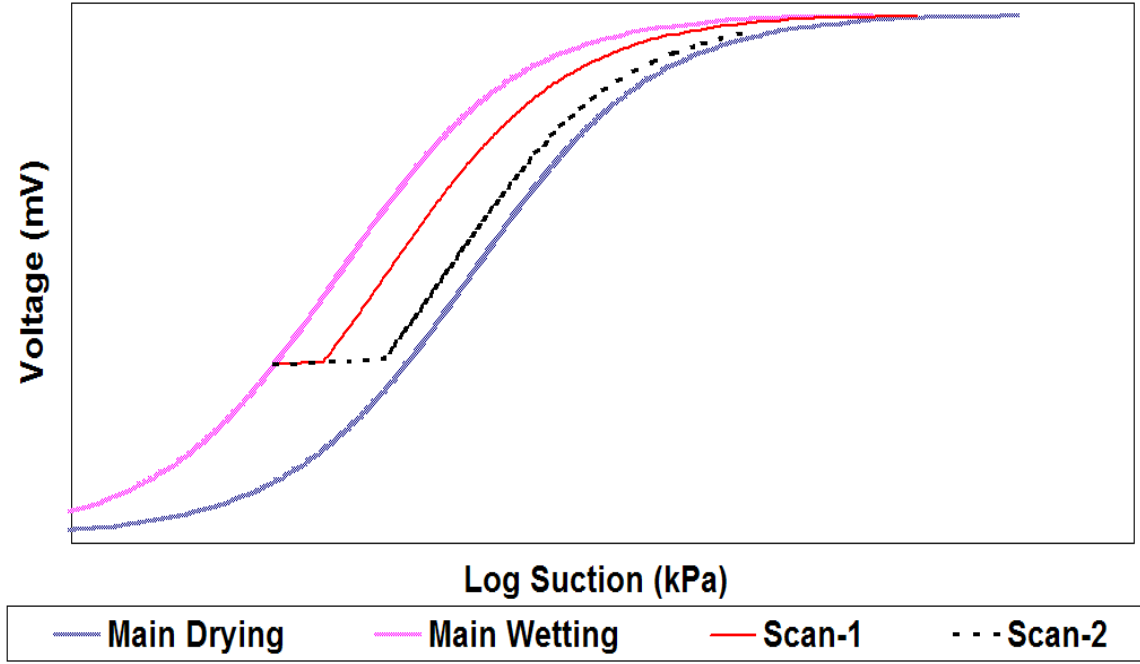


Figure 4.11 Drying scanning curves using Equation 4.6 with different ratios of V_{out}/V_{limit}

4.3.3 Fitting equations regarding bending point of voltage output

Although Shuai's (2001) equations are easy to apply and provide stable results, the accuracy of the equations might be questionable because of an inability to generate unique scanning curves. Shuai's (2001) equations with high ratio of V_{out}/V_{limit} , may derive scanning curves of higher curvatures than the tested scanning curves (Figures 4.8 and 4.9). The high ratio of V_{out}/V_{limit} (or vice versa) is expected from a surface soil as both V_{out} and V_{limit} change simultaneously. In order to eliminate the variations of the horizontal location of the scanning curve, the following fitting equations are proposed for calculating suction on the scanning curves:

Matric suction on wetting scanning curve:

$$\psi_{d-w} = \psi_{wet} + \left(\frac{V_{out}}{V_{bending}} \right)^{23} (\psi_{dry} - \psi_{wet}) \quad (4.7)$$

Matric suction on drying scanning curve

$$\psi_{w-d} = \psi_{dry} - \left(\frac{V_{bending}}{V_{out}} \right)^{23} (\psi_{dry} - \psi_{wet}) \quad (4.8)$$

where:

$V_{bending}$ = the output voltage at which the voltage recorded changes from increasing to decreasing or vice versa.

The other symbols are defined as the same as in Equations 4.5 and 4.6.

The symbols can be graphically visualized in Figures 4.12 and 4.13. The comparisons of the equations with Feng (1999) experimental results can be seen in Figures 4.14 and 4.15.

Equations 4.7 and 4.8 give the closest scanning curves with the experimental results among the reviewed fitting equations. In addition, with the convenient determination of $V_{bending}$ the equations can be applied to large volumes of the field data.

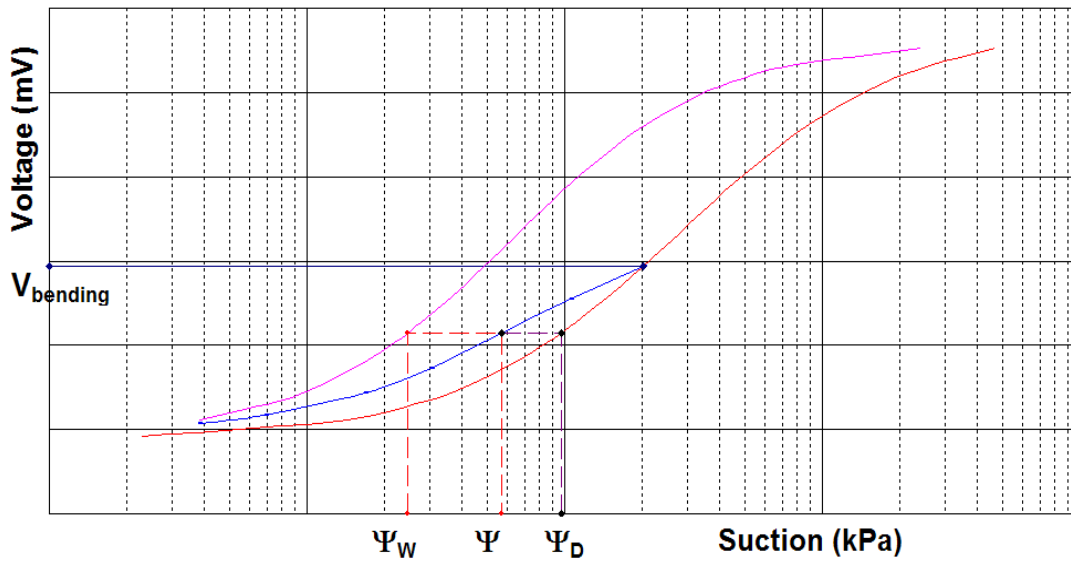


Figure 4.12 Graphical notations for Equation 4.7

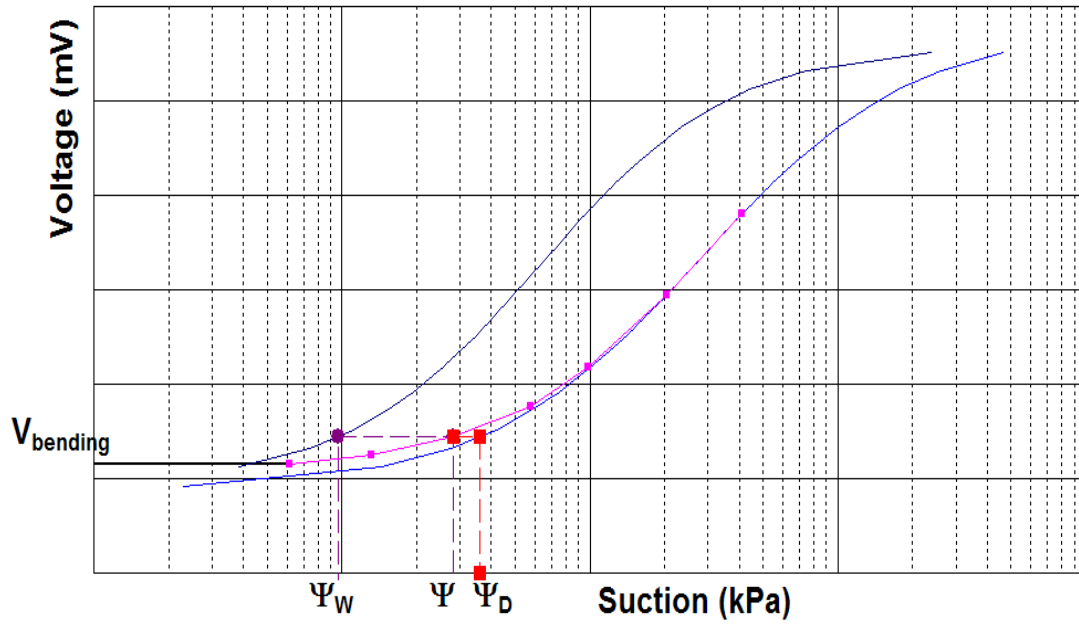


Figure 4.13 Graphical notations for Equation 4.8

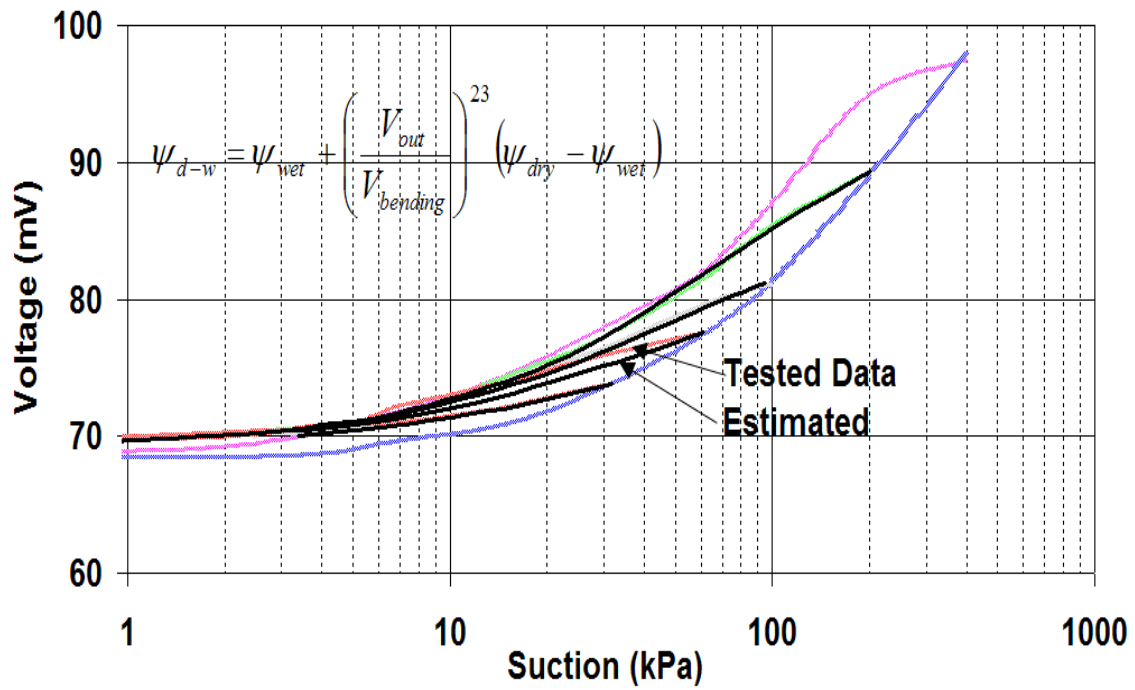


Figure 4.14 Estimated wetting scanning curves using Equation 4.7 for Sensor 2

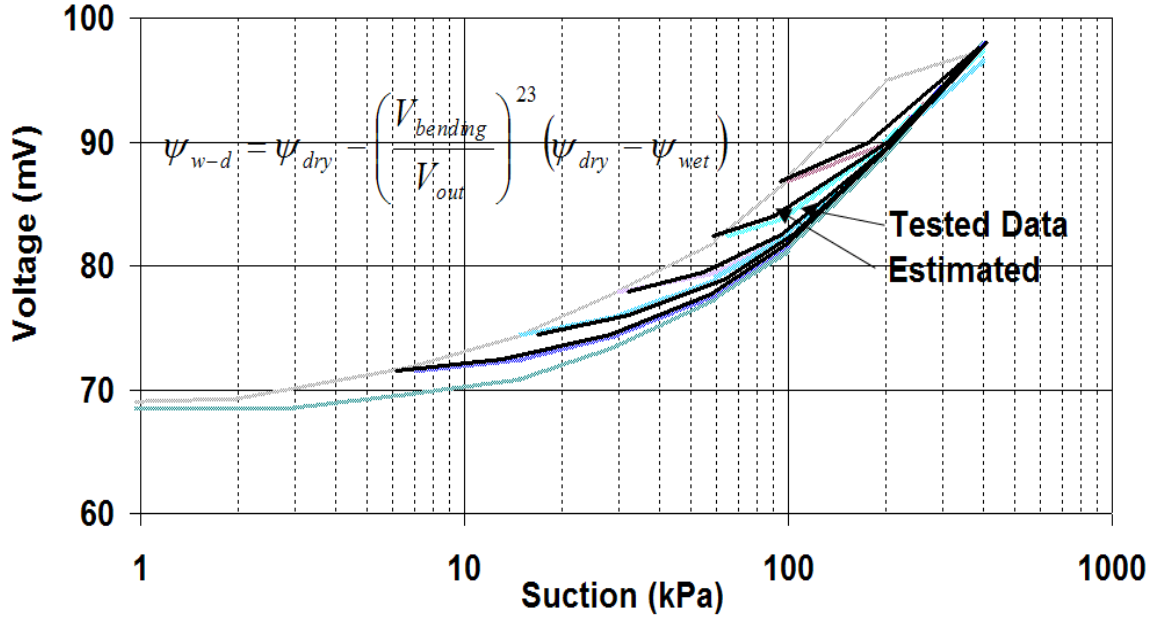


Figure 4.15 Estimated drying scanning curves using Equation 4.8 for Sensor 1

4.4 The field data reduction

The information collected from two field sites through use of a data acquisition system includes temperatures, voltage outputs, accuracy indicators and the date on which the readings were taken. These data were reorganized in vertical columns using a Spread Sheet so that the reduced data were ready for conversion from voltage data to matric suction data. The details on the field data reduction can be found in Appendix B.

4.5 Analysis of in situ suction data

After reducing the field data, the temperature corrections were made using Equation 2.8.

4.5.1 Assumptions for the hysteresis correction and procedural analyses

Six general assumptions are proposed for suction calculations:

1. After being installed in an initially dry state the sensor response followed the main wetting curve until the equilibrium was reached.
2. After every thawing period associated with “spring break-up”, suctions below of 0.8 m downwards were transferred to the main wetting curve. Suctions at depths between 0.3 m and 0.5 m were assumed to reach the main drying curve during freezing.
3. The hysteresis position of a suction reading was determined based on the magnitude of the previous suction reading.
4. The equations for the hysteresis correction were applied for the primary scanning curves and also for the higher order scanning curves.
5. The noise level of the sensors varied from 0.7 to 2.3 mV depending on individual sensor.
6. The accuracy of the main calibration loop was assumed to be higher than the accuracy of the scanning curves.

There are four steps to analyze the field data:

1. The first step is to determine $V_{bending}$. $V_{bending}$ is defined as a voltage output at which the corresponding suction switches from a drying curve to a wetting curve or vice versa. $V_{bending}$ is used for calculating the hysteresis correction (i.e., fitting Equations 4.12 and 4.13).
2. The second step to be taken in suction analysis is to locate the position of currently calculated point on a specific hysteresis branch.
3. The third step is to calculate suction using Equations 4.12 and 4.13 based on the specific position of the measured reading.
4. The fourth step is to choose suction values from the calculated values on the basis of the above-mentioned assumptions.

4.5.2 Determination of $V_{bending}$

A current reading can be chosen as a bending voltage output ($V_{bending}$) if the following conditions are satisfied:

1. The previous point is on the main drying curve or drying scanning curve

- The current reading is the maximum reading between the forty (40) previous and next readings; and
- The previous and current temperature are more than zero

Or:

- The current reading is greater than previous and next readings by a value that is more than the resolution of the sensor; and

- The current temperature is more than zero

2. The previous point is on the main wetting curve or wetting scanning curve

- The current reading is the minimum reading between the forty (40) previous and next readings; and

- The current temperature is more than zero.

Or:

- The current reading is smaller than previous and next readings by a value that is more than the resolution of the sensor; and

- The current temperature is more than zero.

4.5.3 Determination of the location of the current point on the hysteresis curves

The determination of the position of a current point is necessary since this helps locate the next point as mentioned in assumption 3. The hysteresis position of a point can

be specified as ψ_{wet} if the point is on the main wetting curve; or $\psi_{\text{dry-wet}}$ if the point is on a wetting scanning curve; or $\psi_{\text{wet-dry}}$ if the point is on a drying scanning curve; or ψ_{dry} if the point is on the main drying curve (Figure 4.16). ψ_{wet} and ψ_{dry} are calculated using Equation 2.5 while $\psi_{\text{dry-wet}}$ and $\psi_{\text{wet-dry}}$ are calculated using Equations 4.12 and 4.13.

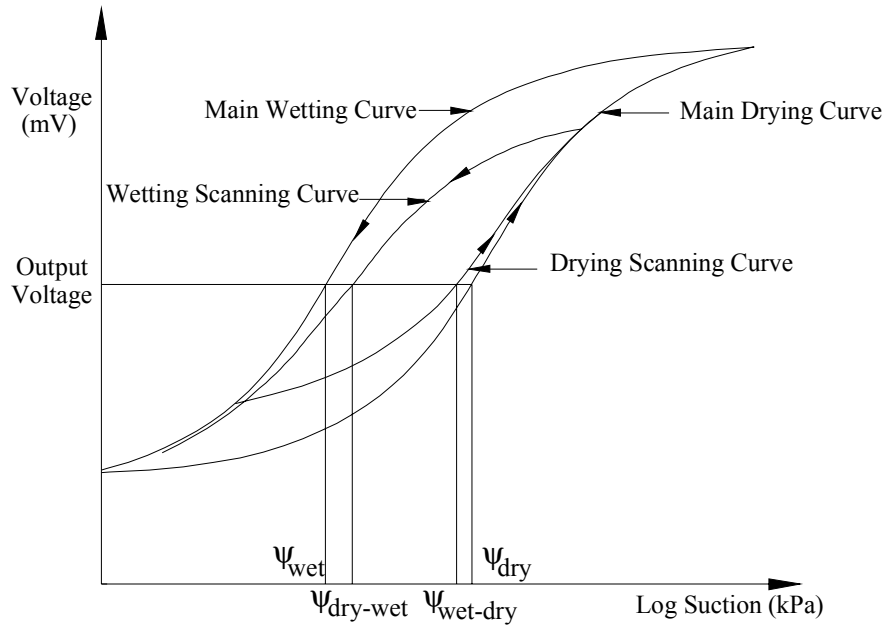


Figure 4.16 Diagram showing possible hysteresis positions of a voltage output from a thermal conductivity sensor

The following rules were applied to determine the current position on a specific hysteresis branch (i.e., ψ_{wet} or $\psi_{\text{dry-wet}}$ or $\psi_{\text{wet-dry}}$ or ψ_{dry}) of a suction reading (Note that the specific location of a suction is determined based on the comparison with the previous suction and with the calculated suctions using the main hysteresis loop of calibration):

1. If the previous reading is on the main drying curve:

- If the current suction is equal to the calculated suction on the main wetting curve, the current reading is on the main wetting curve.
- If the current suction is greater than the calculated suction using the main wetting curve; two possibilities are:

- i. If the current suction is equal to the calculated suction on the main drying curve, the current reading is on the main drying curve.
- ii. If the current suction is smaller than the calculated suction on the main drying curve, the current reading is on wetting scanning curve.

2. If the previous reading is on wetting scanning curve:

- If the current suction is equal to the calculated suction on the main wetting curve the current reading is on the main wetting curve.
- If the current suction is greater than the calculated suction on the main wetting curve; two possibilities are:
 - i. If the current suction is equal to the calculated suction on the main drying curve, the current reading is on the main drying curve.
 - ii. If the current suction is smaller than the calculated suction on the main drying curve, the current reading is on wetting scanning curve.

3. If the previous point is on drying scanning curve:

- If the current suction is equal to the calculated suction on the main drying curve, the current reading is on the main drying curve.
- If the current suction is smaller than the calculated suction on the main drying curve; two possibilities are:
 - i. If the current suction is equal to the calculated suction on the main wetting curve, the current reading is on the main wetting curve.

- ii. If the current suction is greater than the calculated suction on the main wetting curve, the current reading is on drying scanning curve.

4. If the previous suction is on the main wetting curve:

- If the current suction is equal to the calculated suction on the main drying curve, the current reading is on the main drying curve.
- If the current suction is smaller than the calculated suction on the main drying curve; two possibilities are:
 - i. If the current suction is more than the calculated suction on the main wetting curve, the current reading is on drying scanning curve
 - ii. If the current suction is equal to the calculated suction on the main wetting curve, the current reading is on the main wetting curve.

4.5.4 Selection of the current suction

To choose the most reasonable suction from the calculated values, the assumed accuracy of the suction conversion from calibration curve needs to be taken into account. Generally, the accuracy of the main loop is higher than the accuracy of fitting scanning curves. Therefore, if the calculated values from scanning curves do not exceed 5% the values on the main loop the values on main loop should be chosen. Accordingly the followings are applied to select suction values.

1. If the previous reading on the main drying curve or wetting scanning curve:

- If the calculated suction is less than 105 % of the suction on the main wetting curve, choose the suction value on the main wetting curve.

- If the calculated suction is more than 105 % of the suction on the main wetting curve:

- i. If the calculated suction is not smaller than 95 % of the suction on the main drying curve, choose the suction on the main drying curve.
- ii. If the calculated suction is smaller than 95 % of the suction on the main drying curve, choose the calculated suction.

2. If the previous reading on the main drying curve or wetting scanning curve:

- If the calculated suction is more than 95 % of the suction on the main drying curve, choose the suction value on the main drying curve.

- If the calculated suction is less than 95 % of the suction on the main drying curve:

- i. If the calculated suction is not greater than 105 % of the suction on the main wetting curve, choose the suction on the main wetting curve.
- ii. If the calculated suction is greater than 105 % of the suction on the main wetting curve, choose the calculated suction.

Some additional adjustments related to individual resolution of the sensors may be required during the analysis. The results from the hysteresis correction applied are representatively shown in Figures 4.17; 4.18 and 4.19.

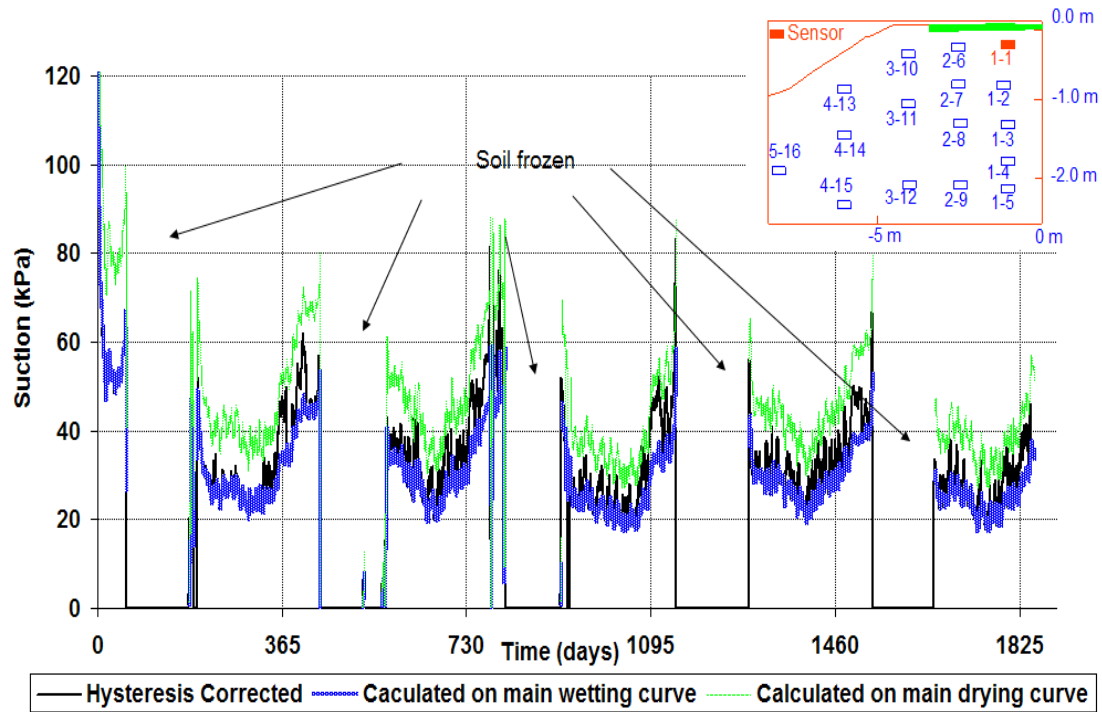


Figure 4.17 Suction with hysteresis correction using $V_{bending}$ for a shallow-depth sensor (T1-1 at 0.3 m depth, Torquay)

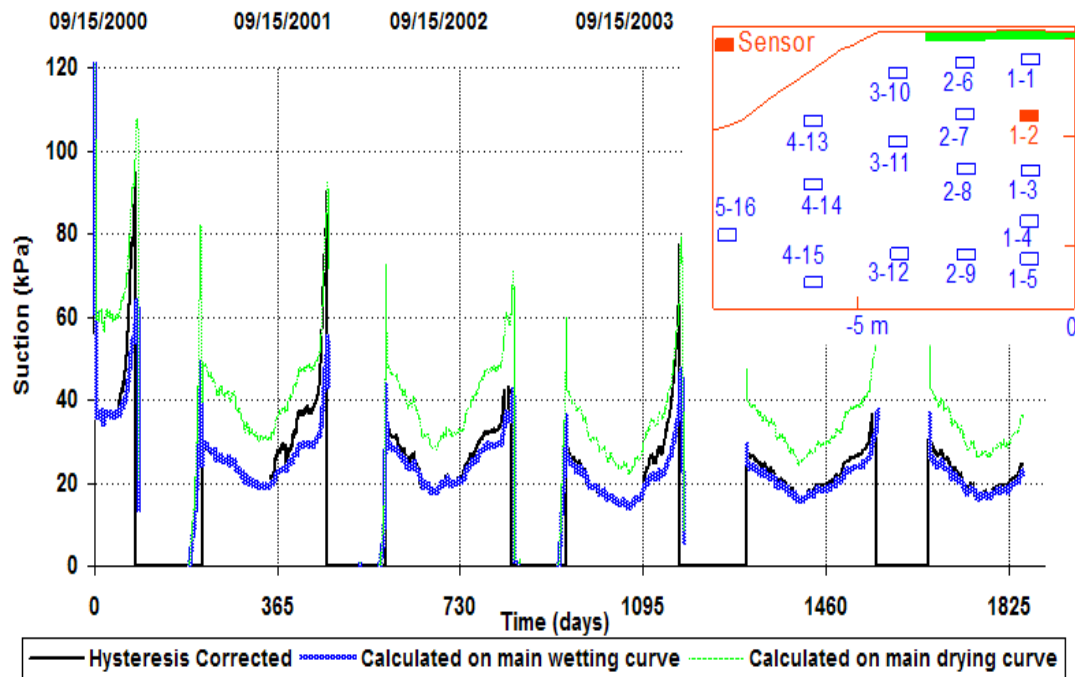


Figure 4.18 Suction with hysteresis correction using $V_{bending}$ for a middle-depth (0.8m) sensor (T1-2 at 0.8 m depth, Torquay)

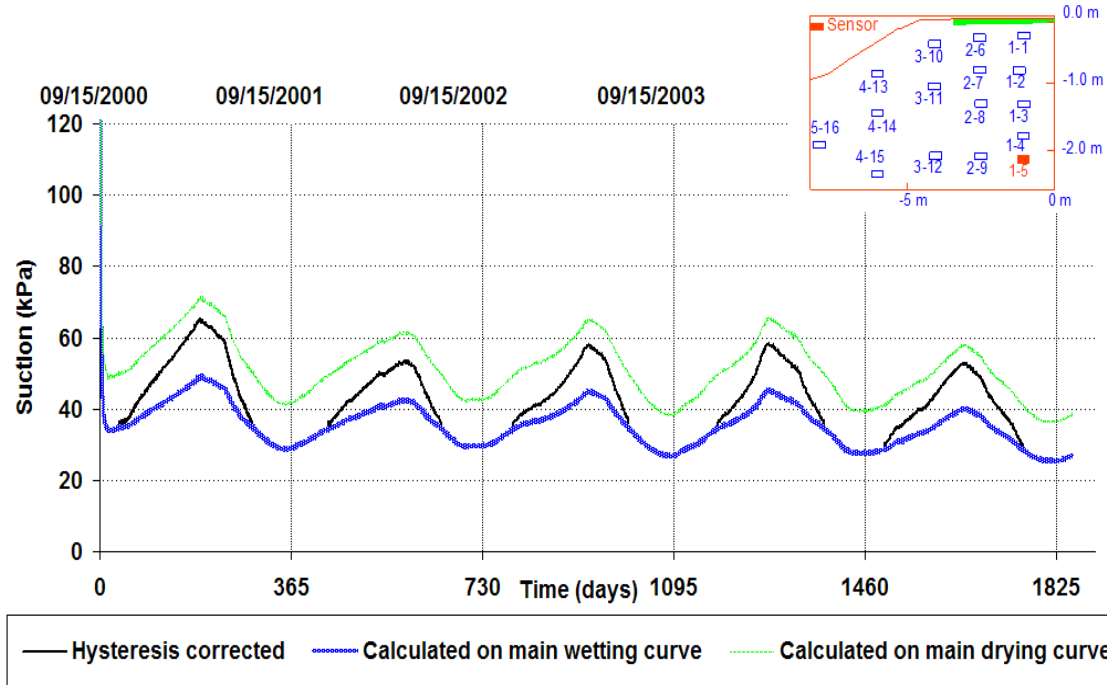


Figure 4.19 Suction with hysteresis correction using $V_{bending}$ for a bottom-depth sensor (T1-5 at 2.2 m depth, Torquay)

The method of hysteresis correction using V_{limit} (i.e., Equations 4.10 and 4.11) is also tentatively applied. The representative results are illustrated in Figures 4.20 and 4.21. The difference between using $V_{bending}$ and V_{limit} can be realized at bottom-depth sensors. Conversely, the difference is hardly noticeable at shallow-depth sensors due to the effect of highly fluctuating readings at this depth. Comparing with experimented results conducted by Feng (1999) the method using V_{limit} tends to exaggerate the amplitude of suction variations (i.e., estimated scanning curves have higher slopes than tested scanning curves). In the laboratory testing program the readings shift from the main wetting curve to the main drying curve only after the suction values reduce at least half or increase by a factor of 2. However, in Figures 4.20 and 4.21 the suction readings switch between these two curves when increasing or reducing less than twice or half. Therefore, Equations 4.12 and 4.13 for hysteresis correction with $V_{bending}$ were selected for use in this research.

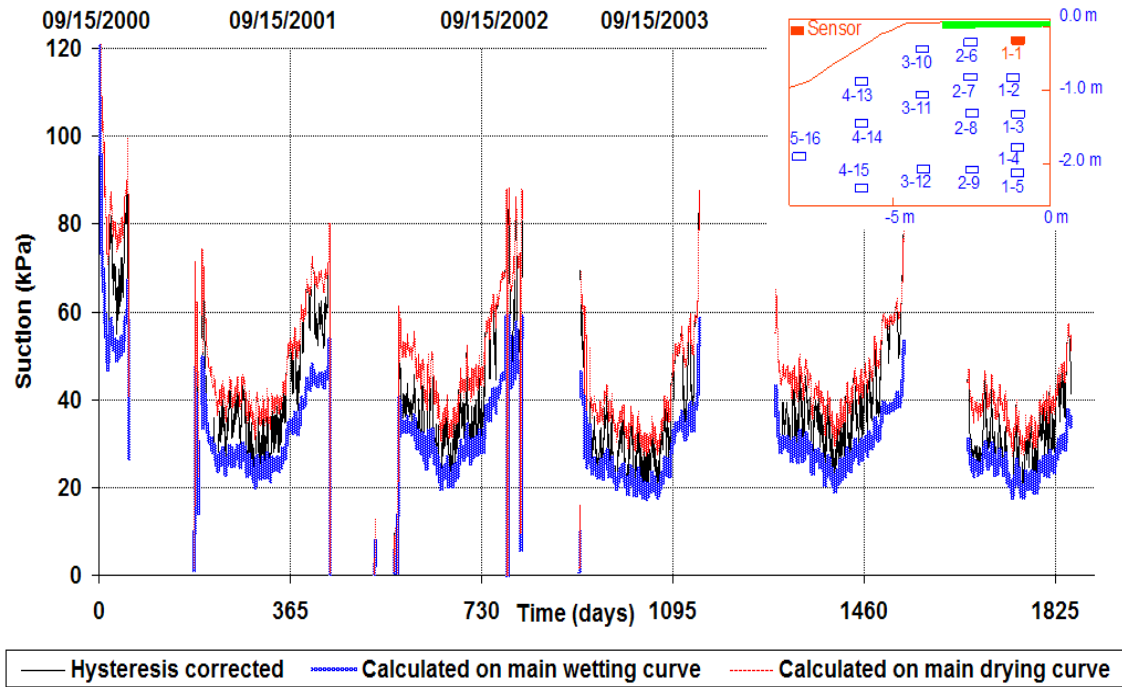


Figure 4.20 Suction with hysteresis correction using V_{limit} for a shallow-depth sensor at Torquay (T1-1)

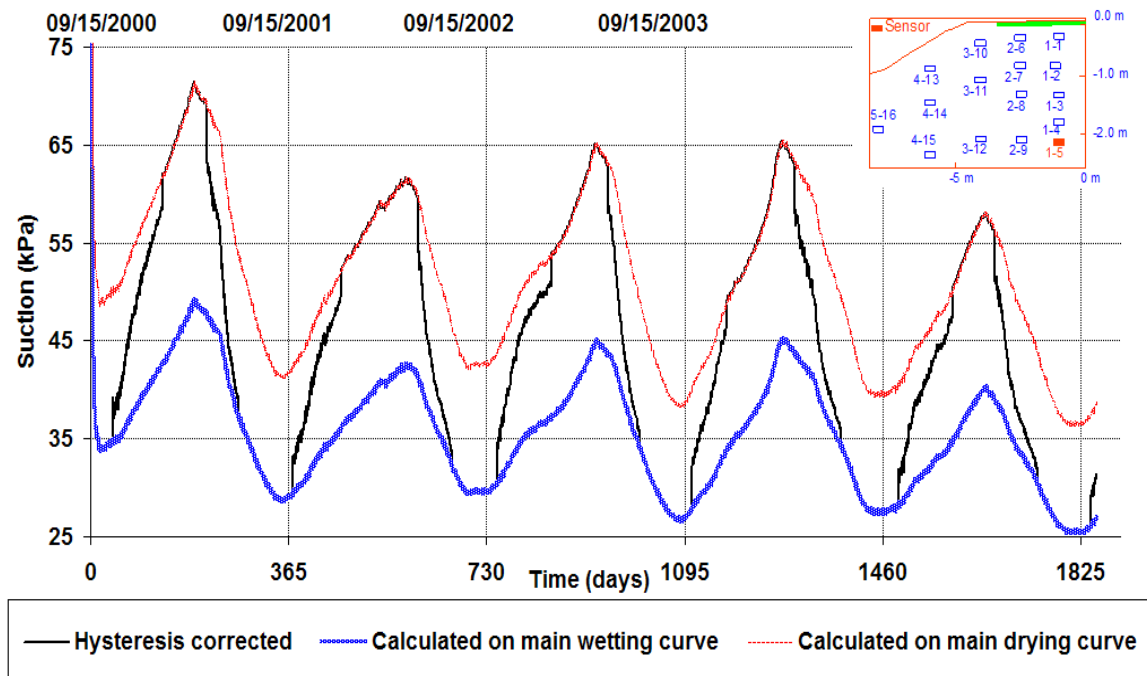


Figure 4.21 Suction with hysteresis correction using V_{limit} for a bottom-depth sensor at Torquay (T1-5)

CHAPTER 5

PRESENTATION OF LABORATORY TEST RESULTS AND *IN SITU* SUCTIONS CALCULATED USING THE MAIN HYSTERESIS LOOP WITH NO TEMPERATURE CORRECTION

This chapter presents the laboratory test results, rainfall data and *in situ* suctions calculated on the main hysteresis loop of the calibration curve with no ambient temperature correction.

5.1 Laboratory test results

The laboratory tests as part of the due diligence investigation were performed to characterize the soils at the two test sites. The testing program was carried out at the geotechnical laboratory at the University of Saskatchewan, Saskatoon. There were eleven (11) soil-water characteristic curve tests, nine (9) consolidation tests, thirteen (13) particle size analysis tests and eleven (11) Atterberg limits tests along with specific gravity, relative density and water content tests performed in the testing program. The results showed the soils (except some thin sand lenses) at both sites were an over-consolidated, lean clay (CL) according to the Unified Soil Classification System (USCS) with approximate 60% particles smaller than 0.074 mm. The stone contents varied from sample to sample. The details of the laboratory results can be found in Appendix C. The results of pre-consolidation stresses and index tests are shown in Figure 5.1.

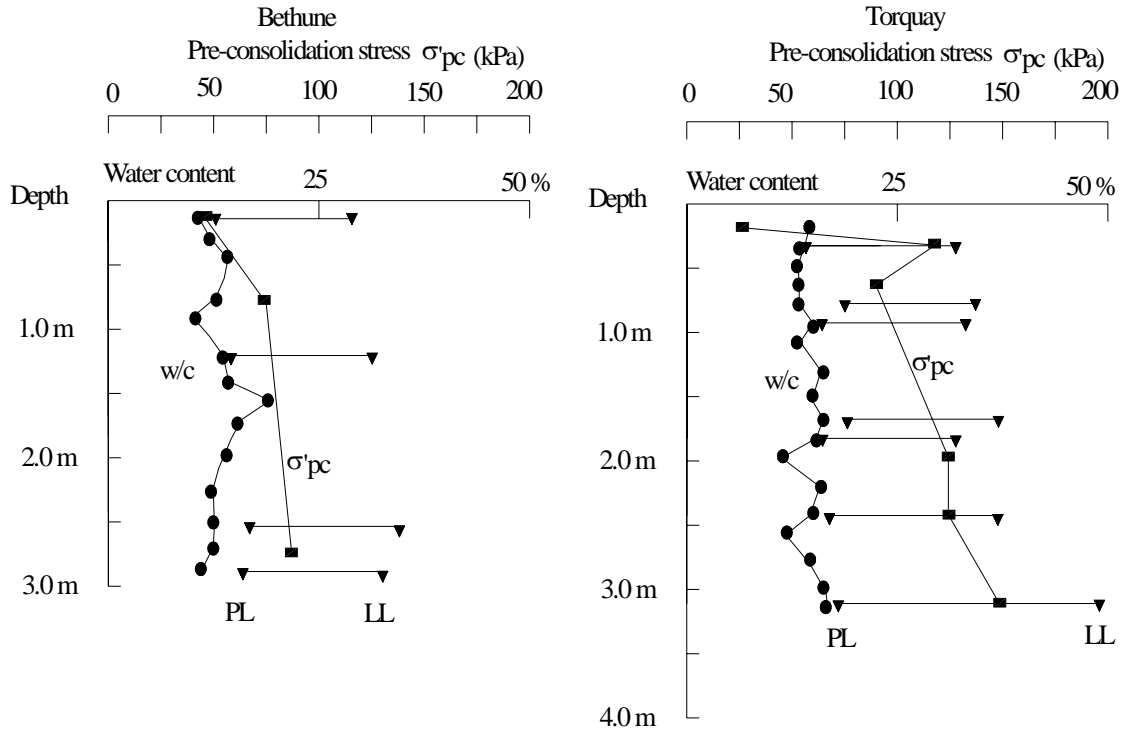


Figure 5.1 Pre-consolidation pressures, water contents (w/c) and Atterberg limits with depth at the Bethune site and Torquay site

The air entry values were difficult to determine on the soil-water characteristic curves. The water content of the samples changed continuously under consecutively applied pressures due to the presence of stones interbedded in the samples. One soil-water characteristic curve is shown Figures 5.2.

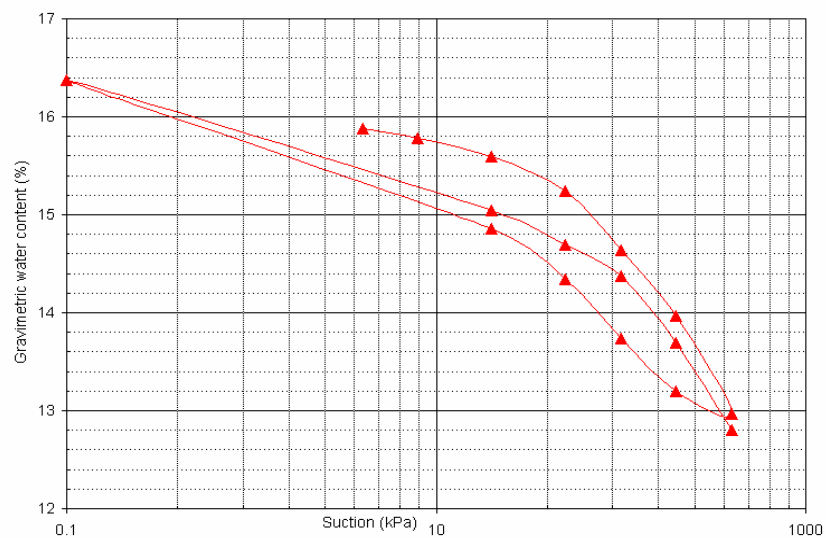


Figure 5.2 Soil-water characteristic curve of sample T5-1 (at a depth of 0.10 to 0.25 m)
at the Torquay site

5.2 Temperature and rainfall data

The temperature and rainfall data which are of assistance in interpreting the variations in matric suctions are presented in this section.

5.2.1 Temperature comparison between sensor and thermister

A representative example of temperatures from the thermal conductivity sensors and the nearby thermisters is given in Table 5.1. A good agreement (i.e., the difference of less than 1.8° C) in temperature measurement was witnessed between the thermal conductivity sensor readings and the thermistor readings.

Table 5.1 Temperatures recorded by the thermister and the thermal conductivity sensor
at 0.3 m depth

Sensor B 1-1 at the Bethune site				
Date	Time	Thermister (° C)	Sensor (° C)	Difference (° C)
5/5/2001	16:00:00	12.2	13.6	-1.4
5/6/2001	16:00:00	11.9	12.9	-1.1
5/7/2001	16:00:00	10.3	11.2	-0.9
5/8/2001	16:00:00	10.3	11.5	-1.2
5/9/2001	16:00:00	11.9	13.4	-1.4
5/10/2001	16:00:00	11.8	13.3	-1.5
5/11/2001	16:00:00	13.0	14.6	-1.7

Figure 5.3 gives mean daily air temperatures at the Torquay site for a five-year period from 2001 to 2005. The temperatures varied from -40°C to $+30^{\circ}\text{C}$.

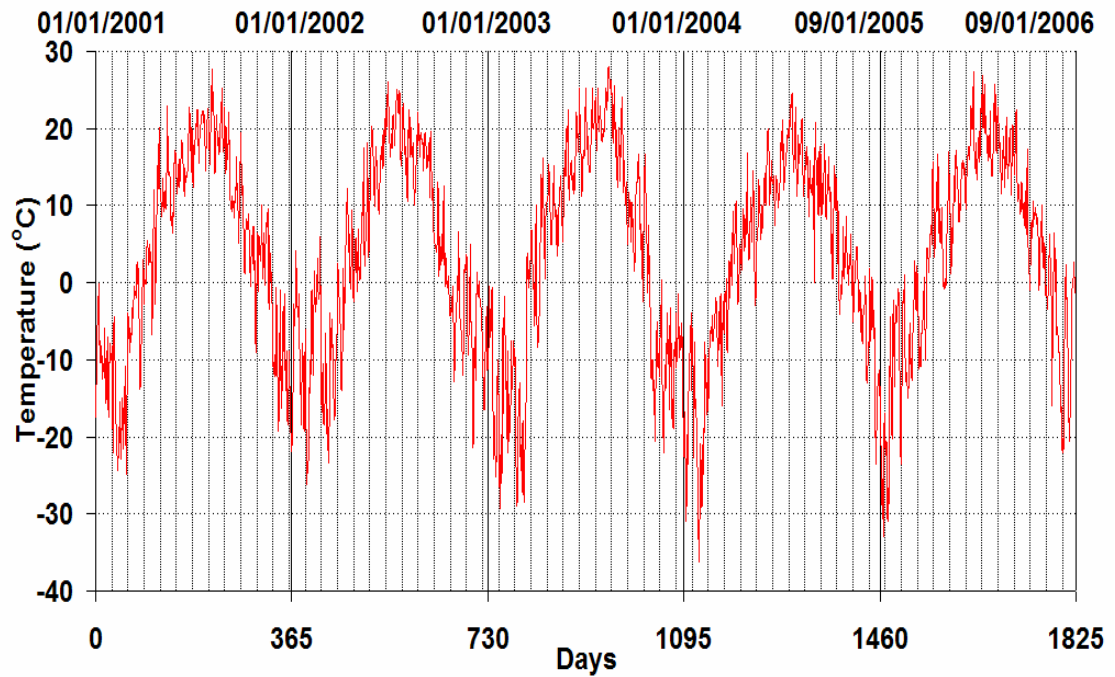


Figure 5.3 The air temperatures at the Torquay site from 2001 to 2005 (After Environment Canada, 2005)

The 14 day-moving average of rainfall data was chosen to investigate the relationship between the rainfalls and the matric suctions (Figure 5.4).

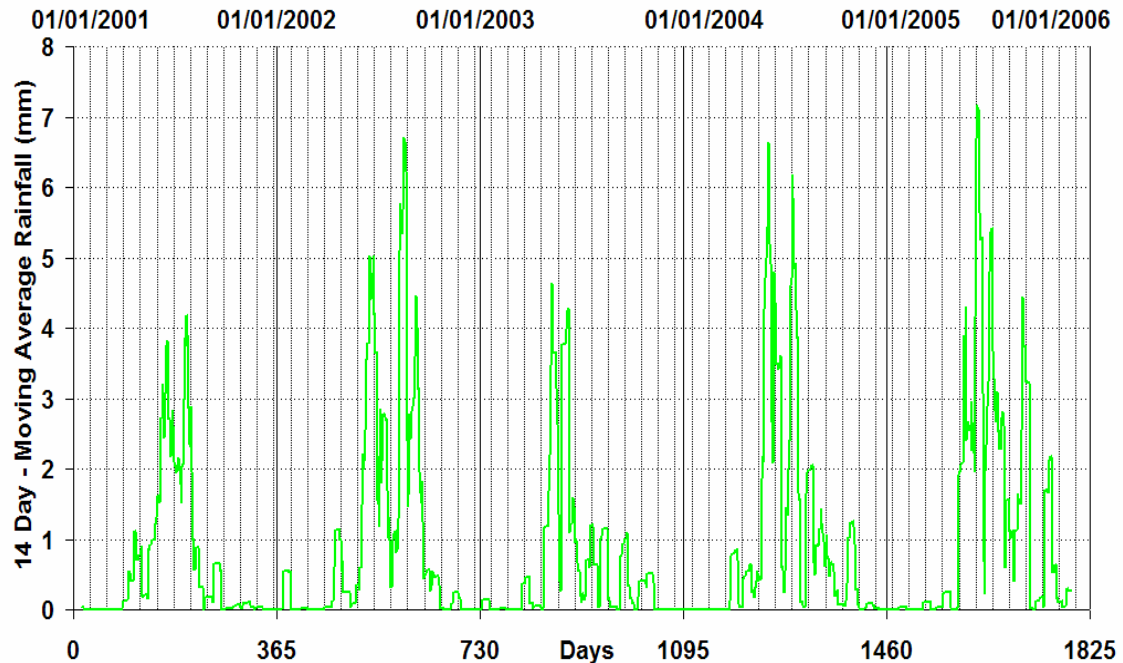


Figure 5.4 The 14-day moving average of rainfall at the Torquay site

5.3 Presentation of *in situ* uncorrected matric suction

This section presents the *in situ* uncorrected matric suctions on vertical grid-lines laid out at each site.

5.3.1 Background of *in situ* uncorrected matric suction

The thermal conductivity sensors indirectly determine the soil matric suction by measuring the voltage difference (or temperature rise) between “prior to” and “after” heating the core element of the sensors. The corresponding suction is then obtained by entering the calibration curve with voltage differences. The calibration curve is predetermined in the laboratory by subjecting a sensor to a sequence of suctions. For the thermal conductivity sensors installed at the Bethune site and Torquay, the main drying curves were generated based on laboratory data and the main wetting curves were estimated. The fitting Equation 2.5 in Chapter 2 was used for the conversion from the voltage outputs to matric suctions.

$$\psi = \left(\frac{b(\Delta V - a)}{c - \Delta V} \right)^d \quad (2.5)$$

The *in situ* uncorrected matric suctions were computed using the main drying and wetting curves without temperature and hysteresis corrections.

5.3.2 Vertical grid-line under driving-lane at the Torquay site

Three sensors; T1-1, T1-2 and T1-5 were selected to present matric suctions on the vertical grid-line under driving-lane at the Torquay site. Sensors T1-1, T1-2 and T1-5 are at depths of 0.3 m, 0.8 m and 2.2 m, respectively.

The *in situ* uncorrected suctions from these sensors for the period of more than 5 years are plotted in Figure 5.5. For the clarity in illustration the uncorrected suctions from individual sensors are presented in two years (i.e., 2002 and 2003 at the Torquay site) in Figures 5.6 to 5.8. The matric suctions under driving-lane varied from 20 to 100 kPa and showed seasonal pattern of the changes. The fluctuations of *in situ* uncorrected suctions happened with the same cycle, frequency and amplitude each year on both main drying and wetting curves. The difference between the suctions calculated on the main drying and wetting curves under driving-lane was approximately 10 to 35 kPa.

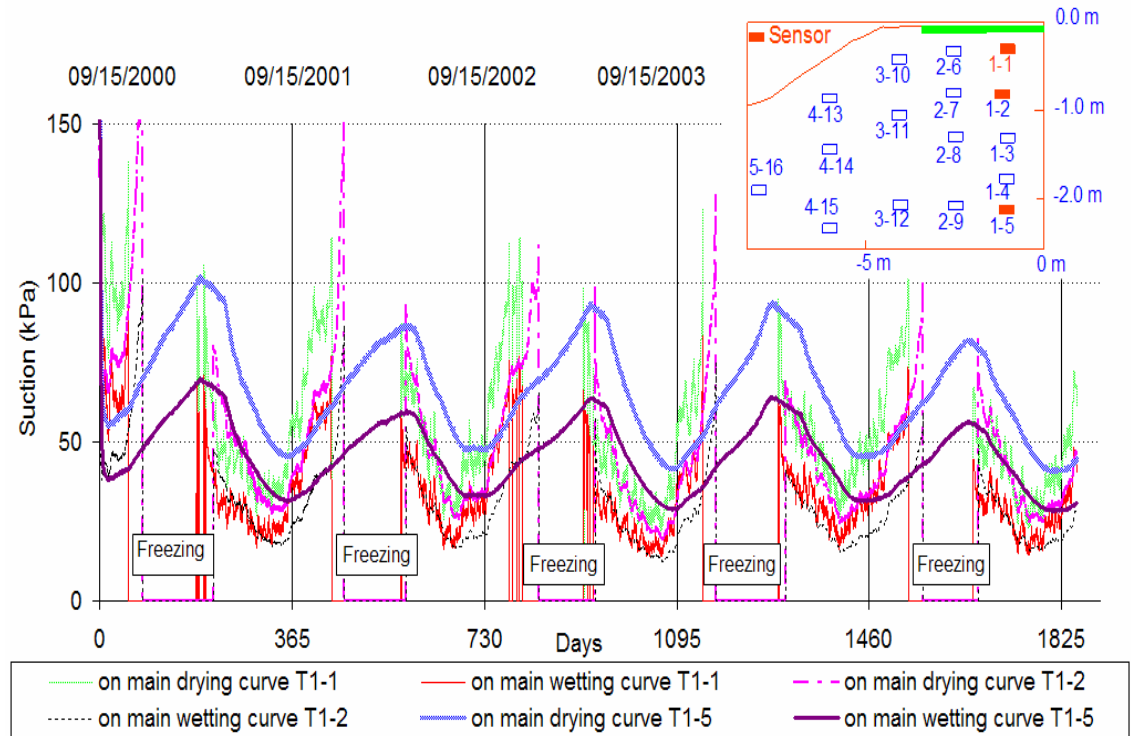


Figure 5.5 *In situ* uncorrected suctions along vertical grid-line under driving-lane at the Torquay site

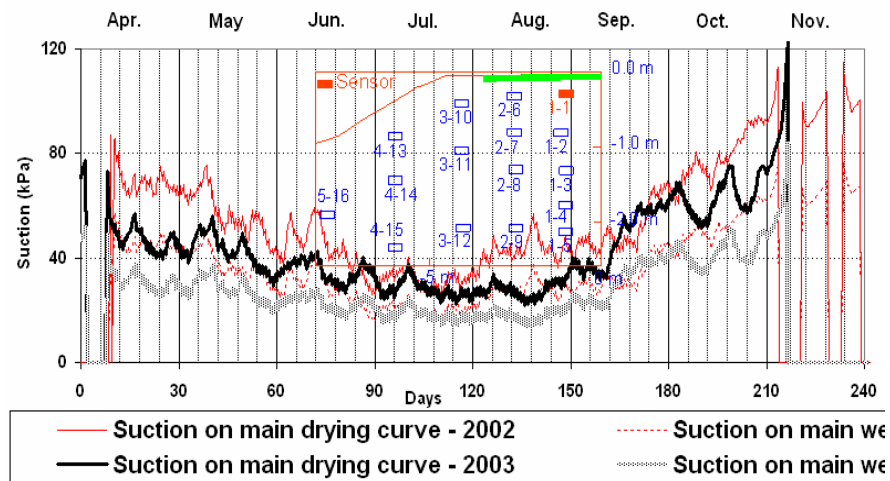


Figure 5.6 *In situ* uncorrected suctions at Sensor T1-1 in 2002 and 2003 at the Torquay site

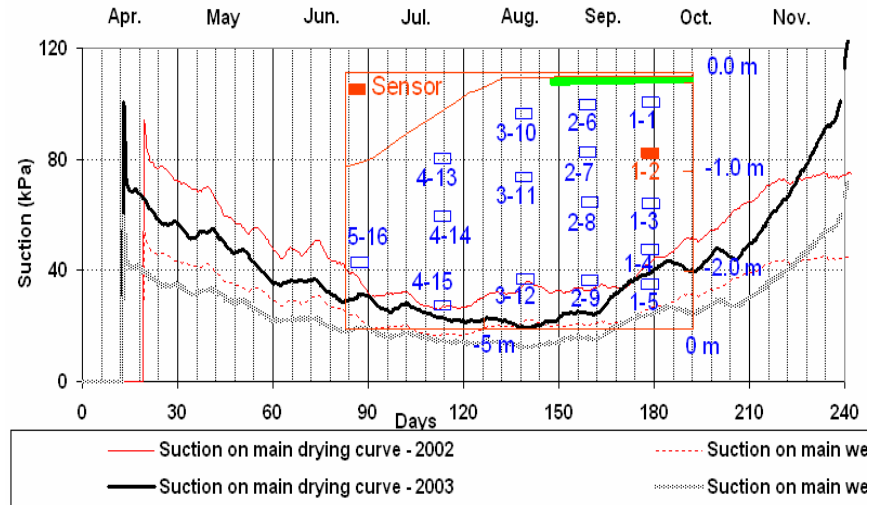


Figure 5.7 *In situ* uncorrected suctions at Sensor T1-2 in 2002 and 2003 at the Torquay site

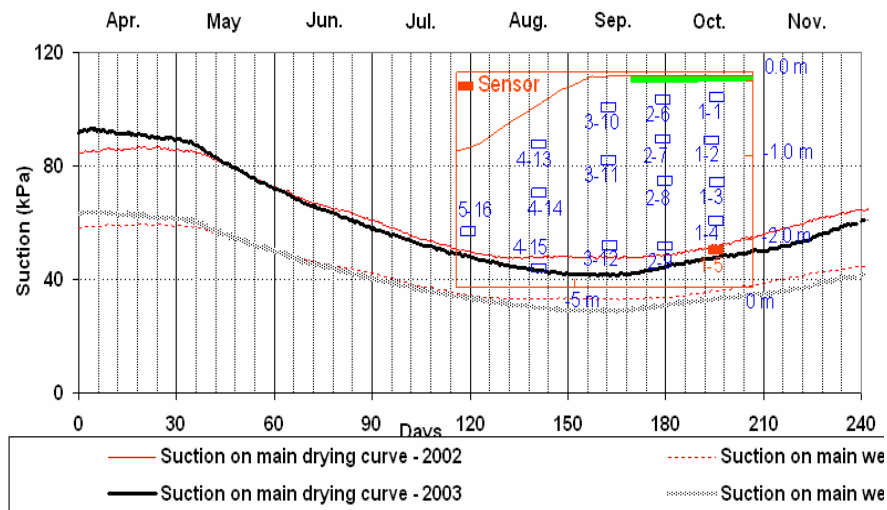


Figure 5.8 *In situ* uncorrected suctions at Sensor T1-5 in 2002 and 2003 at the Torquay site

5.3.3 Vertical grid-line under shoulder at the Torquay site

Three sensors; T3-10, T3-11 and T3-12 were selected to present matric suctions on the vertical grid-line under shoulder at the Torquay site. Sensors T3-10, T3-11 and T3-12 are at depths of 0.4 m, 1.0 m and 2.0 m, respectively.

The *in situ* uncorrected suctions from these sensors for the period of more than 5 years are plotted in Figure 5.9. The uncorrected suctions from individual sensors are presented in Figures 5.10 to 5.12. The variations of suction at Sensor T3-10 were greater than the deeper sensors at the same vertical grid-line. The maximum suction calculated on the main drying curve was 1000 kPa at Sensor T3-10 in October 2001. The difference between the suctions calculated on main drying curves and wetting curves ranged from 20 to 40%. Therefore, when the suctions increased to 1000 kPa this difference could reach as much as 400 kPa.

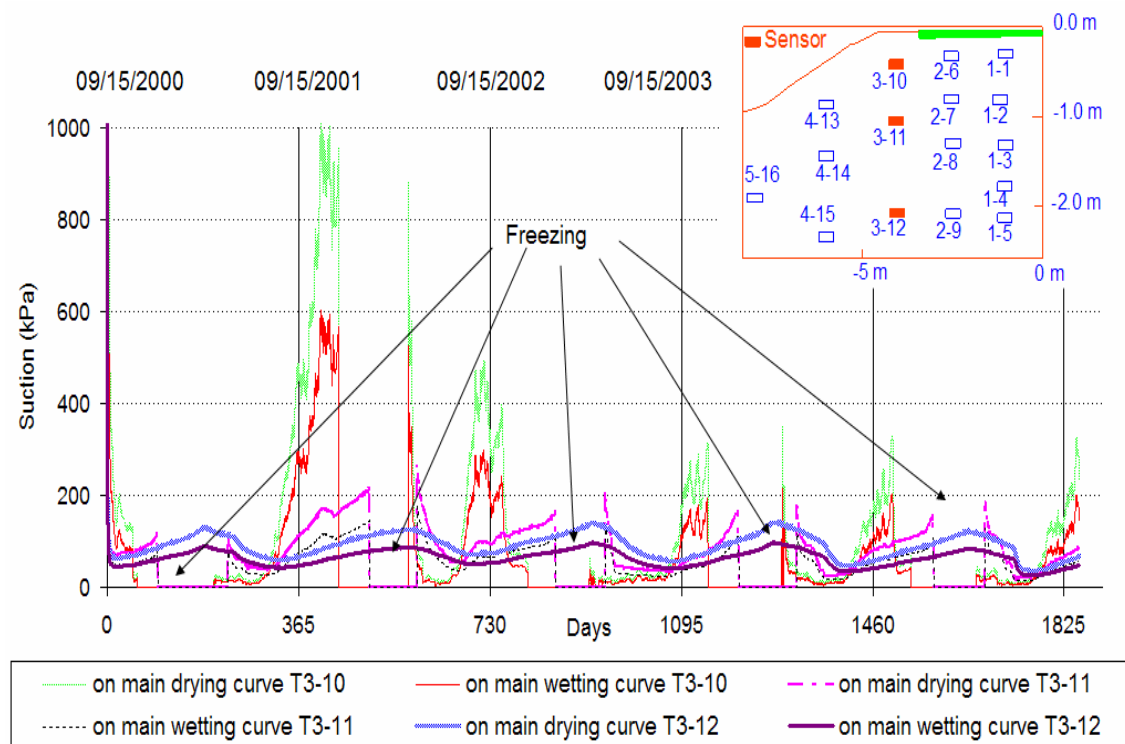


Figure 5.9 *In situ* uncorrected suctions along vertical grid-line under shoulder at the Torquay site

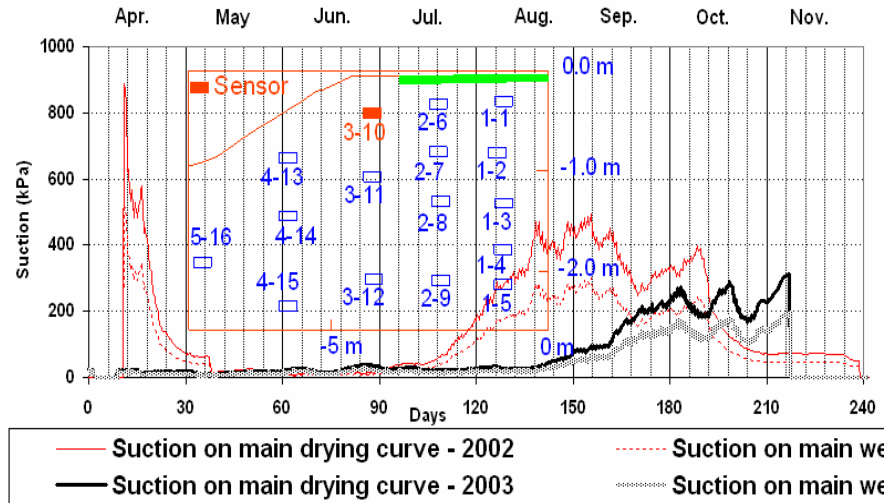


Figure 5.10 *In situ* uncorrected suctions at Sensor T3-10 in 2002 and 2003 at the Torquay site

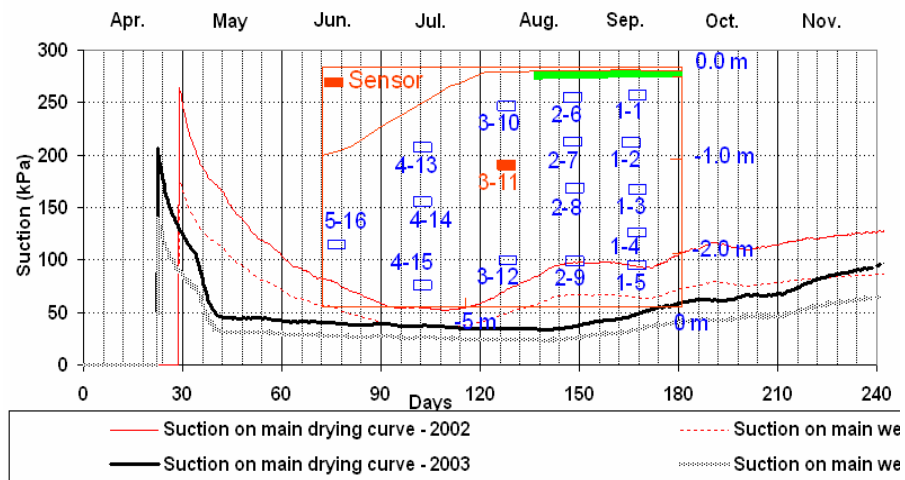


Figure 5.11 *In situ* uncorrected suctions at Sensor T3-11 in 2002 and 2003 at the Torquay site

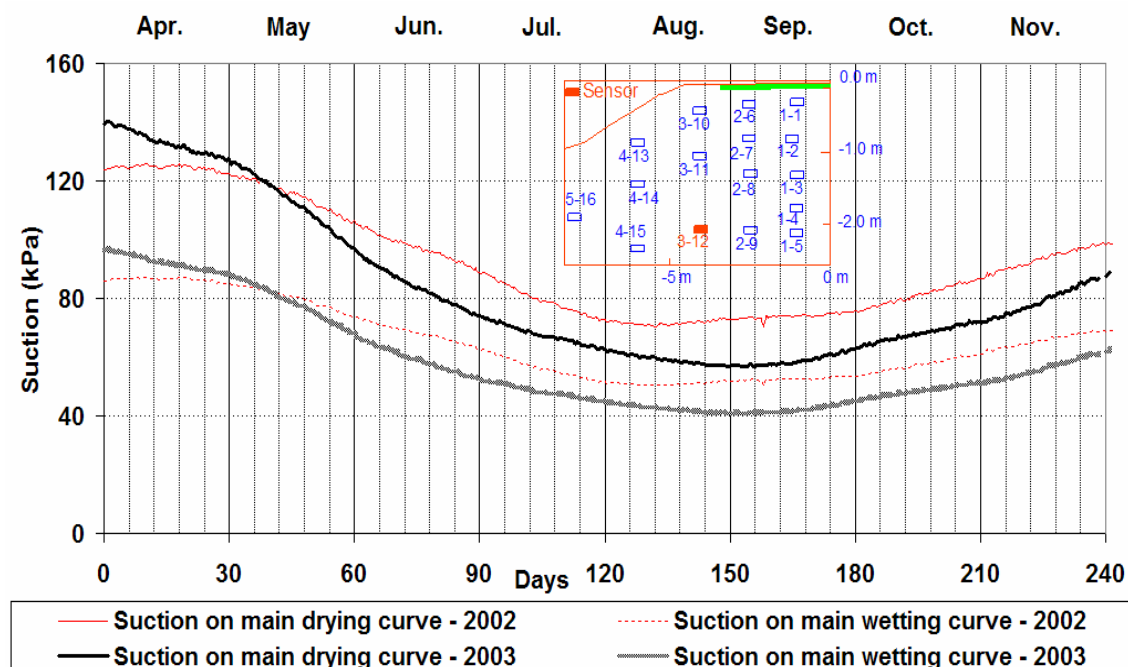


Figure 5.12 *In situ* uncorrected suctions at Sensor T3-12 in 2002 and 2003 at the Torquay site

5.3.4 Vertical grid-line under side-slope at the Torquay site

Three sensors; T4-13, T4-14 and TT4-15 were selected to present matric suctions on the vertical grid-line under side-slope at the Torquay site. Sensors T4-13, T4-14 and T4-55 are at depths 0.5 m, 1.1 m and 1.9 m, respectively.

The *in situ* uncorrected suctions from these sensors for the period of more than 5 years are shown in Figure 5.13. The uncorrected suctions from individual sensors are presented in Figures 5.14 to 5.16. The variations of suction at Sensor T4-13 were significantly greater than the deeper sensors at the same vertical grid-line. The maximum suction calculated on the main drying curve was 27,000 kPa at Sensor T4-13 in November 2002 and 2003 at the Torquay site. Sensor T4-13 showed the difference between the uncorrected suctions calculated on the main drying curve and on the main wetting curve reached as much as 5,000 kPa.

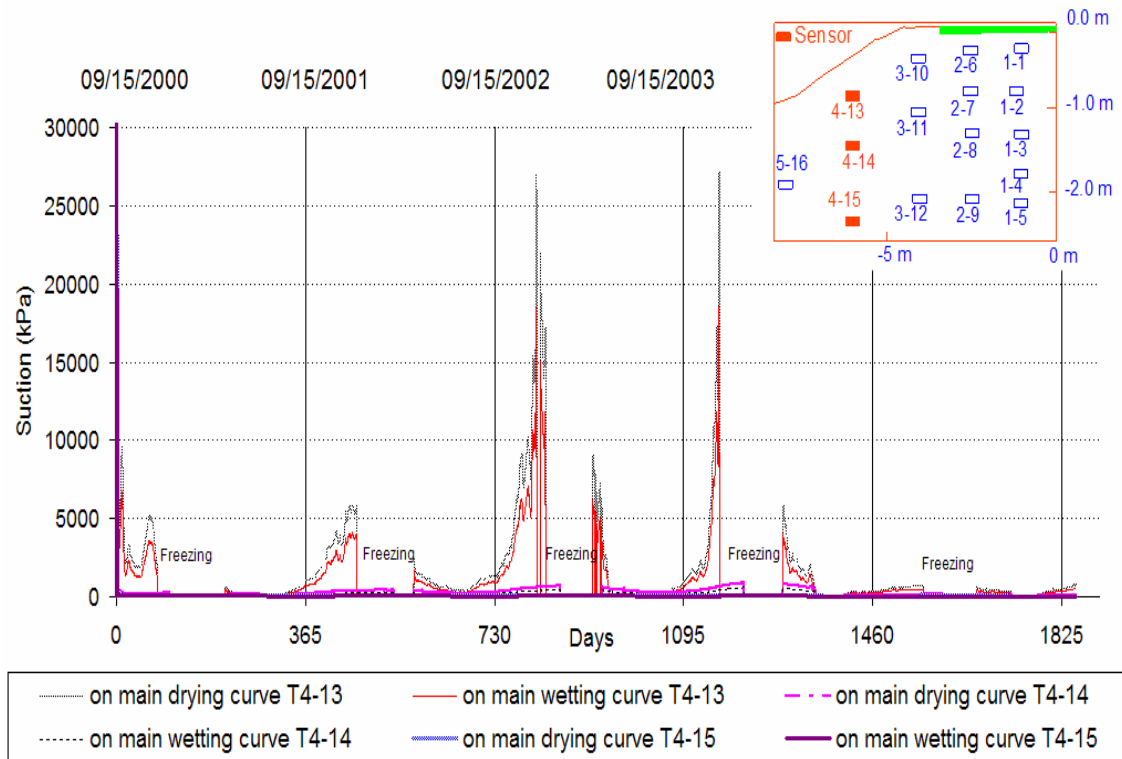


Figure 5.13 *In situ* uncorrected suctions along vertical grid-line under side-slope at the Torquay site

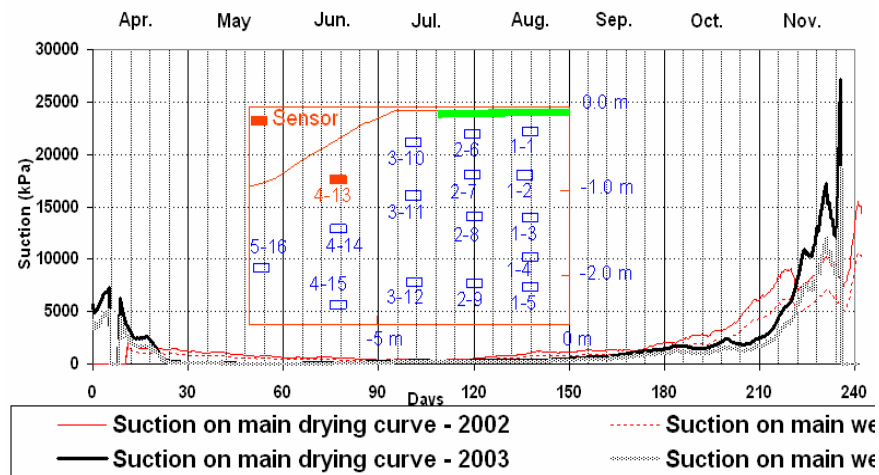


Figure 5.14 *In situ* uncorrected suctions at Sensor T4-13 in 2002 and 2003 at the Torquay site

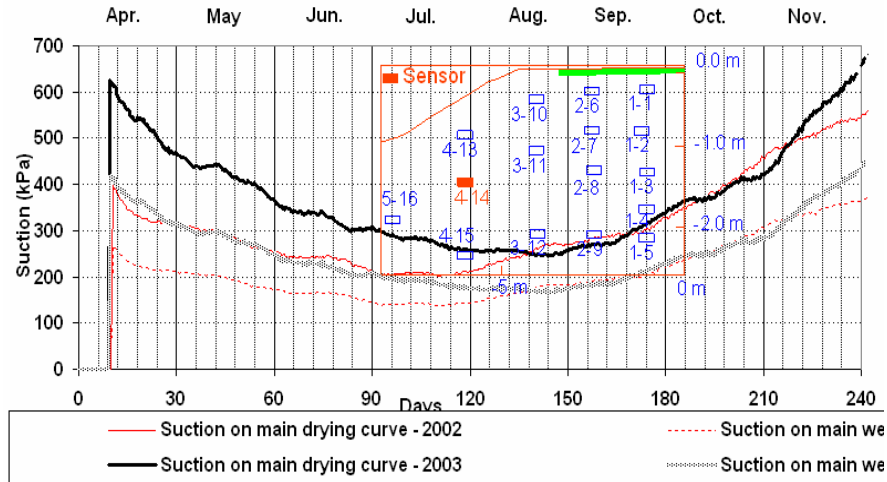


Figure 5.15 *In situ* uncorrected suctions at Sensor T4-14 in 2002 and 2003 at the Torquay site

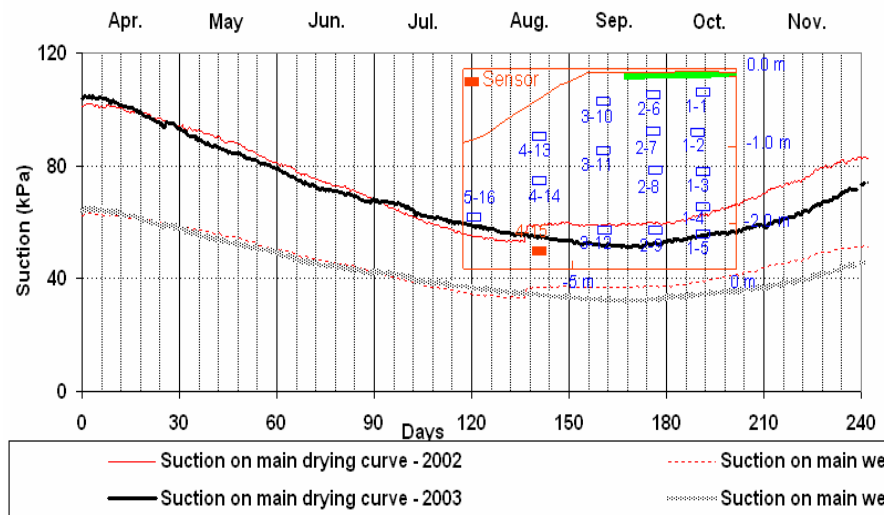


Figure 5.16 *In situ* uncorrected suctions at Sensor T4-15 in 2002 and 2003 at the Torquay site

The *in situ* uncorrected soil suctions showed high values at shallow depths under shoulder and under side-slope. These high uncorrected soil suctions may be less accurate than the recorded suctions of lower than 400 kPa since the maximum applied suction during the calibration was 400 kPa. Large differences between the suctions on the main drying curves and the main wetting curves were also encountered. Therefore,

the temperature and hysteresis corrections need to be taken into account for a more accurate assessment of the suction readings.

CHAPTER 6

PRESENTATION AND DISCUSSION OF *IN SITU* CORRECTED MATRIC SUCTIONS

This chapter presents the *in situ* corrected matric suctions computed from the *in situ* measurements taking into account ambient temperature and hysteresis corrections. The effects of ambient temperature and hysteresis on suction measurement are described in Chapter 2. Equation 2.8 in Chapter 2 was used for the temperature correction.

$$\Delta T(t, T_0) = \frac{0.0014T_l + 0.5743}{0.6065} \Delta T(t, T_l) \quad (2.8)$$

The procedural analysis for the *in situ* corrected matric suctions is outlined in Figure 3.3. Equations 4.7 and 4.8 in Chapter 4 were used for hysteresis correction.

Matric suction on wetting scanning curve:

$$\psi_{d-w} = \psi_{wet} + \left(\frac{V_{out}}{V_{bending}} \right)^{23} (\psi_{dry} - \psi_{wet}) \quad (4.7)$$

Matric suction on drying scanning curve:

$$\psi_{w-d} = \psi_{dry} - \left(\frac{V_{bending}}{V_{out}} \right)^{23} (\psi_{dry} - \psi_{wet}) \quad (4.8)$$

The suction readings from each site are presented in graphical format with depth from the ground surface and with distance from the centerline of the highways. For clarity and ease of visualization, the large volume of the suction data has been presented systematically as follows.

1. The soil suctions are separately presented in three instrumented vertical grid-lines with distinct features. These are the grid-line under the driving-lane (i.e. covered with asphalted pavement), the grid-line under the shoulder (i.e. covered with gravel) and the grid-line under the side-slope (i.e. uncovered);
2. Three instrumented horizontal grid-lines show the soil suctions at different depths from the ground surface (i.e., 0.3 to 0.5 m; 0.8 to 1.1 m and 1.9 to 2.2 m);
3. The contour maps of soil suctions in the cross sections of highway subgrade with the average-monthly suctions were also drawn.
4. To investigate the response of the thermal conductivity sensors to rainfall and temperature changes, the soil suctions were plotted in small time scales. To minimize the rainfall effect, the suction changes under the driving-lane were studied to examine the ambient temperature effect.

The sensors at the Torquay site are denoted by a prefix T (e.g. T1-1) and with a prefix B (e.g. B1-1) for the sensors at the Bethune site.

6.1 Comparison of corrected suctions and uncorrected suctions

The temperature and hysteresis corrections were made and the effects of these corrections on suction measurement are described in this section.

6.1.1 The effect of temperature correction on suction measurement

The comparison of temperature-corrected suctions and temperature-uncorrected suctions is shown in Figures from 6.1 to 6.3. Since the sensor calibration was conducted in the conditions of the laboratory, the field voltage outputs have to be converted to the voltage outputs at 23° C (i.e., the calibration temperature). Since the thermal

conductivity of the sensor is a function of ambient temperature, the voltage outputs reduce with decreasing temperatures. Therefore, if a voltage output were not corrected for temperature, an exaggerated suction would be converted by entering the uncorrected voltage output to the calibration curves.

Figures from 6.1 to 6.3 show the difference was highest during winter when the temperature was close to zero degrees Celsius. In general, the corrected suctions were less than the uncorrected suctions as the temperatures in the subgrade are mostly less than 23° C. Under the driving-lane the difference between corrected suction and uncorrected suction varied from 20% to 40%. This difference could be more than ten times for the sensors on the side-slope. As can be seen in the calibration curves (Figures 4.2 and 4.3, Chapter 4), when suctions are high (i.e. more than 400 kPa) a small change of voltage difference can lead to major change in suction. In Figure 6.3, when the temperature was close to 0° C, the uncorrected suctions reached 21,000 kPa while the corrected suctions were around 1000 kPa.

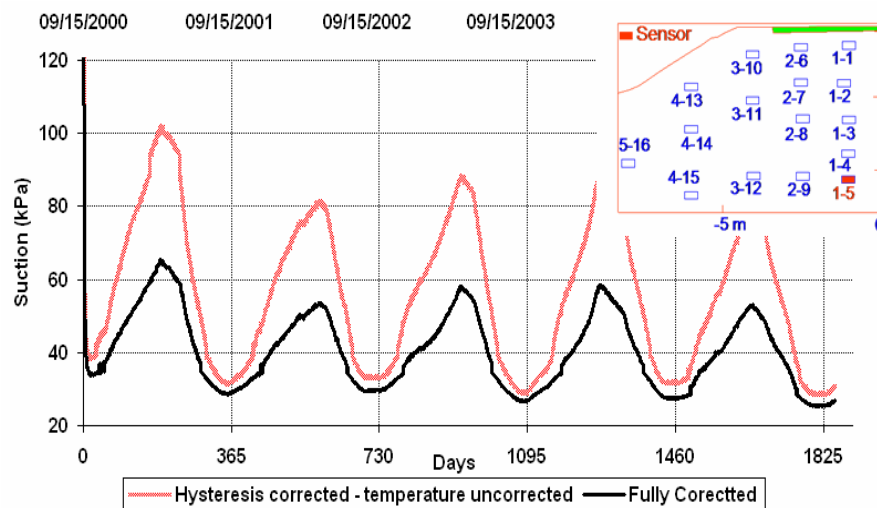


Figure 6.1 Suctions with and without temperature correction at Sensor T1-5

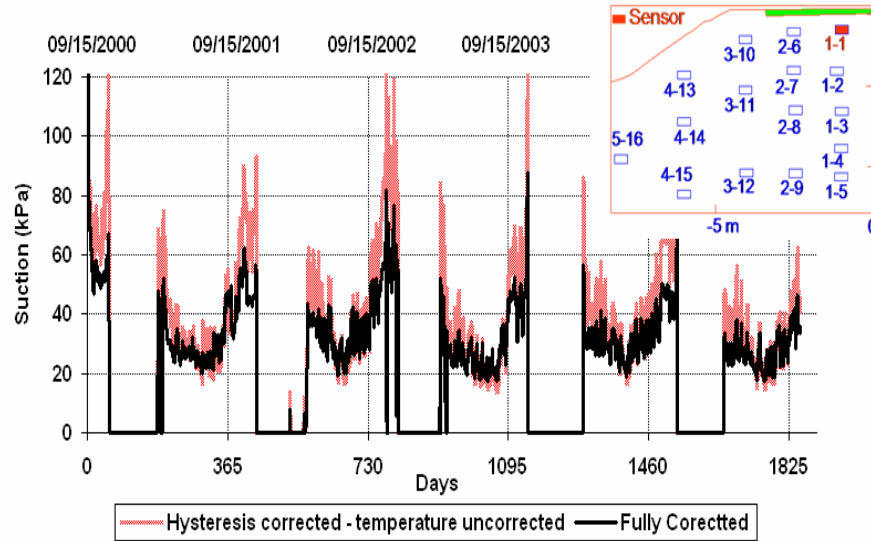


Figure 6.2 Suctions with and without temperature correction at Sensor T1-1

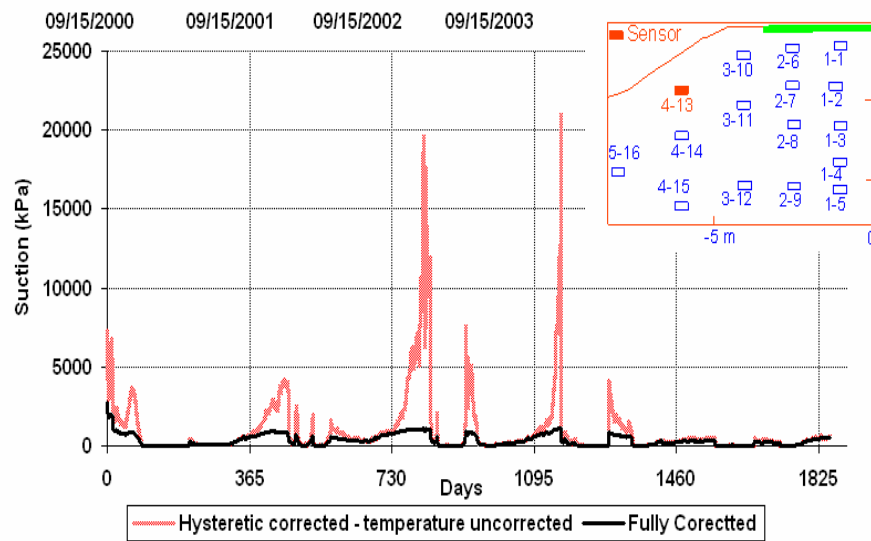


Figure 6.3 Suctions with and without temperature correction at Sensor T4-13

6.1.2 The effect of the hysteresis correction on field suction measurement

The readings of thermal conductivity sensors may follow the main wetting curve, the main drying curve or a scanning curve during the monitoring period based on the soil conditions. The matric suctions were calculated from the voltage outputs using Equations 4.12 and 4.13 depending on the direction of transition. The suctions with and without hysteresis correction are plotted in Figures 6.4 and 6.5. Figure 6.4 exhibits

corrected suctions for a sensor at a shallow depth (0.3 m) and Figure 6.5 for a sensor at a greater depth (2.2 m) under pavement. At the greater depth, the sensor followed a clear trend of cyclic suction changes (i.e., moving towards the main wetting curve during the rainy season and towards the main drying curve during the dry season). This seasonal pattern of suction change accommodates the effectiveness of the hysteresis correction method. The hysteresis correction appeared to be complex for the sensors at a shallow depth and seemed to exaggerate the fluctuations by taking into account the moving effects between scanning curves. In general, the hysteresis correction could increase the accuracy of the suction measurement from 10 to 30% depending on the depth from the ground surface.

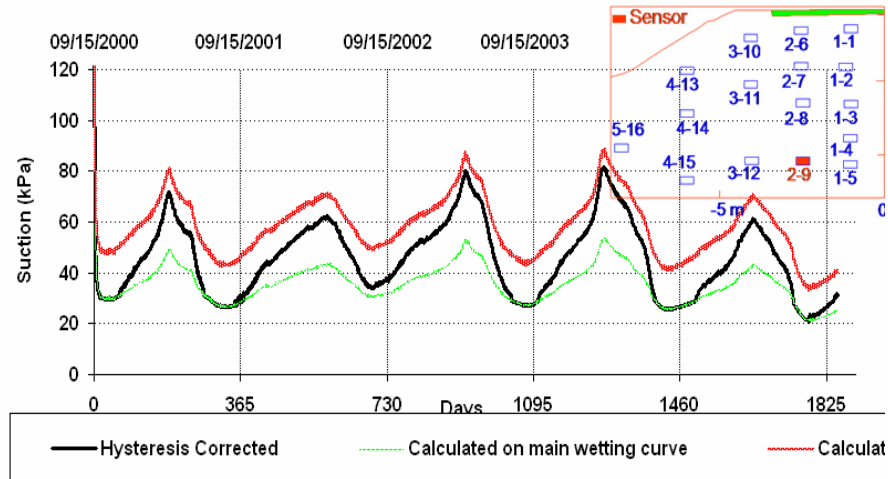


Figure 6.4 Suctions with and without hysteresis correction at Sensor T2-9

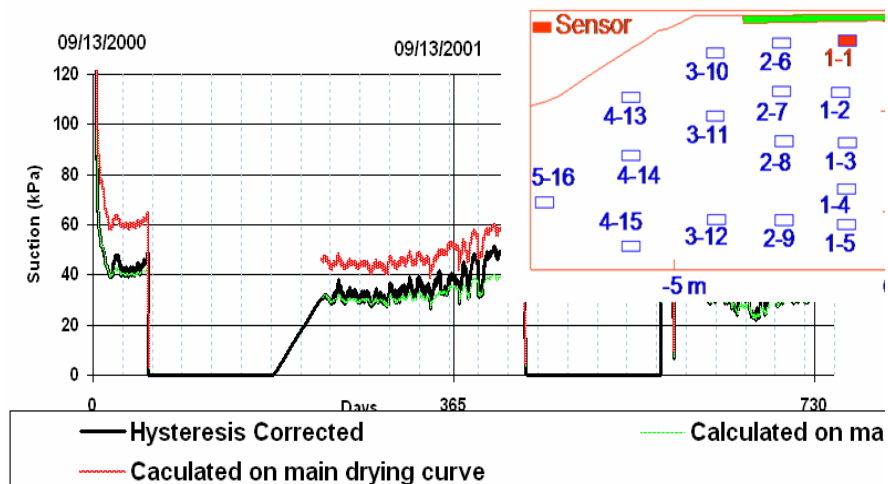


Figure 6.5 Suctions with and without hysteresis correction at Sensor B1-1

The hysteresis correction gave interpretable suctions from season to season even though there was a complex transition between scanning curves at shallow depths. The hysteresis correction improved the accuracy of the sensor measurement and helped understand the historical changes of suctions.

Based on the above-mentioned discussions, the temperature correction appeared to have greater influence than hysteresis correction on the field suction measurement using the thermal conductivity sensor.

6.2 The first “quasi-equilibrium” of sensor with surrounding soil

The initial “quasi-equilibrium” between the sensor and the surrounding soil at the time of installation varied from sensor to sensor. The time for an individual sensor to come to equilibrium depended on the contact between the soil and the sensor. The sensors at greater depths and under the driving-lane might have first reached the suction equilibrium due to higher normal loads. As plotted in Figure 6.6, the readings of Sensor T1-5 became stable after 7 days. Sensors T1-1 and T4-15 came to equilibrium after 15 days. The time for sensors under the shoulder and side-slope to reach equilibrium appeared to be higher with about 30 days for Sensor T4-13, from 20 to 25 days for sensors T4-15, T3-10 and T5-16. Some erratic readings were recorded with sensor 4-13 before the equilibrium. In Figure 6.6, the effect of the rainfall on suction is insignificant since the magnitudes were less than 10 mm (the effect of rainfall on suction is discussed in Chapter 7).

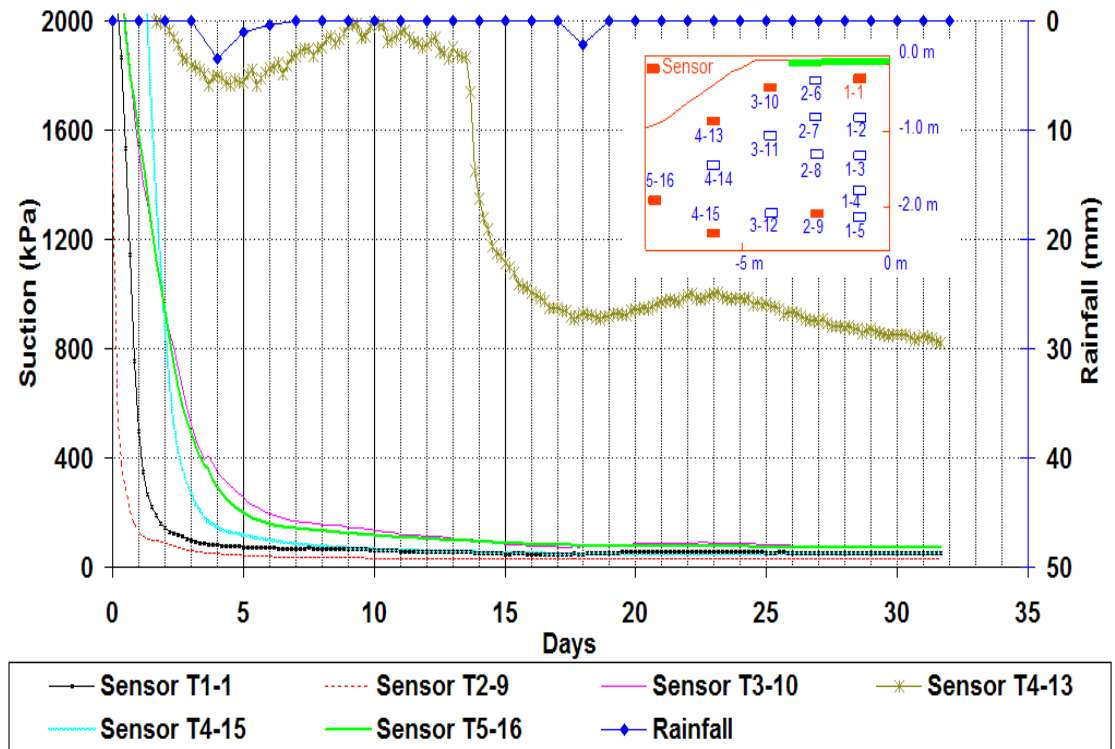


Figure 6.6 Suctions before reaching equilibrium at the Torquay site

The time for the thermal conductivity sensors at the Bethune site to first reach “quasi-equilibrium” with the surrounding soil is shown in Figure 6.7. The effort required for backfilling was probably not equal for every sensor; therefore, some sensors needed more time to stabilize the readings than for others. Sensor B5-16 was an exception with an equilibrium time of 45 days. The reason in this case might possibly be the poor contact between the sensor and the surrounding soil due to the presence of stones. Sensor B4-13 at the Bethune site reached equilibrium in 14 days which was faster than Sensor T4-13 at the Torquay site.

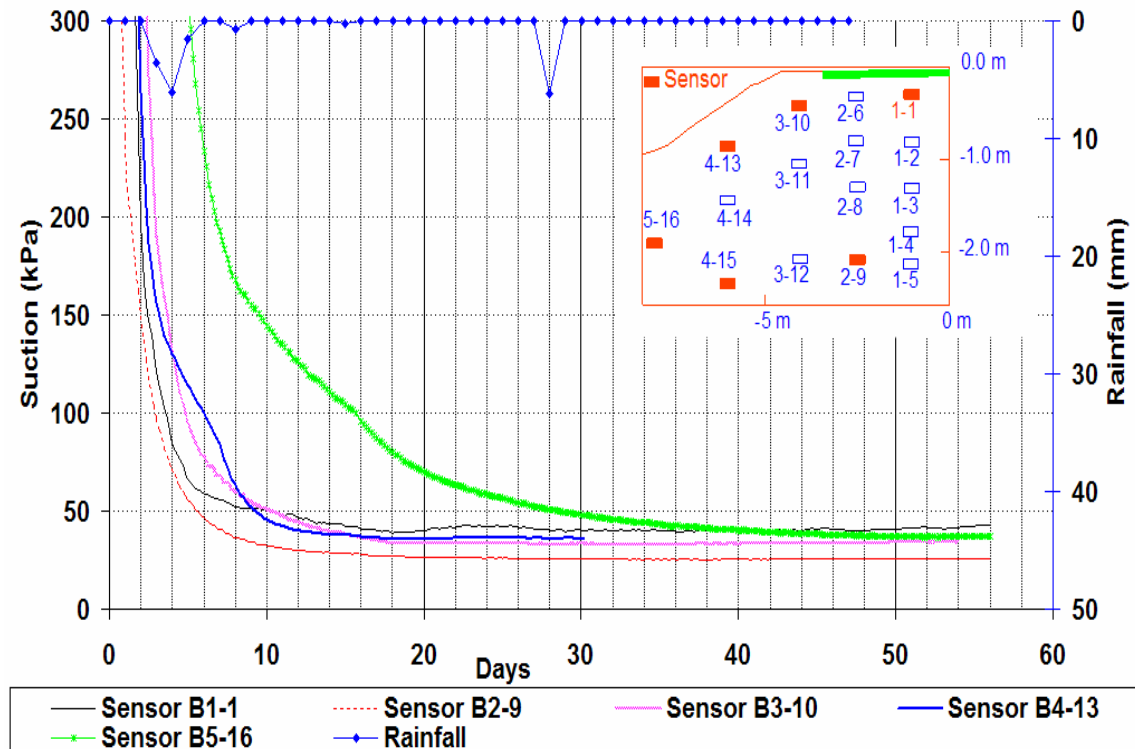


Figure 6.7 Suctions before reaching equilibrium at the Bethune site

Generally, the suctions from the thermal conductivity sensors stabilized after 5 days to 15 days from the time of the installation.

6.3 Suctions along vertical depth versus time

Since the monitoring system in Bethune was damaged due to flooding after two years of operation, the suction values at the Torquay site will be the primary focus.

6.3.1 Vertical grid-line under the driving-lane at the Torquay site

There are five sensors located in the vertical grid-line under the driving-lane at the Torquay site. These are T1-1, T1-2, T1-3, T1-4 and T1-5 at 0.3 m, 0.8 m, 1.3 m, 1.8 m and 2.2 m depths, respectively.

The suctions from these sensors for the period of more than five years are shown in Figure 6.8. The suctions demonstrate sharp changes following a seasonal pattern. The

sensors closer to the ground surface provided more variable readings than the deeper sensors. In addition, the shallower sensors had longer periods of interrupted readings due to freezing. Sensor T1-5 at bottom depth recorded suctions throughout the entire monitoring period.

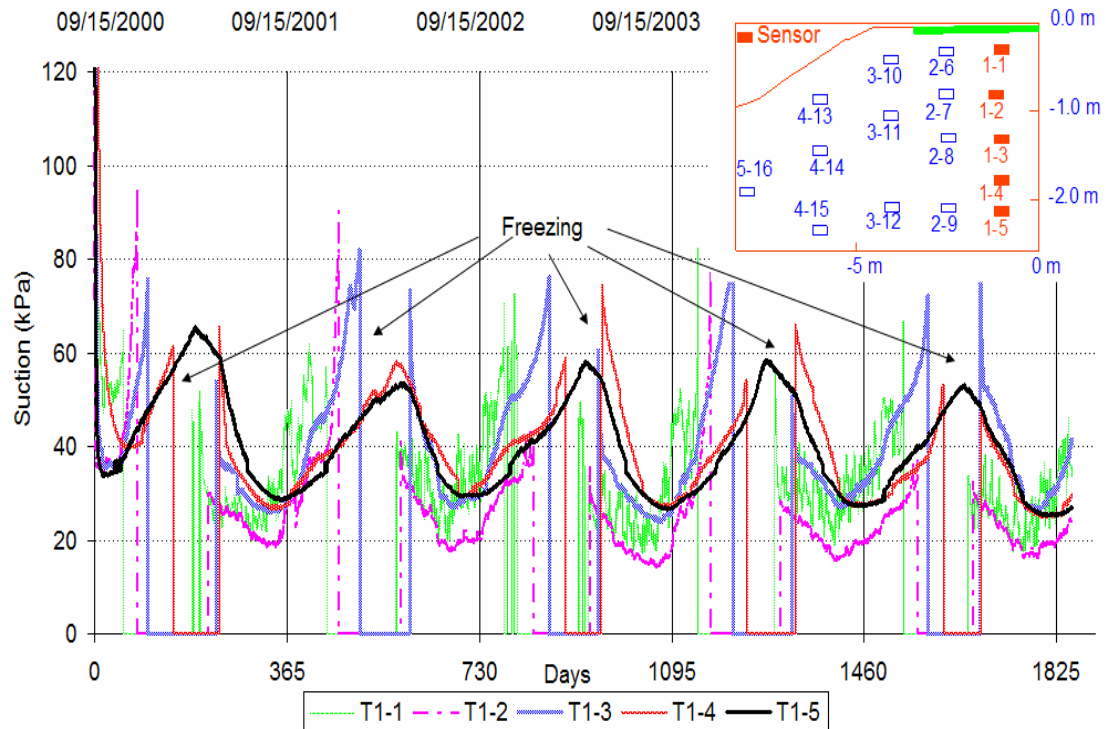


Figure 6.8 Suctions along vertical grid-line under the driving-lane at the Torquay site

The five-year average suctions during the months when the soil was unfrozen are plotted in Figure 6.9. The lowest suctions at Sensor T1-1 at depth of 0.3 m were seen in the middle of July. The deeper sensors recorded the lowest suctions later in the year. Suctions at Sensor T1-2 decreased to the lowest values at the end of July, then Sensor T1-3 at the beginning of August, Sensor 1-4 in the beginning of September and sensor 1-5 in the middle of September.

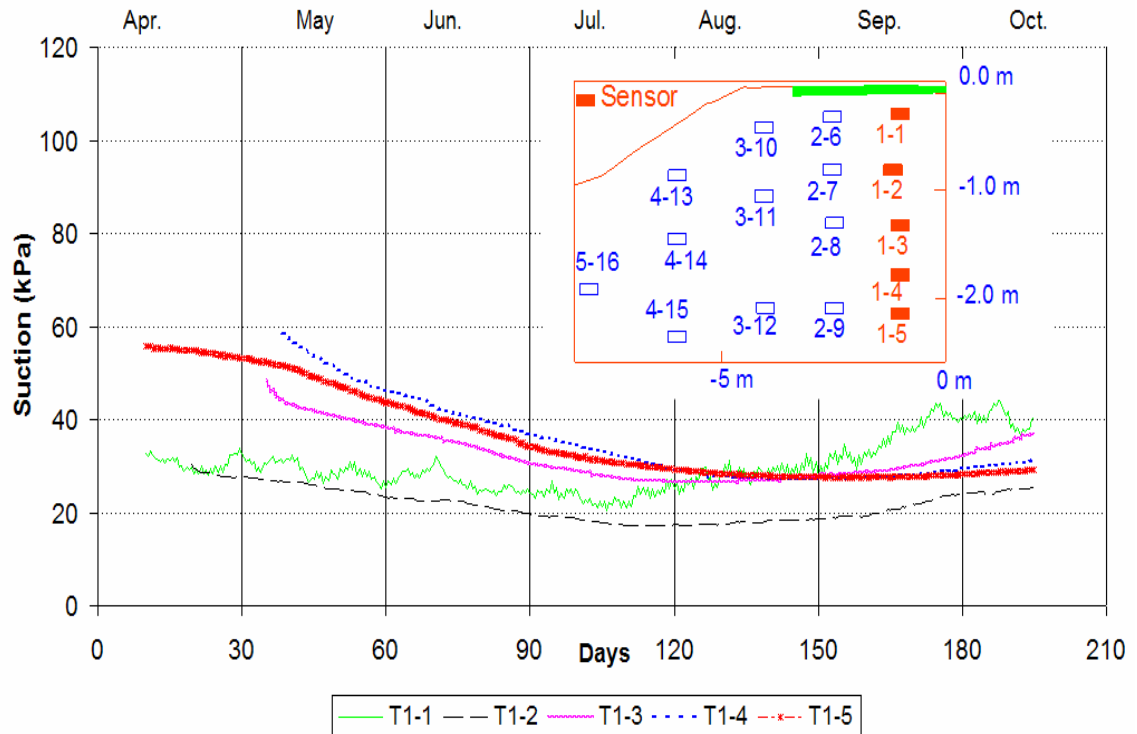


Figure 6.9 Five-year average suctions along vertical grid-line under the driving-lane at the Torquay site

Figure 6.10 gives the five-year average-monthly suctions in the vertical grid-line under the driving-lane from 2001 to 2005 at the Torquay site. The variations in suction in this vertical grid-line ranged from 20 kPa to 60 kPa. Sensor T1-5 (i.e. the bottom sensor) saw the average-monthly suctions varied from 30 to 60 kPa. The suctions were recorded at Sensor T1-4 from 27 to 42 kPa, 18 to 28 kPa at Sensor T1-2, and 24 to 40 kPa at Sensor T1-1. The suction comparisons for sensors T1-1, T1-2 and T1-5 for different years can be seen in Figures 6.11 to 6.13. Although there were differences in magnitude from year to year, the suctions show a clear seasonal pattern. The suctions show the same cycle despite different amplitudes for the sensors in this vertical grid-line. The sensors at greater depths collected more stable suctions with time. The differences in suction at any time from year to year under the driving-lane appear to be less than 10 kPa.

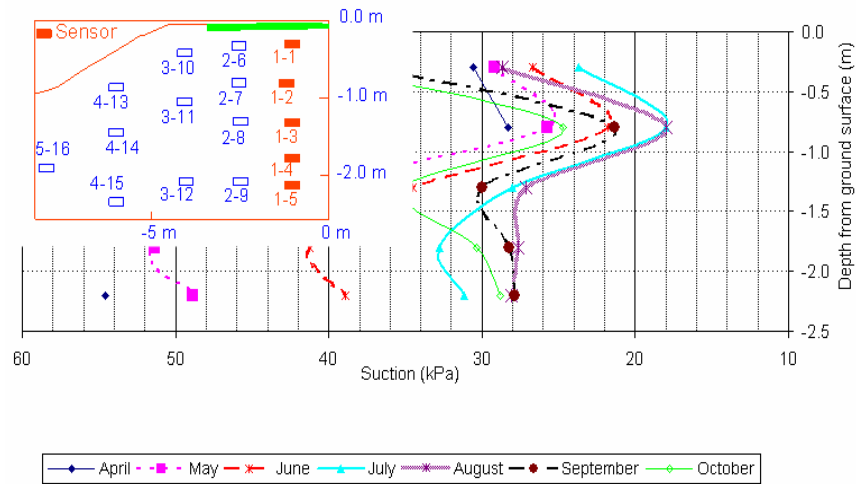


Figure 6.10 Five-year average suctions versus depth along vertical grid-line under the driving-lane at the Torquay site

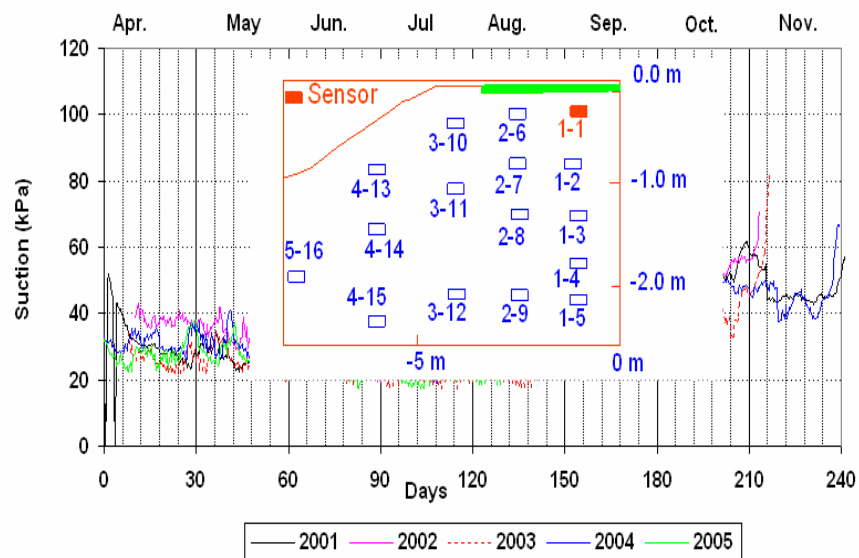


Figure 6.11 Suctions at Sensor T1-1 for years 2001 to 2005 at the Torquay site

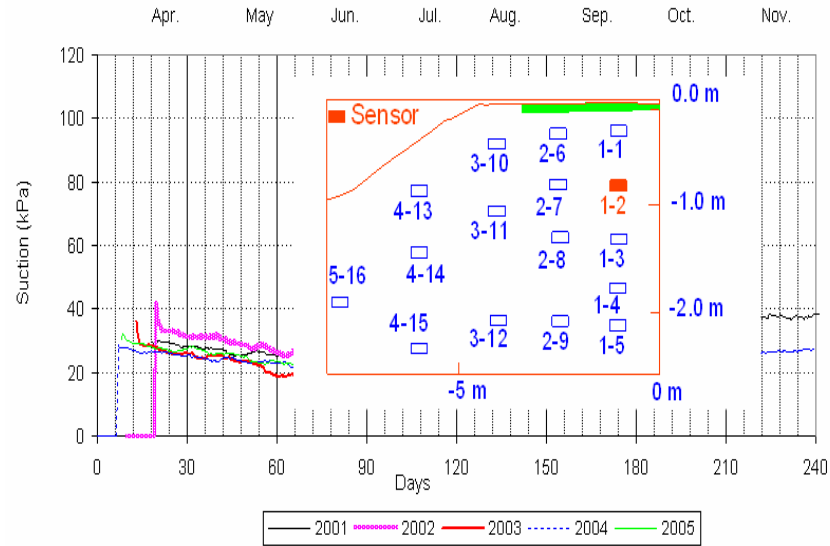


Figure 6.12 Suctions at Sensor T1-2 for years 2001 to 2005 at the Torquay site

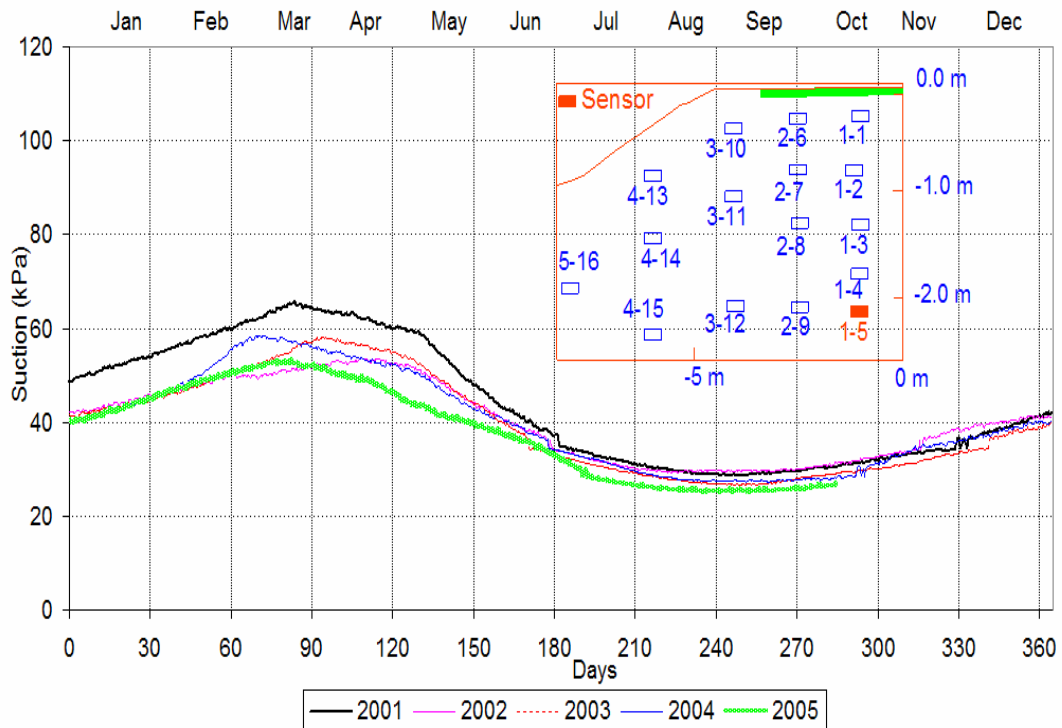


Figure 6.13 Suctions at Sensor T1-5 for years 2001 to 2005 at the Torquay site

6.3.2 Vertical grid-line under the driving-lane at the Bethune site

There were originally five sensors located in the vertical grid-line under the driving-lane at the Bethune site. These were B1-1, B1-2, B1-3, B1-4 and B1-5 at 0.3 m,

0.8 m, 1.3 m, 1.8 m and 2.2 m depths respectively. Sensor B1-4 malfunctioned two days after installation and no signals were transferred from this sensor. The reason was attributed to the damage of the core element of the sensor due to the penetration of water.

The two-year suction data of this vertical grid-line are shown in Figure 6.14 and 6.15. The same cyclic suction changes were noticed at the Bethune site as at the Torquay site. The average-monthly suctions from 2001 to 2002 at the Bethune site are graphed in Figure 6.16. The variations in suction with season ranged from 20 kPa to 40 kPa. The average-monthly suctions were from 20 to 40 kPa at the bottom Sensor B1-5. The suctions at Sensor B1-3 were 22 to 28 kPa, 25 to 30 kPa at Sensor B1-2 and 30 to 36 kPa at Sensor B1-1. There is a shift towards the right in Figure 6.14 for the deeper sensors. Minimum suctions, which are recorded at deeper depths, took longer to reach compared to the sensors at shallower depths.

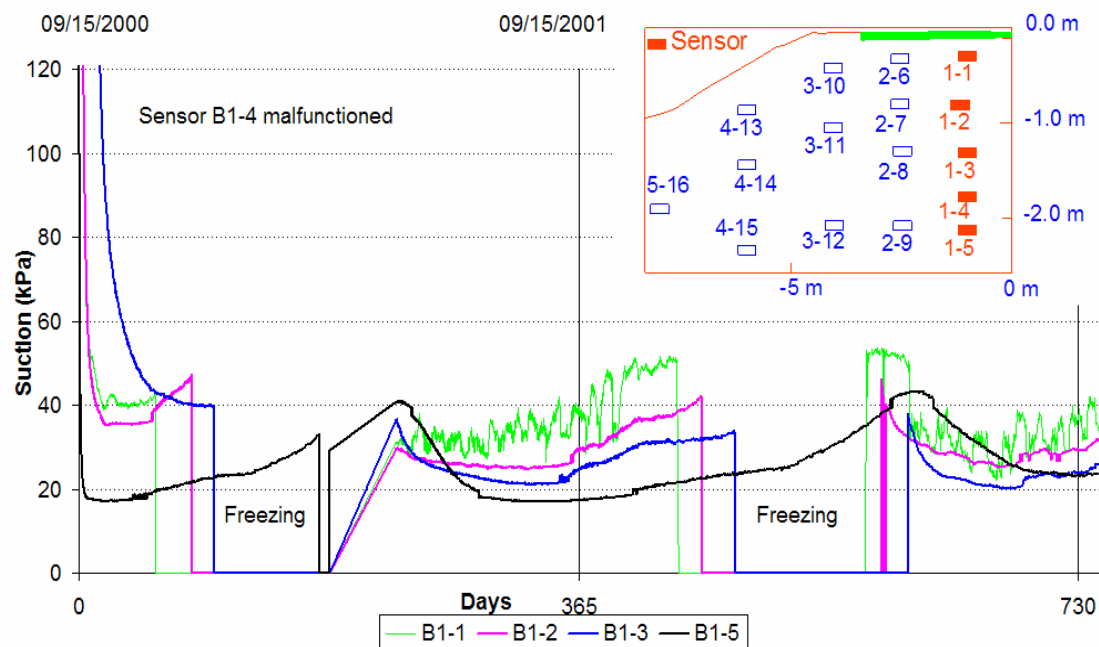


Figure 6.14 Suctions along vertical grid-line under the driving-lane at the Bethune site

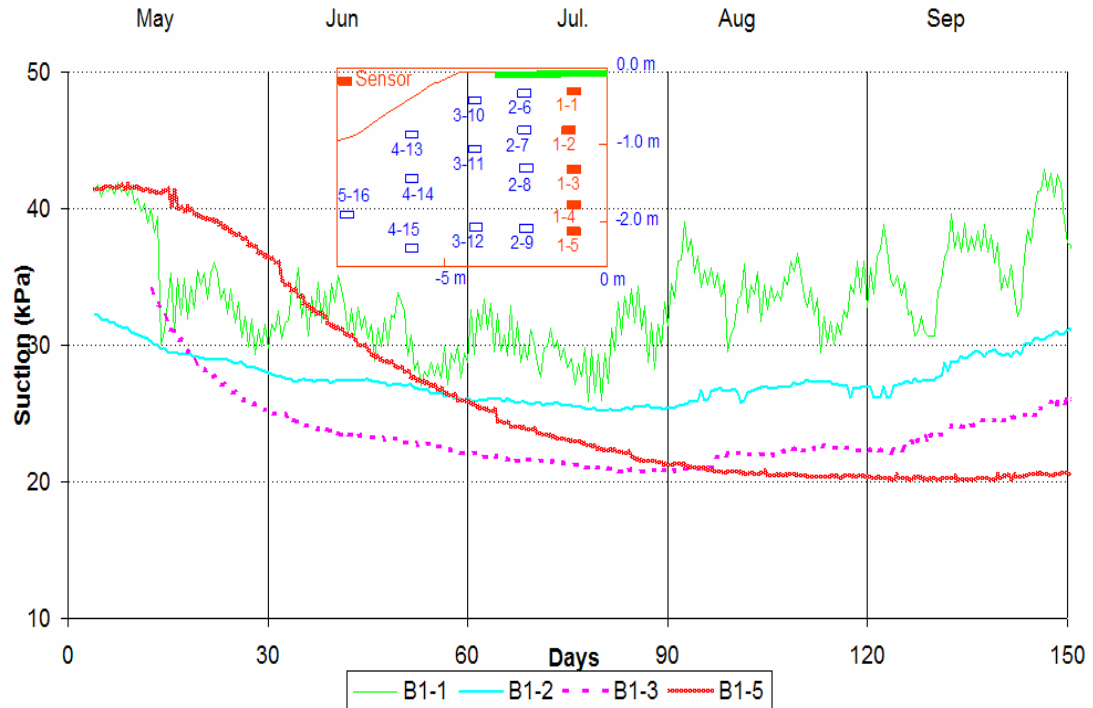


Figure 6.15 Two-year average suctions along vertical grid-line under the driving-lane at the Bethune site

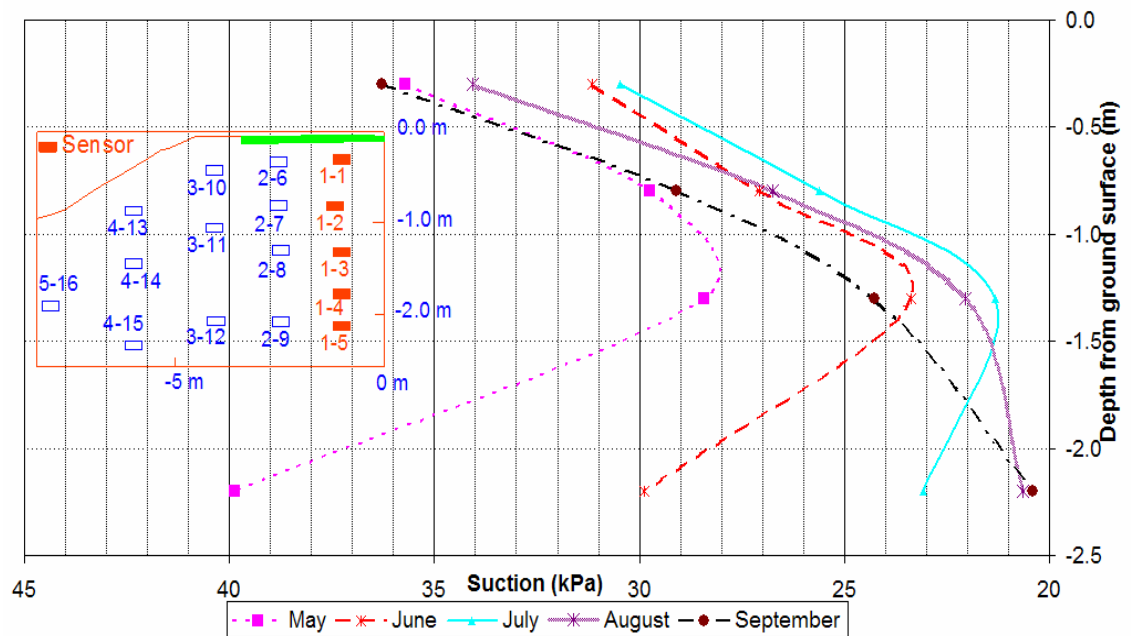


Figure 6.16 Two-year average suctions versus depth along vertical grid-line under the driving-lane at the Bethune site

6.3.3 Vertical grid-line under the shoulder at the Torquay site

There are three sensors located on the vertical grid-line under the shoulder at the Torquay site. These are T3-10, T3-11, and T3-12 at 0.3 m, 1.0 m and 2.0 m depths respectively.

The interruption of readings during freezing time along this vertical grid-line was observed to be the same as along the grid-lines under the driving-lane.

Figures 6.17 and 6.18 show that the suctions under the shoulder experienced the minimum values in June at depth of 0.3 m. At depth of 1.0 m and 2.0 m, the suctions reduced to the lowest numbers in July and in August, respectively. On the other hand, Sensor T3-10 reached the highest suctions in September. The suction at Sensors T3-11 and T3-12 peaked during winter months. The largest variations in suction were recorded at Sensor T3-10. The average-monthly suctions at this sensor were from 10 kPa to 200 kPa (Figure 6.19). Sensor T3-12 gave the average-monthly suctions from 40 to 90 kPa. At middle-depth of 1.0 m, the average-monthly suctions varied from 25 to 75 kPa. The suctions obtained from sensors T3-10 and T3-12 from 2001 to 2005 at the Torquay site are plotted in Figures 6.20 and 6.21. Along this grid-line the variations in suction from year to year were noticeable. At the beginning of July, suctions at Sensor T3-12 were 25 kPa in 2005 while approximately 70 kPa in 2002.

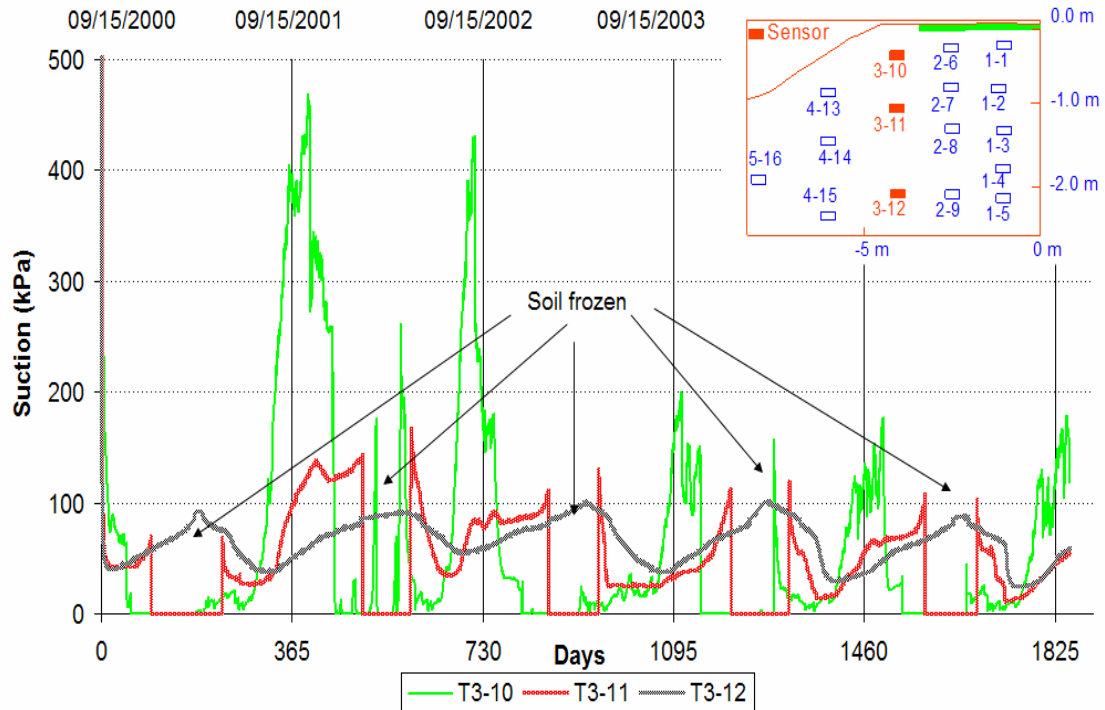


Figure 6.17 Suctions along vertical grid-line under the shoulder at the Torquay site

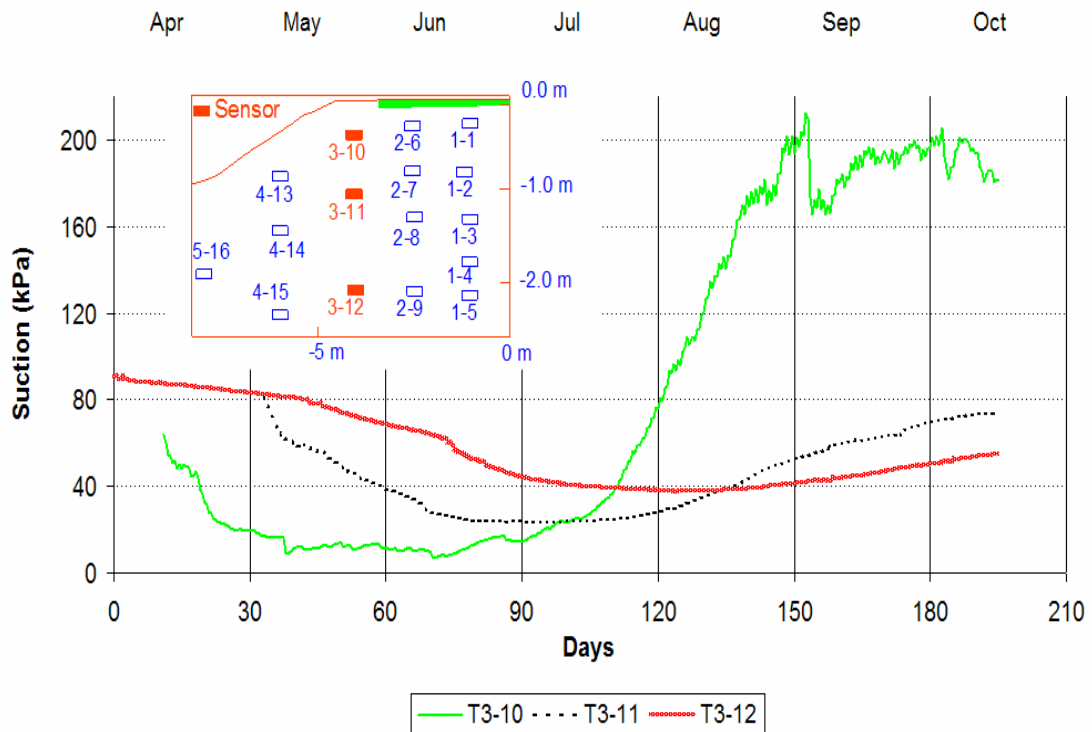


Figure 6.18 Five-year average suctions along vertical grid-line under the shoulder at the Torquay site

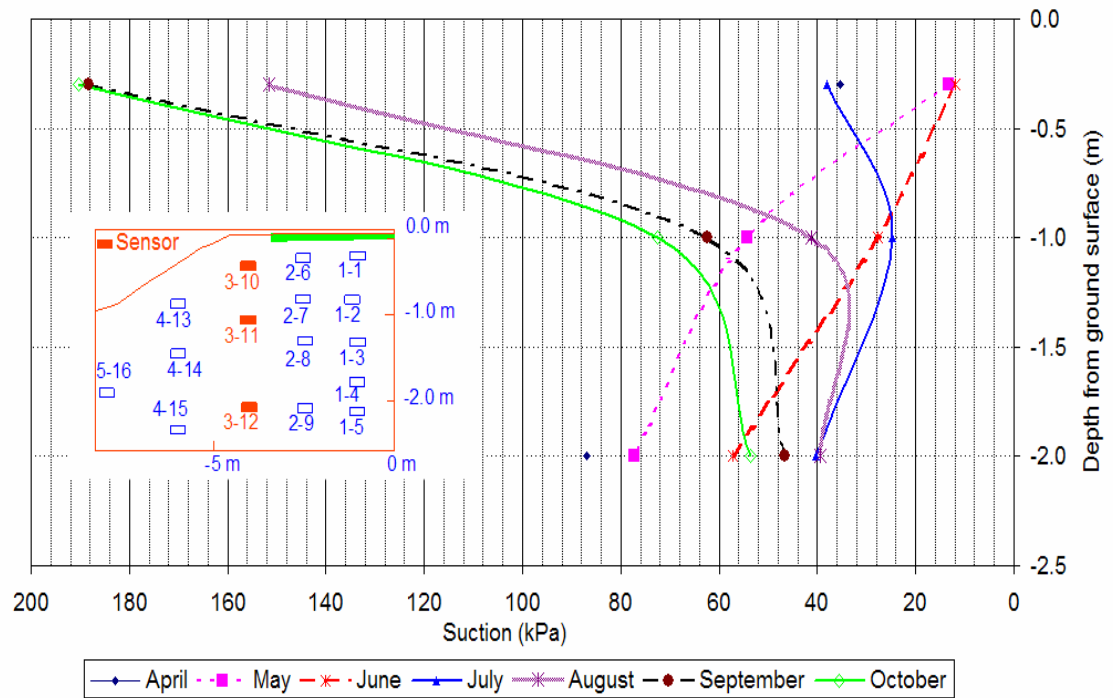


Figure 6.19 Five-year average suctions versus depth along vertical grid-line under the shoulder at the Torquay site

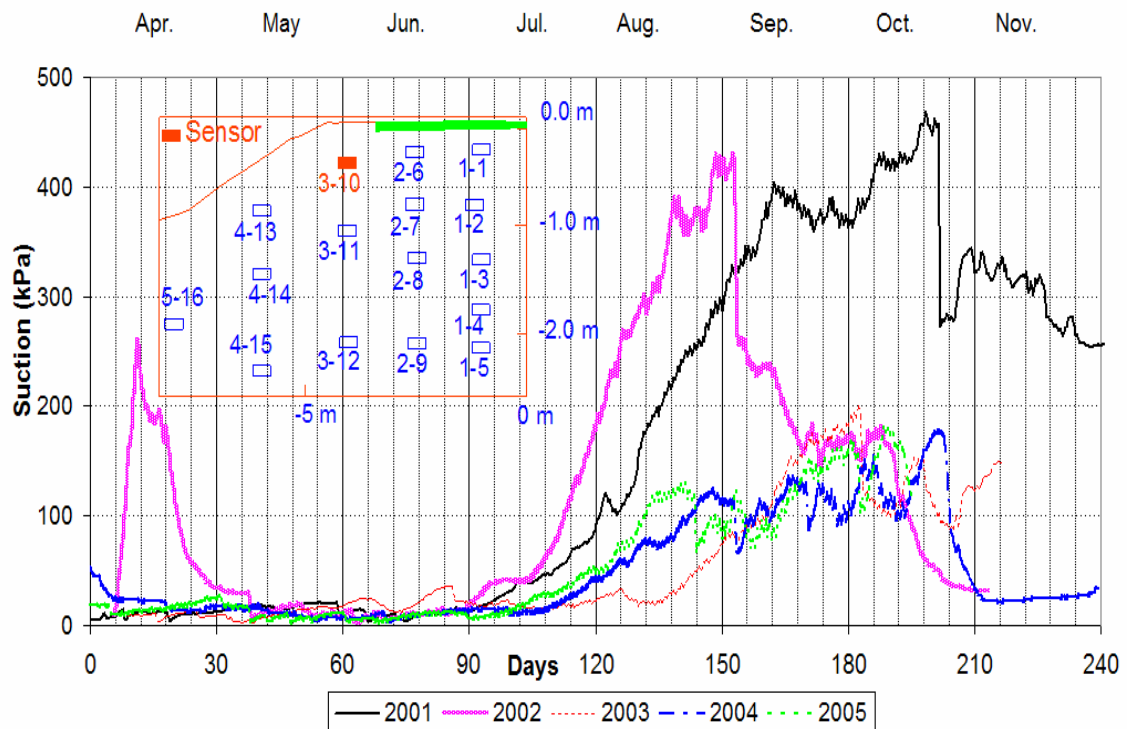


Figure 6.20 Suctions at Sensor T3-10 for years 2001 to 2005 at the Torquay site

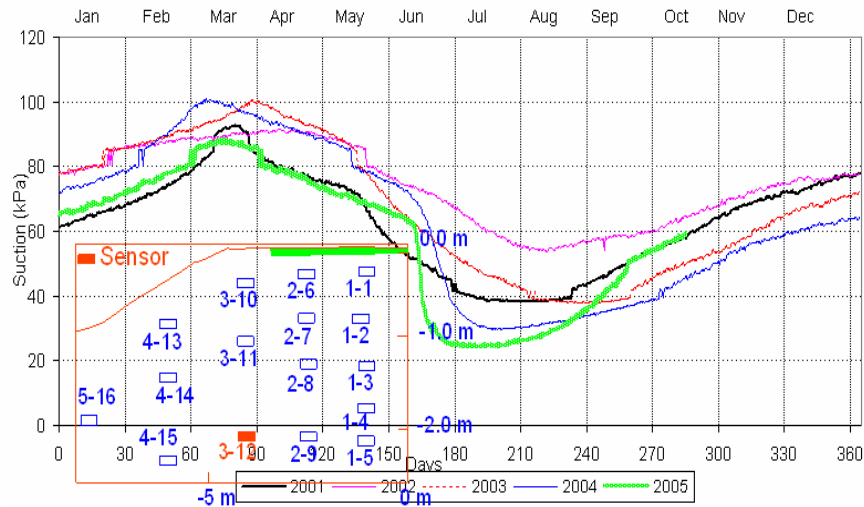


Figure 6.21 Suctions at Sensor T3-12 for years 2001 to 2005 at the Torquay site

6.3.4 Vertical grid-line under the side-slope at the Torquay site

There are three sensors located in the vertical grid-line under the side-slope at the Torquay site. These are T4-13, T4-14, and T4-15 at 0.5 m, 1.1 m and 1.9 m depths respectively.

As shown in Figures 6.22 to 6.25, the vertical grid-line under the side-slope registered large variations in suction at the shallow Sensor T4-13. The individual values reached a maximum value at 1500 kPa in November 2003 and the lowest values were approximately 10 kPa in June 2004 and 2005. Figures 6.31 to 6.33 show that suctions in 2004 and 2005 were relatively lower than those of the previous years. At the beginning of October 2004 and 2005, the suctions were from 200 to 450 kPa at 0.5 m deep, 60 to 175 kPa at 1.1 m deep and 20 kPa at 1.9 m deep. The suctions at the same time in the previous years were 900 to 1100 kPa, 170 to 300 kPa and 30 to 40 kPa respectively.

As can be seen in Figures 6.24, the matric suctions at depth 1.9 m ranged from 20 kPa to 50 kPa. At depth 1.1 m, the average-monthly suctions were 110 to 210 kPa; and 100 to 810 kPa at depth 0.5 m. Thus, the variations in suction became greater when closer to the ground surface. Figure 6.23 illustrates that the suctions at the deepest sensor were the lowest.

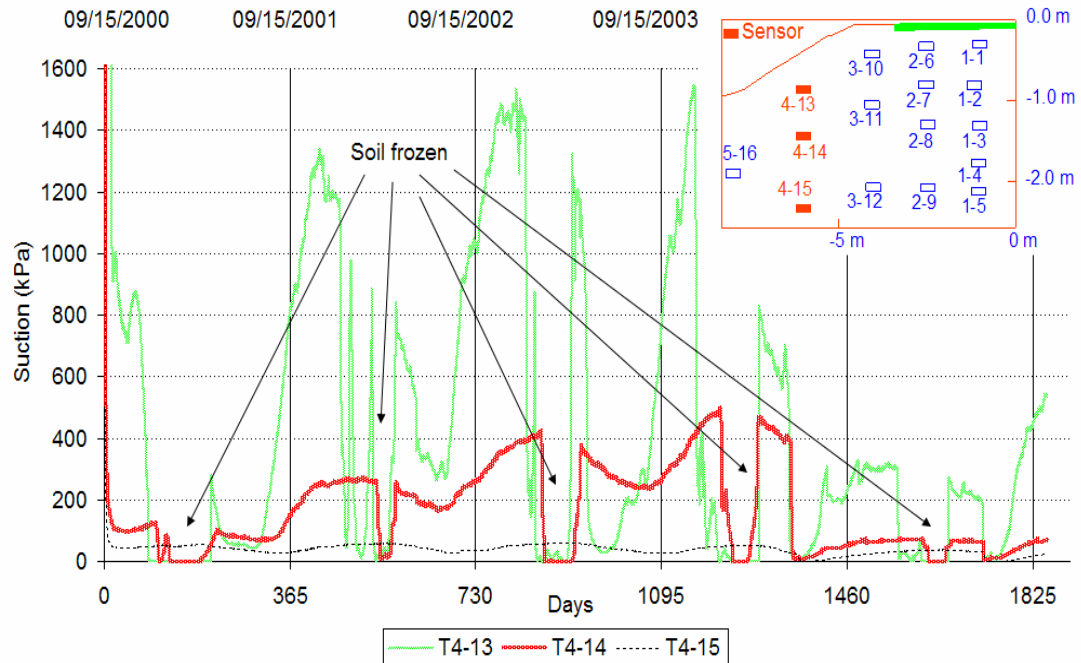


Figure 6.22 Suctions along vertical grid-line under the side-slope at the Torquay site

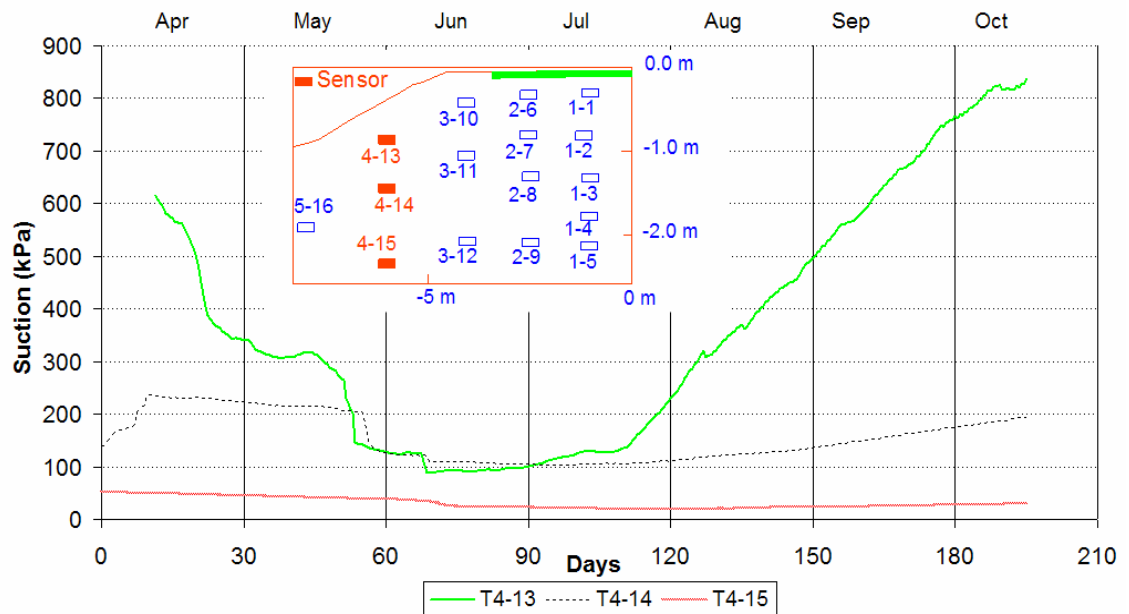


Figure 6.23 Five-year average suctions along vertical grid-line under the side-slope at the Torquay site

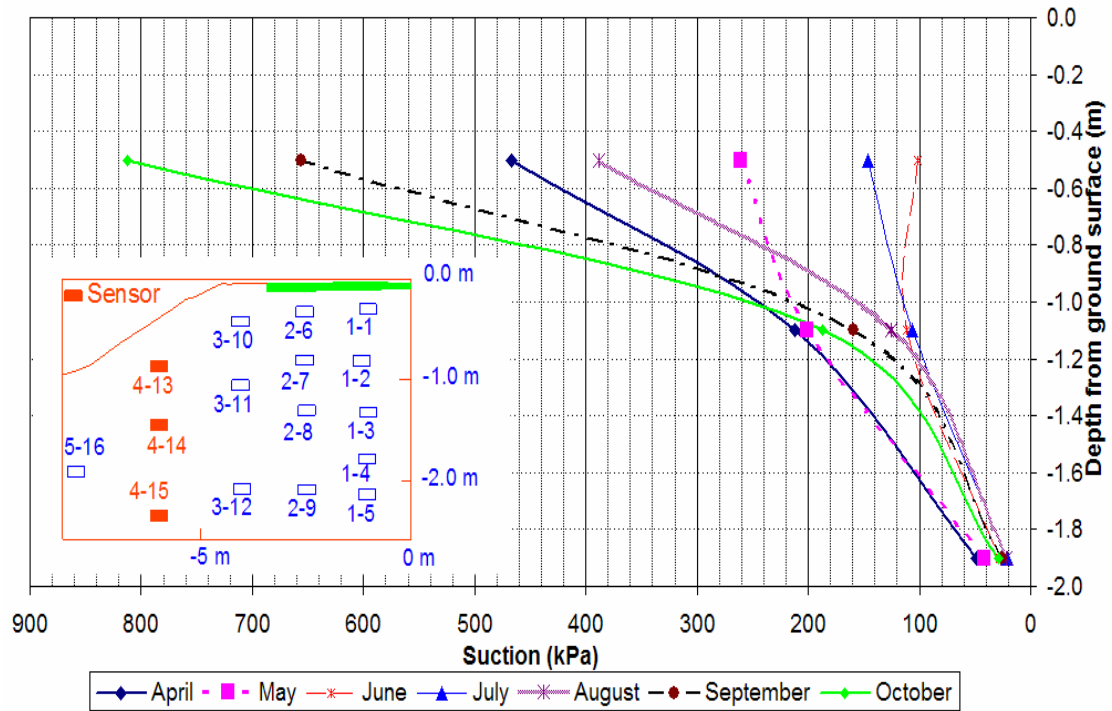


Figure 6.24 Five-year average suctions versus depth along vertical grid-line under the side-slope at the Torquay site

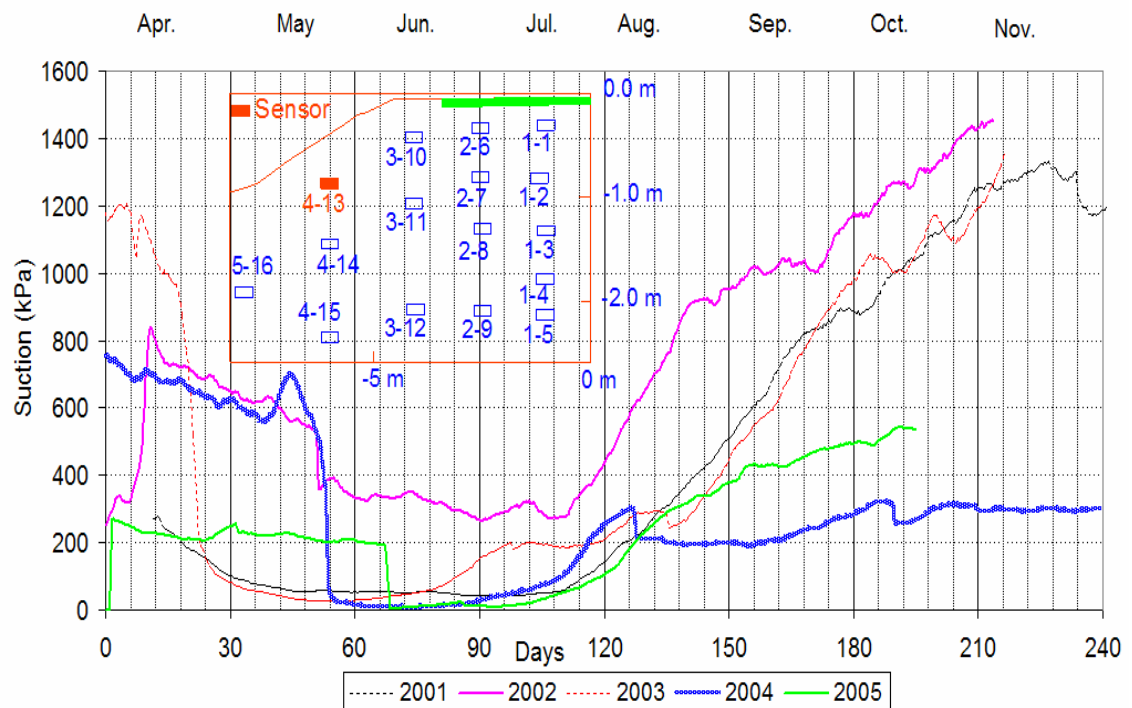


Figure 6.25 Suctions at Sensor T4-13 for years 2001 to 2005 at the Torquay site

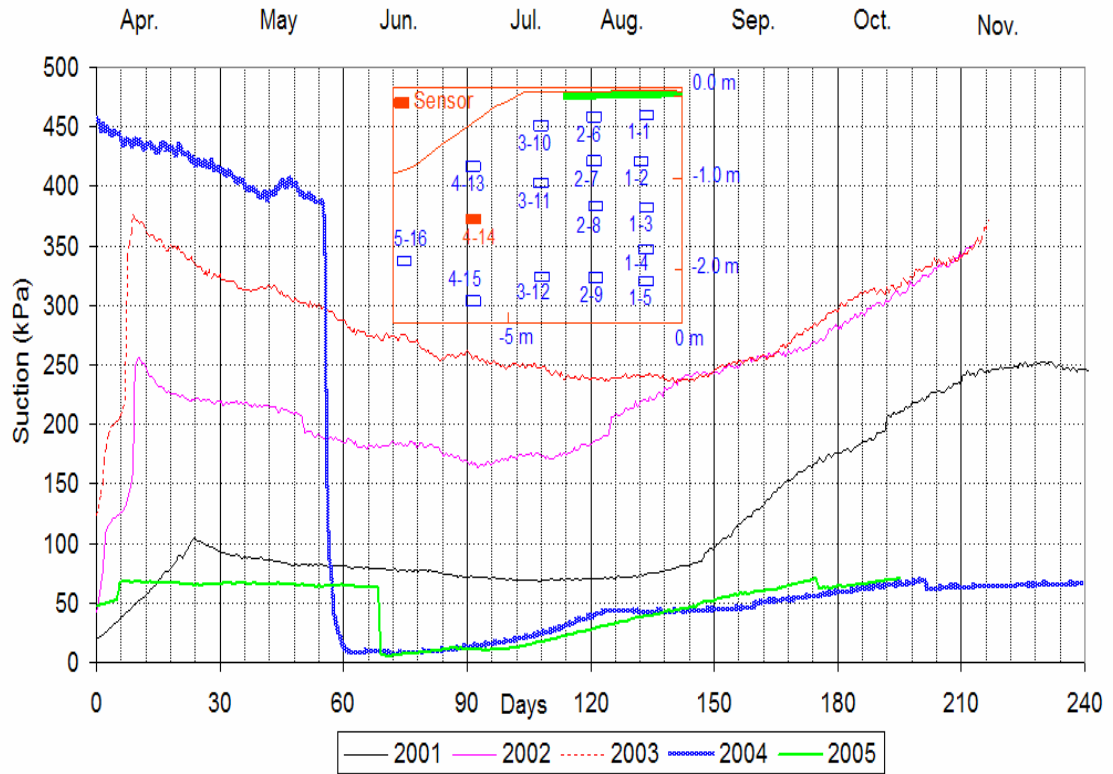


Figure 6.26 Suctions at Sensor T4-14 for years 2001 to 2005 at the Torquay site

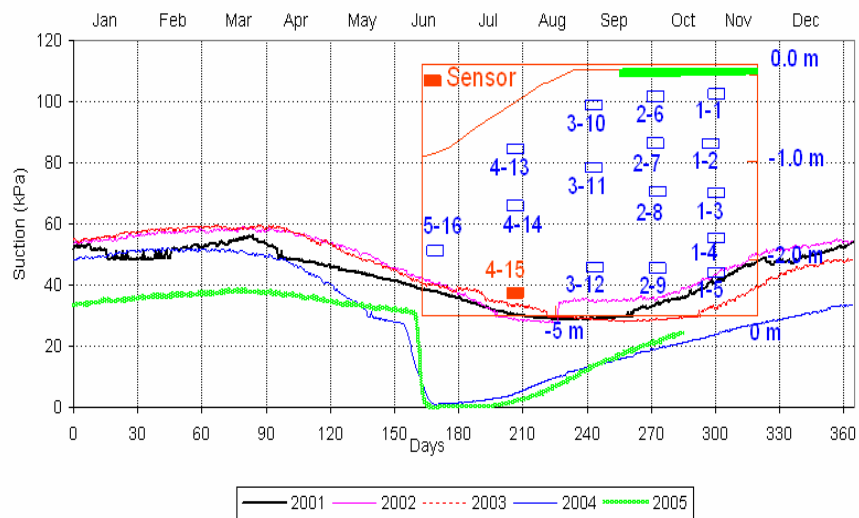


Figure 6.27 Suctions at Sensor T4-15 for years 2001 to 2005 at the Torquay site

The results of the suction measurements in the three instrumented vertical grid-lines at the Torquay site are summarized in Figure 6.28. In general, the suctions at shallower depths showed the greater changes than that at greater depths. The suctions

varied from 10 kPa to 800 kPa at a depth of 0.5 m and 30 to 210 kPa at a depth of 1.1 m. Suctions at a depth of 2.0 m ranged within a narrow band of 20 to 90 kPa. However, these observations were made during unfrozen periods because while frozen the sensors could not measure suctions.

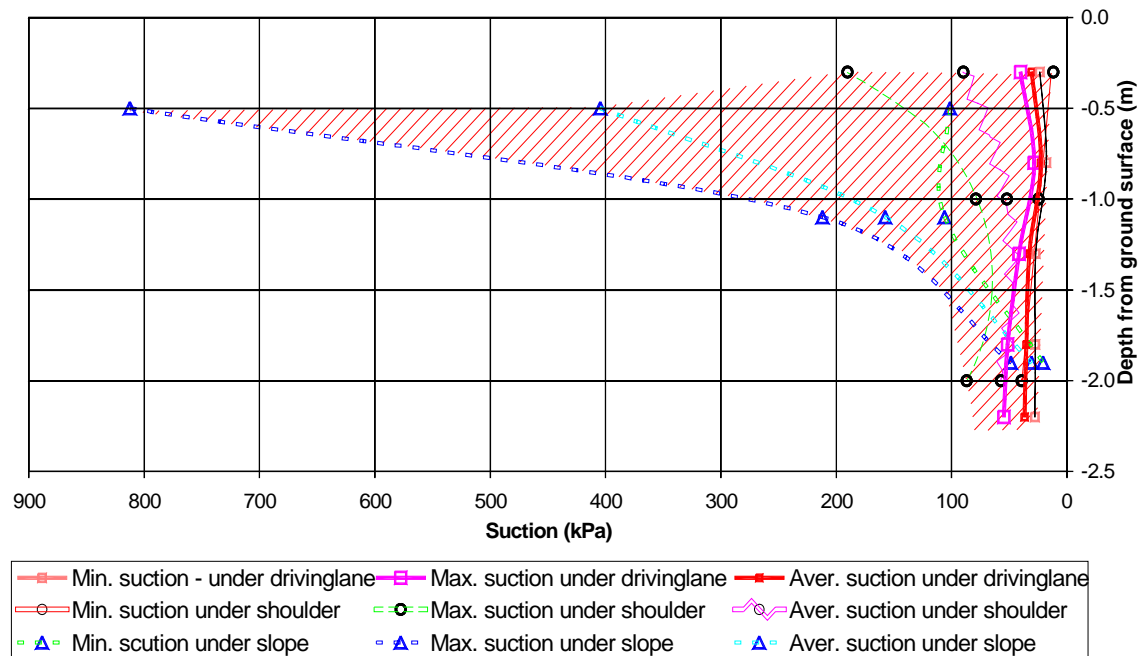


Figure 6.28 Summary of suctions along the three vertical grid-lines: under the driving-lane, under the shoulder and under the side-slope for years 2001 to 2005 at the Torquay site

6.3.5 Vertical grid-line under the side-slope at the Bethune site

A high number of suction variations were also witnessed on the vertical grid-line under the side-slope at the Bethune site. The shallower sensors provided more variable readings than the deeper sensors. During the time when the sensors are not frozen, the average-monthly suctions at depths of 0.3 to 0.5 m changed from 30 to 230 kPa while at depths from 1.9 to 2.2 m these values were 10 to 40 kPa as can be seen in Figures 6.29 to 6.33.

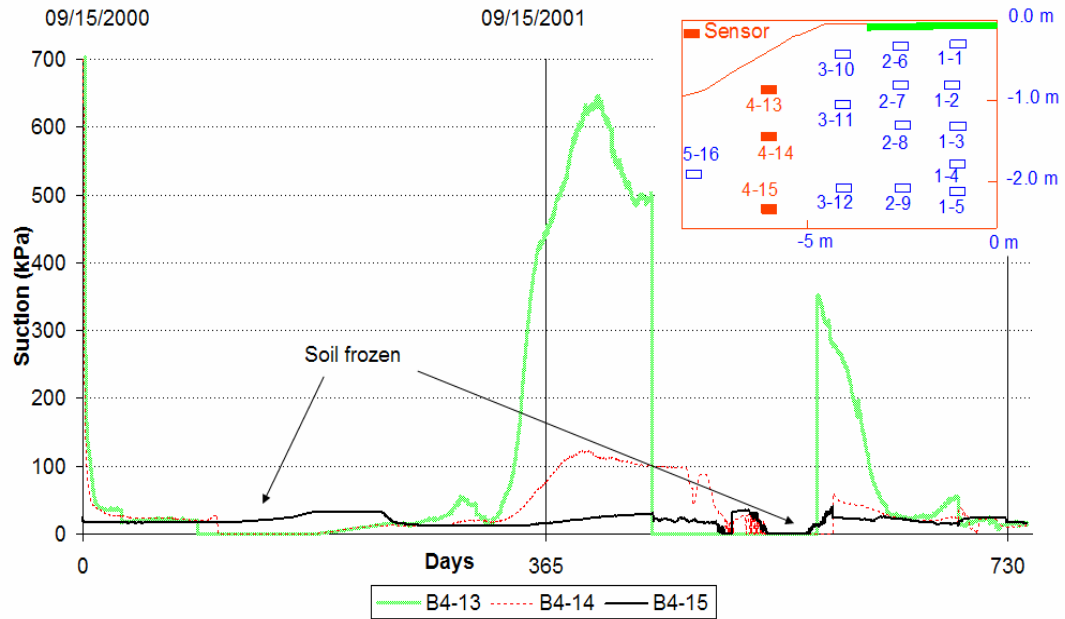


Figure 6.29 Suctions along vertical grid-line under the side-slope at the Bethune site

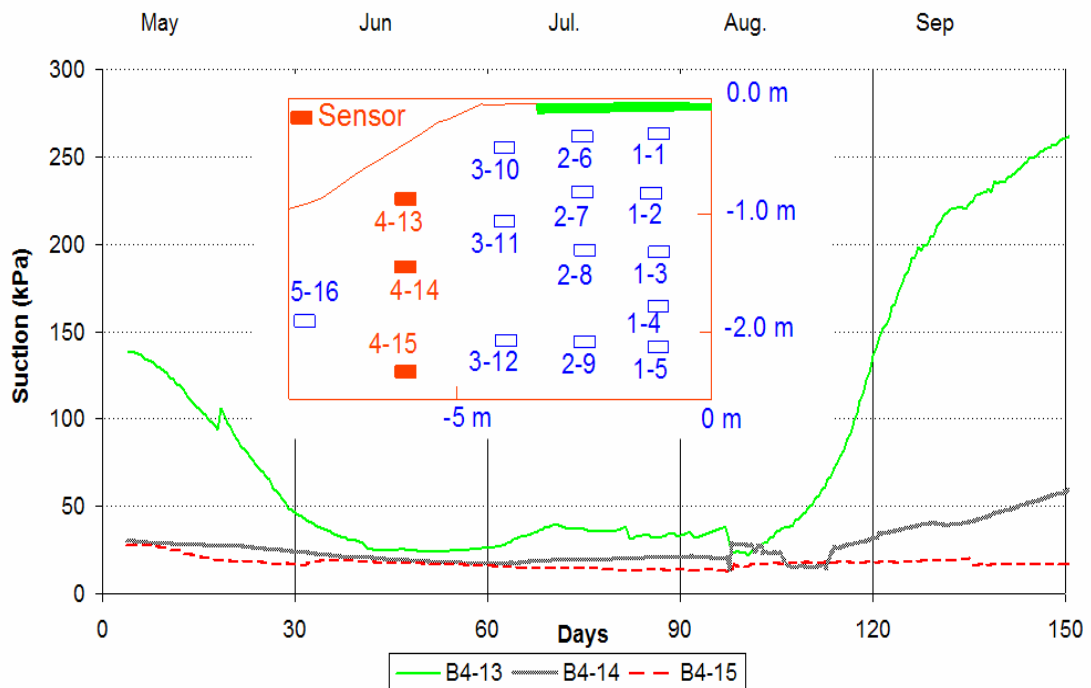


Figure 6.30 Two-year average suctions along vertical grid-line under the side-slope at the Bethune site

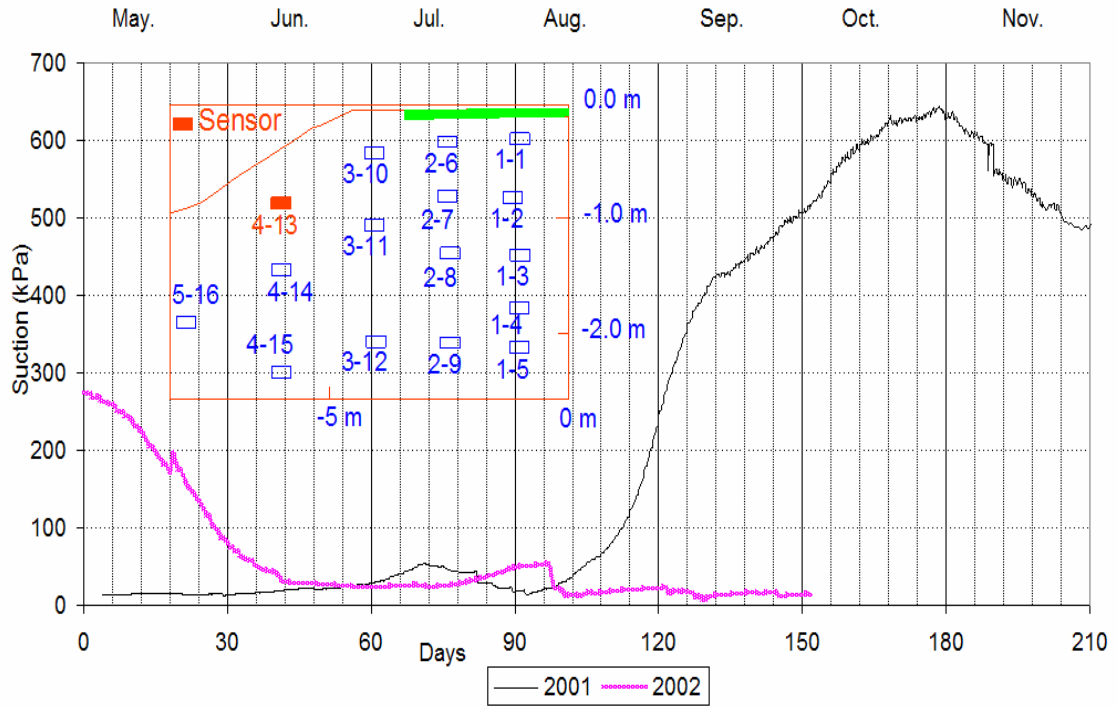


Figure 6.31 Suctions at Sensor B4-13 for years 2001 to 2002 at the Bethune site

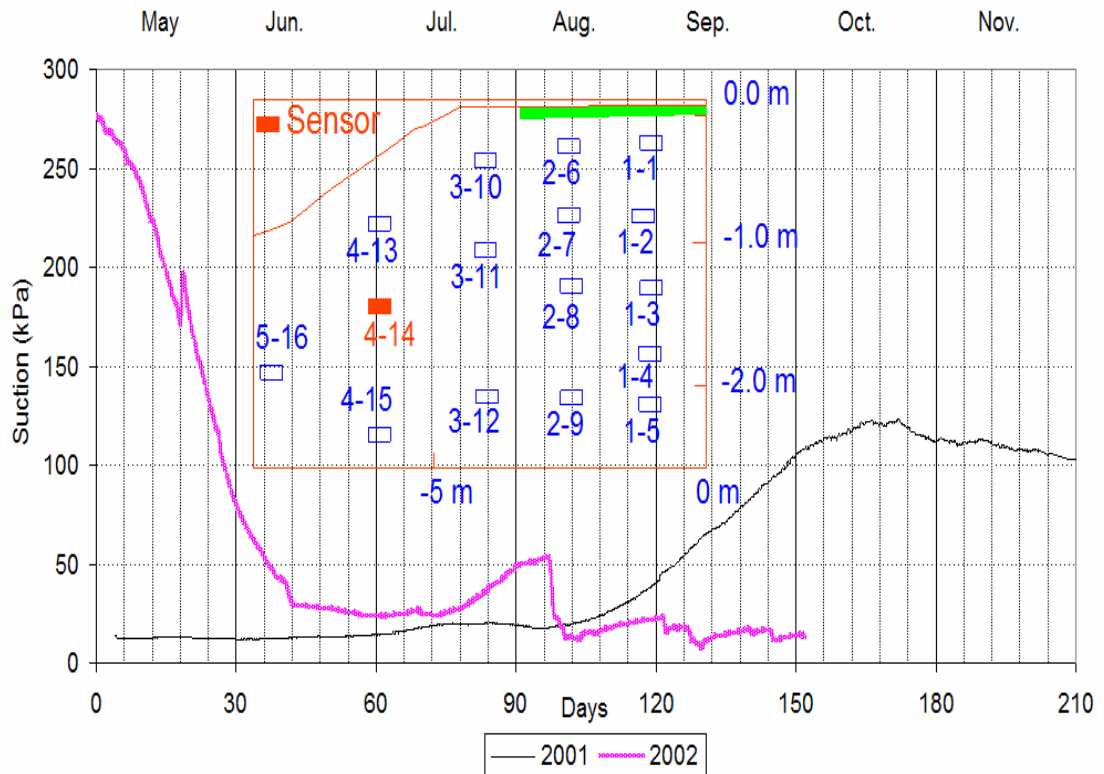


Figure 6.32 Suctions at Sensor B4-14 for years 2001 to 2002 at the Bethune site

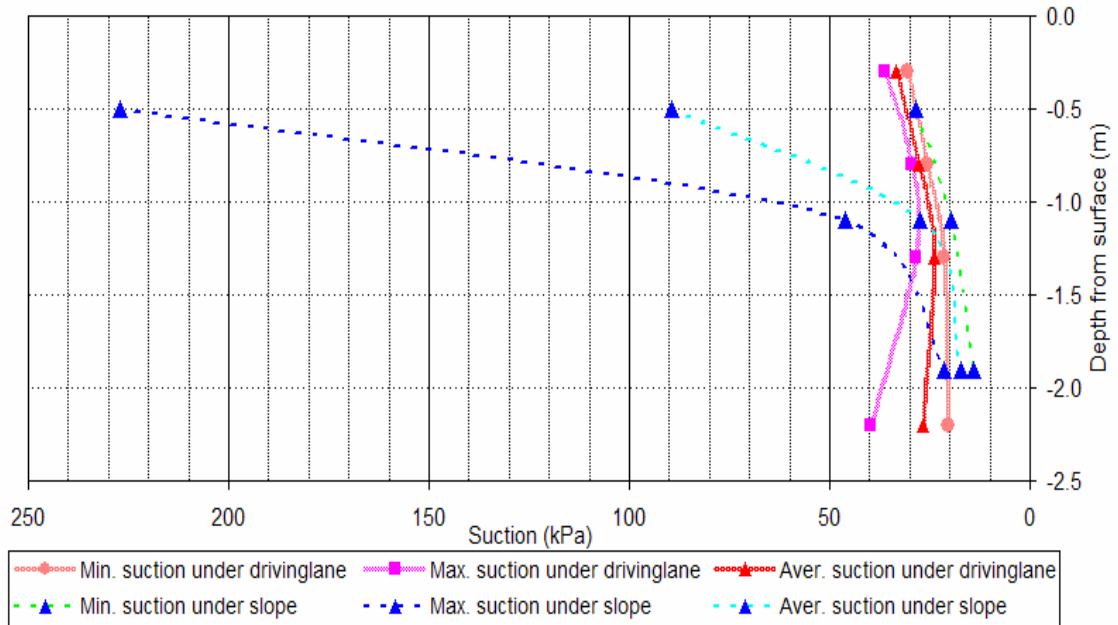


Figure 6.33 Summary of suctions along the three vertical grid-lines: under the driving-lane, under the shoulder and under the side-slope for years 2001 to 2002 at the Bethune site

6.4 Suctions along horizontal grid-line versus time

The measured suctions are plotted on horizontal grid-lines to show the variations with distance from the centerline of the highways.

6.4.1 Horizontal grid-line along top sensors at the Torquay site

There are four sensors installed at depths 0.3 to 0.5 m at the Torquay site. These are T1-1, T2-6, T3-10, T4-12 at distances of 1.0 m, 2.5 m, 4.0 m and 6.0 m from the centerline of the highway, respectively. The suctions determined from these sensors are shown in Figures from 6.34 to 6.36. The suctions increased and became more variable with the distance from the highway centerline. The average-monthly suctions at distances between 1.0 to 2.5 m (i.e. under pavement) from the centerline ranged from 10 to 30 kPa. Under the side-slope, the average-monthly suctions varied from 100 to 800 kPa. The individual suctions can be more than 1000 kPa. There appear to be similar numbers of fluctuations for the sensors along this horizontal grid-line. The occurrence

of these fluctuations also seems to occur at similar amplitudes and times. The lowest suctions were encountered in June and July and the highest suctions could be attained in September and October. The sensors were unable to make meaningful readings when part or all of the moisture in the ceramic block was frozen from the middle of November to the middle of April.

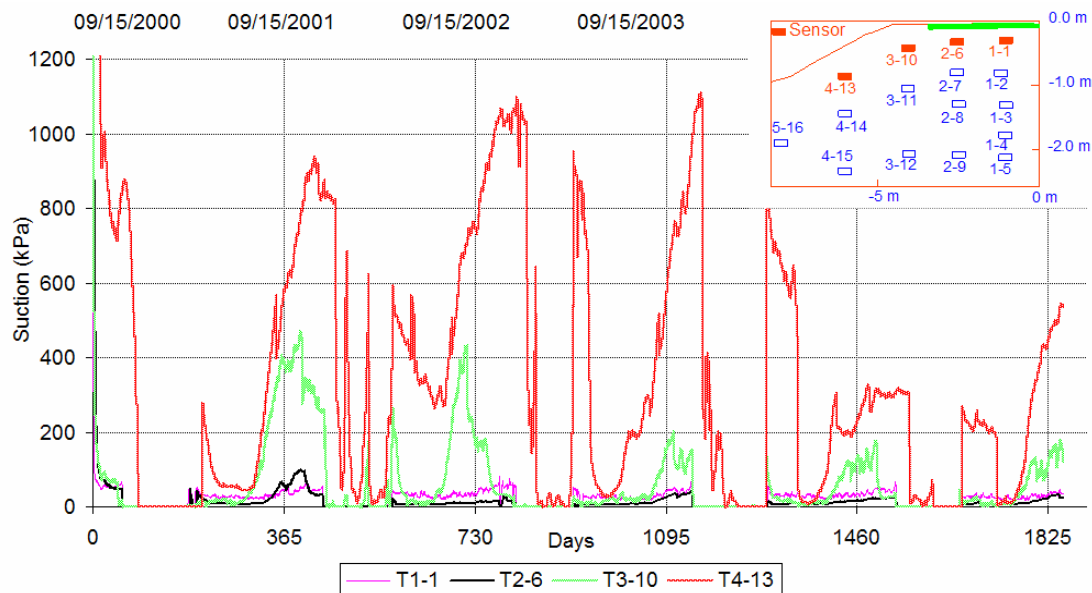


Figure 6.34 Suctions along horizontal top sensors at the Torquay site

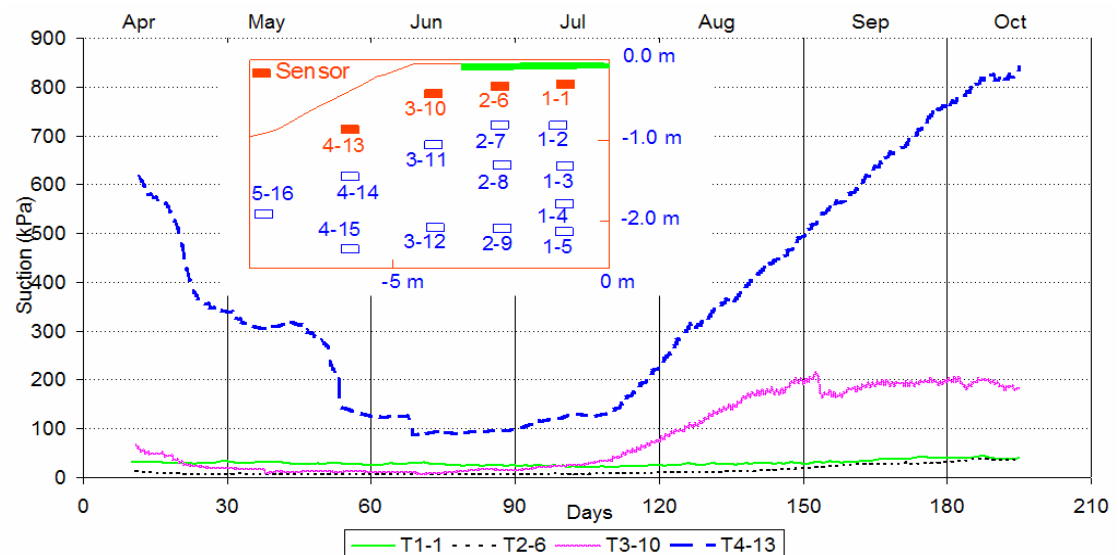


Figure 6.35 Five-year average suctions versus time along horizontal top sensors at the Torquay site

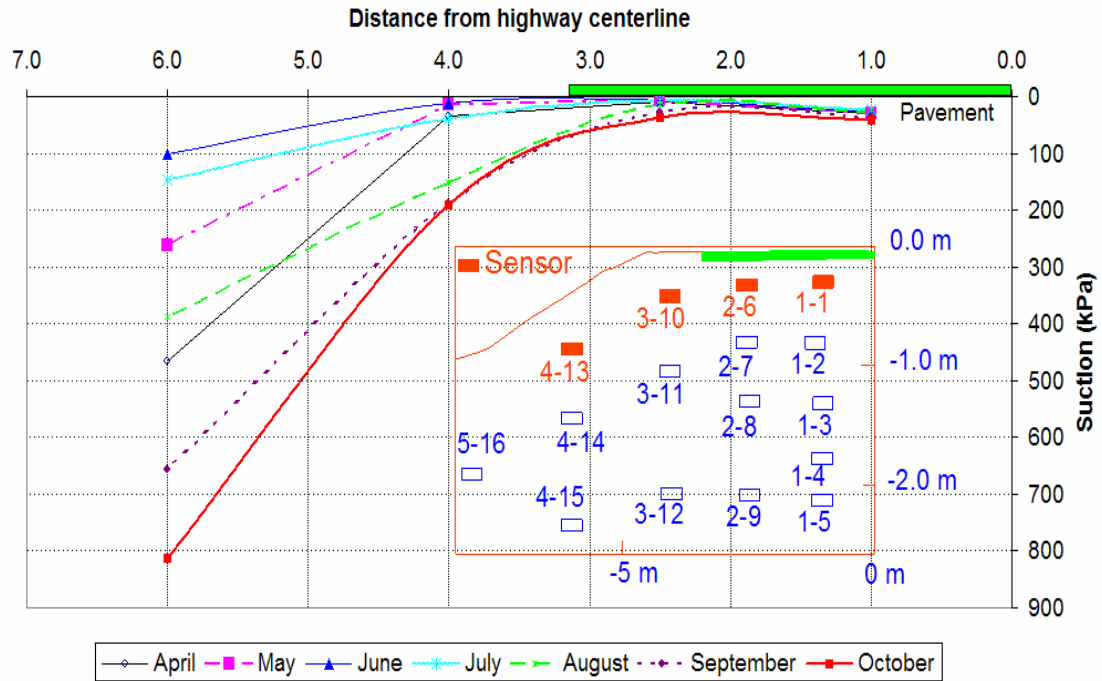


Figure 6.36 Five-year average-monthly suctions along top sensors versus distance from the centerline of highway at the Torquay site

6.4.2 Horizontal grid-line along top sensors at the Bethune site

Figures from 6.37 to 6.39 show that the fluctuations in suction occurred at similar cycles along this horizontal grid-line. However, the amplitude of the fluctuations in suction increased from the centerline to the side-slope. The average-monthly suctions were from 30 to 40 kPa under the driving-lane and 30 to 230 kPa under the side-slope during unfrozen months when the soil was unfrozen.

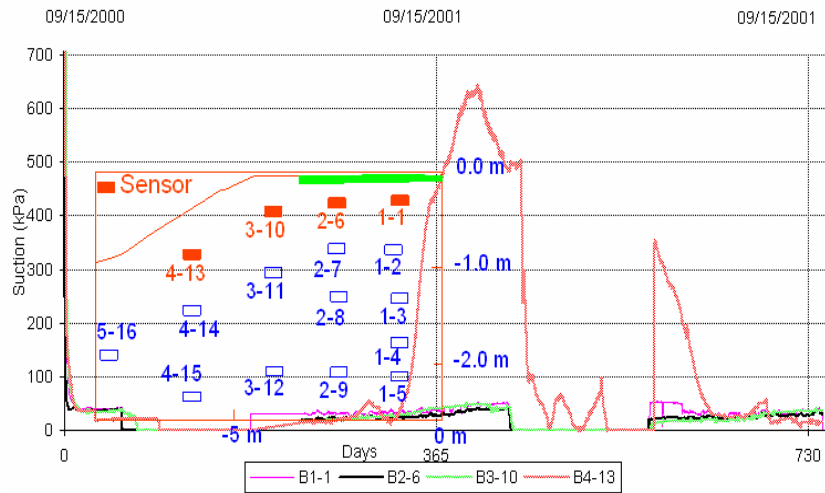


Figure 6.37 Suctions along horizontal top sensors at the Bethune site

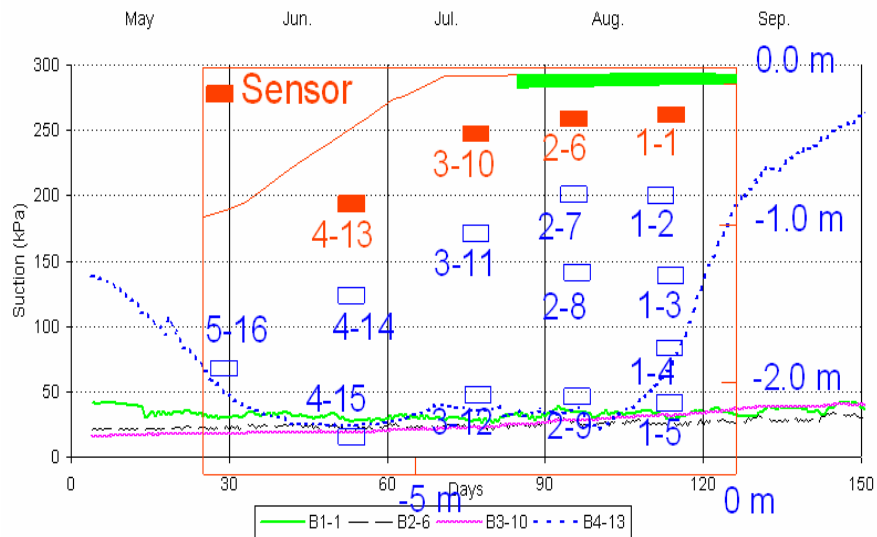


Figure 6.38 Two-year average suctions versus time along horizontal top sensors at the Bethune site

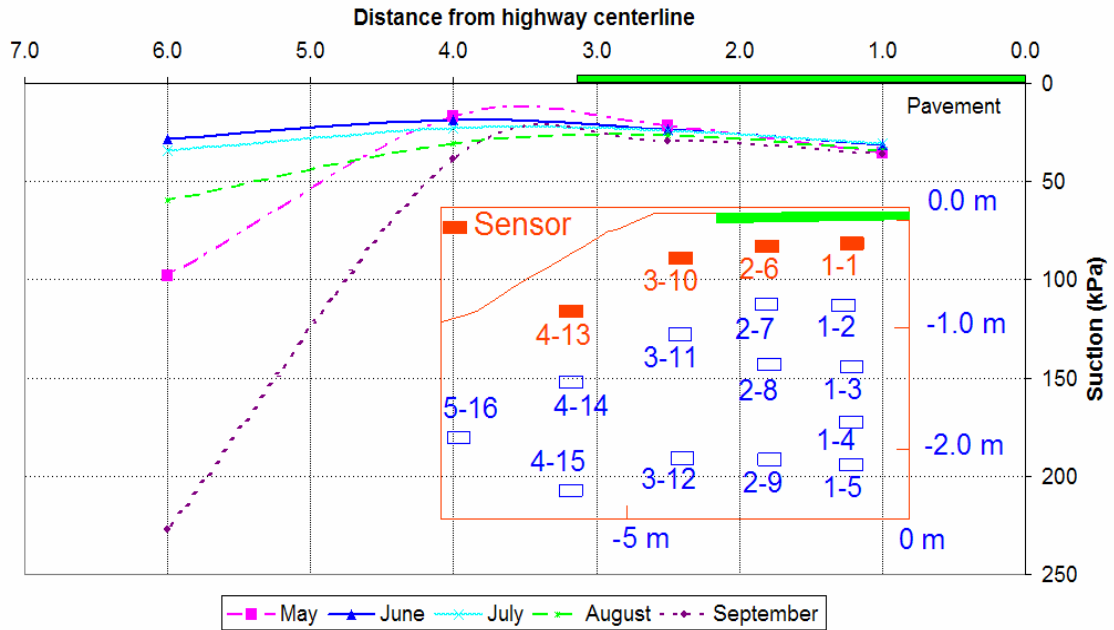


Figure 6.39 Two-year average suctions at top sensors versus distance from the centerline of highway at the Bethune site

6.4.3 Horizontal grid-line along middle-depth sensors at the Torquay site

The variations in suction also increased with the distance from the highway centerline along this grid-line as presented in Figures from 6.40 to 6.42. However, the average-monthly suctions reduced from 100 to 230 kPa from Sensor T4-14 to Sensor T5-16 from 48 to 80 kPa under the side-slope because Sensor T5-16 is close to an irrigated field.

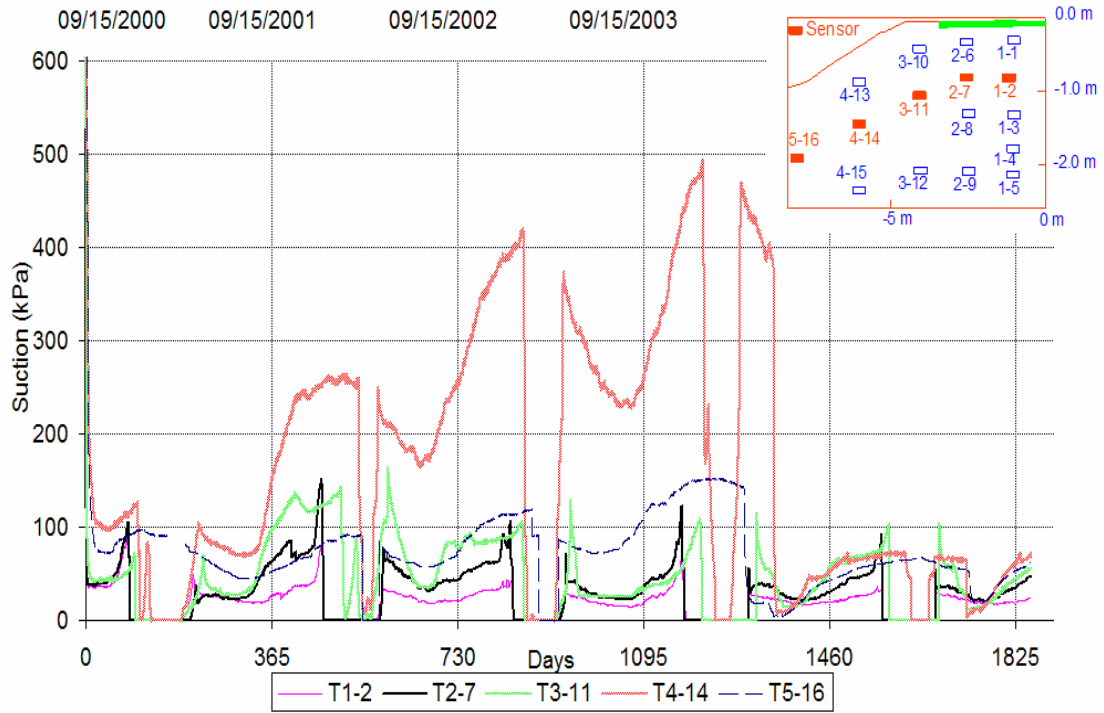


Figure 6.40 Suctions along horizontal middle-depth sensors at the Torquay site

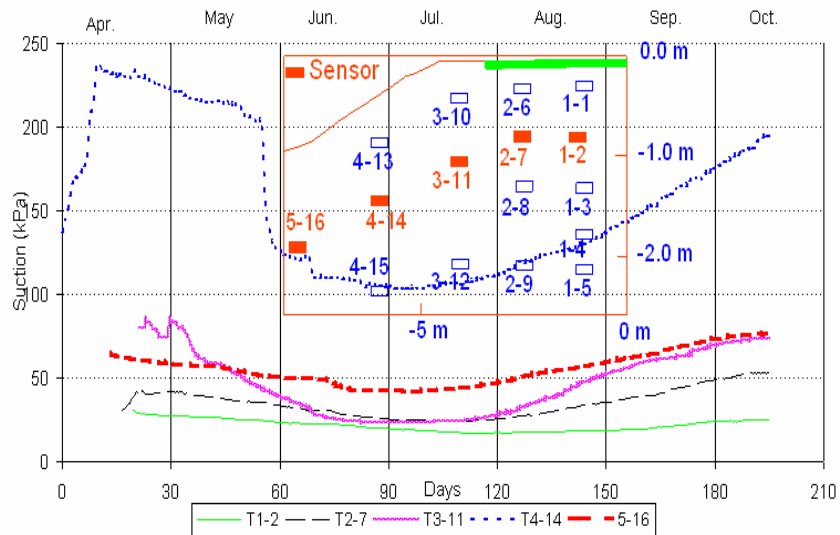


Figure 6.41 Five-year average suctions versus time along horizontal middle-depth sensors at the Torquay site

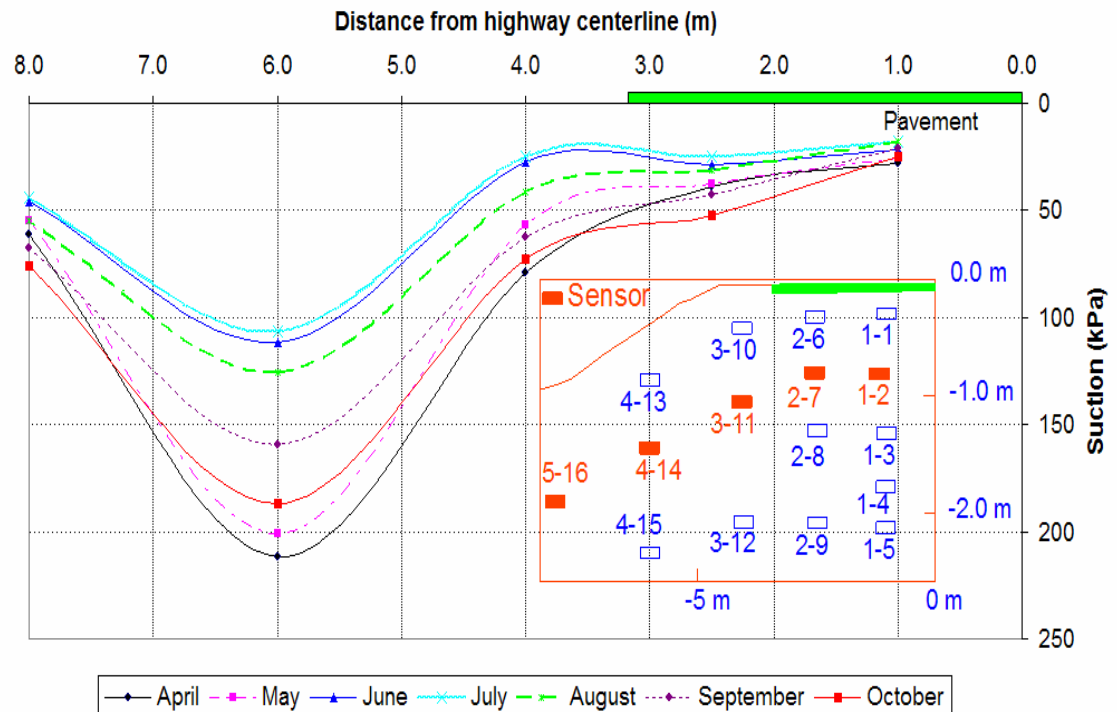


Figure 6.42 Five-year average suctions at middle-depth sensors versus distance from the centerline of highway at the Torquay site

6.4.4 Horizontal grid-line along bottom sensors at the Torquay site

There are four sensors at depths from 1.9 to 2.2 m along this horizontal grid-line. These sensors are T1-5, T2-9, T3-12 and T4-15 at distances of 1.0 m, 2.5 m, 4.0 m and 6.0 m from the centerline of the highway respectively.

In Figure 6.43, like the shallower horizontal grid-lines, in 2004 Sensor T4-15 under the side-slope provided low suctions which were only 60 to 70% of the suctions measured during the same time of the previous years (i.e. from 2001 to 2003). As plotted in Figure 6.44, the highest suctions along this horizontal grid-line were recorded in March with suctions from 52 to 94 kPa. These suctions gradually lowered to the smallest values of 20 to 40 kPa in August. Sensor T3-12 under the shoulder recorded the highest suctions, approximately 20% greater than the other sensors in the same horizontal grid-line. The other three sensors exhibited similar suctions within the range from 20 to 67 kPa. At this depth (i.e. 1.9 to 2.2 m) the sensors could monitor suctions

for the whole year. In Figure 6.45, the suctions increased from the centerline of the highway to the shoulder, however; decreased from 40 to 90 kPa under the shoulder to 20 to 50 kPa under the side-slope.

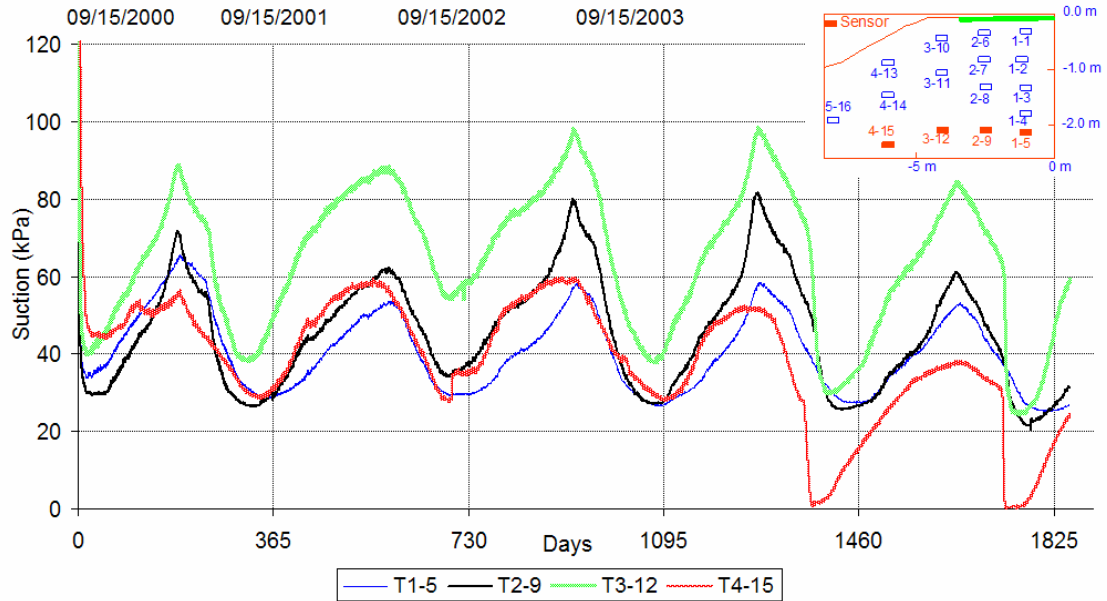


Figure 6.43 Suctions along horizontal bottom sensors at the Torquay site

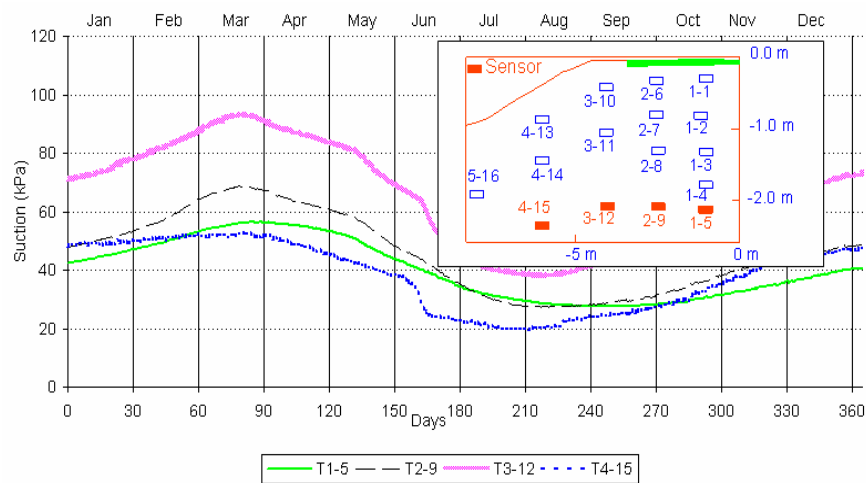


Figure 6.44 Five-year average suctions versus time along horizontal bottom sensors at the Torquay site

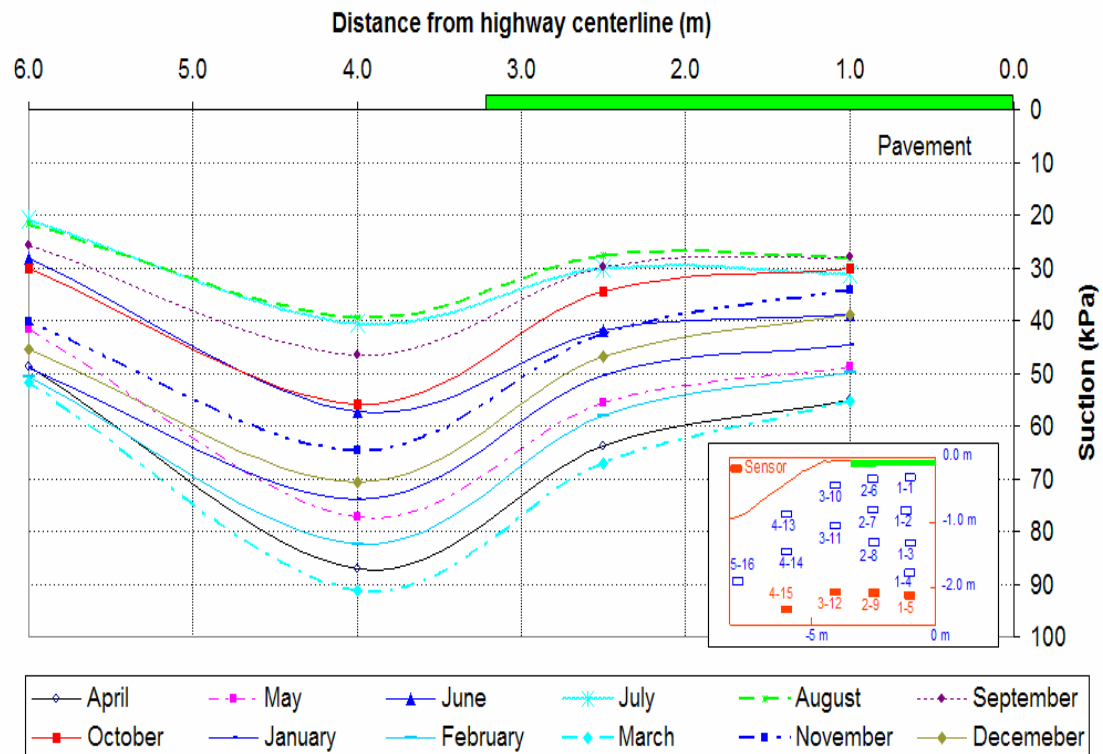


Figure 6.45 Five-year average suctions at bottom sensors versus distance from the centerline of highway at the Torquay site

The summary of the suctions versus distance from the centerline of the highway at the Torquay site is illustrated in Figure 6.46. The suctions at shallow depths (i.e. less than 1.1 m) increased and became more variable with distance from the highway centerline. However, at bottom depths from 1.9 to 2.2 m the suctions appeared to be less variable with distance from the highway centerline.

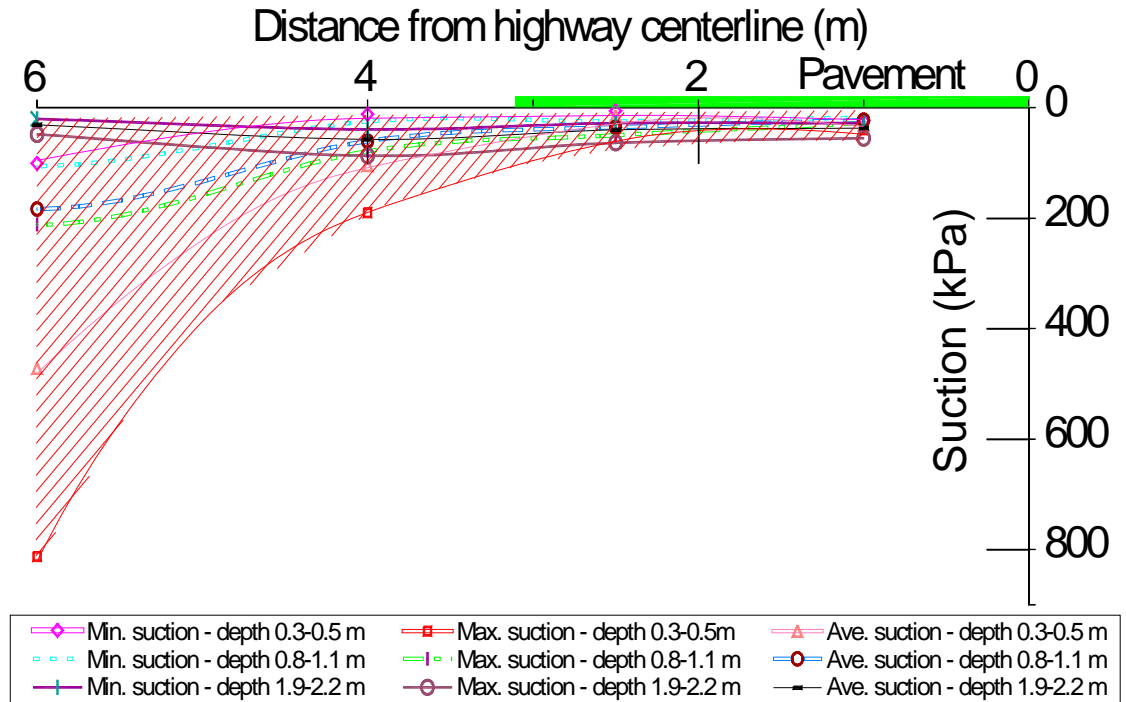


Figure 6.46 Summary of suctions at horizontal grid-lines for years 2001 to 2005 at the Torquay site

6.4.5 Horizontal grid-line along bottom sensors at the Bethune site

The suctions along bottom sensors are presented in Figures 6.47 to 6.49. Although these sensors are at the same depth as those bottom sensors at the Torquay site, the interruption of suction measurement occurred during the winter of 2001 due to freezing. Erratic readings were encountered with Sensor B3-12 in 2002. This could possibly be attributed to the water penetration to the core element of the sensor. Except for these limitations, similar to the bottom sensors at the Torquay site, these sensors showed a stable trend of suction variations. In Figure 6.48, the average-monthly suctions ranged from 20 to 40 kPa. The suctions decreased from the shoulder to the side-slope. The variations in suction reduced from the centerline to edge of the pavement and then went up to the shoulder before falling off within a narrow band under the side-slope as illustrated in Figure 6.49.

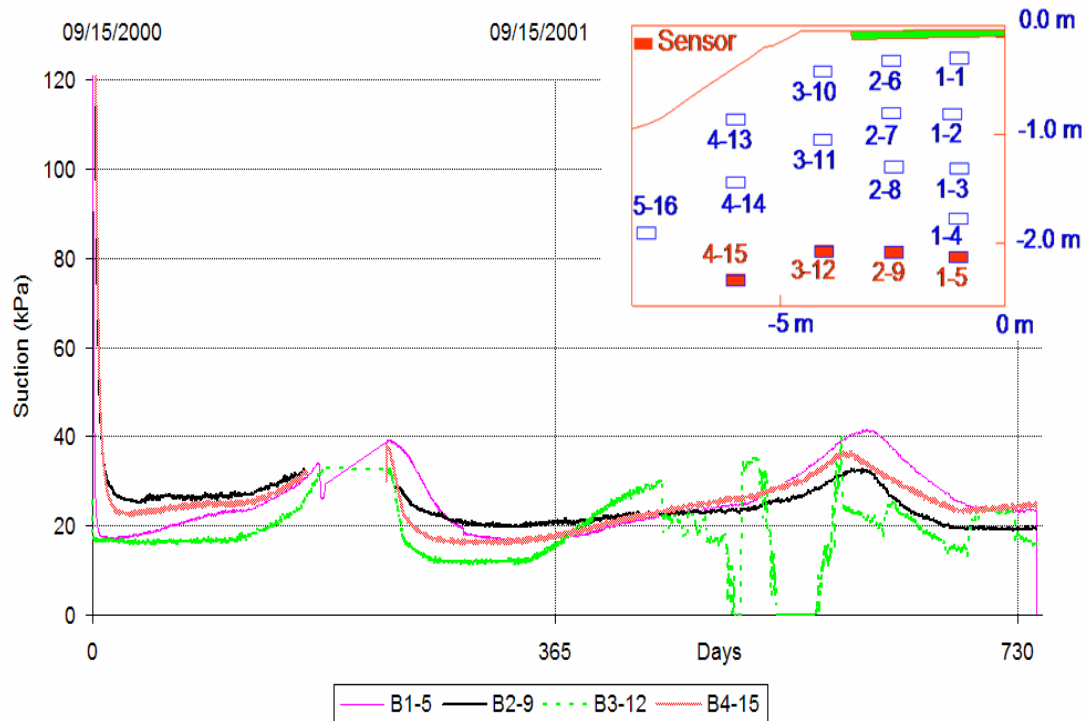


Figure 6.47 Suctions along horizontal middle-depth sensors at the Bethune

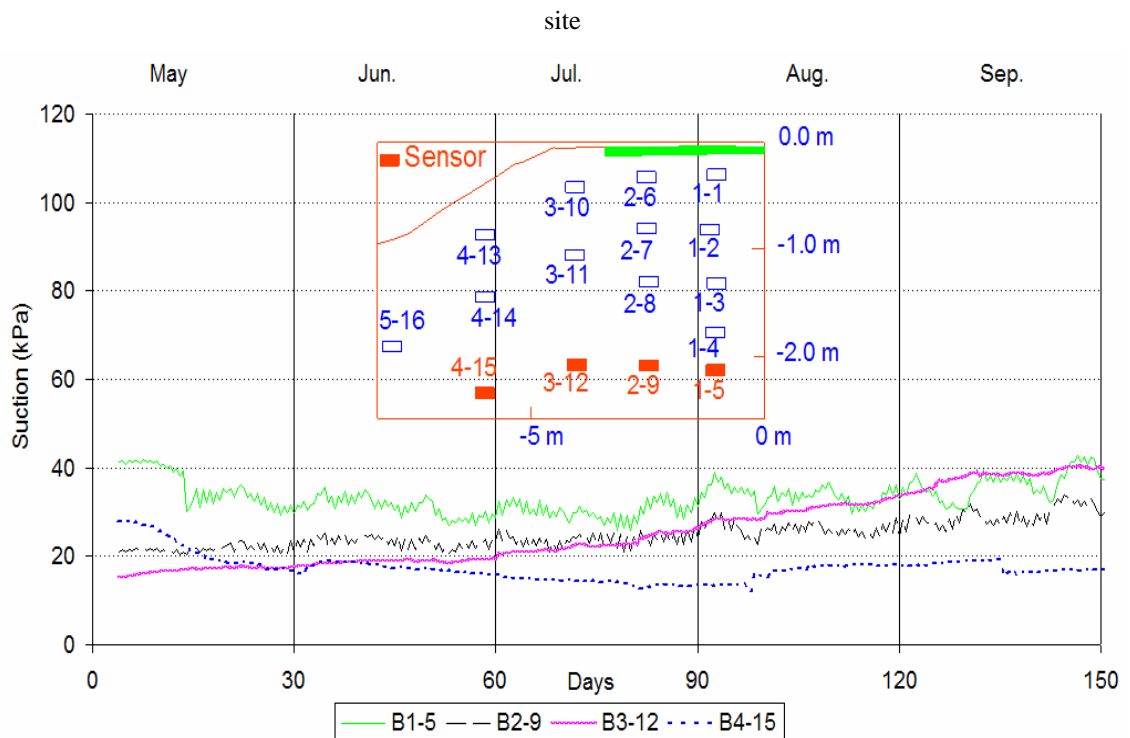


Figure 6.48 Two-year average suctions versus time along horizontal bottom sensors at the Bethune site

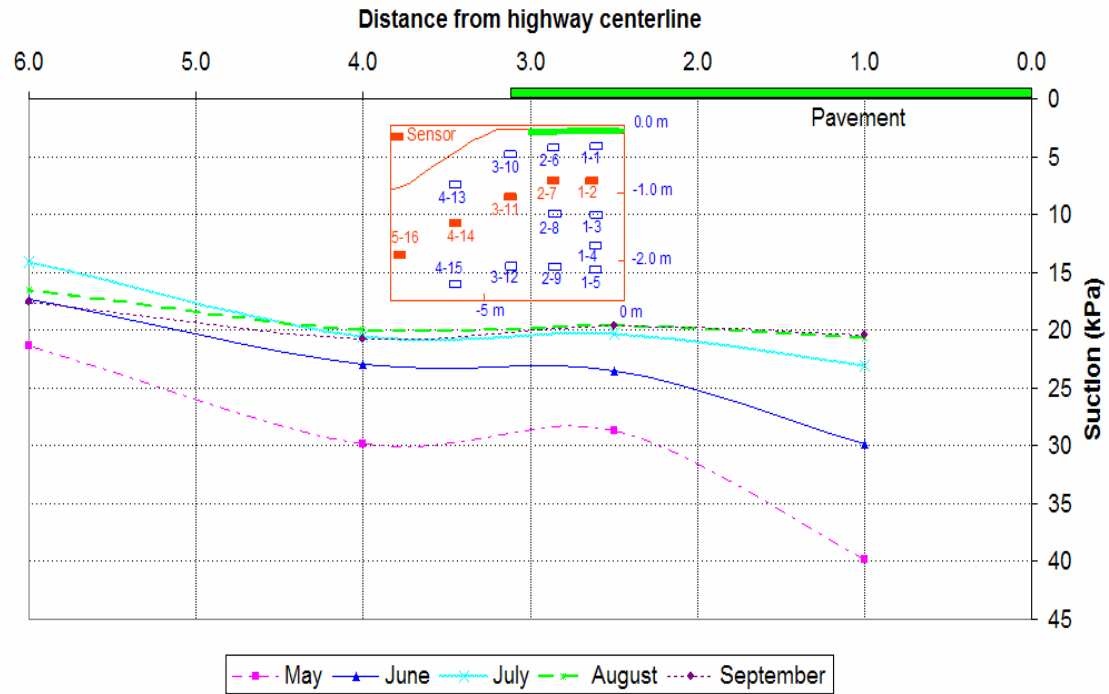


Figure 6.49 Two-year average suctions at middle-depth sensors versus distance from the centerline of the highway at the Bethune site

The suctions along bottom horizontal grid-line are compared with the upper horizontal grid-lines in Figure 6.50. The variations in suction were more pronounced from the centerline to the shoulder for all depths investigated. At depth from 1.9 m to 2.2 m, the suctions became less variable under the side-slope.

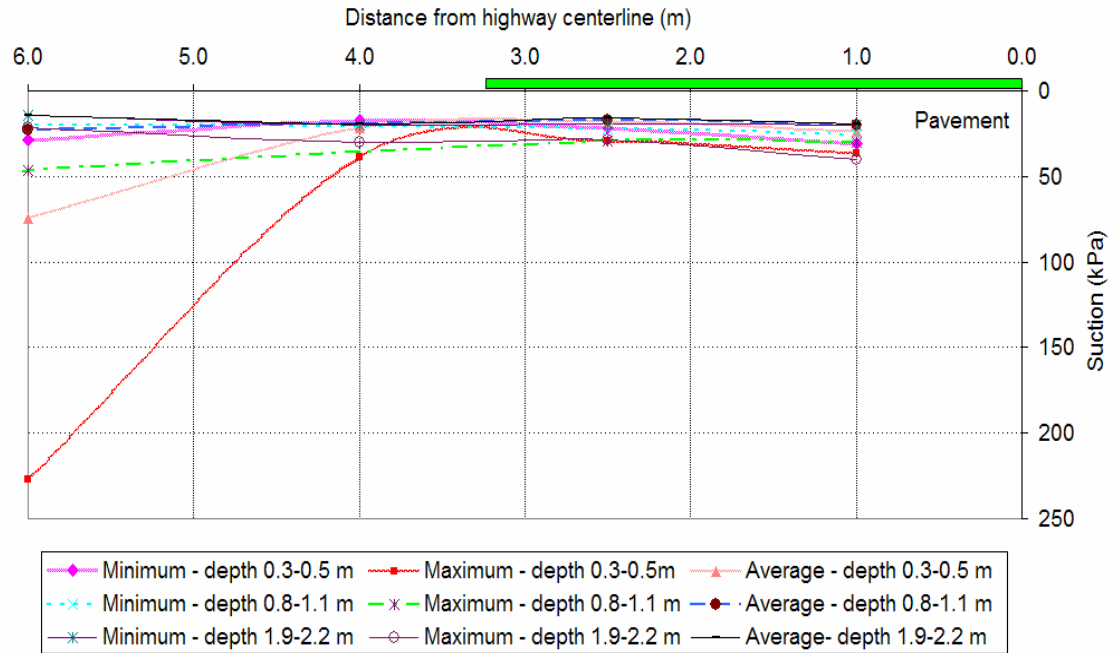


Figure 6.50 Summary of suctions along different horizontal grid-lines for years 2001 to 2002 at the Bethune site

6.5 Contour maps of suction

The contour maps present the suction variations in the cross sections of the highways at the Torquay site and Bethune. The suctions on these contour maps were calculated by taking five-year monthly average of the data.

6.5.1 Contour maps of suctions at the Torquay site

Three contour maps at the Torquay site are shown in this section of the thesis and further maps can be found in Appendix B.

As can be seen on the contour maps of April, July, and September as illustrated in Figures 6.51 to 6.53, the suctions varied the most under the side-slope. April witnessed a great change of the suctions from location to location on the contour map, and then the suction variations became stable until July. The suctions on the contour maps varied more significantly again from July to September, especially under the side-

slope. During the measurable period, the suctions under the driving-lane were mostly less than 50 kPa and smaller than that under the side-slope, where suctions were generally more than 100 kPa.

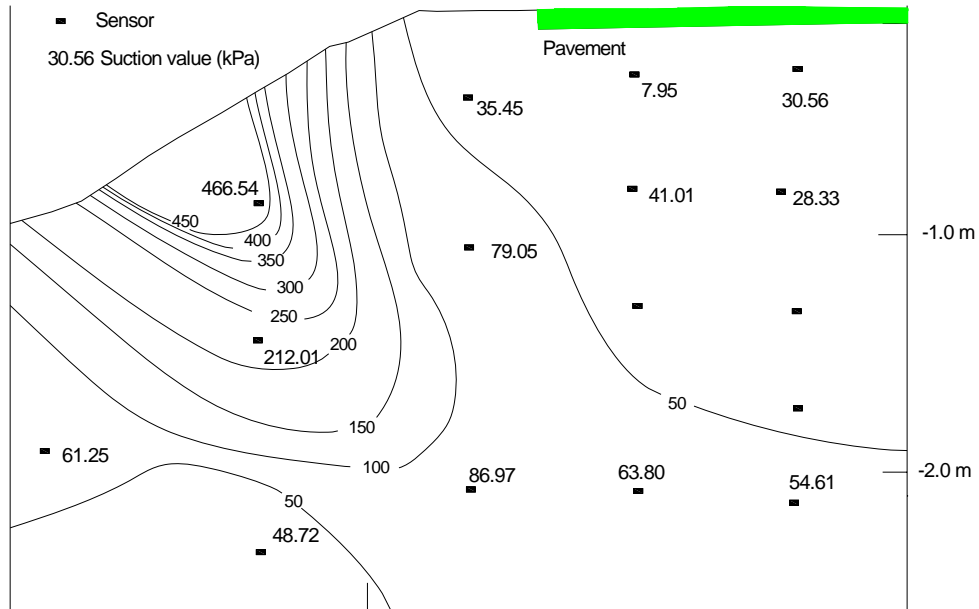


Figure 6.51 Contour map of average suction in April at the Torquay site

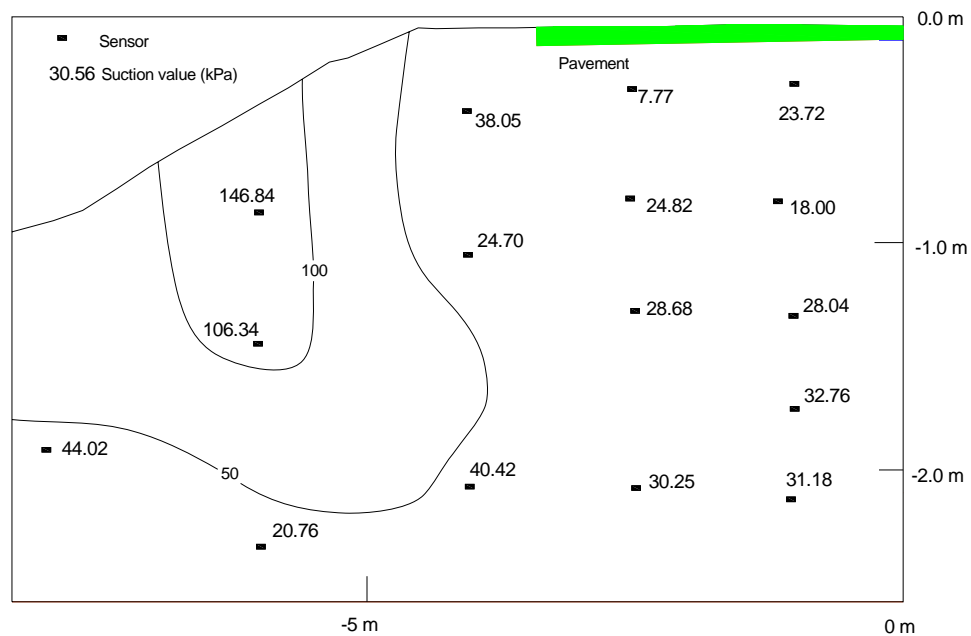


Figure 6.52 Contour map of average suction in July at the Torquay site

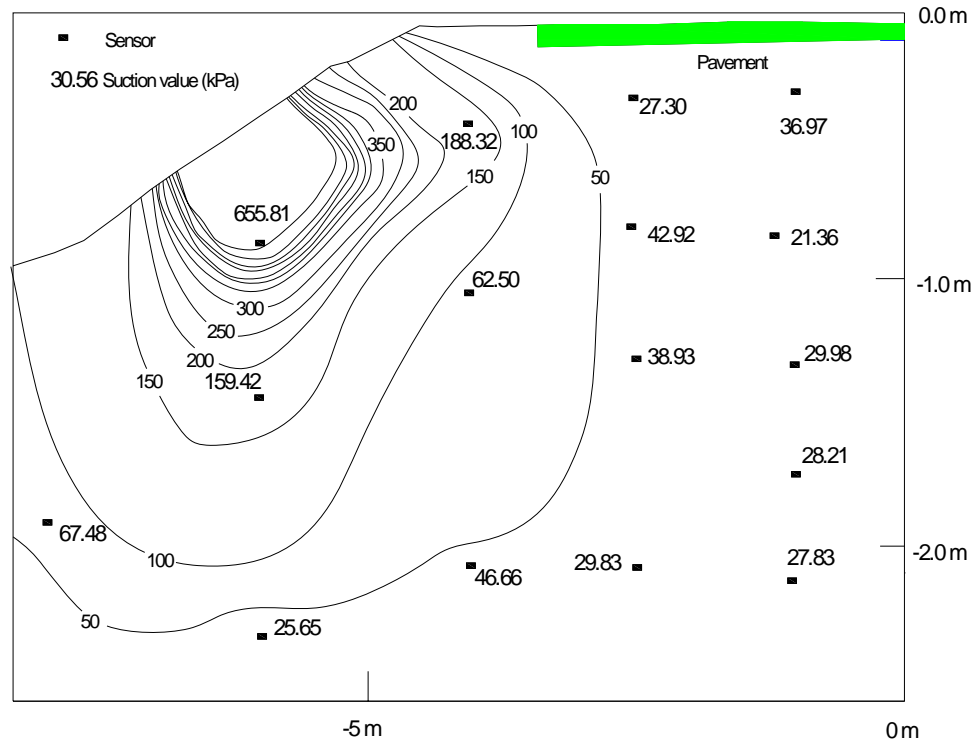


Figure 6.53 Contour map of average suction in September at the Torquay site

6.5.2 Contour maps of suction at the Bethune site

The variations in suction at the Bethune site (Figures from 6.54 to 6.56) were much the same as at the Torquay site. The suctions under the driving-lane appeared the smallest all the time in these contour maps. The suctions in July were least variable from location to location. Under the side-slope, the suctions could reach to more than 200 kPa in September while only 34 kPa in July. The suctions also experienced the most variability under the side-slope.

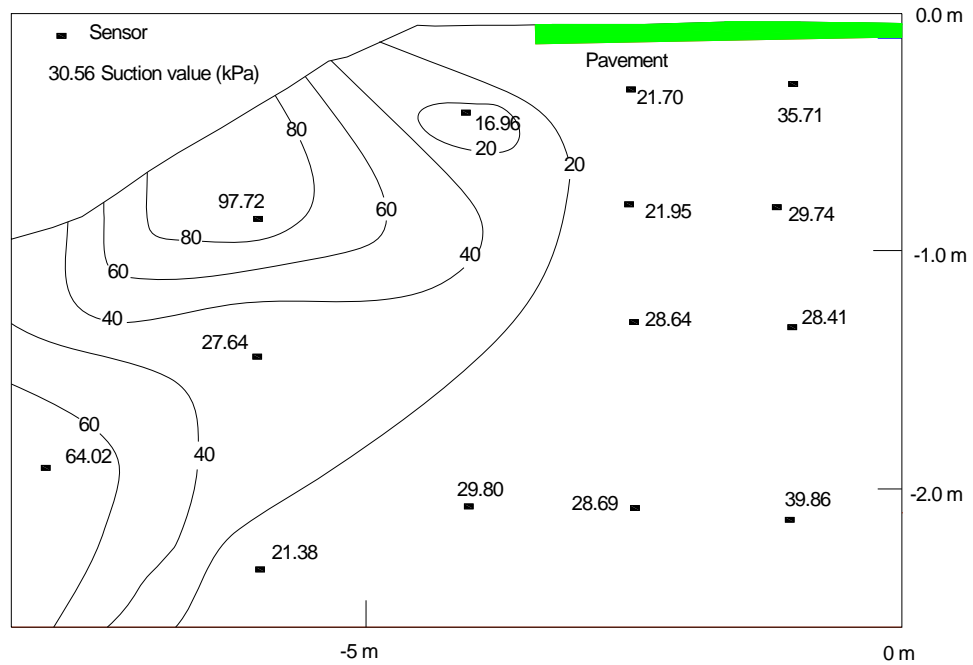


Figure 6.54 Contour map of average suction in May at the Bethune site

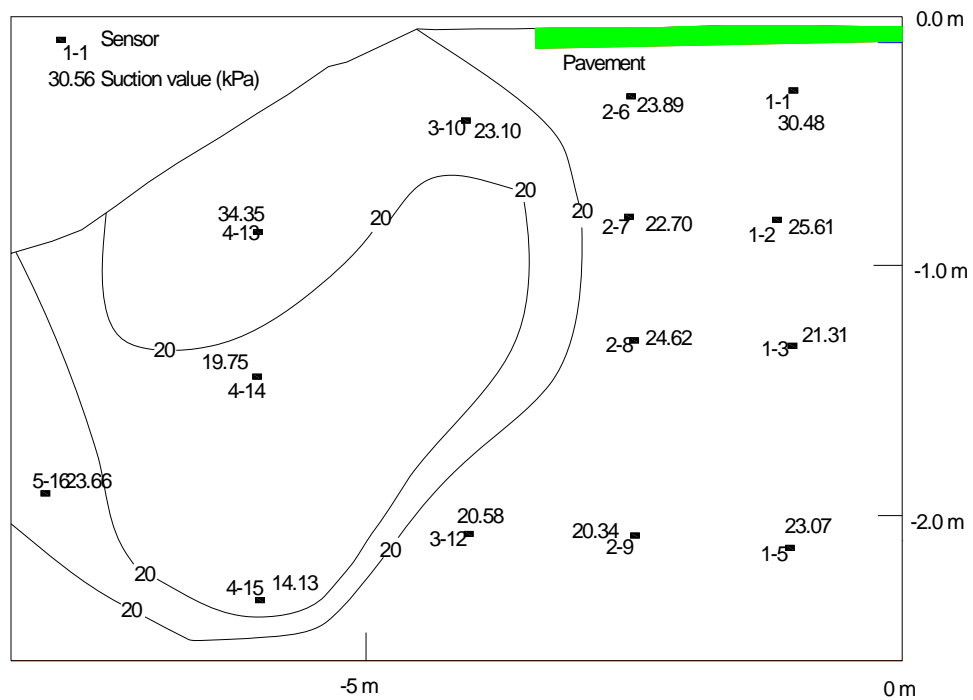


Figure 6.55 Contour map of average suction in July at the Bethune site

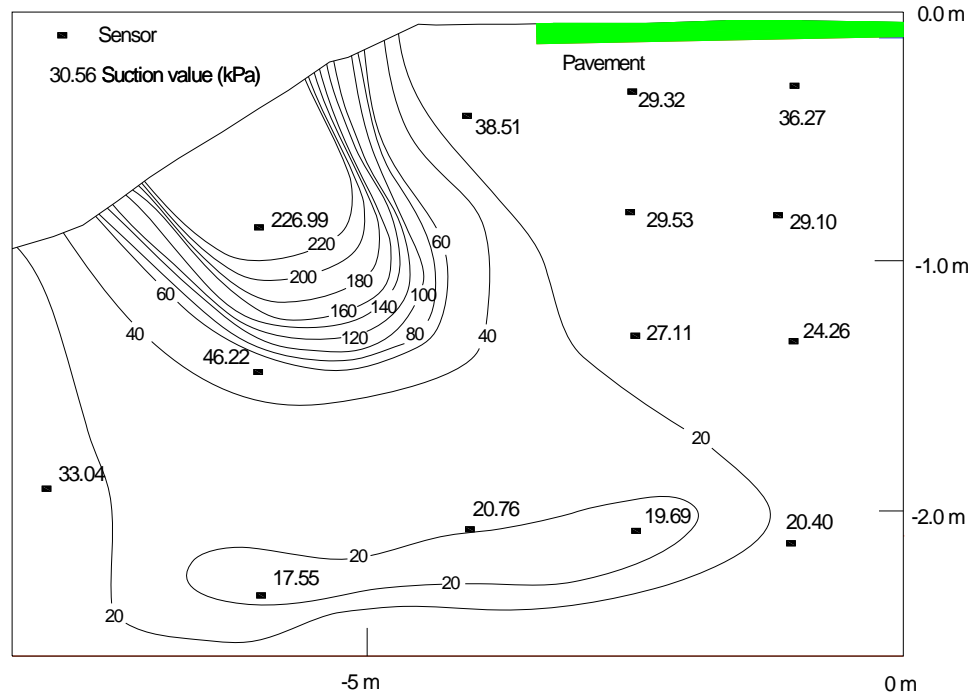


Figure 6.56 Contour map of suctions in September at the Bethune site

6.6 Suction presentation with small time scales

Presentation of suction versus small time scales was examined to investigate the time of the first change in the sensor measurements in response to a rainfall event.

The noise level of the thermal conductivity sensors in measuring suction was also investigated by plotting suctions versus small time scales.

Three sensors at representative locations in the highway cross section at the Torquay site were selected to present the data with different time scales. These sensors are T3-10 and T3-11 at depths of 0.3 m and 0.8 m respectively under the shoulder and T1-5 at a depth 2.2 m under the driving-lane.

6.6.1 Sensor response to rainfall

The data from Sensor T3-10 under the shoulder are plotted to investigate the sensor response to a rainfall event at the uncovered area. As illustrated in Figures from 6.57 to 6.60, the response time of sensor T3-10 (at depth of 0.3 m) appeared to be

within 24 hours after the rainfall events. However, the effect of rainfall was indiscernible in May 2004 as shown in Figure 6.57.

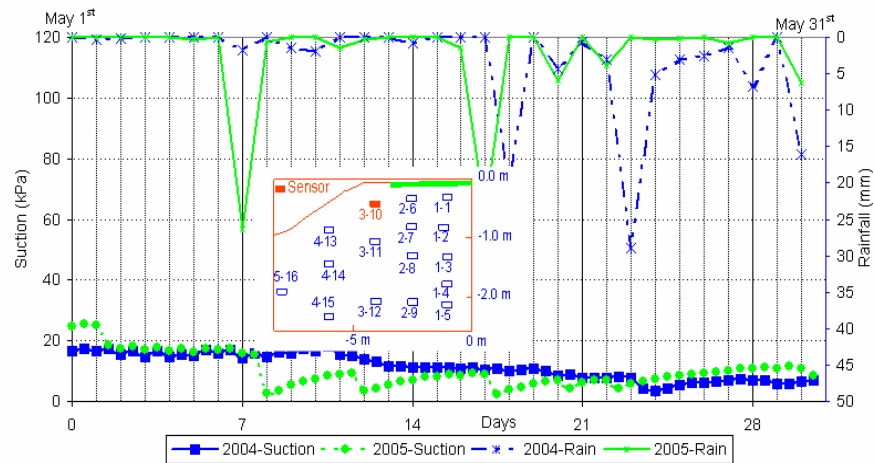


Figure 6.57 Response of suction to rainfall at Sensor T3-10 in May, 2004 and 2005

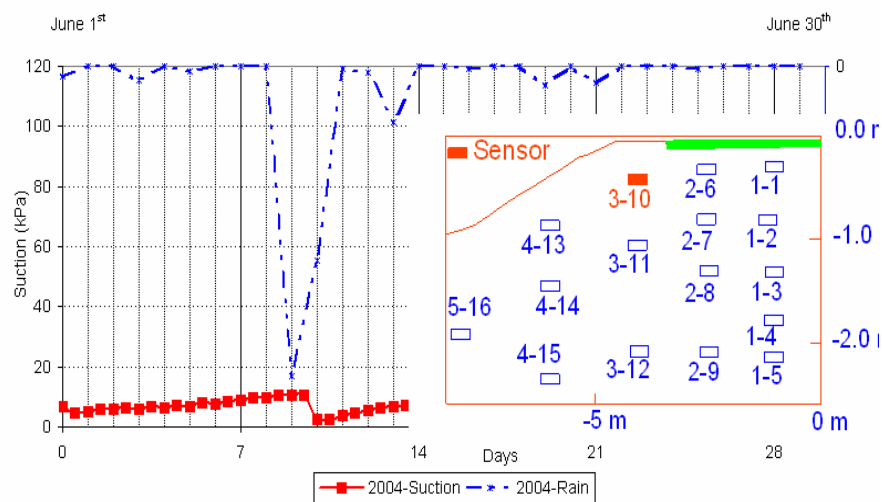


Figure 6.58 Response of suction to rainfall at Sensor T3-10 in June 2004

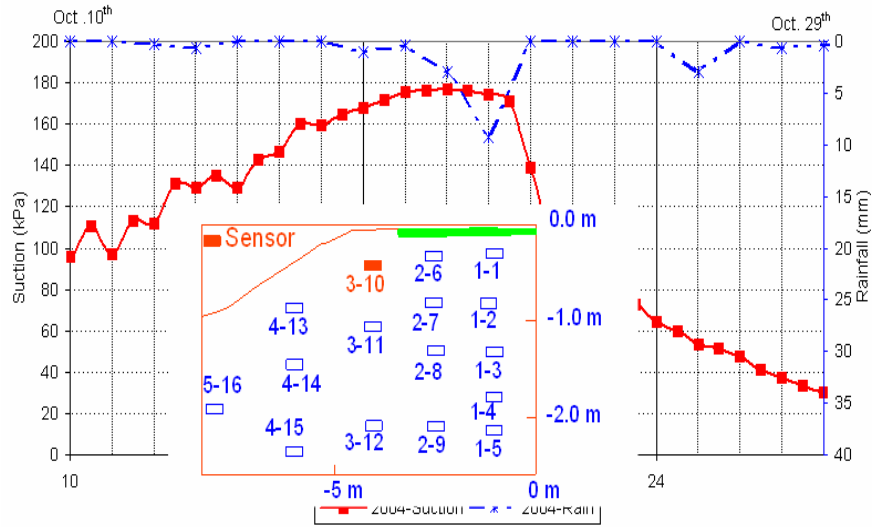


Figure 6.59 Response of suction to rainfall at Sensor T3-10 in October 2004

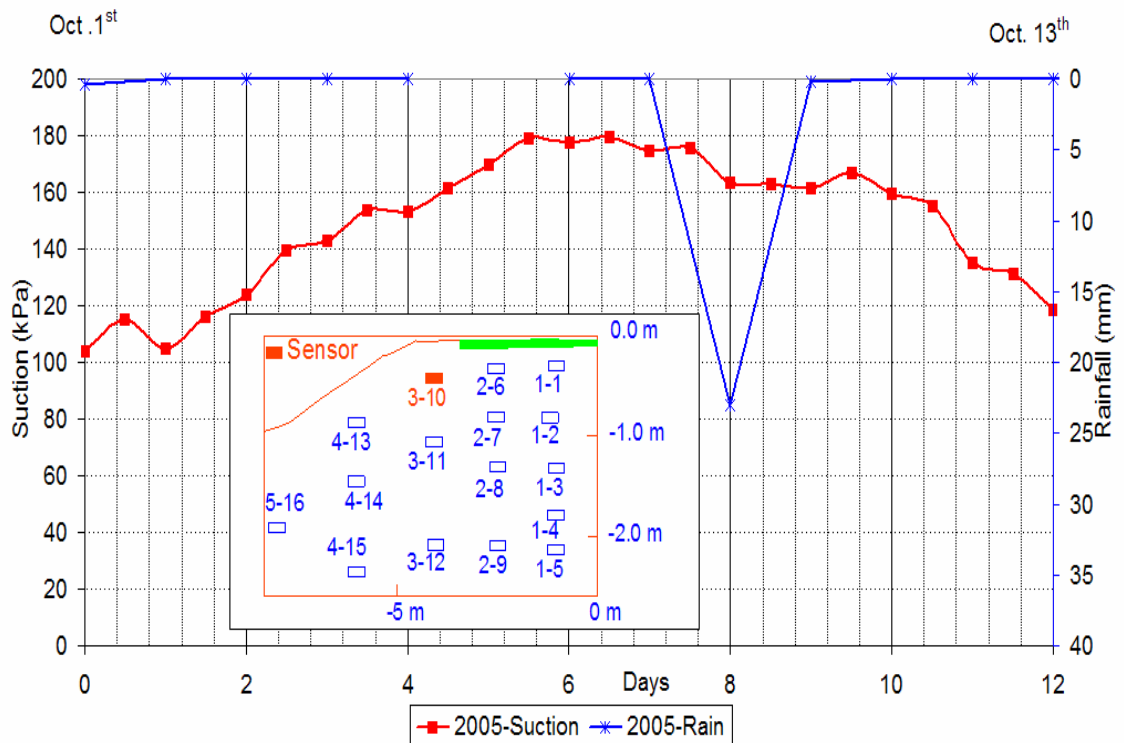


Figure 6.60 Response of suction to rainfall at Sensor T3-10 in October 2005

The correlations between the changes in suction to a rainfall event at greater depths (i.e. more than 0.3 to 0.5 m) could not be interpreted. As can be seen in Figure

6.61, at a depth 1.1 m under the shoulder, no short-term response to rainfall was witnessed at Sensor T3-11 during the monitoring period.

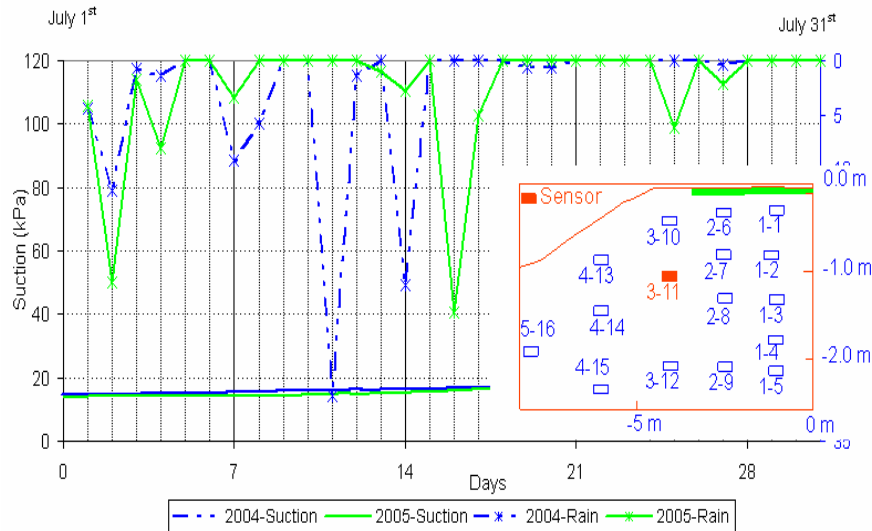


Figure 6.61 Response of suction at Sensor T3-11 in July 2004 and 2005.

6.6.2 Noise levels of the thermal conductivity sensors

High noise levels of thermal conductivity sensors can mask the fluctuations in suctions and reduce the measurement accuracy. The noise level, which is mainly attributed to the cable length and power source, can be assessed by plotting the suctions versus time under no rainfalls and stable temperatures.

The selected data from Sensors T3-10 and T1-5 were presented to examine the reading fluctuations. In Figures 6.62 and 6.63, the suctions varied within the range of $\pm 3\%$ with relatively stable temperatures and no rainfall. These sensors proved the confidence for monitoring the suction in a highway subgrade.

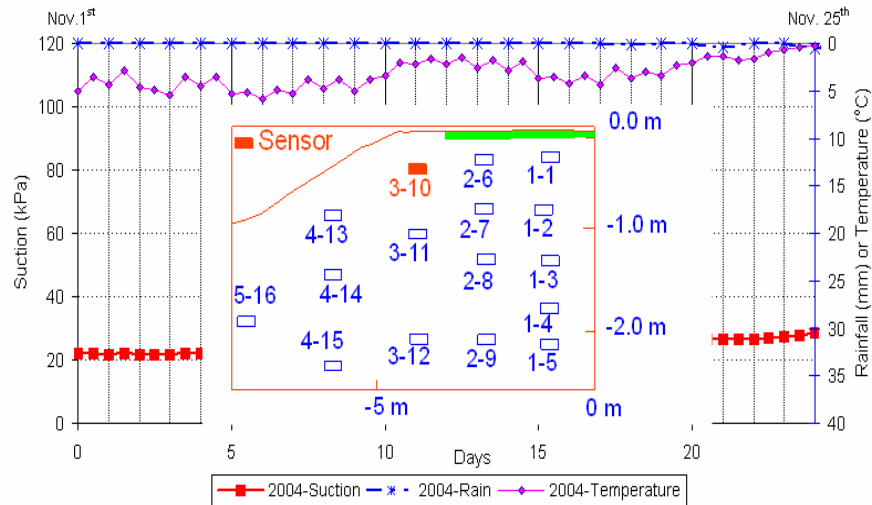


Figure 6.62 Response of suction at Sensor T3-10 (0.3 m deep under the shoulder) to rainfall and temperature in November.

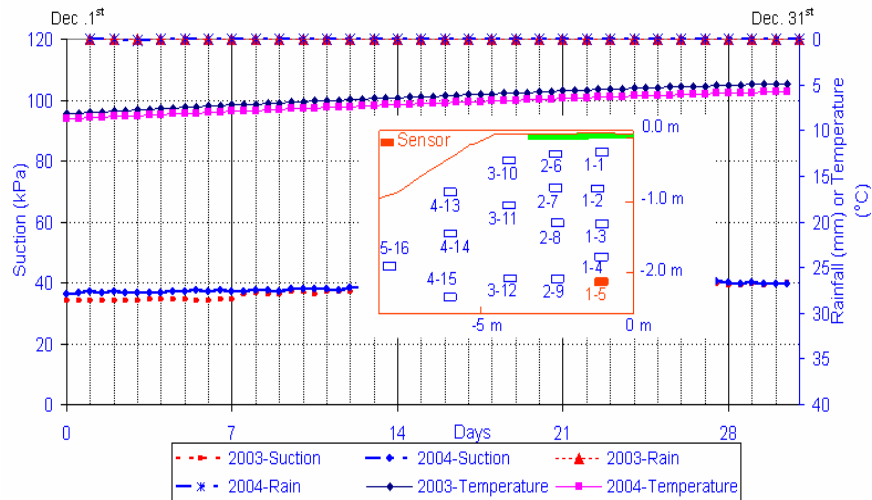


Figure 6.63 Response of suction at Sensor T1-5 (2.2 m deep under the driving-lane) with rainfall and temperature in December 2003 and 2004

6.7 Suction variations with temperature and time

The suction presentation versus temperature was examined to investigate the ambient temperature and freeze-thaw cycle effects on suction measurement using the thermal conductivity sensors.

6.7.1 Suction measurement during freezing

All the sensors behaved in the same manner when the surrounding soils were frozen. The measurement using the thermal conductivity sensors could not provide interpretable readings during freezing. The data during freezing from typical sensors are illustrated in Figures 6.64 and 6.65. When the temperature went below zero degrees Celsius, no data were recorded. However, when the temperature increased to above zero, the suction reading was recovered and the functionalities of the sensors resumed.

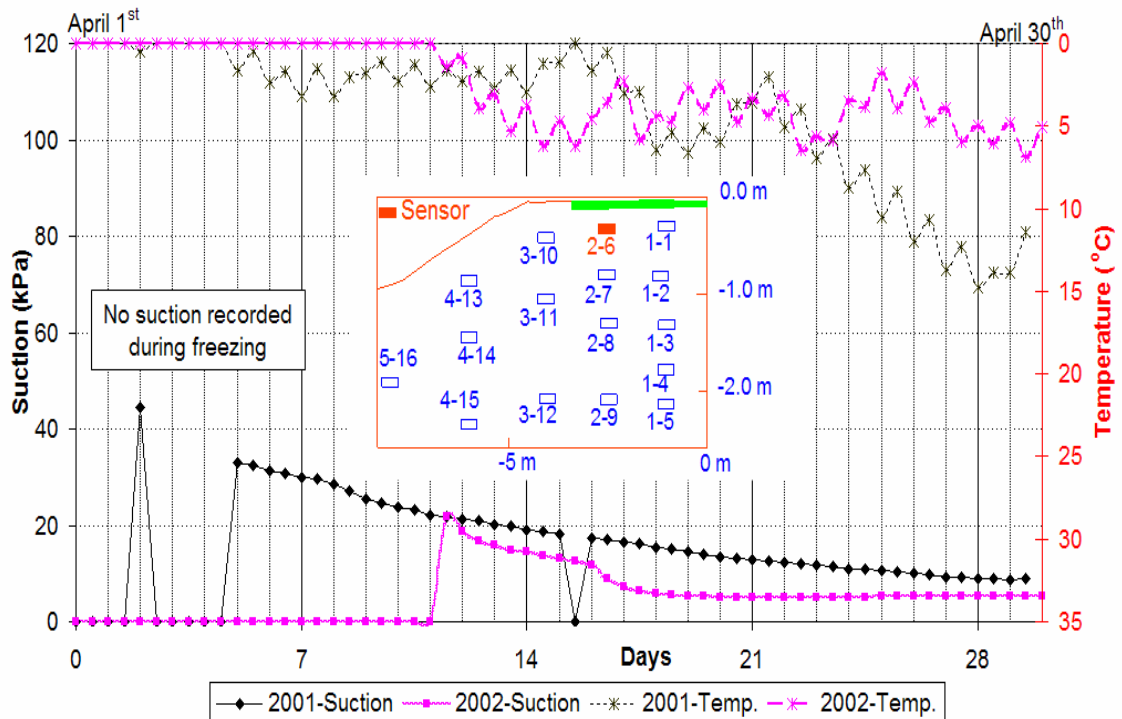


Figure 6.64 Response of suction at Sensor T2-6 at temperatures less than zero in April 2001 and 2002.

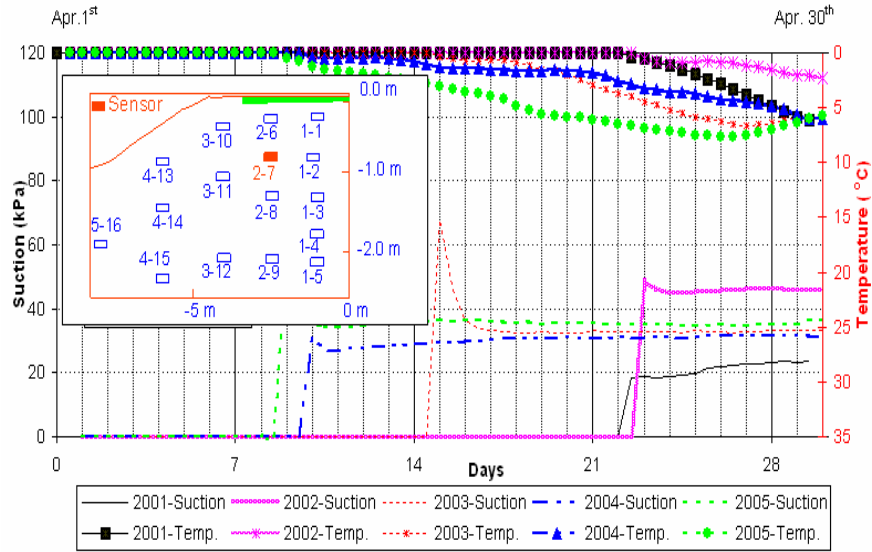


Figure 6.65 Response of suction at Sensor T2-7 at temperatures less than zero in April of 2001 to 2005 at the Torquay site.

6.7.2 Suction measurement with variation of ambient temperature

The correlations of matric suctions with the ambient temperatures at Sensor T1-1 are illustrated in Figures 6.66 and 6.67. The variations in suction appeared to be in phase with the ambient temperature. In general, suction decreased 3 kPa when temperature increased 2° C. However, this observed amplitude was not consistent from time to time. This relationship might require the improvement of the temperature correction method, since the thermal conductivity of the sensor changes depending on temperature.

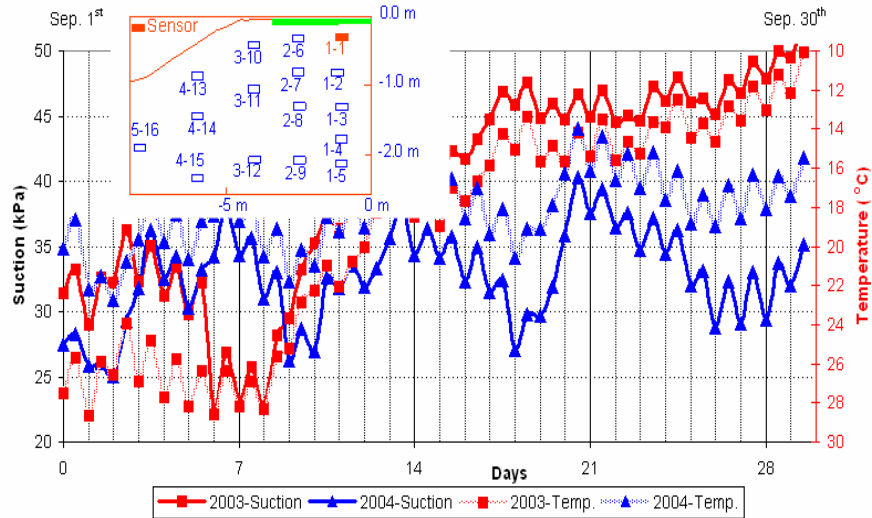


Figure 6.66 Suction and temperature versus time at Sensor T1-1 in September of 2002 to 2004 at the Torquay site

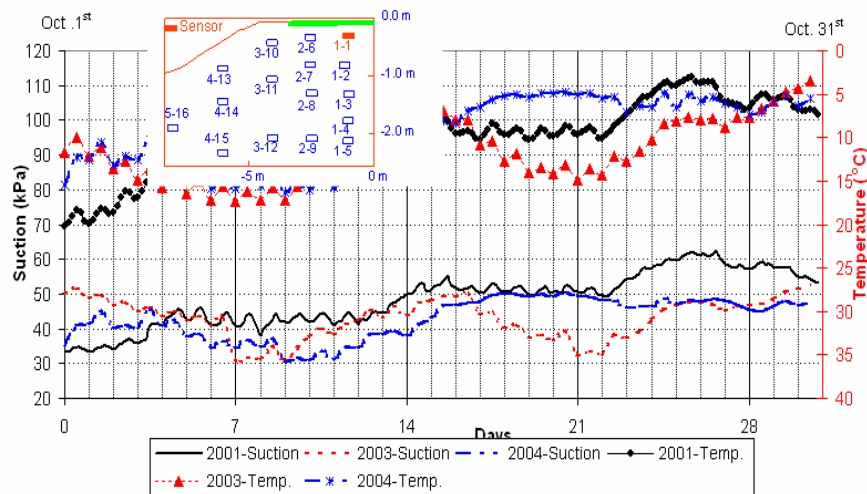


Figure 6.67 Suction and temperature versus time at Sensor T1-1 in October of 2001 to 2004 at the Torquay site

6.7.3 Suction and temperature change cycle

There appeared to be similar numbers of fluctuations between the suctions and air temperatures under the driving-lane in both Torquay and Bethune. The occurrence of these fluctuations also seemed to occur at similar amplitudes and times.

In Figure 6.68, suctions from two shallow sensors T1-1 and T1-2 at the Torquay site varied in the same phase and frequency as the air temperature. The same trend of suction and air temperature change is observed at the Bethune site for sensors B1-1 and B1-2 in Figure 6.69.

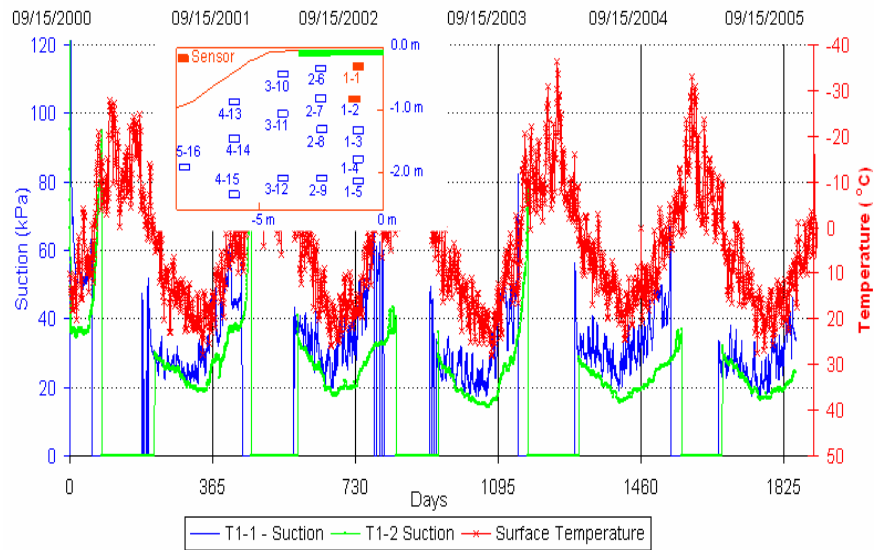


Figure 6.68 Suction and temperature cycles at sensors T1-1 and T1-2 at the Torquay site

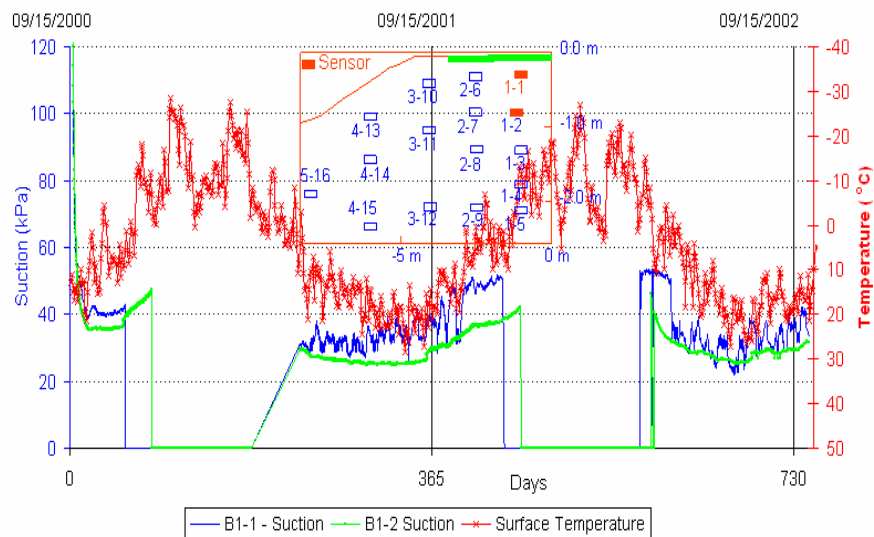


Figure 6.69 Suction and temperature cycles at sensors B1-1 and B1-2 at the Bethune site

The seasonal pattern of suction change is discernable in the data presented in this chapter. The sensor at a shallow depth under the side-slope showed the lowest

suctions in June. The suctions recorded at deeper depths and under the driving-lane took longer to peak compared to the sensors at shallower depths and under the side-slope. The highest suctions in highway subgrade during freezing periods might be extrapolated. Shorter-term patterns could not clearly be determined, especially from the depth of 0.8 m downwards. The interpretations as well as further relevant explanations for the mechanism of suction change are discussed in Chapter 7.

CHAPTER 7

INTERPRETATION OF MEASURED *IN SITU* MATRIC SUCTIONS

Chapter 7 provides an interpretation of the corrected matric suctions presented in Chapter 6. The presentations in Chapter 6 show that for a given climatic condition, relatively constant matric suctions can be maintained in the subgrade under a pavement. In the other regions of the subgrade, the matric suctions varied significantly with time and from location to location.

This chapter provides interpretation and discussion of the variations in matric suctions in highway subgrades with respect to the climatic conditions such as rainfall, regional evaporation conditions and soil type as well as the accuracy of the thermal conductivity sensors.

7.1 Interpretation of the matric suction patterns with respect to the climatic conditions

Variations in matric suctions depend on the net soil-atmosphere moisture flux. This flux is a function of some key components of the hydrologic cycle: namely, precipitation, evapotranspiration and run-off. However, in this research project, the interpretation of matric suctions with respect climatic data is limited to precipitation and regional evaporation conditions.

7.1.1 Matric suction interpretation on the vertical grid-lines

The matric suctions on three vertical grid-lines: namely, under the driving-lane, under the shoulder and under the side-slope are discussed in this section.

Matric suctions under the driving-lane

Matric suction changes in response to rainfall under the driving-lane are illustrated in Figures 7.1 and 7.2. The cyclic patterns of matric suction lagged behind the cyclic pattern of rainfall. These time lags became greater with depth. The time lags could be due to two sources. Firstly, this can be the result of the long distance required for water to travel from the side-slope and shoulder to the locations under the driving-lane. Secondly, the large time lag in 2003 might have been the deviations of rainfall between the weather station (i.e., Estevan) and the test site (i.e., Torquay).

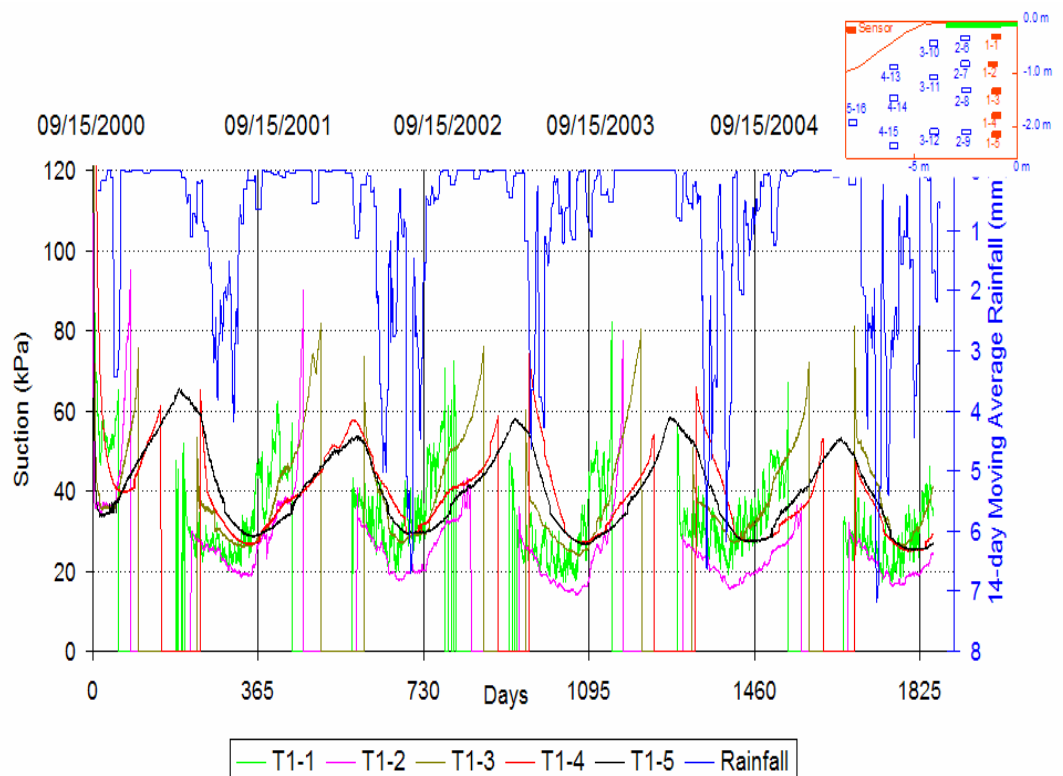


Figure 7.1 Variations in suction with rainfall and time along vertical grid-line under the driving-lane at the Torquay site

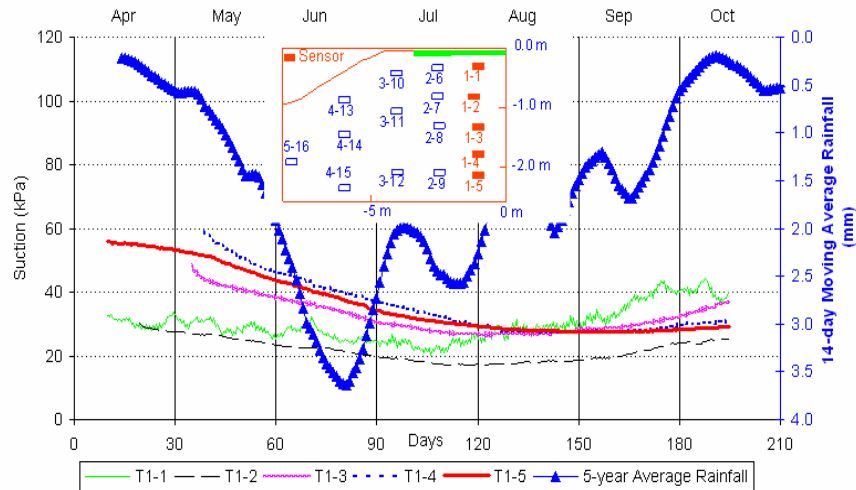


Figure 7.2 Average matric suctions over 5 years (2001 to 2005) and 5-year average rainfall versus time, under the driving-lane at the Torquay site

In Figure 7.2, the rainfall reached the maximum value on the 20th of June. Sensor T1-1 located at depth of 0.3 m gave the minimum matric suction on the 20th of July. Sensor T1-2 reached the minimum suction value on the 25th of July, Sensor T1-3 on the 1st of August, Sensor T1-4 on the 15th of August, and Sensor T1-5 on the 30th of August. The time lags under the driving-lane between rainfall and suctions varied from one month to more than two months.

From April to July, matric suctions in Sensors T1-1 and T1-2 were significantly lower than the deeper sensors. It is possible that the excess pore-water might have been trapped near Sensors T1-1 and T1-2 after thawing during “spring break-up”. The melting water might not be able to drain laterally as well as vertically since the snow covered the side-slope and shoulder and the underlying soil was still frozen. The precipitation that followed the “spring break-up” could have caused the lower suctions at Sensor T1-1 and T1-2 in June and July.

Conversely, Sensor T1-1 (Figure 7.2) recorded higher matric suctions from September to winter months because evapotranspiration probably exceeded the rainfall during that time.

The suction values at Sensor T1-1 in Figures 7.1 and 7.2 fluctuated the most amongst the sensors located in the same vertical grid-line. This trend might be attributable to the effect of rainfall, evapotranspiration and air temperature on the soil at shallower depths.

Matric suctions under the shoulder

The time lags between matric suctions and rainfall became greater with depth as can be seen in Figures 7.3 and 7.4, under the shoulder. The time lags under the shoulder between rainfall and matric suction were smaller than under the driving-lane. Reasonable agreement was observed between matric suction changes and rainfall changes as shown in Figure 7.4.

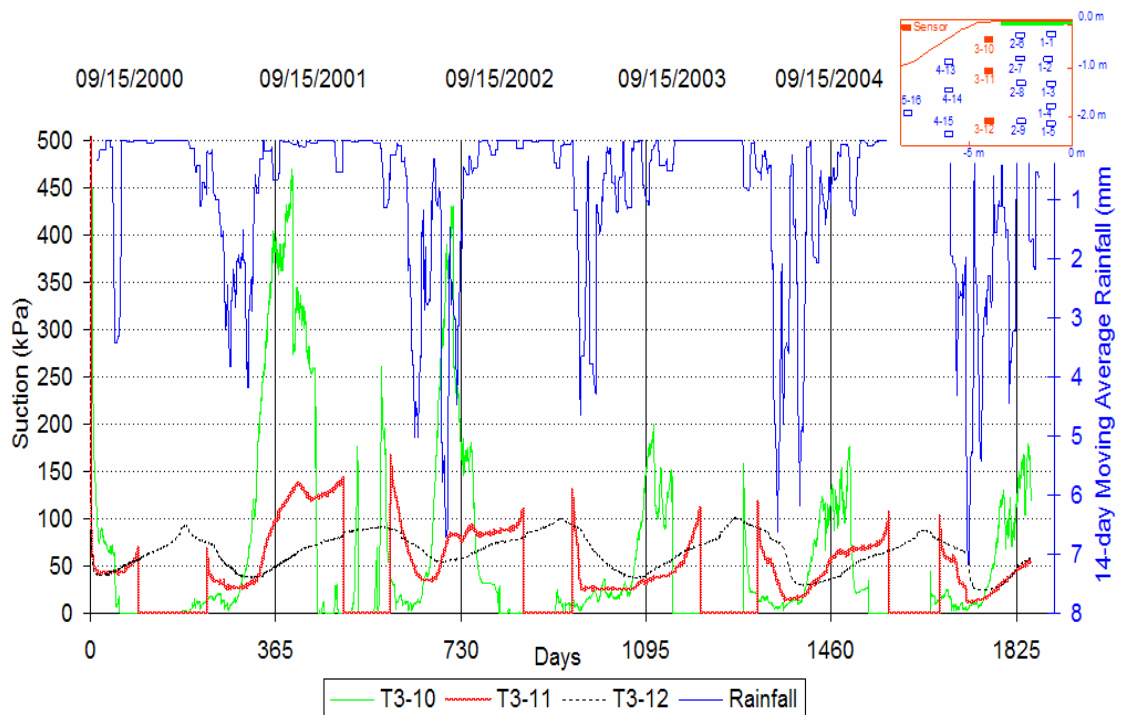


Figure 7.3 Variations in suction with rainfall and time along a vertical grid-line under the shoulder at the Torquay site

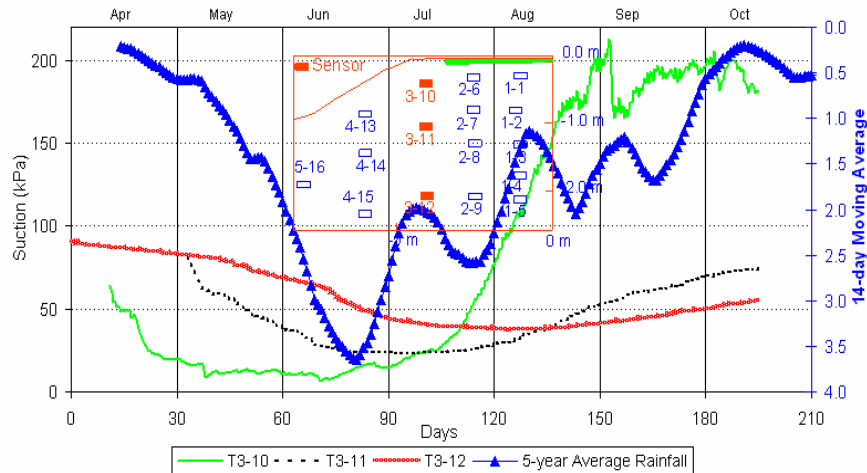


Figure 7.4 Average matric suctions over 5 years (2001-2005) and 5-year average rainfall versus time, under the shoulder at the Torquay site

From the end of July onwards, Figures 7.3 and 7.4 show that the matric suctions at a depth of 0.3 m were larger than the matric suctions at greater depths. These five-year average matric suctions reached as high as 200 kPa at the beginning of September. Evapotranspiration was possibly greater than the rainfall during that time, as this region is defined by a combination of large water deficit and relatively high temperatures (Lundquist, 2005). The matric suctions at Sensor T3-10 in 2001 and 2002 were from 400 to 500 kPa (Figure 7.3) during the fall months and approximately double the matric suctions in the same months in the following years. The evapotranspirations in 2001 and 2002 might have been higher than the other years.

Matric suctions under the side-slope

The correspondence between the rainfall and the matric suctions under the side-slope was interpretable as shown in Figures 7.5 and 7.6. In general, the lowest matric suctions and largest rainfall were recorded at the end of June. Matric suctions at Sensor T4-13 appeared to be the highest among the sensors installed in the highway subgrade. This could be explained by the high evapotranspiration on the side-slope area. On the other hand, these measured matric suctions could have been considered less accurate than measured matric suctions of less than 400 kPa. It should be noted that the sensors were calibrated to a maximum suction of 400 kPa.

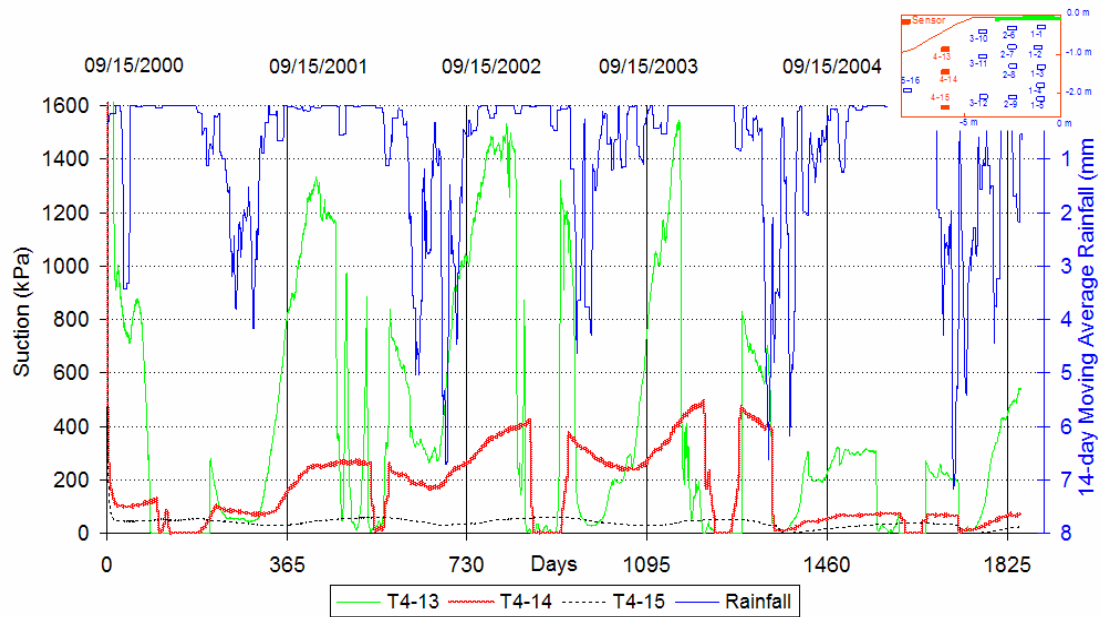


Figure 7.5 Variations in suction with rainfall and time along a vertical grid-line under the side-slope at the Torquay site

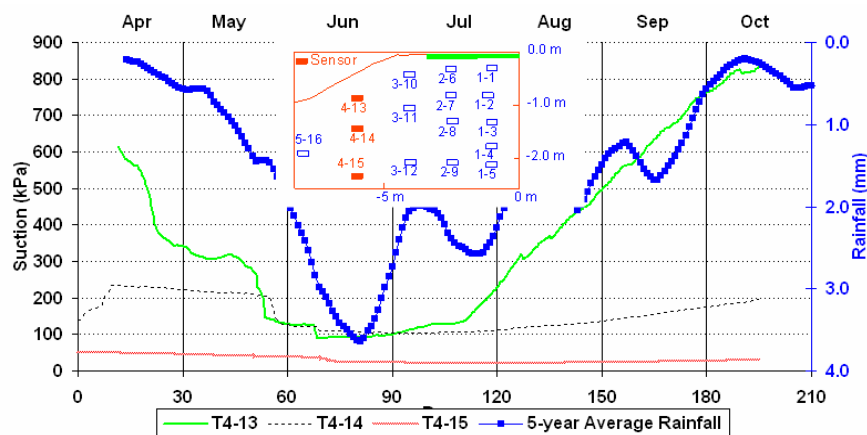


Figure 7.6 Average matric suctions over 5 years (2001-2005) and 5-year average rainfall versus time under the side-slope at the Torquay site

Figures 7.5 and 7.6 show lower soil suction values in 2004. This observation is discussed in the next section explaining low matric suctions on the side-slope in 2004.

7.1.2 Matric suction interpretation on the horizontal grid-lines

This section interprets the suction changes with respect to the distance from the highway centerline.

Matric suctions along the sensors nearest to the road surface

At the Torquay site (a semi-arid area), the matric suctions at shallow depths were expected to be higher at the uncovered area than the covered area during the dry season from September to April. During the dry season, the matric suctions increased from the center-line to the side-slope. In addition, the variations of suction were expected to be greater under the side-slope than under the shoulder. During the rainy season (i.e. from May to August), the matric suctions under the side-slope might possibly be higher than at the shoulder due to the greater amount of precipitation run-off. These trends in suction change are noticeable in Figures 7.7 and 7.8. As well, the seasonal pattern in suction change can be seen on the horizontal grid-line along the sensors nearest to the road section in Section 6.4.1, Chapter 6. However, some exceptions were witnessed. In Figure 7.9, during the summer season (i.e. from June to August), matric suctions from Sensor T2-6 appeared to be more stable than from Sensors T1-1 and T3-10. In Figure 7.10, matric suctions from Sensor B3-10 fluctuated less than from other sensors at the same depth below the ground surface. These exceptions could probably be due to the different coefficients of permeability in the surrounding soils, or different permeabilities of these sensor ceramics. The thermal conductivity sensors might show irregular trends in the short-term; however, these sensors gave the seasonal pattern of suction changes as shown in Figure 7.7.

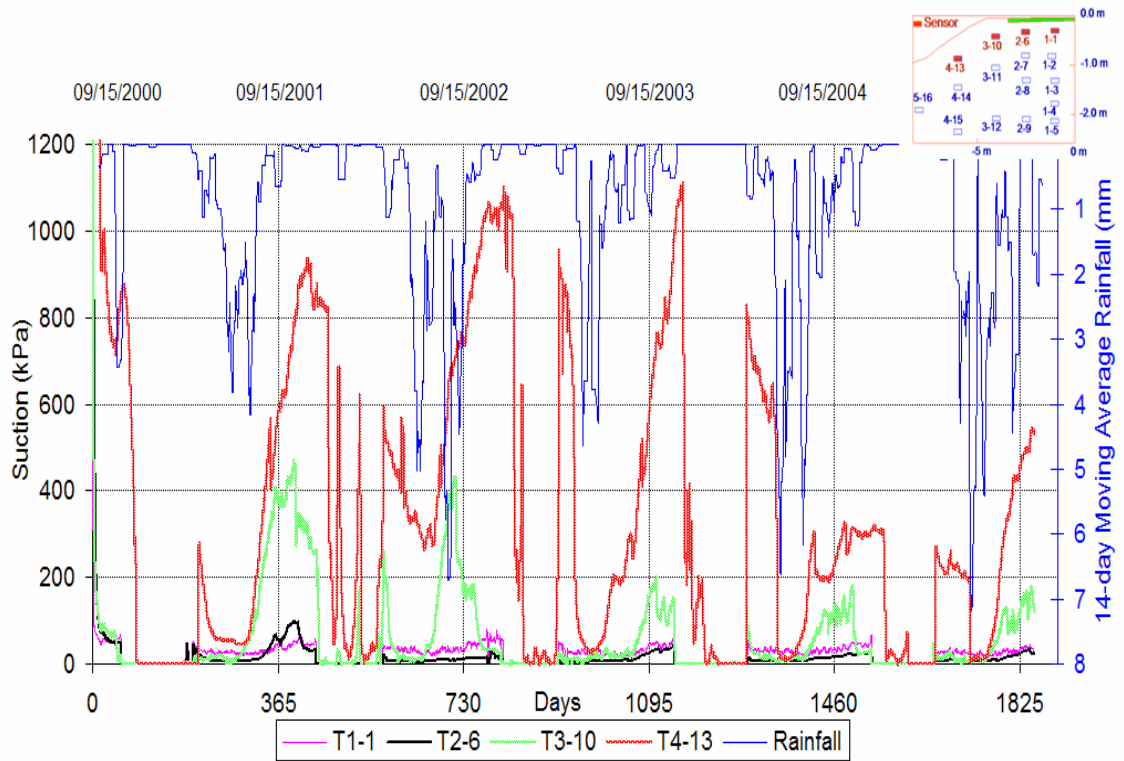


Figure 7.7 Variations in suction with rainfall and time along horizontal top sensors at the Torquay site

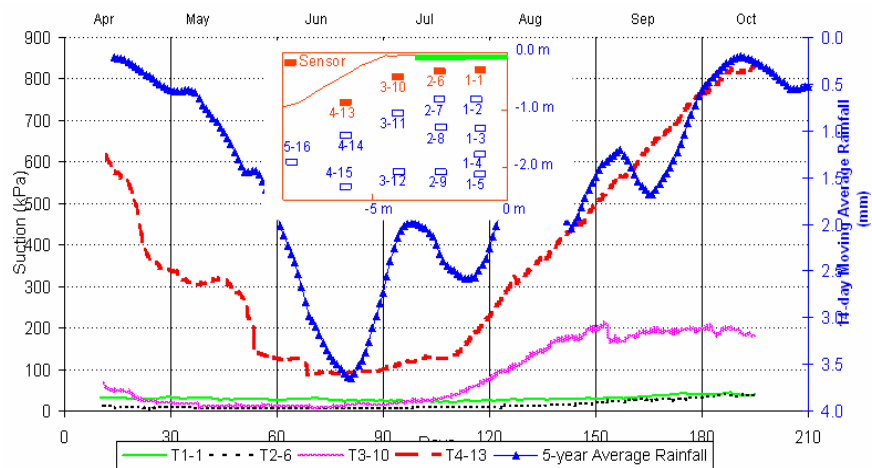


Figure 7.8 Average matric suctions over 5 years (2001-2005) and 5-year average rainfall versus time, along horizontal top sensors at the Torquay site

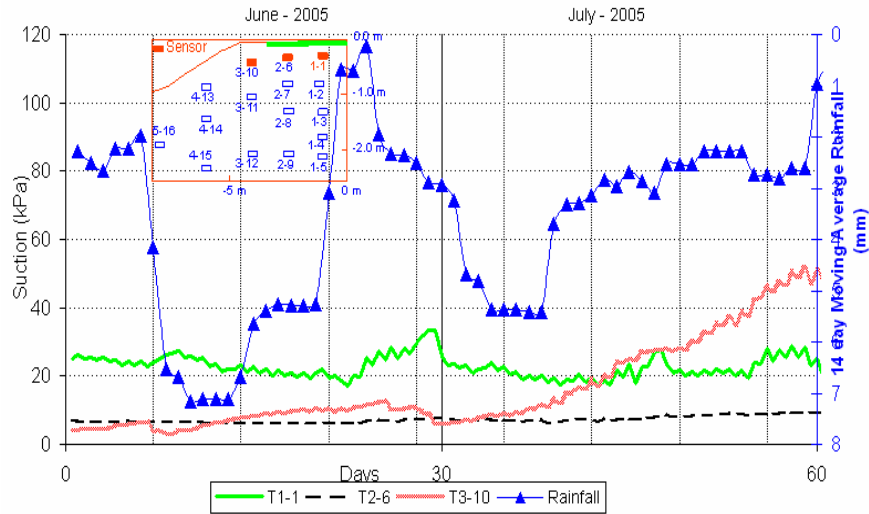


Figure 7.9 Variations in suction with rainfall and time in June and July 2005, along horizontal top sensors at the Torquay site

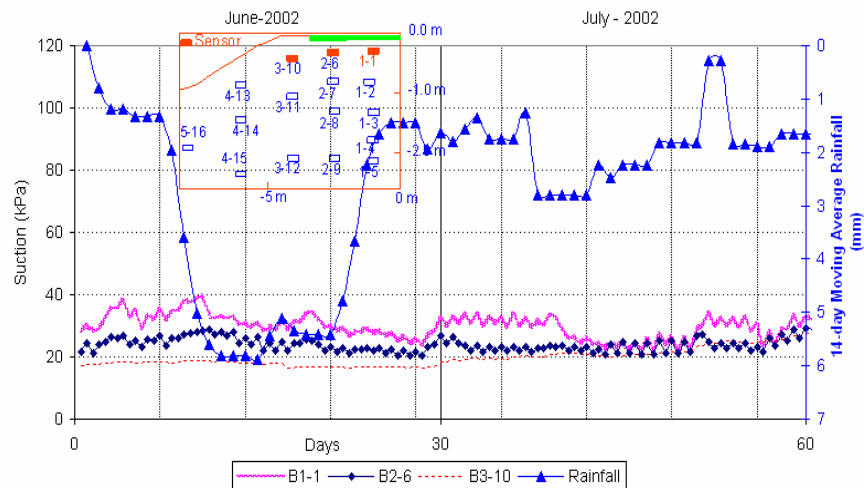


Figure 7.10 Matric suctions versus time and rainfall in June and July 2002, along horizontal top sensors at the Bethune site

Matric suctions along middle-depth sensors

Matric suctions under the side-slope were significantly higher for middle-depth sensors than those under the driving-lane and under the shoulder due to the higher evapotranspiration on the side-slope as seen in Figure 7.11. The sudden drop of matric suction at Sensor T4-14 under the side-slope in 2004 is discussed in the next section of

this thesis. Figures 7.11 and 7.12 show that matric suctions along these middle-depth sensors changed in accordance with rainfall. The matric suctions decreased when rainfall increased. The matric suctions under the pavement decreased to the lowest suctions later than uncovered soils due to the longer path for moisture flow. The agreement between rainfall and matric suctions was also noticeable at the Bethune site as illustrated in Figure 7.13.

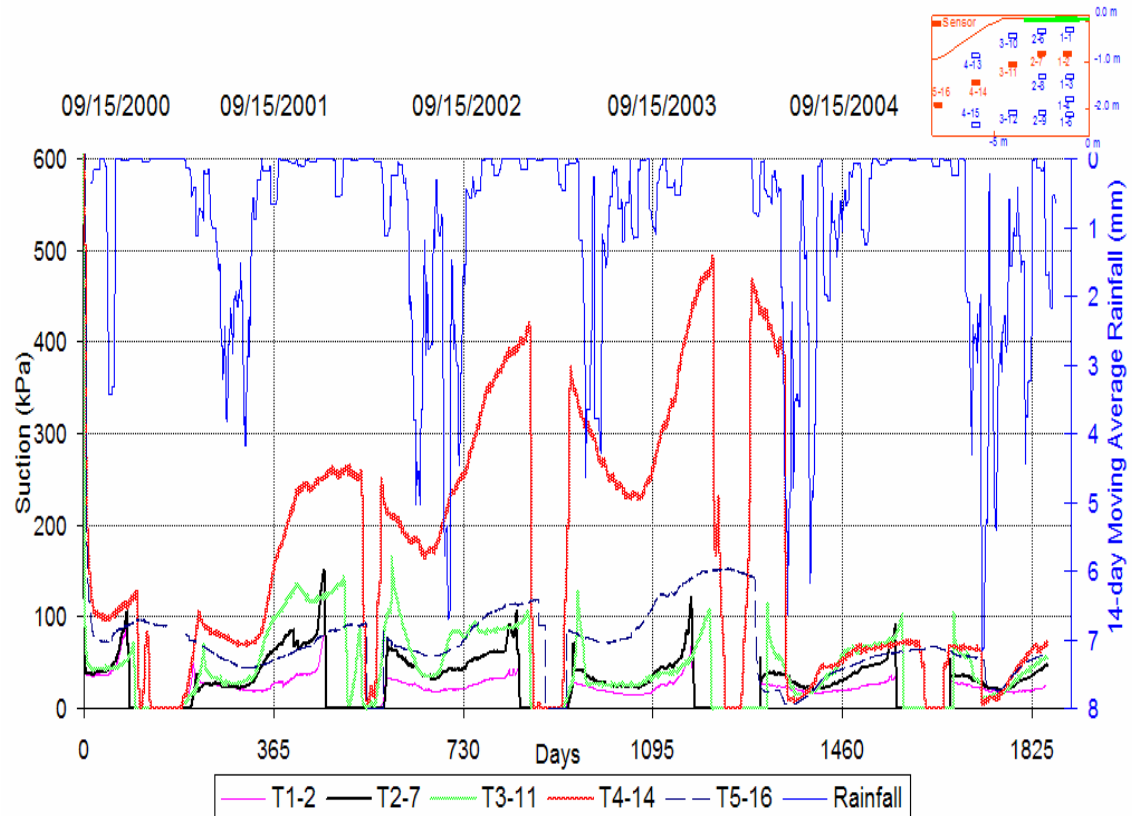


Figure 7.11 Variations in suction with rainfall and time along horizontal middle-depth sensors at the Torquay site

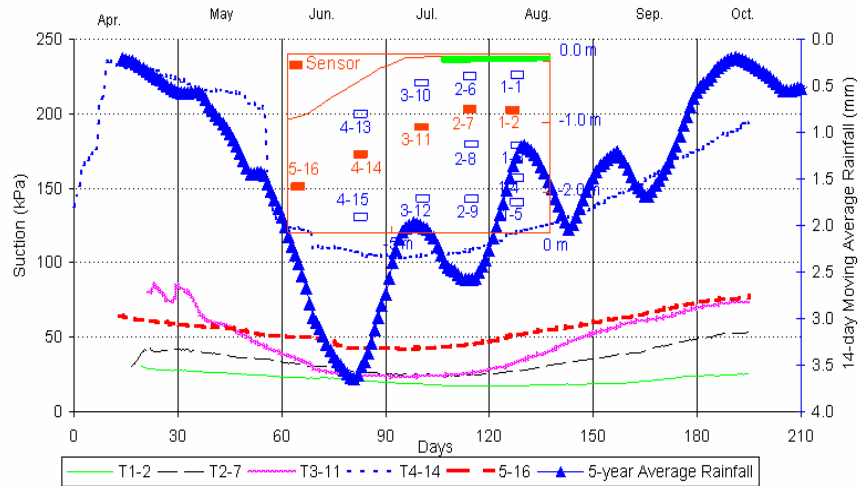


Figure 7.12 Average matric suctions over 5 years (2001-2005) and 5-year average rainfall versus time along horizontal middle-depth sensors at the Torquay site

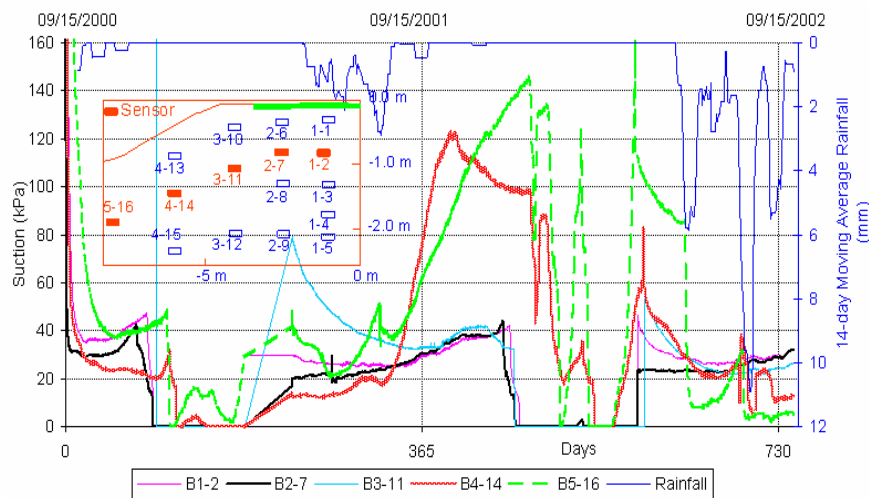


Figure 7.13 Variations in suction with rainfall and time along horizontal middle-depth sensors at the Bethune site

From this depth downwards (i.e., 0.8 to 1.0 m), the influence of rainfall on matric suctions in soils under pavement was less than in uncovered soils as can be seen at sensors B1-2 and B2-7 in Figure 7.13.

Matric suctions along bottom sensors

Figures from 7.14 to 7.16 show that the matric suctions at the bottom sensors (i.e., at depths of 1.9 to 2.2 m) changed with the same cycle, frequency and amplitude each year. The differences in suction between soils under pavement and uncovered soils were negligible. The highest matric suctions at the Torquay site were attained in March before precipitation (Figures 7.14 and 7.16). The same trend could be realized at the Bethune site in Figure 7.15. Figures 7.14 to 7.16 provide the interpretable correlation between the rainfall average and the matric suctions. The matric suctions decreased with rainfall although there were time lags between the rainfall and the matric suctions. The maximum rainfall occurred in the middle of June. The matric suctions decreased to the lowest in August.

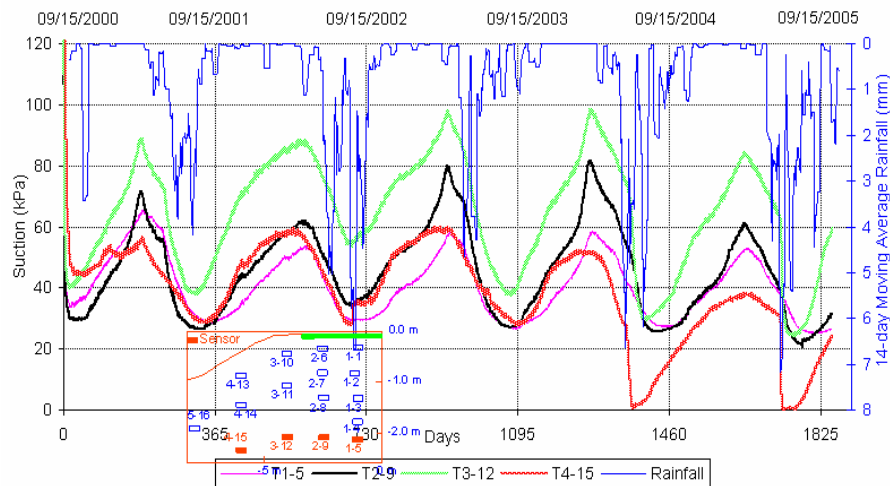


Figure 7.14 Variations in suction with rainfall and time along horizontal bottom sensors at the Torquay site

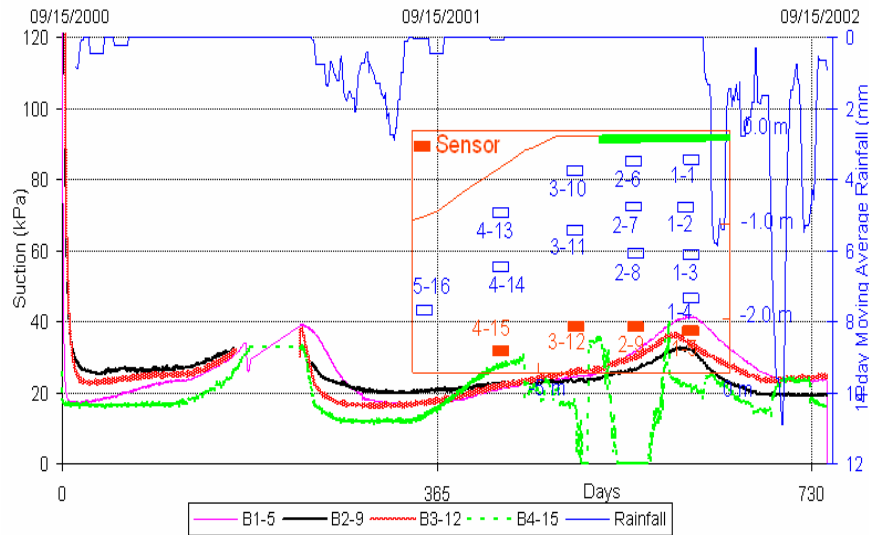


Figure 7.15 Variations in suction with rainfall and time along horizontal bottom sensors at the Bethune site

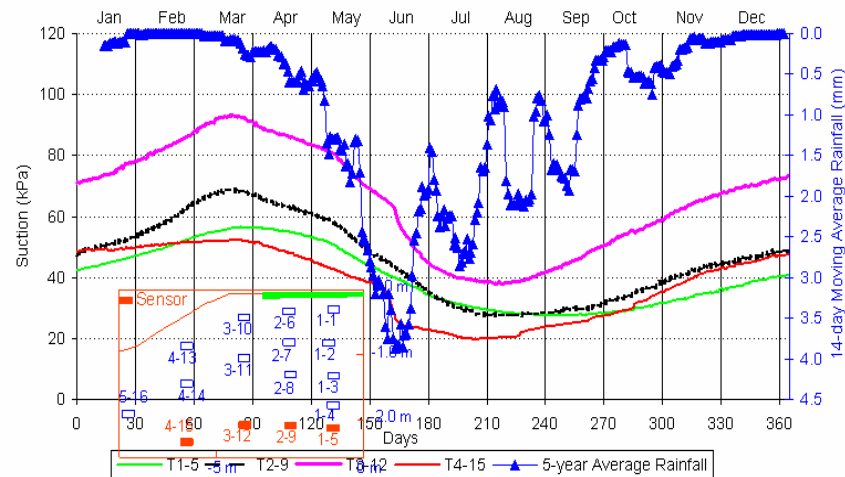


Figure 7.16 Average matrix suctions over 5 years (2001-2005) and 5-year average rainfall versus time, along horizontal bottom-depth sensors at the Torquay site

Matric suctions at Sensor T4-15, under the side-slope, reduced sharply in 2004. This decrease in suction is discussed in the next section of the thesis. The higher matric suctions from Sensor T3-12, which is about 20 kPa higher than the other sensors on the same section, might have been due to minor errors during the laboratory calibration.

7.1.3 Matric suction interpretation on contour maps

The contour maps show that the side-slope encountered the most variable matrix suctions as illustrated in Figure 7.17 and as presented in Chapter 6. The area under pavement was less vulnerable to microclimatic conditions, thus it experienced more stable matrix suctions.

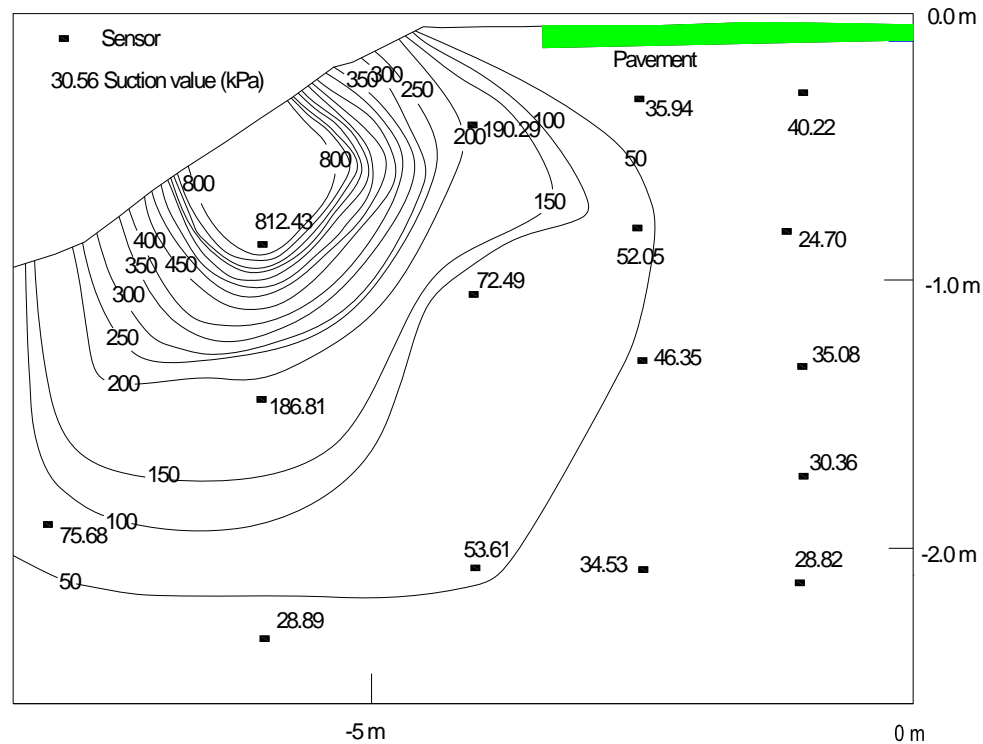


Figure 7.17 Contour map of five-year average matric suction in October at the Torquay site

As discussed in the previous sections, Torquay and Bethune are in semi-arid areas and the matric suctions reached the highest values during the dry season from September to April at uncovered areas. Therefore, the great differences in matric suction could be realized from location to location under the side-slope during the dry season (Figure 7.17). The difference from location to location in highway subgrade reduced during rainy season from May to August due to the decreases in matric suction under the side-slope and under the shoulder.

7.1.4 Possible explanations for low matric suctions under the side-slope at the Torquay site in 2004

At the Torquay site, in 2004 low matric suctions were recorded under the side-slope, which were only 30 to 40% of the matric suctions recorded in the previous years (Figure 7.18). Figures 7.19 and 7.20 present matric suctions at sensors T4-13 and T4-14 from May to September, 2004. The appearance of a good correlation between the matric suction and rainfall can be seen in Figures 7.19 and 7.20. Therefore, the lower matric suctions in 2004 could be due to the higher amount of rainfall.

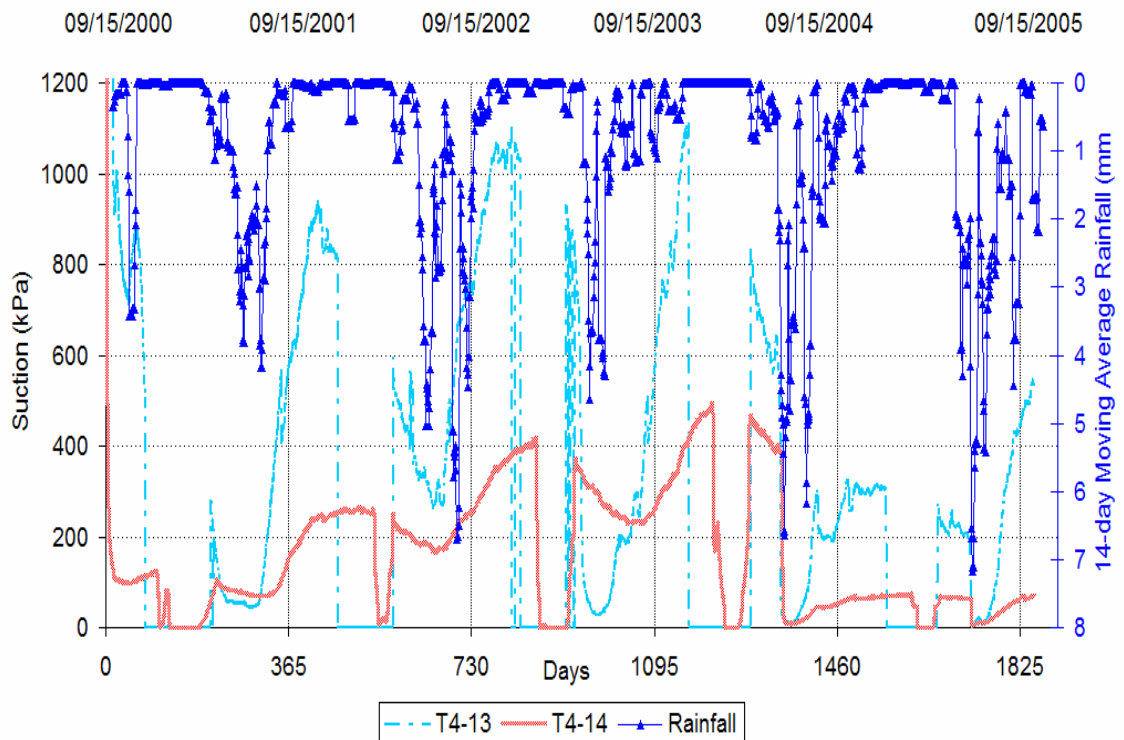


Figure 7.18 Variations in suction with rainfall and time under the side-slope at the Torquay site

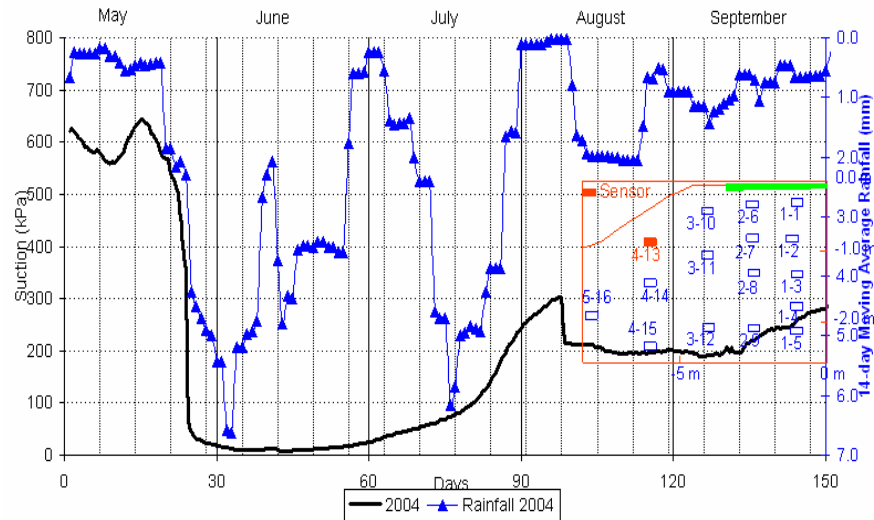


Figure 7.19 Variations in suction with rainfall and time at Sensor T4-13, from May to September at the Torquay site

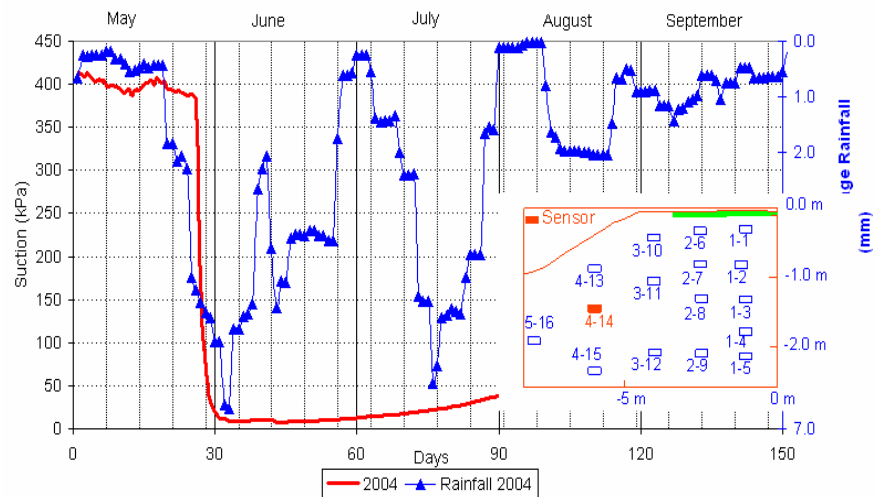


Figure 7.20 Variations in suction with rainfall and time at Sensor T4-14, from May to September at the Torquay site

The low matric suctions (i.e., close to zero) occurred for more than 40 days as observed in Figures 7.19 and 7.20. This might have reduced of air-trapped in the sensors by the replacement of water over a long period. As a result, the matric suctions might have moved out of the main hysteresis loop of calibration to a position between the initial drying curve and the main drying curve. Therefore, for the same voltage output,

the suction calculations from the main loop and scanning curves might have given lower matric suctions than calculated from outside the main loop.

The decreases of matric suction in 2004 were also recorded under the shoulder. However, these decreases were not as pronounced as under the side-slope. Probably, the side-slope was also exposed to precipitation run-off from the shoulder in addition to rainfall.

Similar variations of matric suction from year to year were also recorded under the side-slope at the Bethune site (Figure 7.21). Therefore, the matric suctions on the side-slope could be vulnerable to microclimatic changes.

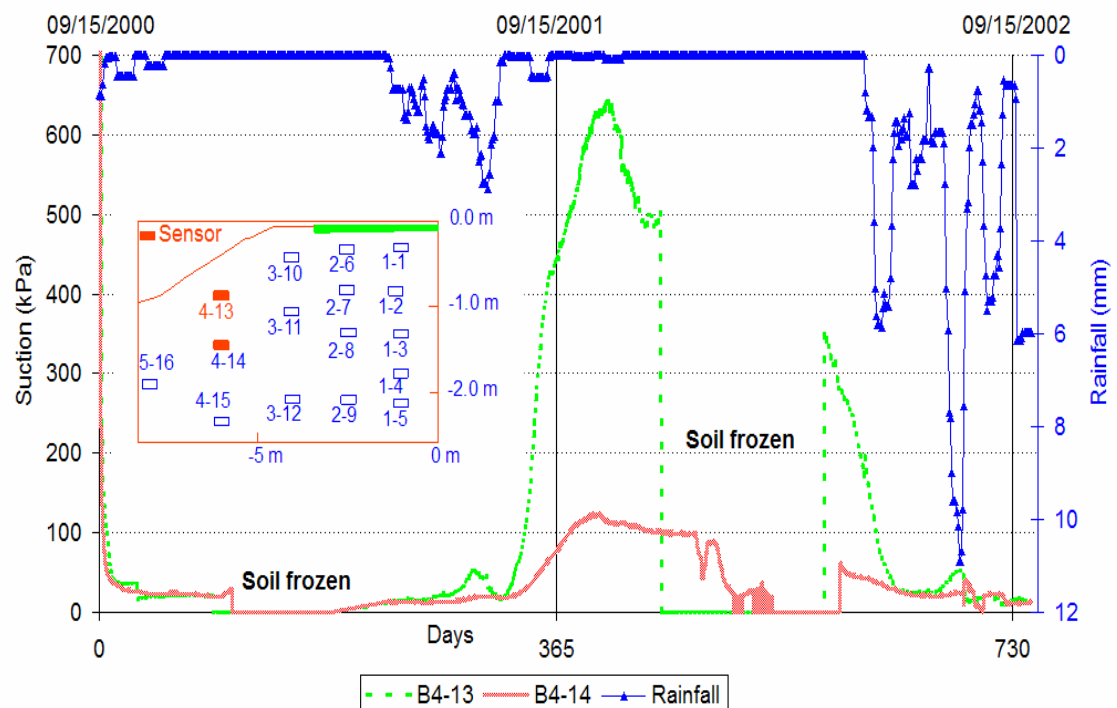


Figure 7.21 Variations in suction with rainfall and time under side slope at the Bethune site

7.1.5 Effects of thawing on the drop of matric suction during “spring break-up”

The matric suctions generally decreased when the temperature increased from under zero degrees Celsius to above zero degrees Celsius. The water produced from phase change increased pore-water pressure while the underlying and laterally adjacent

soils were still frozen. As a result, this water was prevented from draining and caused a large drop in matric suction. These drops in matric suction are evident at Sensor T2-7 at the Torquay site (Figure 7.22). The matric suctions reduced by 20 to 40 kPa within 36 to 48 hours after the temperatures rose over zero degrees Celsius. However, at greater depths and close to the side-slope, with more favorable conditions for drainages, this trend was not observed.

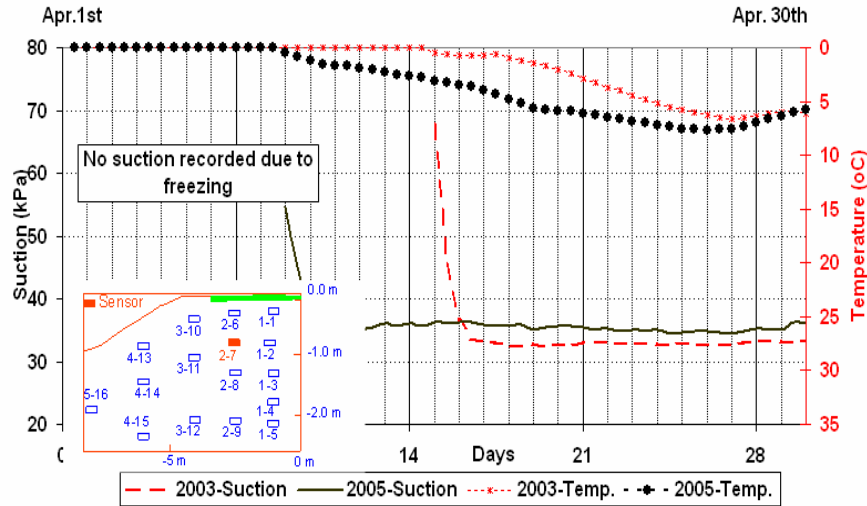


Figure 7.22 Effects of thawing on matric suction measurement during “spring break-up” at Sensor T2-7 (0.8 m deep) under the driving-lane at the Torquay site

7.2 *In situ* matric suctions in conjunction with SWCC and water content

This section compares the matric suctions measured from the sensors and the matric suctions estimated from the soil-water characteristic curves obtained from the laboratory tests (Section 5.1). The distance between the boreholes and the sensors is approximately 3.0 m.

The drying curve was obtained in the laboratory and the main wetting curve was estimated by moving the main drying curve 0.2 to 0.5 log cycles to the left (Fredlund, 2005) as shown in Figure 7.23. The matric suctions were estimated using the soil-water characteristic curve and the water contents obtained from the field investigation to the interval between the wetting curve and drying curve. The matric suctions from the

thermal conductivity sensors at the time of the field investigation are shown in Figure 7.24. The comparison results are tabulated in Table 7.1.

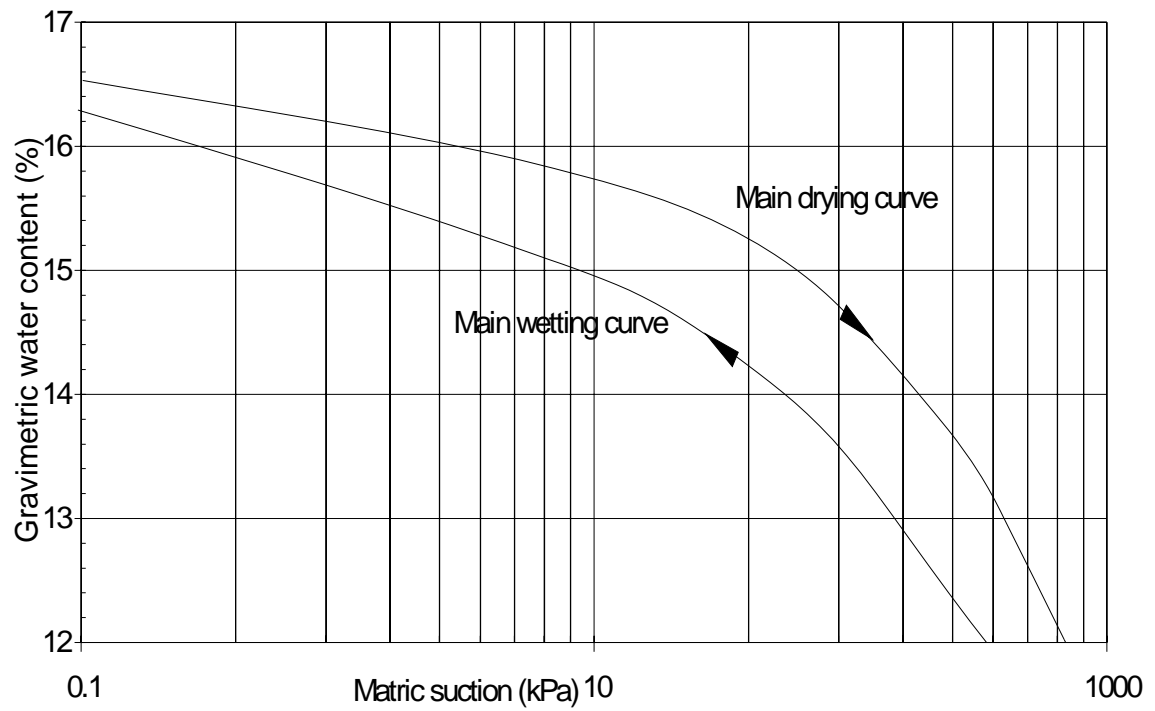


Figure 7.23 Soil-water characteristic curve for soil at depths of 0.10 to 0.25 m at the Torquay site

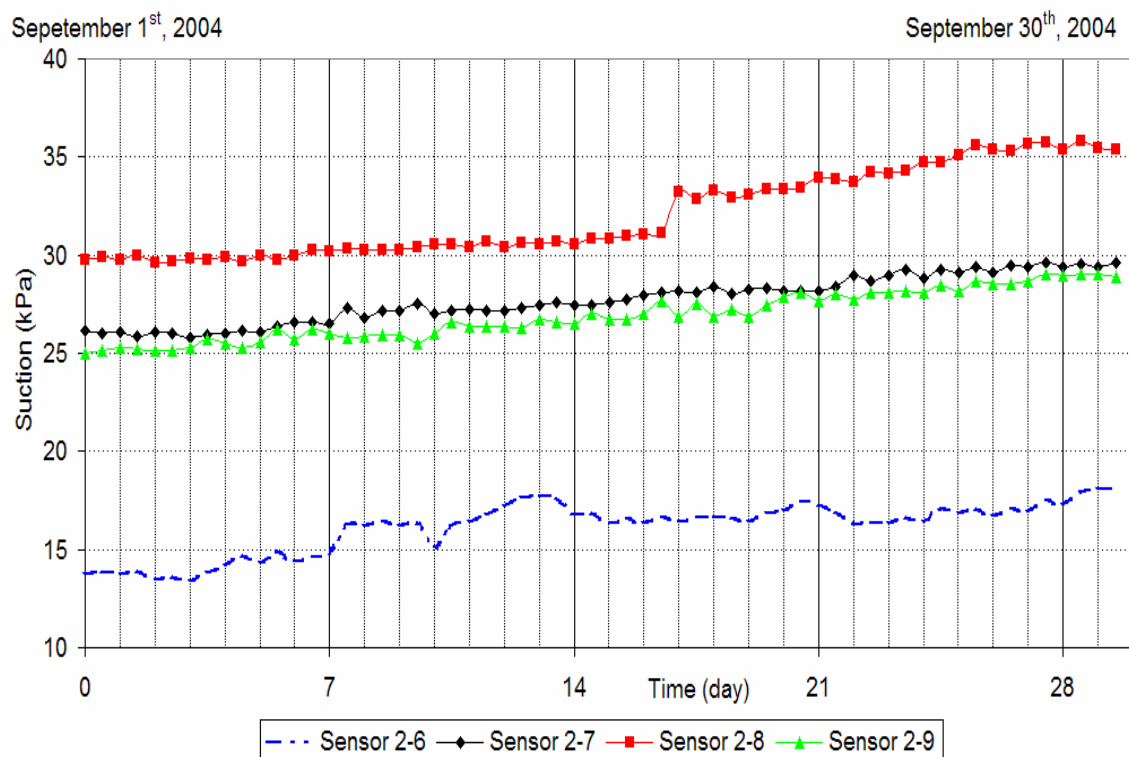


Figure 7.24 Matric suctions at the sensors closest to the borehole at the Torquay site in September 2004

Table 7.1 Comparison between sensors suctions and estimated matric suctions from SWCC

Depth from surface (m)	Gravimetric Water content (%)	Matric suction (kPa) Estimated from SWCC	Matric suction (kPa) from the sensors
0.1-0.3	14.60	10 to 30	17
0.70-0.85	14.56	20 to 45	28
1.30-1.75	17.21	25 to 50	31
1.75-2.2	17.36	17 to 40	27

The matric suctions obtained from the sensors show similar values to those estimated matric suction from the soil-water characteristic curves obtained in the laboratory.

7.3 Noise levels of the thermal conductivity sensors

Sensor T1-5 is located at a depth of 2.2 m under driving lane. Figure 7.25 shows the suctions varied by 0.2 to 0.5 kPa around the average. There were three sensors with the suction variations around the average of more than 1 kPa. These are sensors T1-1, B1-1 and B2-7. These sensors are at a depth 0.3 m under the driving-lane. The matric suctions from Sensor T1-1 is illustrated in Figure 7.26. In order to remove the fluctuation caused by rainfall, (which could mask the fluctuation of readings caused by ambient temperatures), the matric suctions from Sensor T1-1 were plotted for November, 2001. The daily fluctuations in matric suctions around the average appeared to be in phase with temperature and the amplitude was anti-correlated.

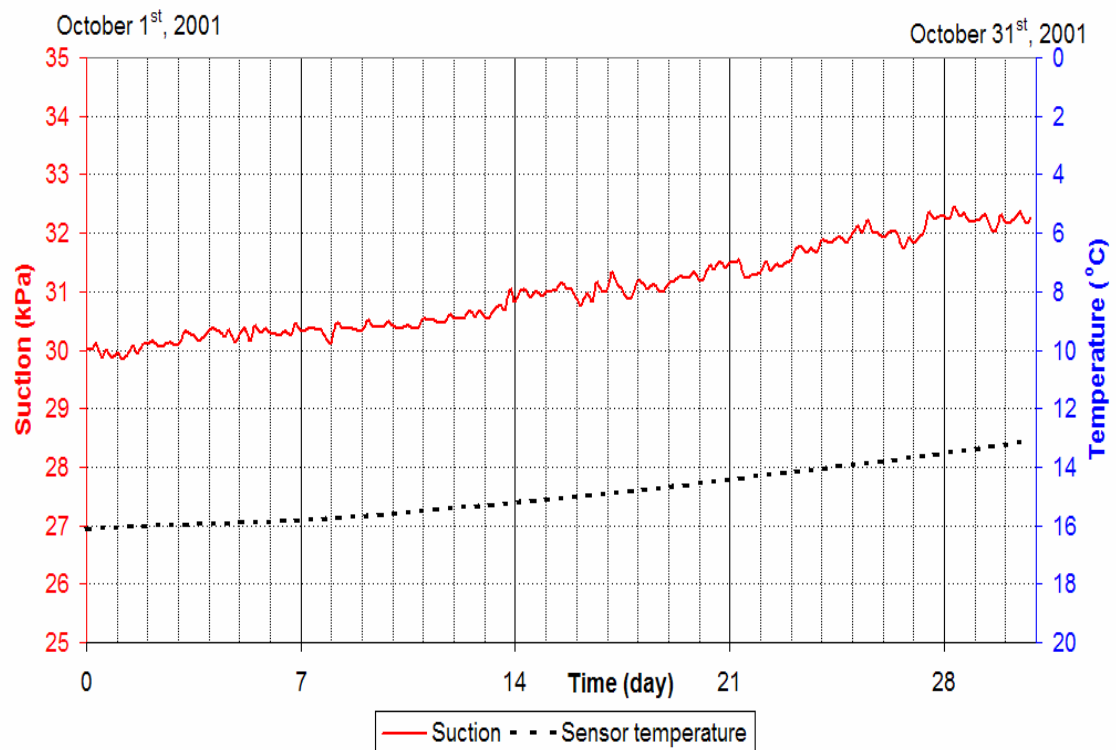


Figure 7.25 Matric suction versus temperature in October 2001 at Sensor T1-5

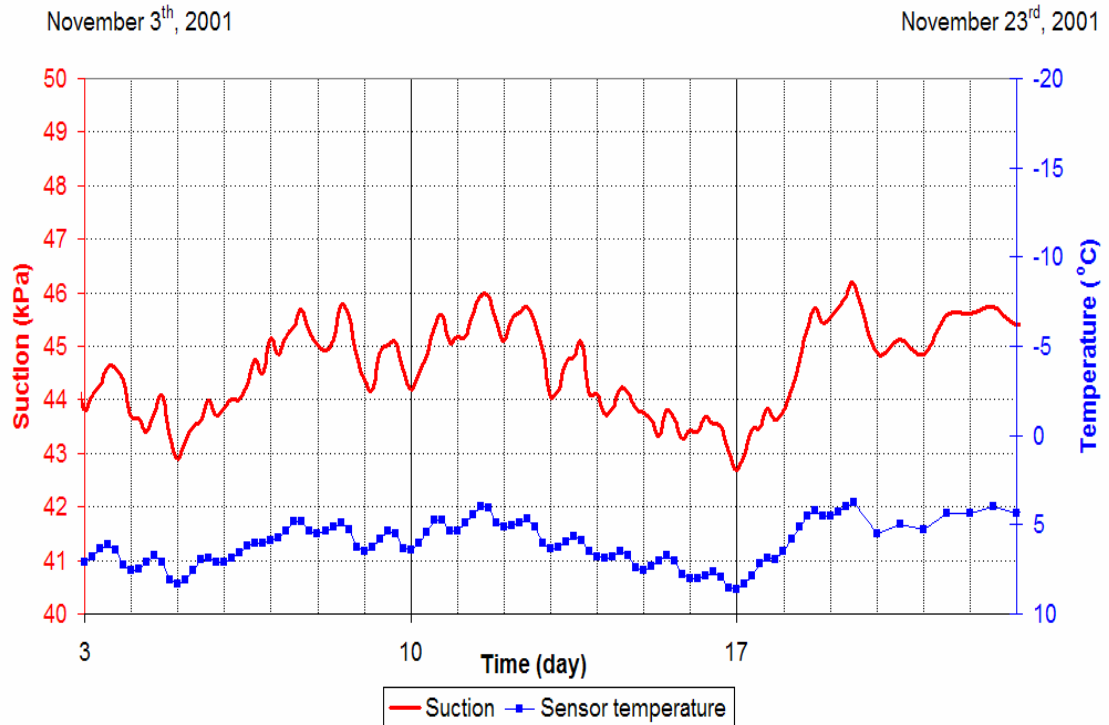


Figure 7.26 Matric suctions versus temperature in November 2001 at Sensor T1-1

The noise level as observed in Figure 7.26 was approximately 1 kPa. This noise level could be attributed to the sensitivity of the measurement to ambient temperature and length of the sensor cable since the constant current was controlled using analog signals. Therefore, the elimination of the ambient temperature dependency and reduction of the cable resistance effect should be investigated in future research. In addition, the method of temperature correction should be improved.

7.4 Response time of the thermal conductivity sensors with rainfall

The equilibrium between a soil suction and a rainfall event is assumed to have been reached when the lowest suction following a rainfall event was exceeded. As presented in Chapter 6, the time for top sensors under the side-slope and shoulder to reach equilibrium in matric suction with a rainfall event of more than 10 mm was estimated as 12 to 24 hours. For rainfall events of less than 10 mm, the relationship could not be determined. The response time in suction at a depth of 1.1 m under the side-slope is roughly estimated from 3 days to 5 days as shown in Figure 7.27. The

correlation between a rainfall event with suctions from deeper sensors or sensors under the pavement could not be directly observed on a plot of matric suction and rainfall versus time. However, in a long-term measurement the sensors at the lowest depths (i.e., from 1.9 to 2.2 m) decreased to the lowest matric suctions within approximately 60 days from the peak of rainfall as illustrated in Figure 7.16.

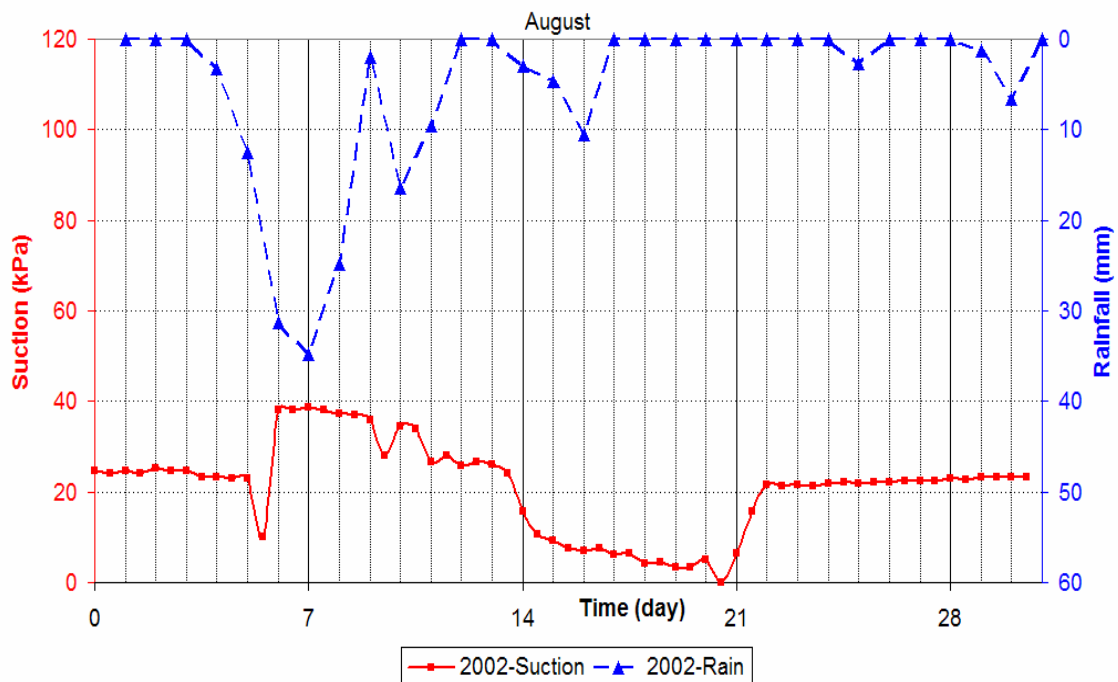


Figure 7.27 Correlation between a rainfall event and matric suctions at Sensor B4-14, at depth of 1.1 m under the side-slope

7.5 Malfunction and possible erratic readings and of the sensors

Sensor B1-4 transmitted data correctly for the first two days, but subsequently exhibited erratic results and no signals were obtained from this sensor after May 6, 2001. The malfunction of Sensor B1-4 could be due to seepage of water into the core that contains electronic devices such as the IC sensor and the heating element. Sensor B3-12 also provided erratic readings from January 1, 2002 as shown in Figure 7.28. The temperatures from this sensor appeared to be irregular as well. The reason could possibly be the effect of low temperature on the relay of the data acquisition system.

Aside from the non-recoverable malfunctions, some minor erratic readings were also witnessed with other sensors, but these sensors recovered shortly and now work properly. The data from the recovered sensors are presented in Figure 7.29. The reason for these erratic readings and subsequent recoveries cannot be explained.

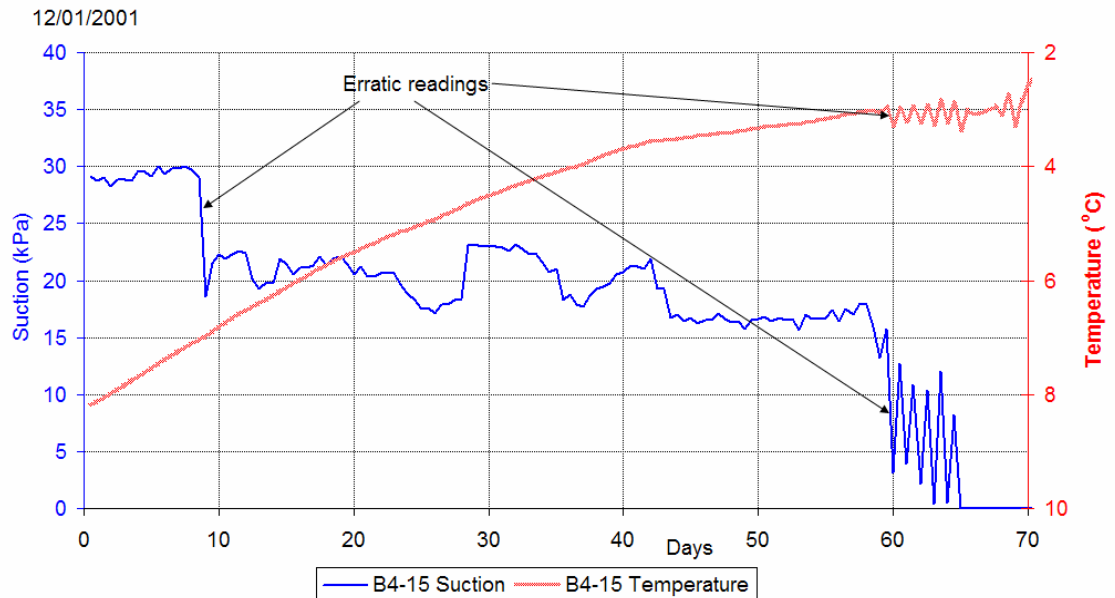


Figure 7.28 Non-recoverable erratic readings of Sensor B3-12 from January 1, 2002

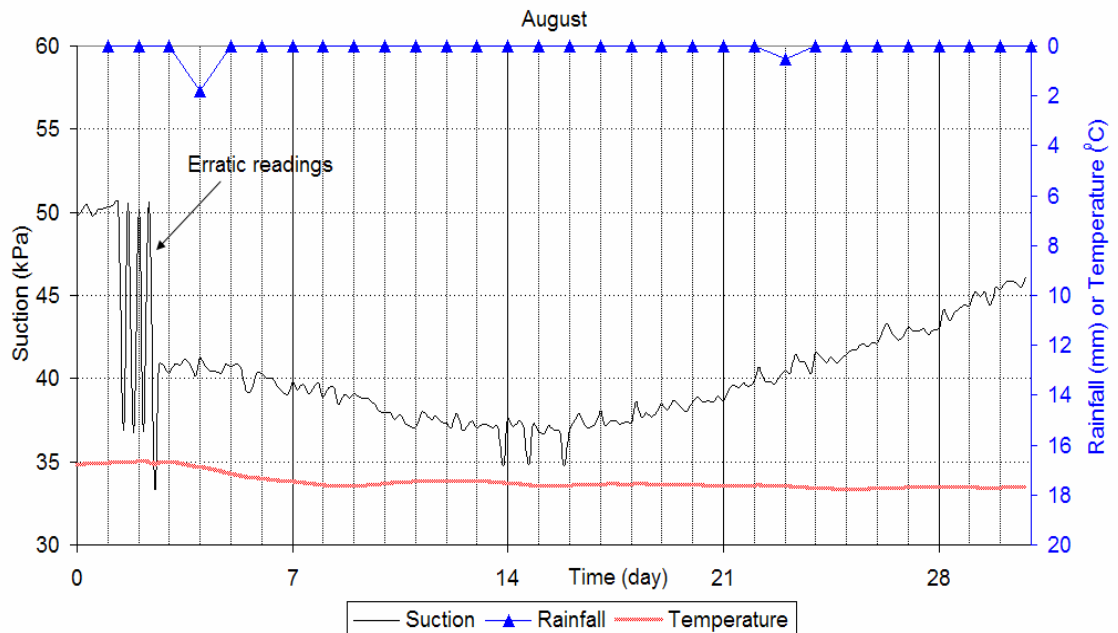


Figure 7.29 Recoverable readings at Sensor B5-16 from August 2, 2001

7.6 General discussion of the field suction measurements at the Bethune and Torquay sites

The matric suctions under the driving lane for both the sites varied from 20 to 60 kPa. This shows matric suctions in the subgrade under the pavement stay within a narrow band.

During the dry season, relatively high matric suctions under the side-slope and under the shoulder were generally observed at the test sites from September to April. At a depth of 0.3 m, matric suctions could reach up to 1500 kPa at the Torquay site and 600 kPa at the Bethune site. The lower matric suctions under the driving-lane at both the sites showed that less evapotranspiration occurred in this area. The only way for water to enter or exit is from cracks and the unpaved surfaces.

The test sites are both in the same regional climate. Therefore, despite different amplitudes, the matric suction variations with time at both the sites appeared to be in phase. At depths of 0.3 to 0.5 m, the lowest matric suctions were usually recorded in mid-July. At depths from 1.9 to 2.2 m, the matric suctions were lowest in August and highest in March.

The greatest changes in matric suction in the highway subgrades occurred at the times of thawing, freezing and significant rainfall events. Although, the bottom sensors at depths of 1.9 to 2.2 m might not experience freezing and thawing, the matric suctions at these sensors with respect to time changed in phase with these events. This is interpreted to have occurred because the soils at these depths are influenced by the water content changes in the near-surface soils.

The magnitudes of the soil suctions were different at the two test sites but the results show that similar mechanisms are controlling matric suction change.

CHAPTER 8

CONCLUSIONS AND RECOMMENDATIONS FOR FUTURE RESEARCH

The following conclusions and recommendations can be drawn from the results of this study.

8.1 Conclusions

- 1 Soil suctions obtained from the thermal conductivity sensors at the Bethune and Torquay sites changed in response to changes in precipitation and temperature. The thermal conductivity sensor proved its ability to provide matric suctions over five years.
- 2 Good agreement in temperature measurements was observed between the thermal conductivity sensors and the thermistors.
- 3 The difference between matric suction values without temperature correction and matric suction values with temperature correction varied from 10% under the driving-lane to more than ten times under the side-slope.
- 4 The correction for hysteresis in the matric suction measurements varied from 5% at shallower depths to 30% at greater depths. The hysteresis correction at shallow depths is less effective than at greater depths due to the noise level of the thermal conductivity sensor and microclimatic changes.

- 5 The soils at the Bethune and Torquay sites mainly consist of a hard glacial till, interbedded with some small sand lenses. Some rocks from 5 to 10 cm in diameter are encountered throughout the depth of the subgrade.
- 6 At the Bethune and Torquay sites, the suction changes appeared to be mainly due to changes in microclimatic conditions and to a lesser extend due to the soil type. Since the ground-water tables were deep and stable, the only way for water to enter and exit the subgrade was from cracks in the asphalt pavement and/or from the unpaved surface. Relatively constant equilibrium suctions were encountered under the driving-lane. Under the side-slope, the matric suctions were found to vary considerably with time and location. The soil suction measurements showed a strong seasonal pattern. More specifically, suctions showed a correlation to rainfall. At depths from 0.3 to 0.5 m, the lowest suctions were recorded in mid-July and highest suctions occurred during the winter (i.e., from January to March). The suctions were lowest in August and highest in March at depths from 1.9 to 2.2 m below the ground surface.
- 7 Under the driving-lane, the matric suctions ranged from 20 to 60 kPa. At the side-slope the matric suctions varied from 100 kPa in July to 1500 kPa in September. The evapotranspiration is likely to be higher than rainfall during the dry season (i.e., from September to April). However, for the depths below 2.0 m, the short-term effects of microclimatic condition were dampened. In addition, at these depths the differences in matric suctions under the driving-lane and under the side-slope were indiscernible.
- 8 Contour maps of matric suctions at the two test sites showed that April witnessed a great change of matric suctions from location to location each year. The suctions became less variable until June before these figures varied dramatically again from July to October. These trends showed the effect of thawing during “spring break-up” in April and high evapotranspiration from July to October.
- 9 The time for the thermal conductivity sensors to first come to equilibrium with the surrounding soil ranged from 5 to 15 days after installation. The response time for

the shallow thermal conductivity sensors under the side-slope to reach equilibrium in suction with a rainfall event of more than 10 mm was estimated from 12 to 24 hours. For rainfall events of less than 10 mm, the relationship could not be determined. At depth of 1.1 m under the side-slope, the response time was estimated from 3 days to 5 days. Correlations between rainfall events with deeper sensors or sensors under pavement could not be directly determined.

- 10 At shallow depths, the meaningful measurements of matric suction could not be obtained during the months when the sensor is frozen. However, from depths below 2.2 m, above the zero degree isotherm, the thermal conductivity sensors were able to measure matric suctions throughout the year.
- 11 Matric suction measurements in 2004 were smaller than the previous year due to higher rainfalls. The drift of the thermal conductivity sensors caused by long term saturation might also show this trend.
- 12 The noise level (i.e., deviation) associated with most of the thermal conductivity sensors in terms of matric suctions is less than 3%. However, the fluctuation in matric suctions at shallow depths under the driving-lane appears to be in phase with temperature changes.
- 13 Erratic readings of some sensors were recorded. The penetration of water into the core of the sensor that contains electronic parts such as the IC sensor and the heating element might be the cause of the malfunction of the sensors.
- 14 Matric suction measurements obtained from the sensors show reasonable agreement with estimated matric suctions obtained using the soil-water characteristic curves measured in the laboratory.

8.2 Recommendation for future research

- 1 The location of field sensor installations in the future should be close to an available weather station or a weather station should be installed at the test site.

This would assist in better interpreting the collected data and can provide more accurate data for numerical modeling and simulations.

- 2 The method of ambient temperature correction should be improved. At the same time attempts should be made to eliminate dependency of suction measurements on ambient temperature.
- 3 Matric suctions presented in this thesis can be used to calibrate numerical models. The material properties for modeling such as SWCCs and saturated permeability can be obtained from the laboratory test results presented in this thesis. The boundary conditions for numerical simulations can also be obtained from the *in situ* suction presented in this thesis.
- 4 The variations in soil suction with time can be correlated to the variations in unsaturated shear strength and bearing capacity of the highway subgrades.
- 5 On the basis of *in situ* matric suction, regulations on optimizing road bans and utilization of the TMS highway system can be studied and developed.

LIST OF REFERENCES

- Aitchison, G.D, and Holmes, A., 1961. Suction profiles in soils beneath covered and uncovered areas. Proceedings of the Fifth International Conference on Soil Mechanics and Foundation Engineering. 2: 187-191.
- Aitchison, G.D, 1965. Moisture Equilibria and Moistures Changes in Soils beneath Covered Areas. A Symp. In Print. Butterworths, Australia.
- Anderson, D.M., and Morgenstern, N.R., 1973. Physics, Chemistry and Mechanics of Frozen Ground: A Review. Proc., 2nd International Conference on Permafrost, Yakutsk, U.S.S.R., North American Contribution, National Academy of Sciences, Washington, D.C, pp. 257-288.
- Blight, G.E., 1980. The Mechanics of Unsaturated Soils. Notes for series lectures delivered as part of Course 270C at the University of California, Berkeley.
- Bloodworth, M.E., and Page, J.B. 1957. Use of thermistor for the measurement of soil moisture and temperature. Soil. Sci. Soc. Amer. Proc. 21: 11-15.
- Edlefsen, N.E., and Anderson, A.B.C., 1943. Thermodynamics of Soil Moisture. Hilgardia, vol. 15, pp 31-298.
- Environment Canada, 2005. Website: <http://climate.weatheroffice.ec.gc.ca/climateData>
- Feng M., 1999. The effects of capillary hysteresis on the measurement of matric suction using thermal conductivity sensors. M.Sc. thesis, University of Saskatchewan, Saskatoon, SK.
- Feng, M., and Fredlund, D.G, 1999. Hysteretic influence associated with thermal conductivity sensor measurements. *In* Proceeding From Theory to the Practice of Unsaturated Soil Mechanics in Association with the 52nd Canadian Geotechnical Conference and the Unsaturated Soil Group. Regina, SK, Canada, October 23-24. pp. 14:2:14-14:2:20.

- Feng, M., Fredlund, D.G., and Shuai, F. 2002. A laboratory study of the hysteresis of a thermal conductivity soil suction sensor. *Geotechnical Testing Journal*, 25(3): 303-314.
- Feng, M., and Fredlund. 2003. Calibration of thermal conductivity sensors with consideration of hysteresis. *Technical Note, Canadian Geotechnical Journal*, 40(5): 1048-1055.
- Fredlund, D.G., and Morgenstern, N.R., 1977. Stress state variables for unsaturated soils. *Journal of Geotechnical Engineering Division, Proceedings, American Society of Civil Engineers*, GT5, 103: 447-466.
- Fredlund, D.G., Gan, J.K. and Rahardjo, H., 1991. Session on Moisture Migration in Freezing and Thawing Soils, Transportation Research Board, Transportation Research Record 1307, Washington, DC, January 1991. pp 291-299.
- Fredlund, D.G. 1992. Advances in Measurement of Soil Physical Properties: Bringing Theory into Practice. *Soil Science of America, Special publication No.3*: 249-262
- Fredlund, D.G., Sattler, P.J. and Gan, J.K-M. (1992) “*In situ* suction measurements using thermal sensor”, 7th International Conference on Expansive Soils, Dallas, Texas, August 3-5, pp. 325-330.
- Fredlund, D.G. and Rahardjo, H. 1993. *Soil mechanics for unsaturated soils*. New York: John Wiley and Sons, Inc.
- Fredlund, D.G. 2000. The 1999 R.M. Hardy Lecture: The implementation of unsaturated soil mechanics into geotechnical engineering. *Can. Geotech. J.* 37: 963-986.
- Fredlund, D.G., Shuai, F., and Feng, M. 2000. Increased accuracy in suction measurements using an improved thermal conductivity sensor. *Proceedings of the Seventh International Conference on Tailing and Mine Waste*, Fort Collins, Colorado, USA. January 23-26: 443-450.

- Fredlund, D.G., Shuai, F., and Feng, M. 2000. Use of a new thermal conductivity sensor for laboratory suction. Proceedings of the Asian Conference on Unsaturated Soils, UNSAT ASIA 2000, Singapore. May 18-19: 275-280.
- Fredlund, D.G., 2005. The Terzaghi Lecture 2005, Austin, Texas. January 23, 2005.
- Greg P.N., and Wilson, G.W., 1997. Heat and mass transfer in unsaturated soils during freezing. Canadian Geotechnical Journal J. 34: 63-70.
- Hillel, D. 1980. Fundamentals of soil physics. New York: Academic Press.
- Hukseflux Thermal Sensors B.V. 2005. Introduction homepage of the company. Thermal science section: <http://www.hukseflux.com/thermalconductivity/thermal.htm>
- Khogali, W.E.I., Anderson, K.O., Gan, J.K. and Fredlund, D.G., "Installation and Monitoring of Thermal Conductivity Suction Sensors in a Fine-Grained Subgrade Soil Subjected to Seasonal Frost", Second International Symposium on Pavement Response Monitoring Systems for Roads and Airfields, September 1991.
- Klausner, Y., 1991. Fundamentals of continuum mechanics of soils. London, New York: Springer-Verlag.
- Kreyszig, E. 1997. Advanced Engineering Mathematics 8th Edition. New York: John Wiley and Sons, Inc.
- Lee, R.K., 1983. Measurement of Soil Suction using the MCS 6000 Sensor. M.Sc. thesis, University of Saskatchewan, Saskatoon, SK.
- Lee, R.K., and Fredlund, D.G. 1984. Measurement of soil suction using the MCS 6000 gauge. Proceedings, 5th International Conference on Expansive Soils, The Institution of Engineers, Adelaide, South Australia, 21-23 May, pp. 50-54.
- Lundquist, O., 2005. The climate of Saskatchewan.
- <http://satellite.usask.ca/~eripley/olivier.html>

- Marjerison B., 2001. Measurement of Matric Suction In Thin Membrane Surface Highways Using Thermal Conductivity Sensors. M.Sc. thesis, University of Saskatchewan, Saskatoon, SK.
- Marjerison, B., Richardson, N., Widger, A., Fredlund D.G., and Berthelot, C. 2001. Installation of sensors and measurement of soil suction below thin membrane surface pavements in Saskatchewan. Proceedings of the 54th Canadian Geotechnical Conference, Calgary, Alberta. September 16-19: 1328-1334.
- Nichol C., Smith L., Beckie R. 2003. Long-term measurement of matric suction using thermal conductivity sensors. Can. Geotech. J. 40: 587-597.
- Pham H., 2002. An engineering model of hysteresis for Soil-Water Characteristic Curves. M.Sc. thesis, University of Saskatchewan, Saskatoon, SK.
- Phene, C.J., Hoffman, G.J., and Rawlins, S.L. 1970. Measuring Soil Matric Potential *in situ* by sensing heat dissipation within a porous body: I. Theory and sensor construction. Soil Science Society of America Proceedings, 35: 27-32.
- Padday, J.F. 1969. Theory of surface tension: Surface and colloid science. Vol.1, Wiley-Interscience, Toronto, Canada.
- Padilla J.M., Perera Y.Y. 2004. Performance of a New Thermal Conductivity Sensor. GCTS Company, 6103 South Maple Avenue, Tempe, AZ 85283, USA. Special publication: 1-9.
- O’Kane, M., Wilson, G.W., and Barbour, S.L., 1998. Instrumentation and monitoring of an engineered soil cover system for mine waste rock. Canadian Geotechnical Journal J. 35: 828-846.
- Richards, L.A. 1955. Electro-thermal element for measuring moisture in porous media. U.S. Patent 2 718 141. Date issued: 20 September.
- Rahardjo, H., Leong, E.C., and R.B. Rezaur, 2001. Instrumented slopes for the study of rainfall-induced slope failures. Invited Presentation. Workshop on Rain-Induced Landslides. Proceedings of the 14th Southeast Asian Geotechnical Conference, Hong Kong. 10 -14 December 2001. Vol. 3.

- Reece, C.F. 1996. Evaluation of line heat dissipation sensor for measuring soil matric potential. *Soil Science Society of America Journal*, 60: 1022-1028.
- Saskatchewan Industry and Resources, 2005. Introduction to Saskatchewan's Geology. Website: <http://www.ir.gov.sk.ca/Default.aspx>
- Shaheen, N. J., 2005. Drawdown of Saskatchewan's Estevan Valley Aquifer. *Sask Water, Agriculture and Agri-Food Canada*. The website: http://res2.agr.ca/publications/hw/09d_e.htm.
- Shaw, B., and Baver, L.D. 1939. An electrothermal method for following soil-moisture changes of the soil *in situ*. *Soil Sci. Soc. Amer. Proc.* 4:78-83.
- Shuai, F., Yazdani, J., Feng, M., and Fredlund, D.G. 1998. Supplemental report on the thermal conductivity matric suction sensor development (Year II). Department of Civil Engineering, University of Saskatchewan, Saskatoon, Sask.
- Shuai, F., and Fredlund, D.G. 2000. Use of a new thermal conductivity sensor to measure soil suction. *Proceedings of the GeoDenver Conference*, Denver, Colorado, USA. August 3-8: 1-12.
- Shuai F., Clements C., Ryland L., Fredlund D.G., 2002. Some factors that influence soil suction measurement using a thermal conductivity sensor. *Third International Conference on Unsaturated soils, UNSAT 2002*, March 10-13, 2002, Recife, Brazil: 325-329.
- Shuai F., Fredlund D.G, Samarasekera L. 2003. Numerical simulation of water movement in the suction equalization of a thermal conductivity sensor. *Geotechnical Testing Journal*. Vol. 26. No. 2: 142-150.
- Solomon, K. H., and Jorgensen, G. 1993. *Subsurface Drip Irrigation*. The Center for Irrigation Technology (CIT) of California State University, Fresno. CATI Publication #930405. Website: <http://cati.csufresno.edu/cit/rese/93/930405/>.

- Szafron B., 1991. The Measurement of soil suction and its influence on the bearing capacity of subgrades. M.Sc. thesis, University of Saskatchewan, Saskatoon, SK.
- Szafron, B.J. and Fredlund, D.G. (1992) "Monitoring matric suctions in the subgrade of unpaved roads", 45th Canadian Geotechnical Conference, Toronto, October 26-28, pp. 52.1-52.10.
- Tan, E., Fredlund, D.G. and Gitirana Jr, G.F.N., 2002. Comparisons of Correction Methods for Factors Influencing Thermal Conductivity Suction Sensors. Proceedings of the third International conference on Unsaturated Soils. Recife, Brazil.
- Tan, E., Marjerison, B., and Fredlund, D.G., 2003. Measurements and analysis of temperature and soil suction below thin membrane surface (TMS) in Saskatchewan. Proceedings of the 56th Canadian Geotechnical Conference, Winnipeg, Manitoba, Volume 2. Sept. 29-Oct. 1: 107-114.
- Tan, E., 2004. Analysis of temperature and soil suction for the purpose of optimizing road bans in Saskatchewan. M.Sc. thesis, University of Saskatchewan, Saskatoon, SK.
- van der Raadt, P., Fredlund, D.G., Clifton, A.W. and Jubien, W.E. 1987. "Soil suction measurements at several sites in western Canada", Transportation Research Record, 1137.
- van der Raadt, P., 1988. Field measurement of Soil Suction using Thermal Conductivity Matric Potential Sensors. M.Sc. thesis, University of Saskatchewan, Saskatoon, SK.
- Williams, P.J., 1982. The Surface of the Earth: An Introduction to Geotechnical Science. Longman, New York, 212 pp.
- Wulfsohn, D., Adams, B.A., and Fredlund, D.G., 1996. Application of unsaturated soil mechanics for agricultural conditions. Canadian Agricultural Engineering, 38(3): 173-181.

Xing, A., Fredlund D. 1994. Numerical Modeling of a thermal conductivity matric suction sensor. *Geotechnical Testing Journal*, GTJODJ, Vol. 17, No. 4: 415-424.

APPENDIX A

A STUDY ON NEW THERMAL CONDUCTIVITY SENSORS

To better understand the data obtained from the thermal conductivity sensors installed at the Bethune and Torquay sites, a study on new thermal conductivity sensors were implemented in this research. The new thermal conductivity sensor was developed by Geotechnical Consulting and Testing Systems Company (GCTS) based on previous models of the University of Saskatchewan thermal conductivity sensor. The new thermal conductivity sensor was of the same size and of the same ceramic material as the field-installed sensor, except for some new technical improvements as described below. Two thermal conductivity sensors were tested in the laboratory in 2004 and six other sensors were tested in 2005. The objective of the study was to investigate the function of the new thermal conductivity sensor on matric suction and temperature measurement under laboratory conditions. The studies focused on the calibration curve, noise level (i.e., deviation of measurement), resolution (i.e., the ability of the sensor to distinguish suctions separated by recording small temperature differences as discussed in Section A.8) of the new thermal conductivity sensor. This appendix presents the results including advantages as well as limitations of the new thermal conductivity sensor.

A.1 Introduction of new thermal conductivity sensor

The main features of the new thermal conductivity sensor included state-of-the-art digital design, high resolution (0.004°C) in temperature measurements, high accuracy in matric suction measurements and ability to use cables of more than 100 m

long. The improvements also contained a moisture barrier around the electronics that prevent the cracking and moisture penetration. These improvements could eliminate the ambient temperature influence and mitigate the cable resistance effect.

A cross-section of the new thermal conductivity sensor is illustrated in Figure A.1. The ceramic tip is 28 mm in diameter and 38 mm in height. The core element consists of a small heating element and a digital temperature sensor. This element is surrounded by a bonding material and a moisture barrier. The barrier protects the electronics from moisture as well as prevents expansion of bonding material that could cause cracking of the ceramic block.

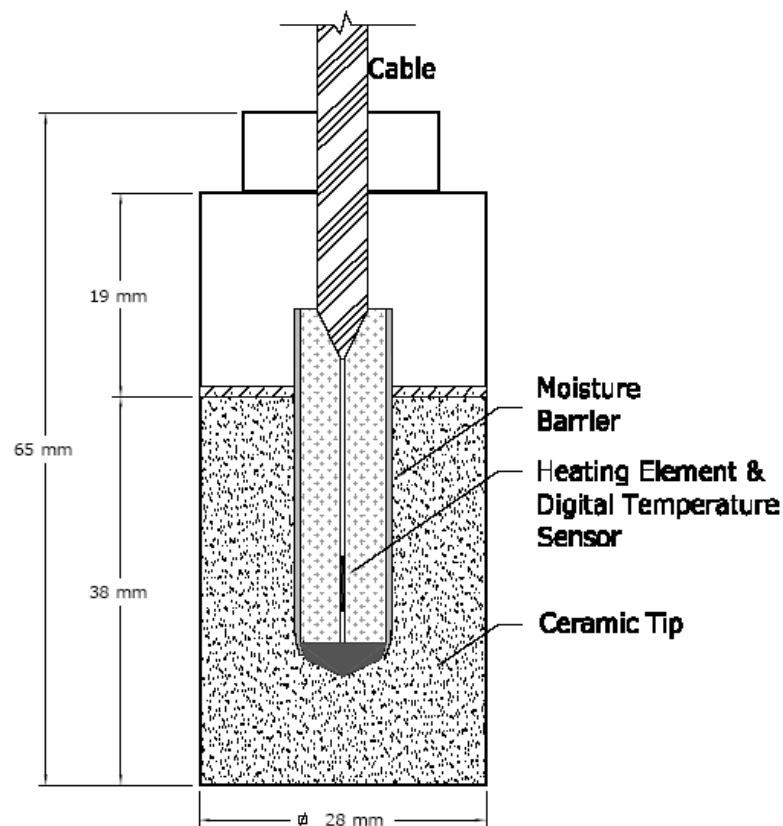


Figure A.1 Cross-section of a new thermal conductivity sensor (Padilla et al. 2004)

The University of Saskatchewan thermal conductivity sensors used analog signals. Therefore, the magnitude of the current transmitted through cables varied depending on the ambient temperature. Moreover, the intensity of signal output decreased with the cable length due to cable resistance restricting cable lengths to a

minimum (these limitations are fundamentals in electrical engineering). Some efforts made in the past to correct temperature correction were not successful since the intended quantity of heat varied from one data point to another. Pictures of the new thermal conductivity sensors and the digital tester are shown in Figures A.2 and A.3.



Figure A.2 Picture of the new thermal conductivity sensor

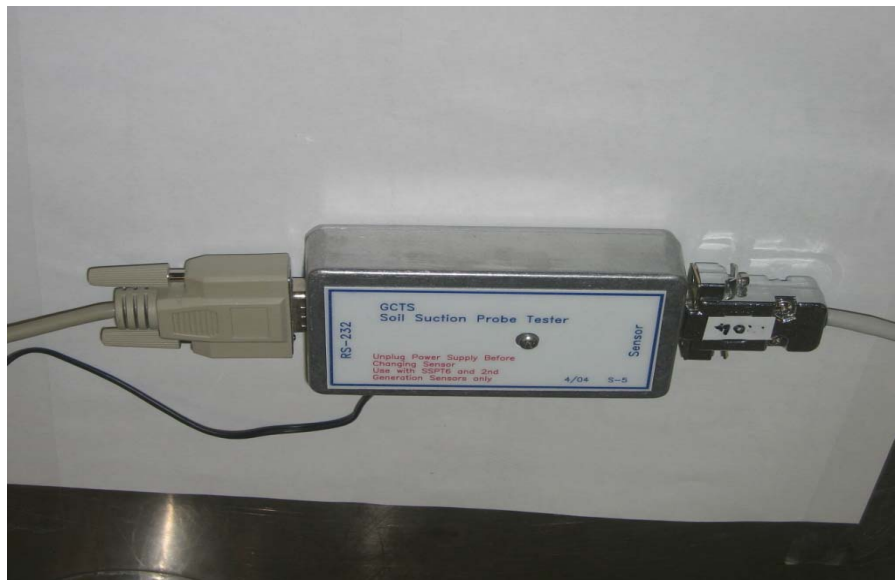


Figure A.3 Digital tester for controlling constant current

During testing, a constant current was maintained by the digital design minimizing the effect of the ambient temperature. Additionally, the digital signals were

not affected by cable length. This digital design was performed using a software program developed by the manufacturer.

A.2 Operation procedure for new thermal conductivity sensor

In order to connect a sensor to a computer, the following steps were implemented.

The wires were run through feed on the top plate of the chamber and the apparatus was sealed;

The tester was connected to a computer using the cable provided by the manufacturer;

The software program was opened and the pertinent parameters for the heating were set. An example could be: Port = 1 (i.e., output port on computer); Current = 200mA; Time = 60 sec (i.e., heating time); Period = 1.0 sec (i.e., taking readings every second); Samples = 120 (i.e., taking readings in 120 seconds); Pod = 1 (i.e., standard output = 1); Sensor = 1 (i.e., sensor number);

Run button was clicked and the readings were watched on computer screen until the heating curve was completed;

The data could be extracted from the curve (initial temperature and peak temperature) by moving the cursors along the curve; and

The data were saved.

A.3 Equipment and procedure for calibration

In order to calibrate the thermal conductivity sensor in the laboratory, the following apparatus were needed (Figure A.4).

Special Tempe cells were designed with three holes on top for running cables (Figure A.5);

A two-way switch was made at the Central Shop in the College of Engineering, University of Saskatchewan, Saskatoon. This switch connected the thermal conductivity sensors to the matric suction tester and was able to handle 5 wires. The switch had 6 ports enabling measurements of six sensors and could be extended to 12 ports;

The kaolin paste was placed on the cell plate to provide good contact between sensor and high air entry disk;



Figure A.4 Connection of apparatuses for sensor calibration

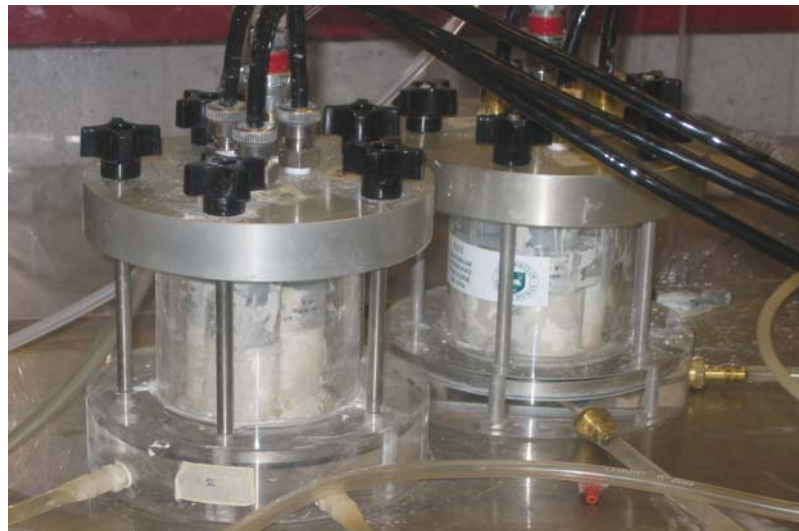


Figure A.5 Special Tempe cells with three holes on top for running cables

The calibration curve was obtained by increasing the matric suction of the thermal conductivity sensor from the zero to a maximum value of 400 kPa or vice versa. Each increment was maintained constant until the equilibrium was reached.



Figure A.6 A two-way switch for handling six sensors

A.4 Temperature comparison between sensor and thermometer

Figure A.7 shows the good agreement between temperature from Sensor 1204 and a precision thermometer. The similar results were also seen between other sensors and a thermometer. The maximum difference between the thermometer and the thermal conductivity sensor was 0.15 degrees Celsius.

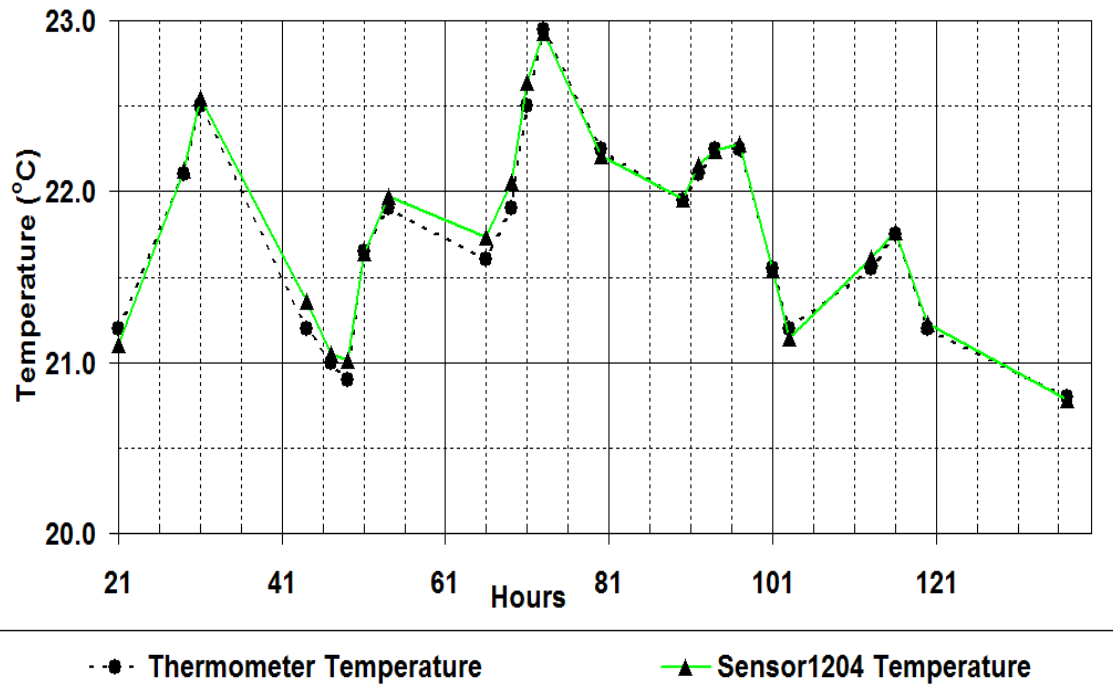


Figure A.7 Temperatures from the thermal conductivity sensor and thermometer

A.5 Saturation techniques

During the summer of 2004, the first two sensors with identification numbers (IDs) of 1201 and 1204 from GCTS were obtained for testing. These two sensors were saturated four times using different tentative techniques as described below. After each saturation process, the thermal conductivity sensors were dried out with a fan then put in desiccators until the readings showed that the sensors were fully dry. An electrical current of 200 mA was applied in 60 seconds to optimize the heat pulse (i.e., preventing heat dissipation outside the thermal conductivity sensor and providing the highest resolution).

The two thermal conductivity sensors were saturated in one step for 87 hours for the first time;

The two sensors were saturated in three steps for the second time. Half the height of the ceramic was submerged for 24 hours, then three fourth of the height of

ceramic in 50 hours, finally total the height of ceramic in 66 hours. The total amount of saturation time was 140 hours;

The thermal conductivity sensors were saturated in three steps for the third time. At the beginning, 1 cm of the height of the ceramic was submerged for 32 hours, then half the height of ceramic for the next 20 hours and last, saturated fully them in 66 hours. The total saturation time of the third time was 98 hours; and

The thermal conductivity sensors were saturated in a Tempe cell with applying air pressure in the order of 40→60→80→150→20 kPa for the fourth time. Each pressure step was maintained 12 hours.

The summary of the saturation techniques were graphically presented in Figure A.7.

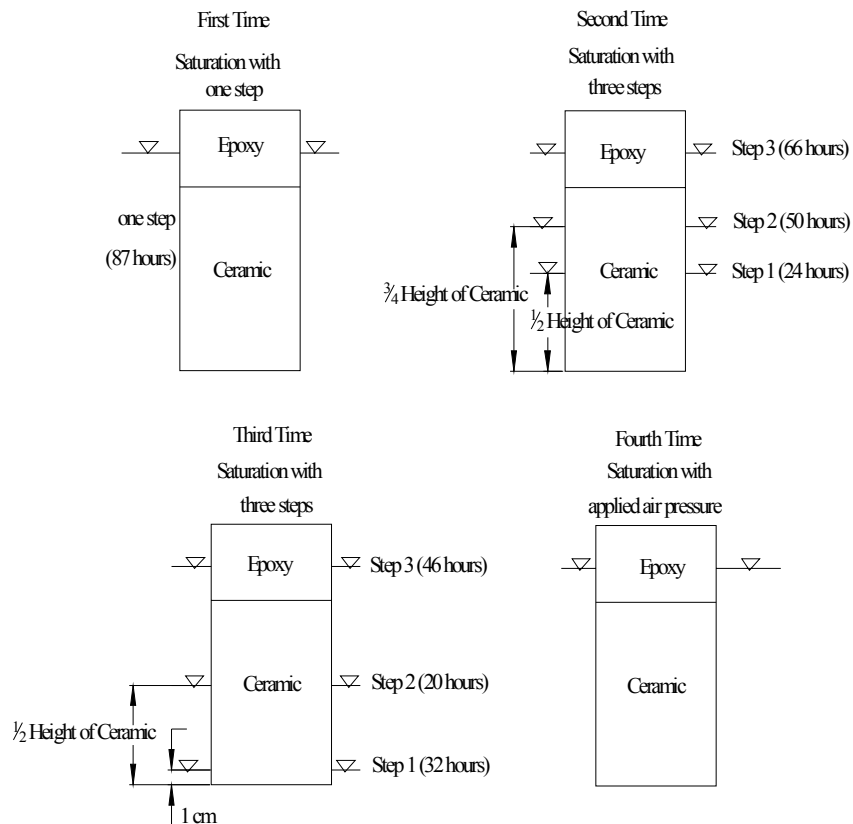


Figure A.7 A diagram showing different techniques for saturating the sensors

The results from the different saturation techniques are summarized in Table A.1. The saturation technique with the application of an air pressure of 80 kPa for 12 hours appeared to be the most suitable method for saturating the thermal conductivity sensors. This pressure saved time for saturation and gave a reasonable temperature rise corresponding to a high degree of saturation on the calibration curve.

Table A.1 The results of saturation for the first two sensors

Trial	Temperature rise (°C)	
	Sensor 1201	Sensor 1204
1	13.0	12.9
2	11.91	12.4
3	12.05	12.5
4		
Under 40 kPa	11.80	12.26
↓		
Under 60 kPa	11.77	12.09
↓		
Under 80 kPa	11.75	12.04
↓		
Under 150 kPa	11.75	12.03
↓		
Under 20 kPa	11.74	12.03

The graph showing the heating curve of Sensor 1201 for the second attempt of saturation is presented in Figure A.8.

The two sensors of the first shipment from GCTS were later damaged for the causes which are discussed in Section A.9.

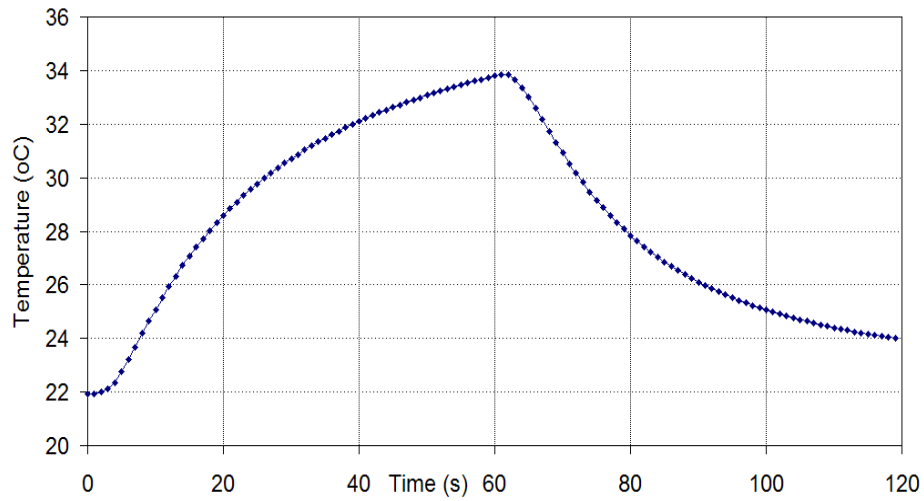


Figure A.8 The heating curve of Sensor 1201 during the second attempt of saturation

A.6 Equilibrium time for the thermal conductivity sensor

The presentation of temperature rise versus time for the saturation process of Sensors 1201 and 1204 are illustrated in Figures A.8 and A.9. The equilibrium was assumed to reach once a turning point on temperature versus log time had adequately passed. These figures show that the equilibrium time for the saturation was 12 hours.

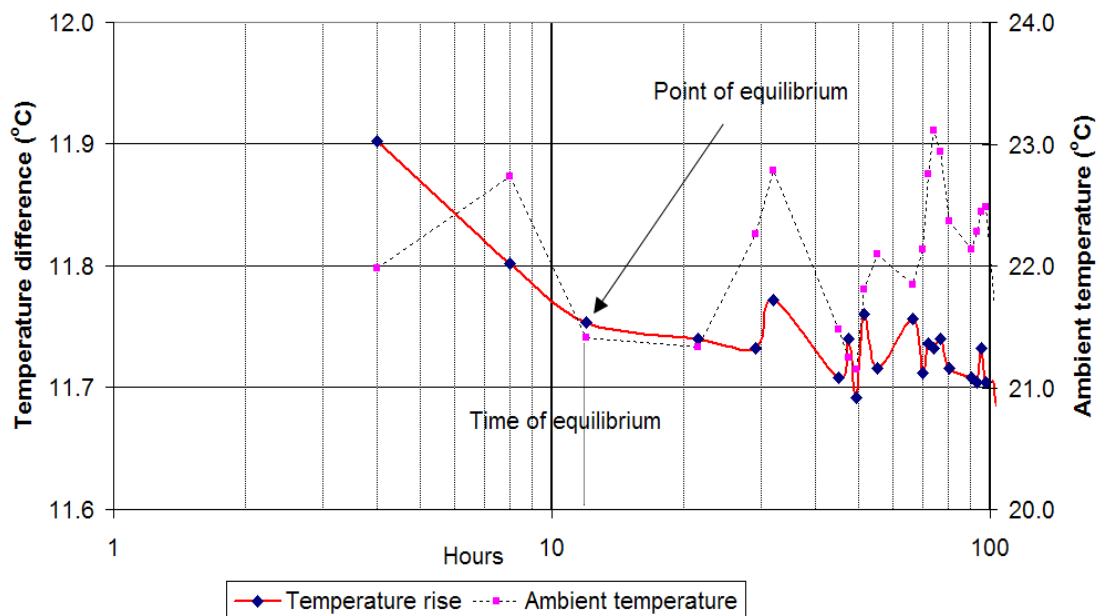


Figure A.9 Saturation process of Sensor 1201

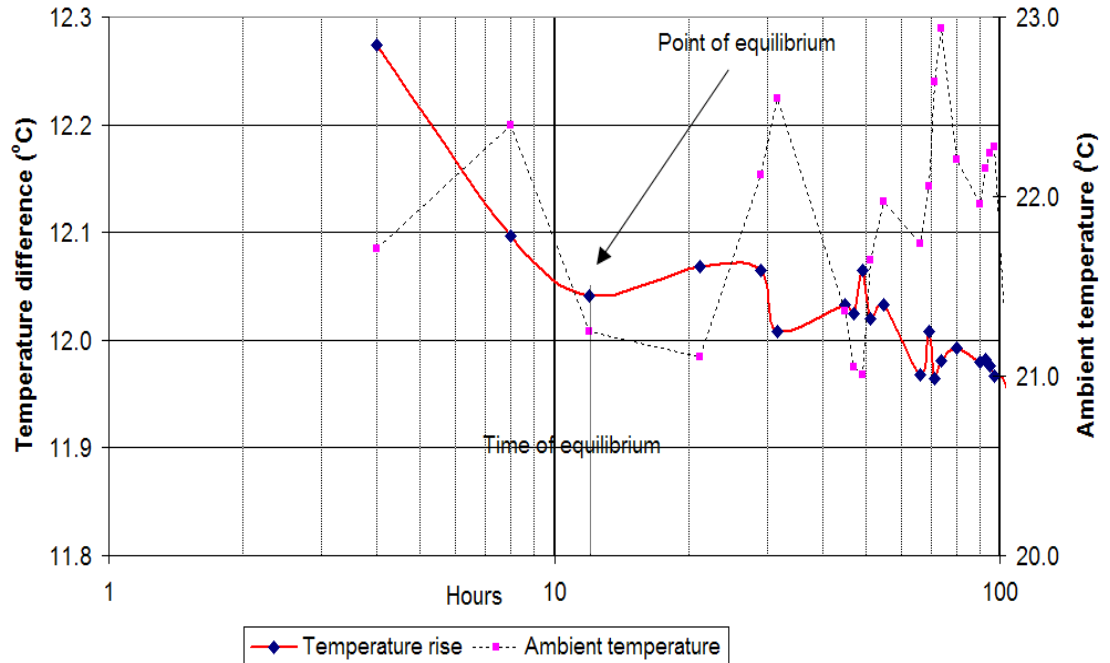


Figure A.10 Saturation process of Sensor 1204

During the calibration process, the equilibrium time for each pressure of the applied matric suctions ranged from 1 to 7 days varying from sensor to sensor. The time for a sensor to respond with a suction change in the field might be faster since both the bottom and side surfaces of a sensor would be in contact with the surrounding soils. The effective surface area of sensor on site is 5.3 times greater than the effective surface area in the laboratory. In addition, the water migration through low permeable high air entry disks might prolong the response time of the calibration process.

A.7 Presentation of the calibration results

After the damage of the first two sensors, the second shipment of the new sensors arrived at the geotechnical lab of University of Saskatchewan in December 2005 including 6 sensors denoted from 1 to 6.

The results of the laboratory testing program of the new six sensors are presented in Figures A.9 to A.14. These figures show that the shape of the main hysteresis loop of calibration and the scanning curves varied from sensor to sensor. The

scanning curves tended to move towards opposite branch of main hysteresis loop of calibration (i.e., convex moving). Six sensors could not reach the initial drying curve during the rewetting process. However, Sensor 4 returned to a point between the main hysteresis loop of calibration and the initial degree of saturation at zero suction after 357 hours. The porosity of the ceramic tip of Sensor 4 was possibly different from other sensors. The results of sensor testing are tabulated in Table A.2.

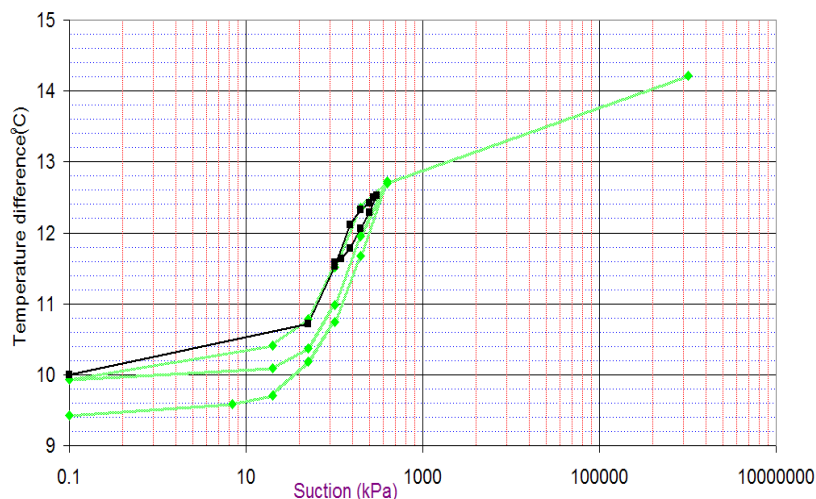


Figure A.9 Calibration of Sensor 1 including main hysteresis loop of calibration and the scanning curves

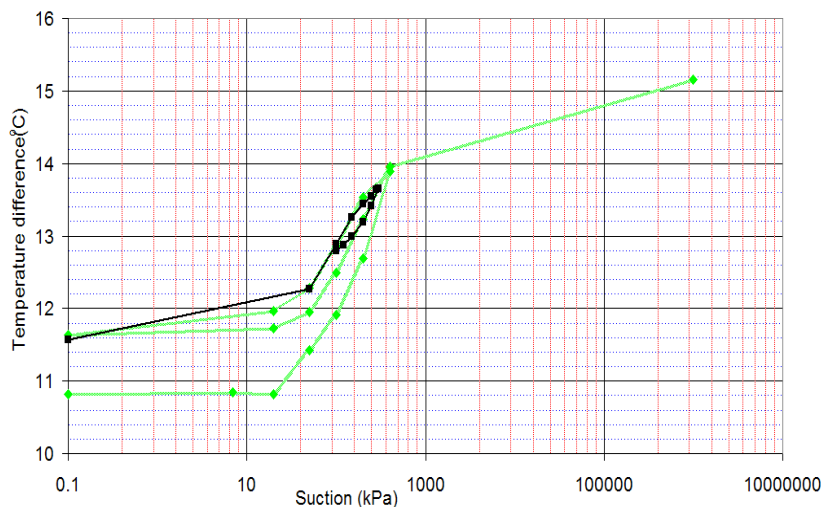


Figure A.10 Calibration of Sensor 2 including main hysteresis loop of calibration and the scanning curves

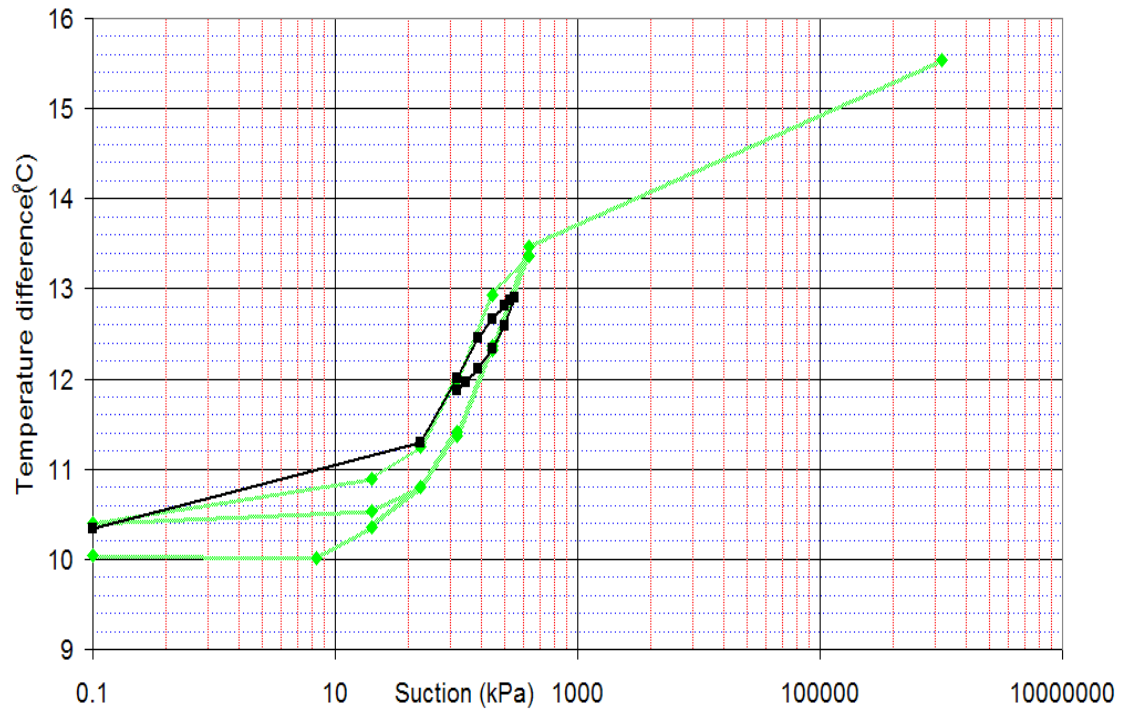


Figure A.11 Calibration of Sensor 3 including main hysteresis loop of calibration and the scanning curves

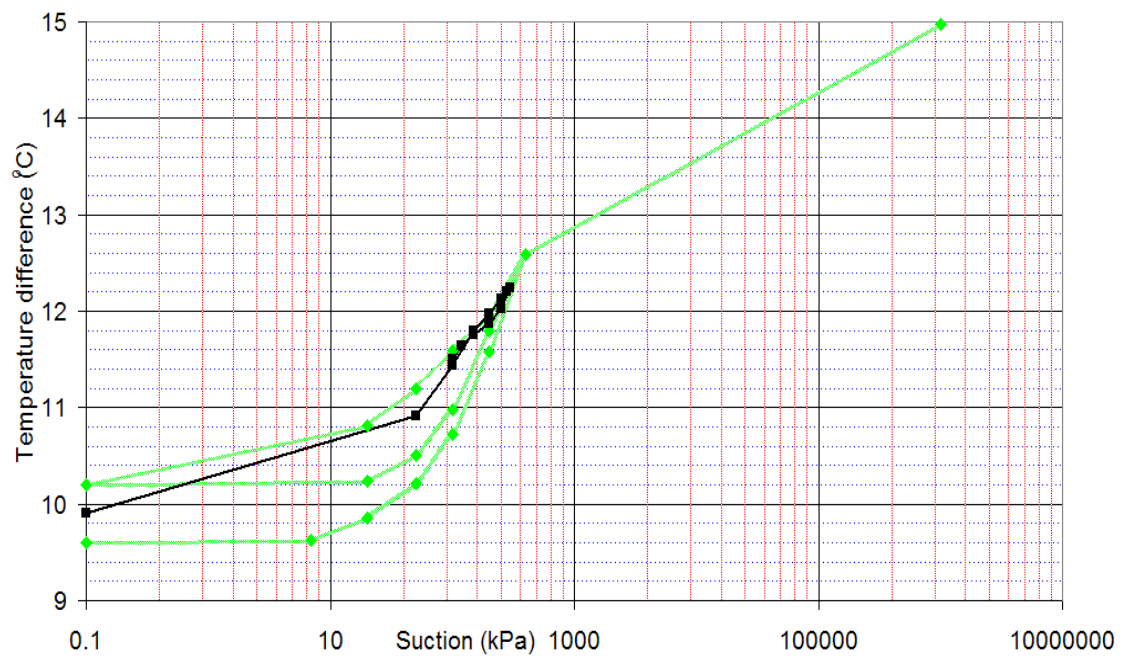


Figure A.12 Calibration of Sensor 4 including main hysteresis loop of calibration and the scanning curves

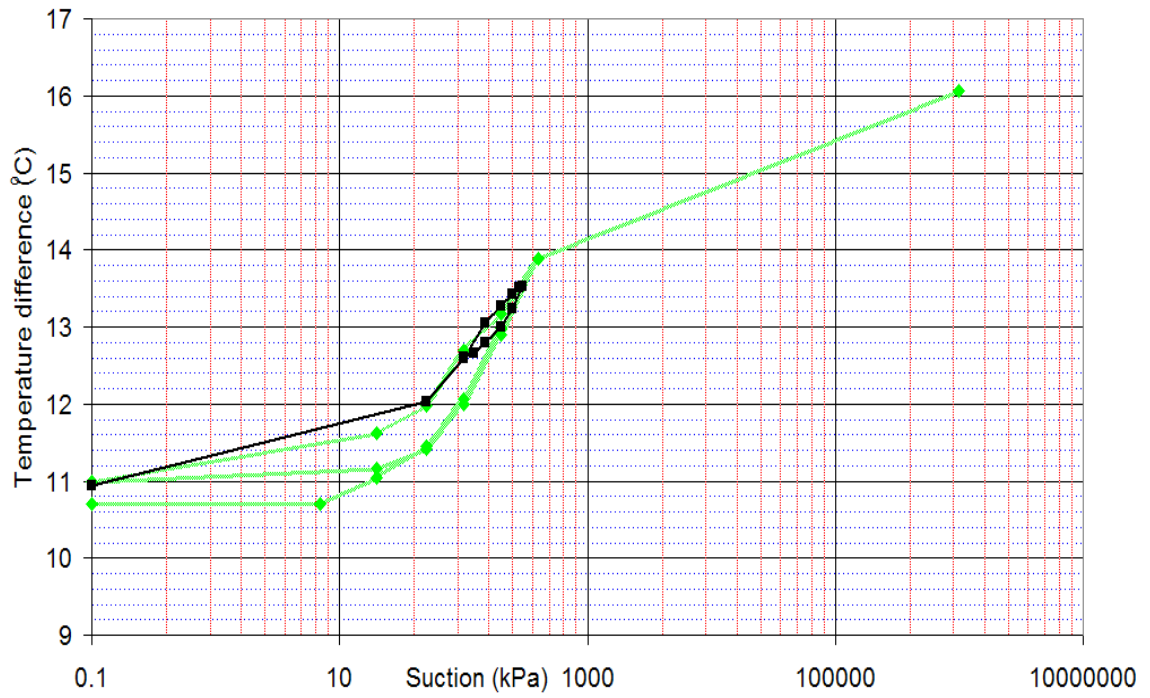


Figure A.13 Calibration of Sensor 5 including main hysteresis loop of calibration and the scanning curves

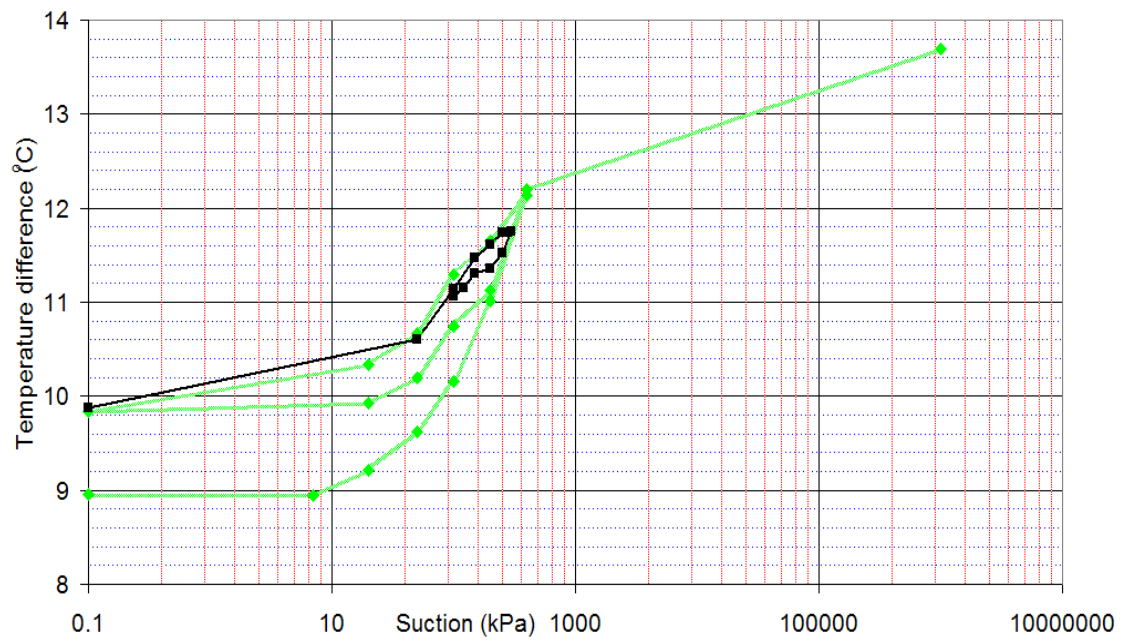


Figure A.14 Calibration of sensor 6 including the main hysteresis loop of calibration and the scanning curves

Table A.2 The initial drying curves, main hysteresis loop and scanning curves of the six sensors

Matric suction kPa	Temperature rise (°C)					
	Sensor 1	Sensor 2	Sensor 3	Sensor 4	Sensor 5	Sensor 6
0.1	9.4231	10.8133	10.0361	9.5994	10.6971	8.9543
7	9.5873	10.8494	10.0120	9.6234	10.7091	8.9463
20	9.7075	10.8213	10.3566	9.8598	11.0457	9.2147
50	10.1843	11.4183	10.8013	10.2083	11.4543	9.6274
100	10.7452	11.9151	11.3622	10.7292	12.0633	10.1563
200	11.6747	12.6923	12.3277	11.5825	12.9808	11.0096
400	12.7204	13.8862	13.3574	12.5881	13.8862	12.1314
200	12.3500	13.5296	12.9247	11.9591	13.1691	11.6546
100	11.5104	12.8606	11.9992	11.5865	12.6963	11.2901
50	10.7772	12.2756	11.2500	11.1899	11.9712	10.6691
20	10.4167	11.9591	10.8894	10.8133	11.6146	10.3325
0.1	9.9359	11.6346	10.3926	10.2043	10.9936	9.8397
20	10.0881	11.7268	10.5329	10.2444	11.1619	9.9279
50	10.3726	11.9511	10.8013	10.5008	11.4183	10.1923
100	10.9776	12.4880	11.4183	10.9816	11.9992	10.7452
200	11.9471	13.2292	12.3598	11.7909	12.8926	11.1338
400	12.7043	13.9623	13.4655	12.5921	13.8822	12.2035
1000000	14.2107	15.1563	15.5449	14.9800	16.0577	13.6939
100	11.5825	12.7968	11.8776	11.5000	12.6082	11.0643
120	11.6306	12.8769	11.9657	11.6484	12.6563	11.1524
150	11.7829	12.9891	12.1059	11.7526	12.7885	11.3127
200	12.0593	13.1854	12.3343	11.8768	12.9968	11.3551
250	12.2837	13.4178	12.5827	12.0290	13.2412	11.5194
300	12.5280	13.6582	12.8952	12.2413	13.5337	11.7558
280	12.5000	13.6381	12.8712	12.2013	13.5056	11.7397
250	12.4199	13.5500	12.8111	12.1292	13.4335	11.7438
200	12.3237	13.4418	12.6628	11.9689	13.2652	11.6115
150	12.1154	13.2575	12.4625	11.7966	13.0529	11.4713
100	11.5306	12.8930	12.0018	11.4343	12.5921	11.1348
50	10.7135	12.2628	11.3007	10.9095	12.0232	10.5979
0.1	9.9920	11.5708	10.3351	9.5833	10.9455	9.8728

A.8 Sensor resolution and noise level of the new thermal conductivity sensor

Noise level is defined as a random disturbance in the reception of a signal that causes deviations in output readings.

The resolution of matric suction measurements (ψ_{res}) for the main hysteresis loop of calibration could be expressed by the following equation.

$$\psi_{\text{res}} = (\psi_{\text{max}} - \psi_{\text{min}}) / (\Delta T|_{\psi_{\text{max}}} - \Delta T|_{\psi_{\text{min}}}) T_{\text{res}} \quad (\text{A.1})$$

where:

ψ_{max} = maximum matric suction in the main hysteresis loop of calibration = 400 kPa;

ψ_{min} = minimum matric suction in the main hysteresis loop of calibration = 0 kPa;

$\Delta T|_{\psi_{\text{max}}}$ = temperature rise at ψ_{max} ;

$\Delta T|_{\psi_{\text{min}}}$ = temperature rise at ψ_{min} ; and

T_{res} = temperature resolution (i.e., the smallest temperature difference can be distinguished by the sensors) and is assumed as the difference between the temperature readings at time of 0 and 1 second after heating = 0.004 °C.

The resolutions for the new thermal conductivity sensors are summarized in Table A.3. The matric suction resolutions varied from 0.55 to 0.71 kPa or 0.13 to 0.17 (%).

Table A.3 Resolution of matric suction measurements for the new sensors

	Sensor 1	Sensor 2	Sensor 3	Sensor 4	Sensor 5	Sensor 6
ψ_{res} (kPa)	0.574618	0.710606	0.539676	0.671193	0.55313	0.698182
Resolution as %	0.143655	0.177651	0.134919	0.167798	0.138283	0.174546

The maximum accuracy of the new thermal conductivity sensors are governed by the noise level (deviation) of the measurements. The noise levels were determined by plotting the temperature rise versus time at the dry state. The deviation of reading of Sensor 1 at dry condition is presented in Figure A.16. The other sensors showed similar deviations. The maximum noise level of the new thermal conductivity sensor was 0.05°C irrespective of the ambient temperature.

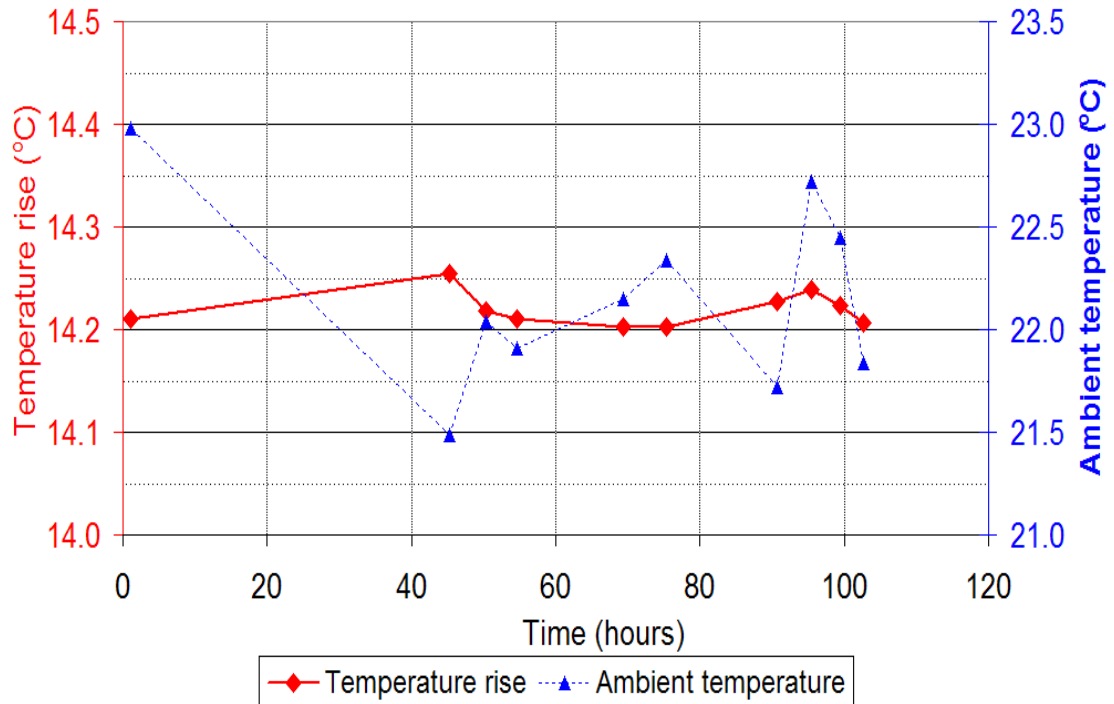


Figure A.16 Deviation of temperature rise and ambient temperature versus time for Sensor 1 at dry state

By taking the difference in matric suctions of the main hysteresis loop of calibration divided by the difference in temperature rise, the maximum possible error of the thermal conductivity sensor could be expressed:

$$\psi_a = (\psi_{\max} - \psi_{\min}) / (\Delta T|_{\psi_{\max}} - \Delta T|_{\psi_{\min}}) T_{\text{noise}} \quad (\text{A.2})$$

where:

ψ_{\max} ; ψ_{\min} ; $\Delta T|_{\psi_{\max}}$ and $\Delta T|_{\psi_{\min}}$ defined as the same as in Equation A.1; and

T_{noise} = temperature noise level 0.05 °C.

The maximum possible error calculated from Equation A.2 is approximately 6 to 7 kPa or 1.6 %.

A.9 Sensor malfunction during calibration

This section discusses some possible reasons for the malfunctions of Sensor 1201 and 1204 during the laboratory calibration.

After working properly for one month, Sensor 1204 did not respond to change in matric suction and recorded approximately the same temperature rise for both wet and dry conditions. This led to the suspicion that there may not have been an adequate contact between the stainless steel tube that covers the heating element and the digital temperature sensor and the surrounding ceramic. In other words, there might have been a thermal barrier of air between the core element and the surrounding ceramic block. Another reason could be the deterioration of the bonding material surrounding the small heating element and the digital temperature sensor.

There seemed to be a different problem encountered with Sensor 1201. After functioning well for both dry and wet conditions, the thermal conductivity sensor became non-responsive to the applied current controlled by the tester. It is likely that water has reached the electronics and short circuited the board. Probably, the tightness of the top of the plastic screw failed and the leaking occurred. The later forensic

confirmed that water was found in the cavity of the top plastic cap and near the roof of the cable indicating water penetration from the top of the thermal conductivity sensor.

The penetration of water into the IC sensor and heating element that was found in Sensor 4 could also be the cause of the damage of Sensor B1-4 as well as other erratic readings encountered at Sensors B4-15 and B5-16 at the Bethune site.

The movement of Sensor 4 out of the main hysteresis loop of calibration after rewetting showed that the thermal conductivity sensors might drift out of the hysteresis loop after a long period of saturation.

APPENDIX B

PRESENTATION OF *IN SITU* MATRIC SUCTIONS

B.1 The form and the meanings the original data

The data collected from the sites were in the following original form.

107,183,1200,0
164,22.602,247.4,.6803,1601.2
164,20.107,230.09,.34021,1434.2
.....

Using a Spread Sheet to separate the data into columns, the original form can be converted to table texts as in Table B.1.

Table B.1 A sample of the field data

107	110	1200	0	
164	9.8569	227.9	0.33551	818.32
164	5.807	291.36	0.33551	639.15
164	0.16249	353.8	0.3421	363.7
164	0.1905	263.97	0	275.46
164	1.0063	359.25	0.33551	419.73
164	9.198	142.3	0.33551	692.84
164	5.881	183.54	0.33551	535.82
164	0.35524	369.23	0.33552	390.87
164	1.1105	314.44	0.33552	381.14
164	8.7733	360.53	0.67102	886.09
164	2.3645	342.42	0	484.15
164	1.561	274.42	0.67103	368.06
164	7.8611	602.18	0	1073.3
164	4.1071	168.66	0	414.36
164	2.6458	344	0.33553	502.26
164	4.0096	469.12	0.33551	709.61

In the first column of table B.1, 107 is an indicator showing the beginning or ending of a reading collected by the data acquisition system. The number 164 is a registration of a reading for an individual sensor. The temperatures are presented in the second column. The number 110 at the top shows the day of year on which the readings were taken. The voltage outputs are shown in the third column and the number at the top indicates the clock time at which the readings were recorded. The fourth column is indices showing electronic function. A reading is correct if the index is less than 1.0 and is variable if more than 1.0. The last column illustrates the readings of voltage drop after heating. Only data in the second and third column are used to convert to soil matric suction.

The final step is to arrange the data of individual sensor into vertical columns. This can be made using three Spread Sheet functions, which are INDIRECT, ADDRESS and ROW functions. ROW function designates the row number to which the specific value (i.e. temperature or voltage output) of an individual sensor is referred. ADDRESS sets up a cell reference as text, given individual row and column number (i.e. it shows a position a targeted temperature or voltage output in an original data

sheet). INDIRECT returns the referred datum specified by a text string. A syntax sample can be expressed as follows:

The selected value: “= INDIRECT(ADDRESS(17*ROW(A1)-14,3))”

B.2 Matric suctions with no temperature correction

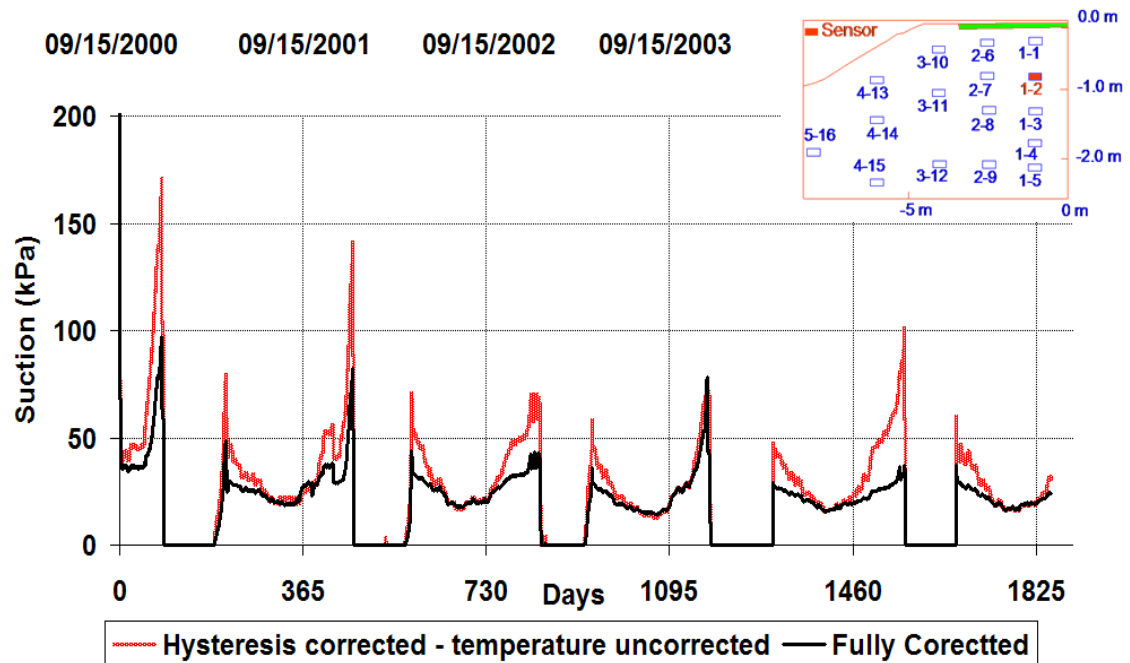


Figure B.1 Suctions with and without temperature correction at Sensor T1-2

B.1 Matric suctions with no hysteresis correction

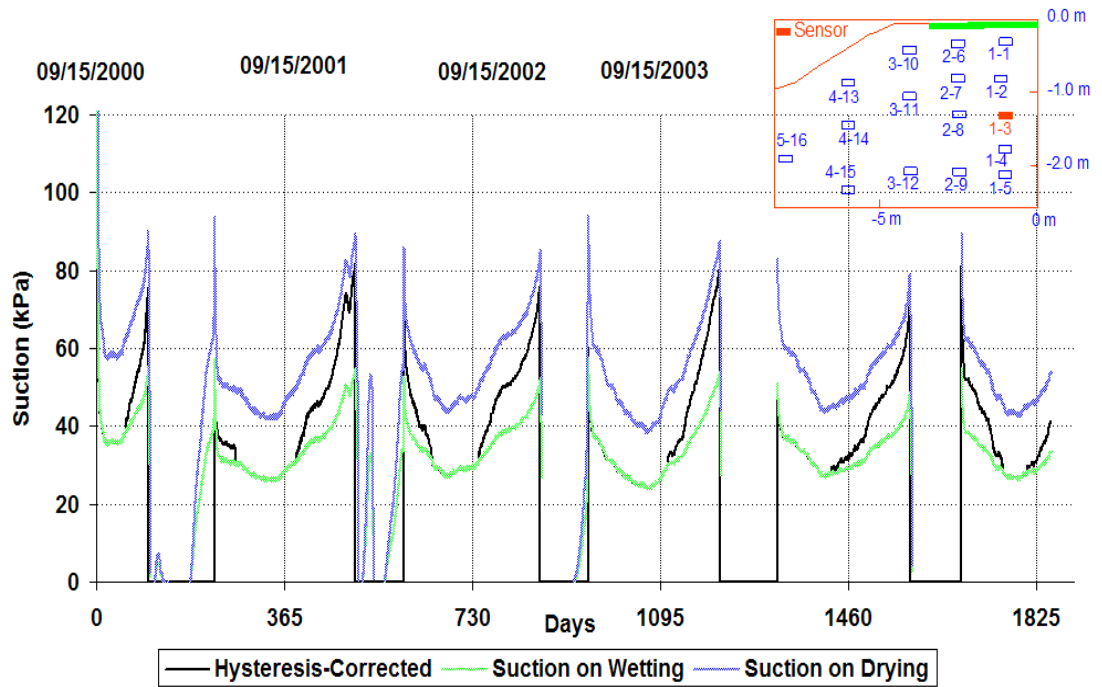


Figure B.2 Suctions with and without hysteresis correction at Sensor T1-3

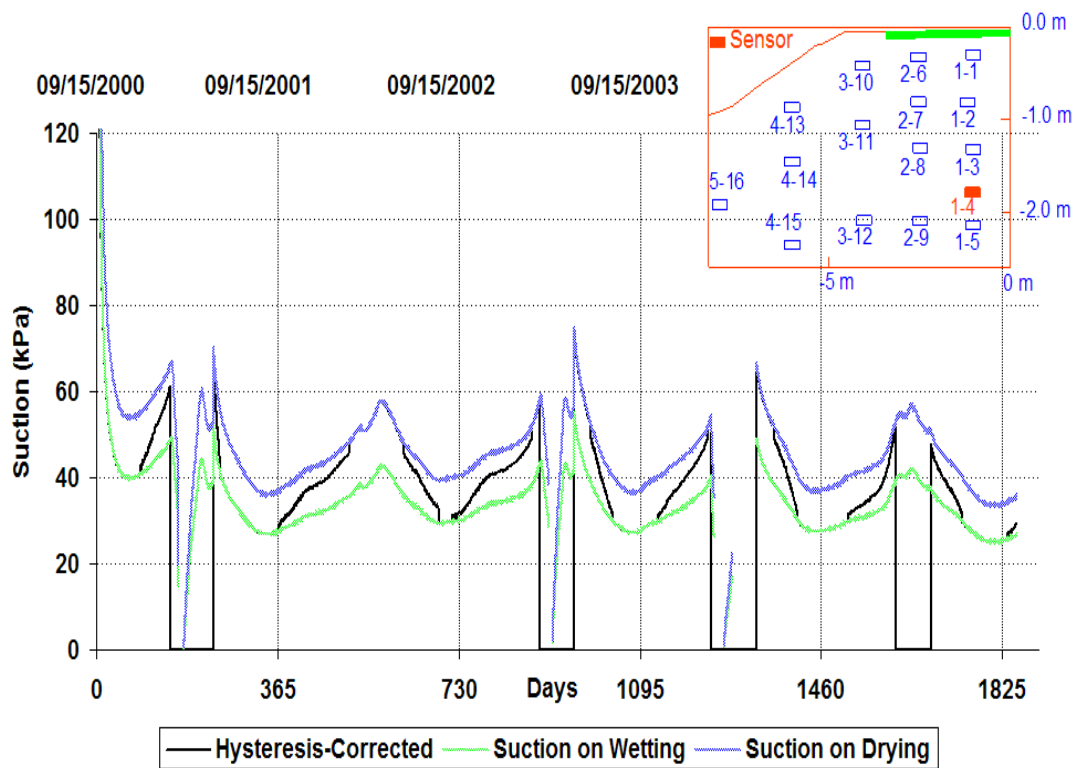


Figure B.3 Suctions with and without hysteresis correction at Sensor T1-4

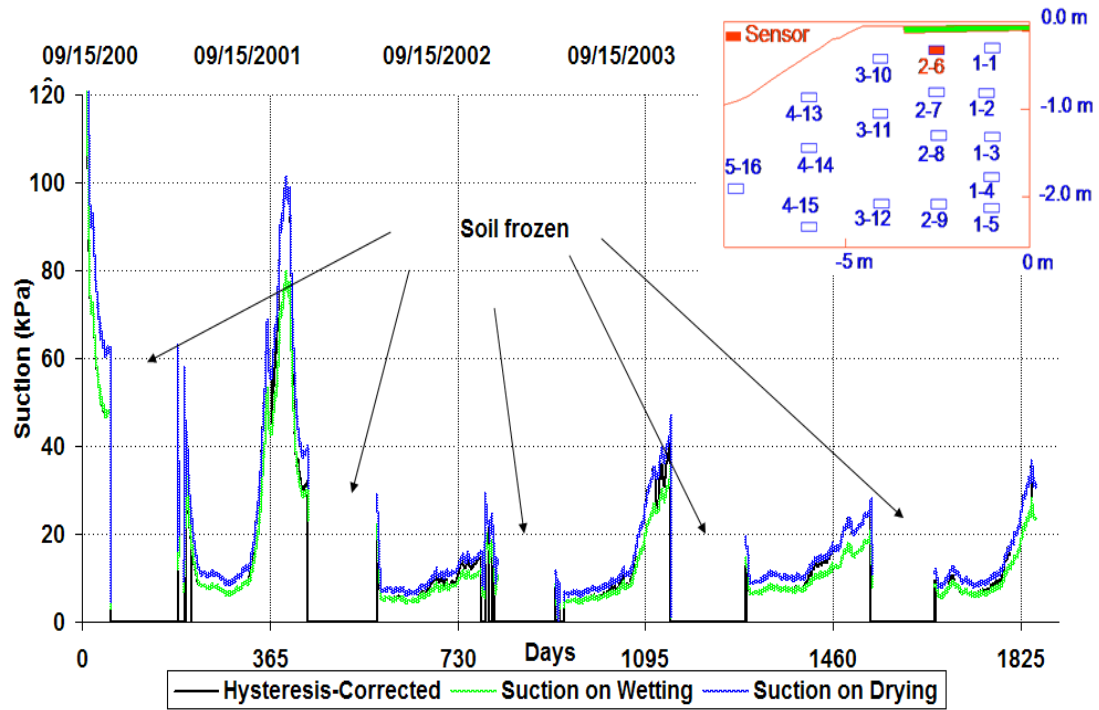


Figure B.4 Suctions with and without hysteresis correction at Sensor T2-6

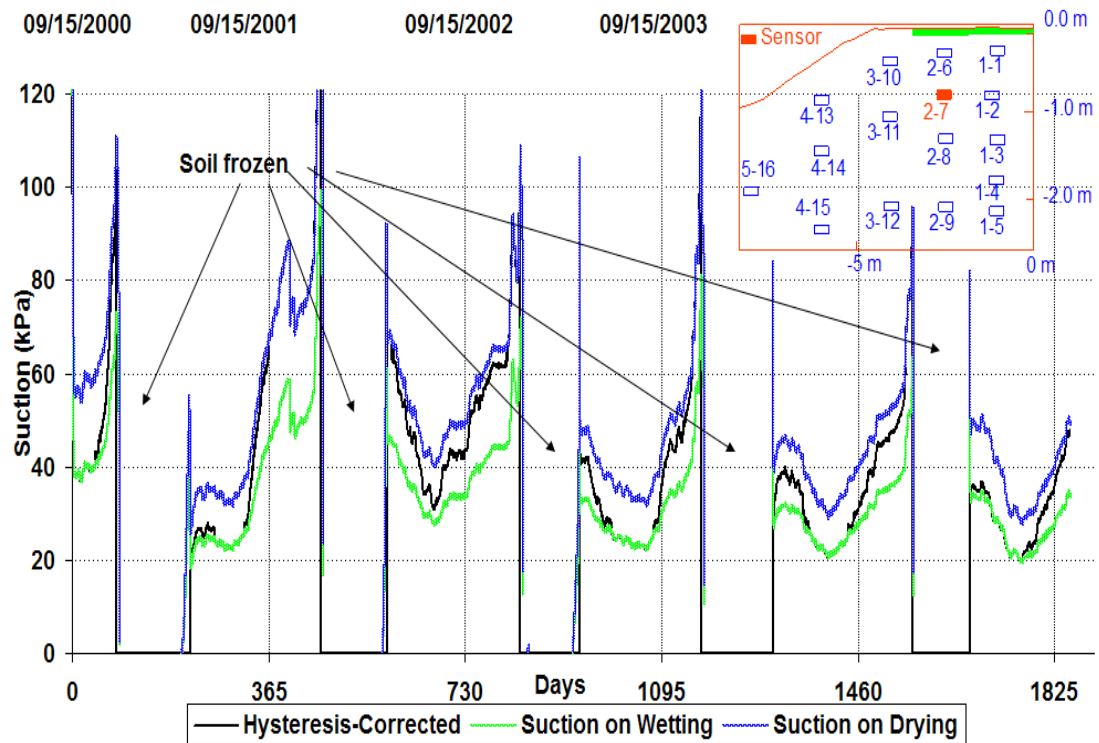


Figure B.5 Suctions with and without hysteresis correction at Sensor T2-7

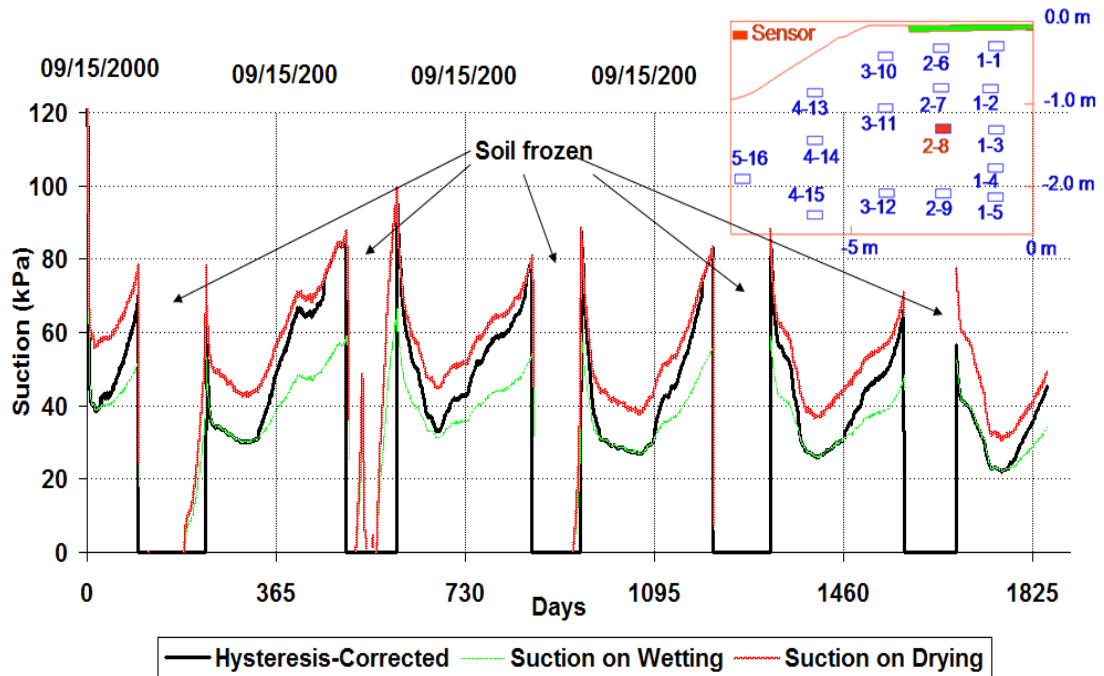


Figure B.6 Suctions with and without hysteresis correction at Sensor T2-8

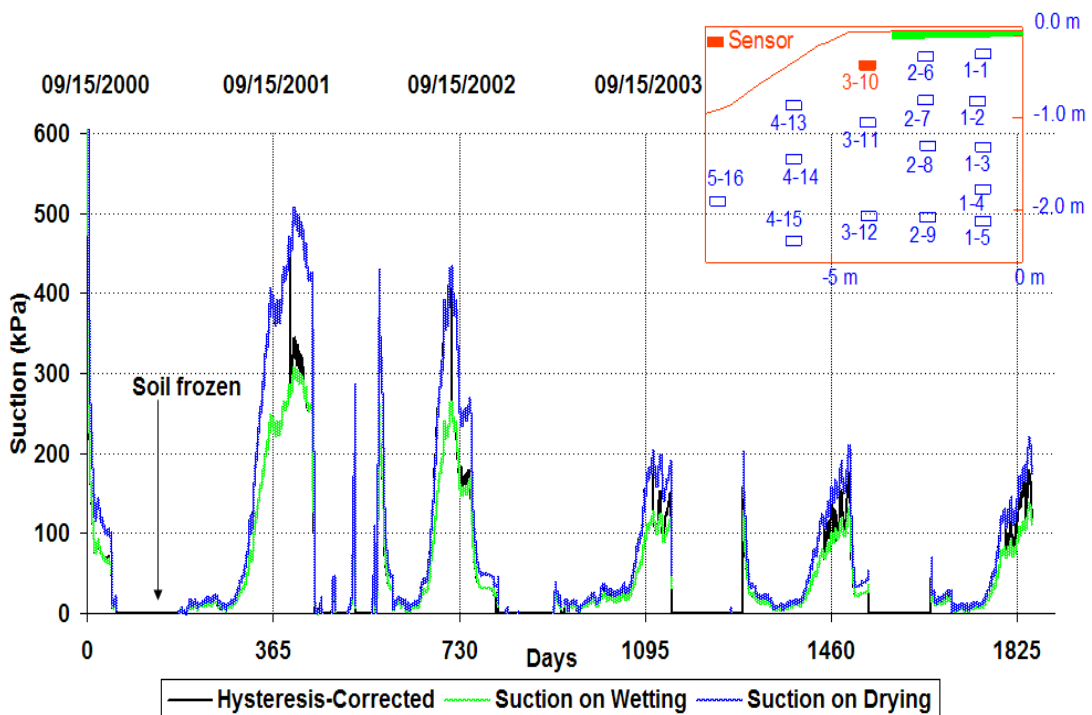


Figure B.7 Suctions with and without hysteresis correction at Sensor T3-10

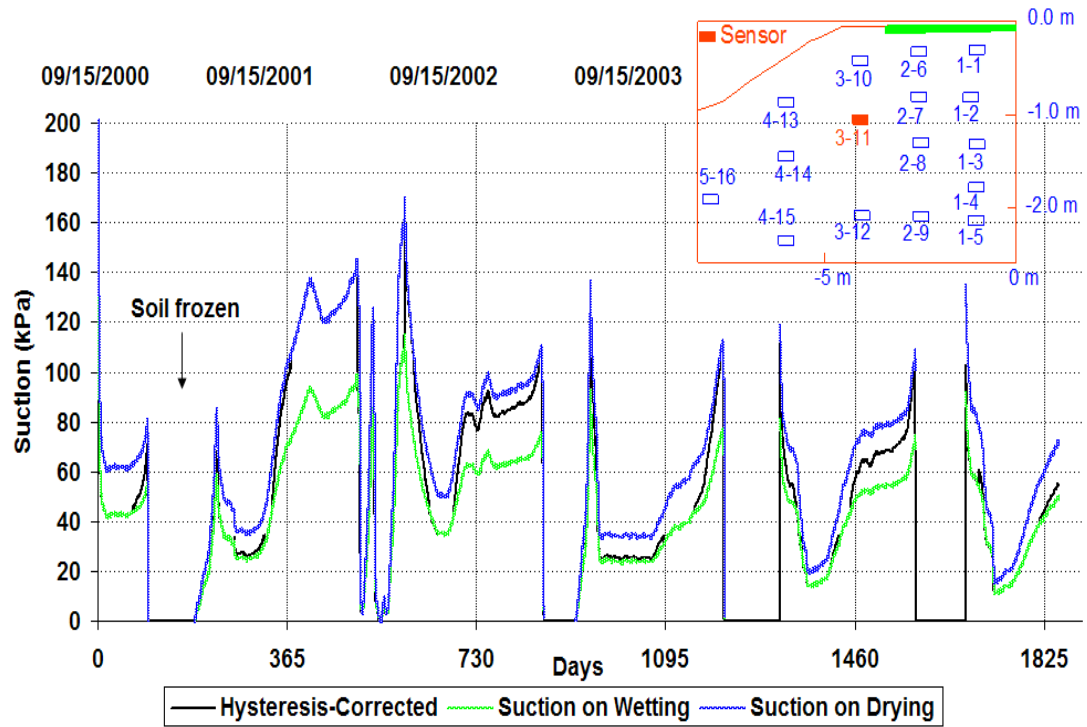


Figure B.8 Suctions with and without hysteresis correction at Sensor T3-11

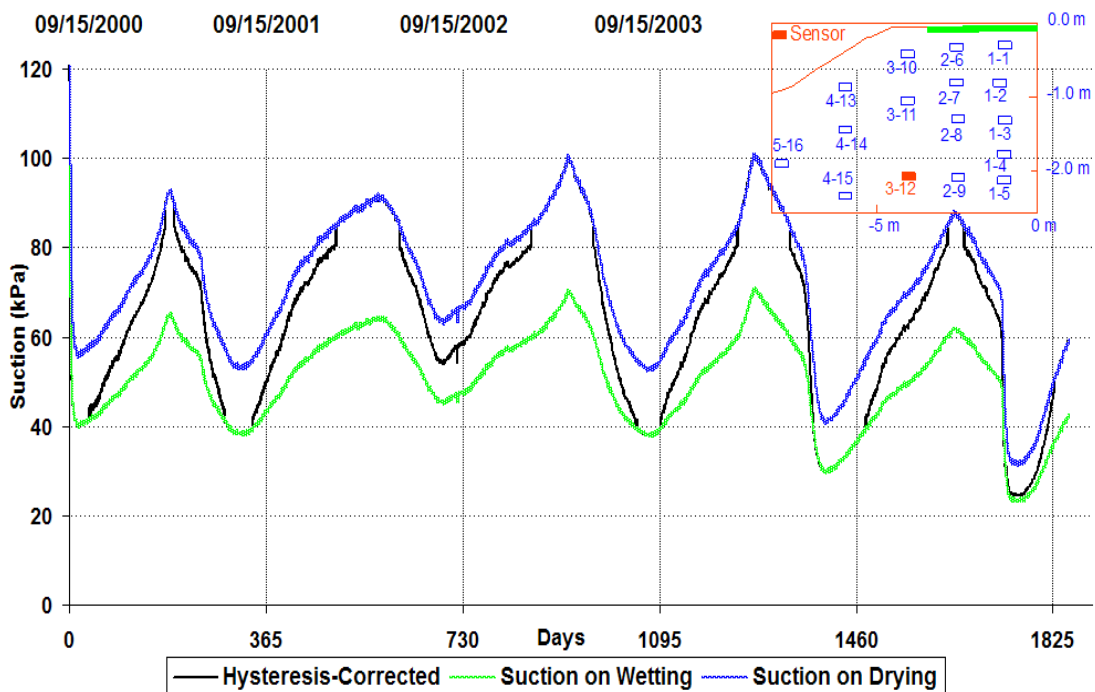


Figure B.9 Suctions with and without hysteresis correction at Sensor T3-12

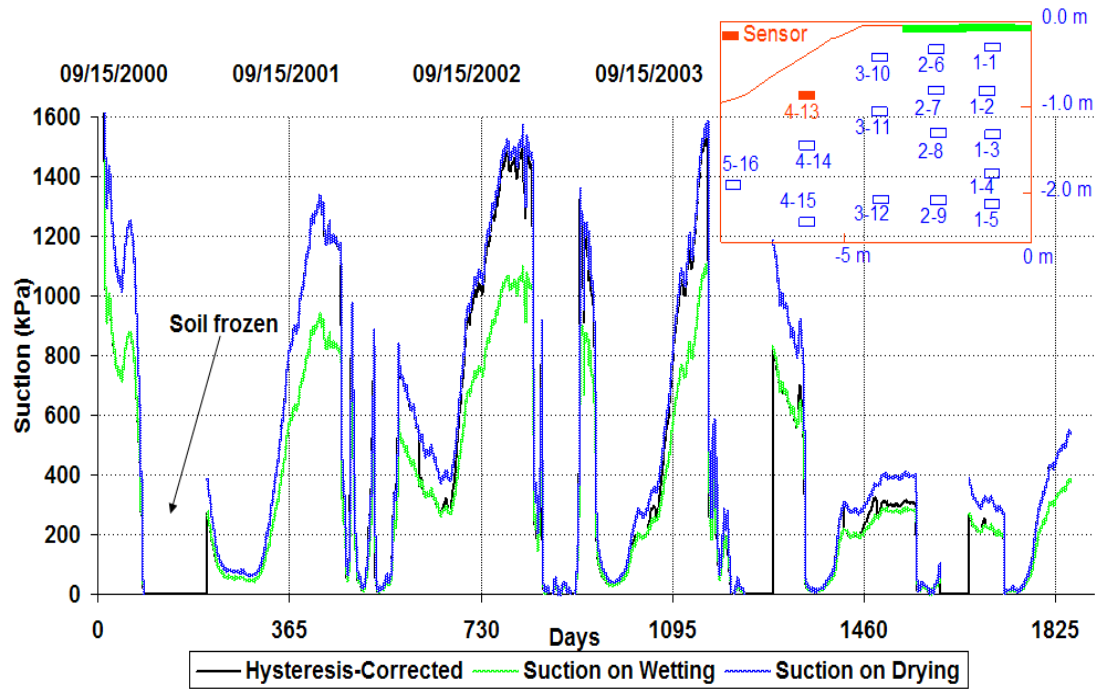


Figure B.10 Suctions with and without hysteresis correction at Sensor T4-13

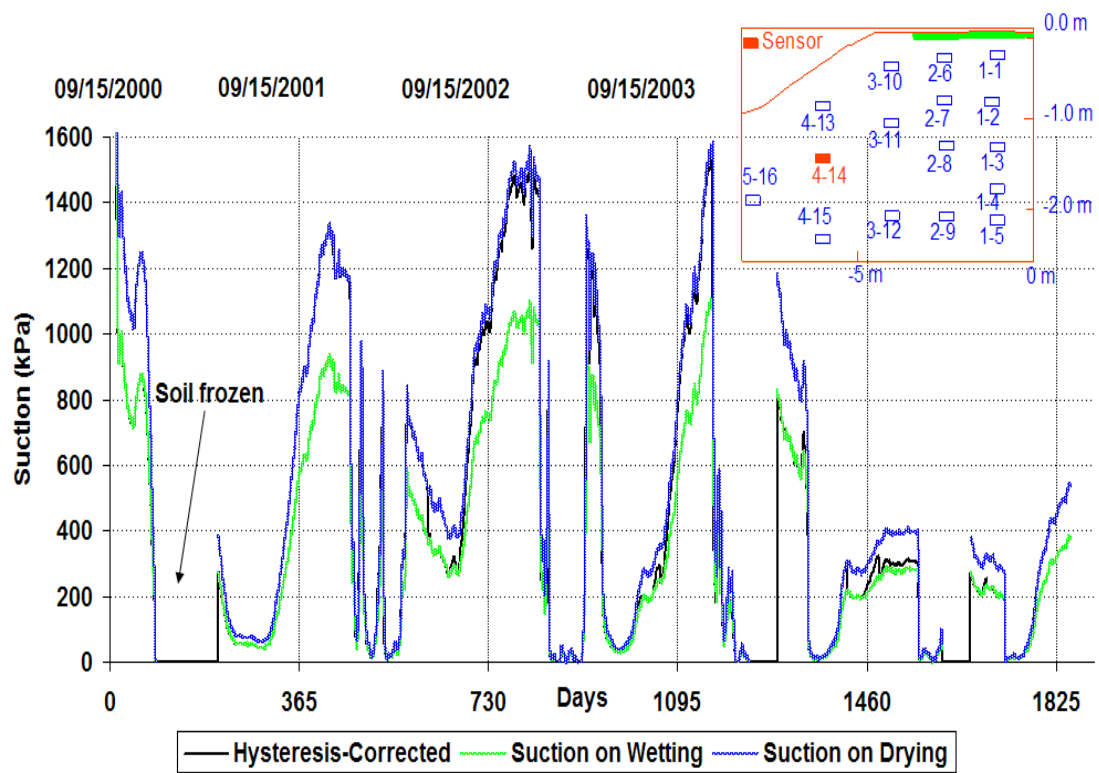


Figure B.11 Suctions with and without hysteresis correction at Sensor T4-14

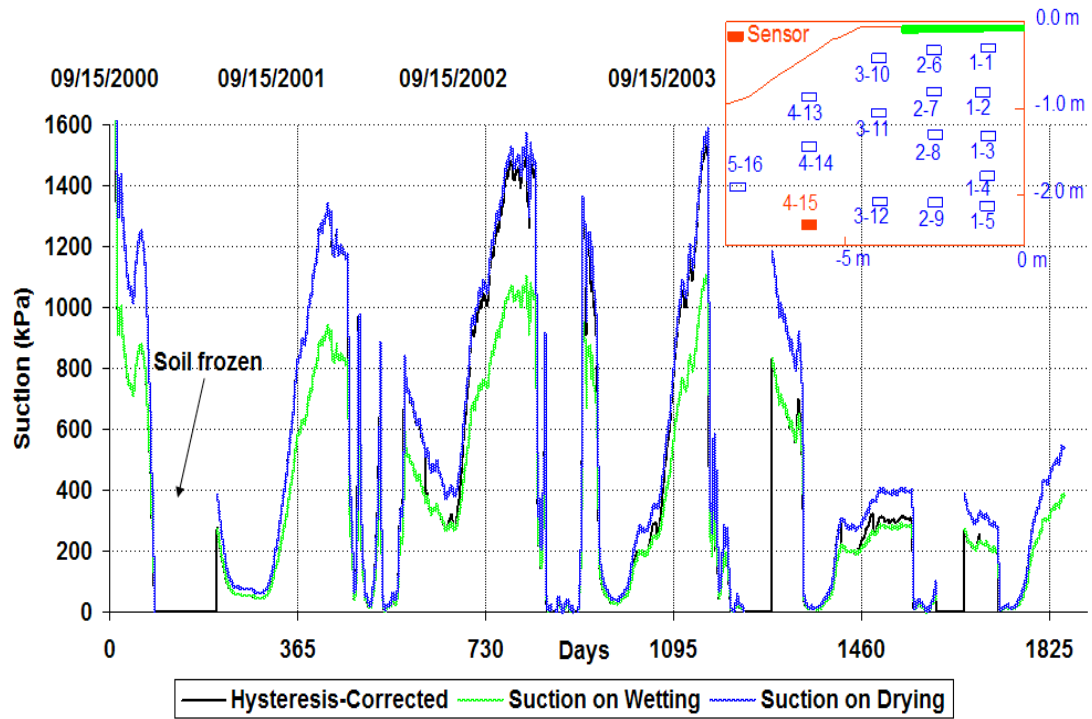


Figure B.12 Suctions with and without hysteresis correction at Sensor T4-15

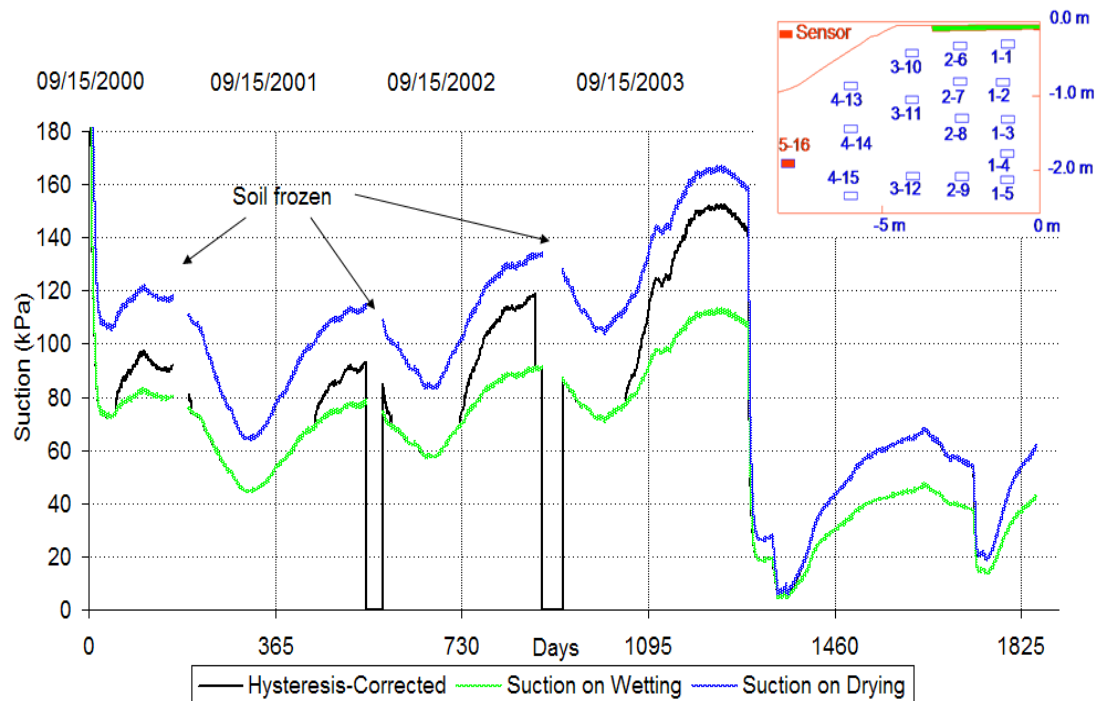


Figure B.13 Suctions with and without hysteresis correction at Sensor T5-16

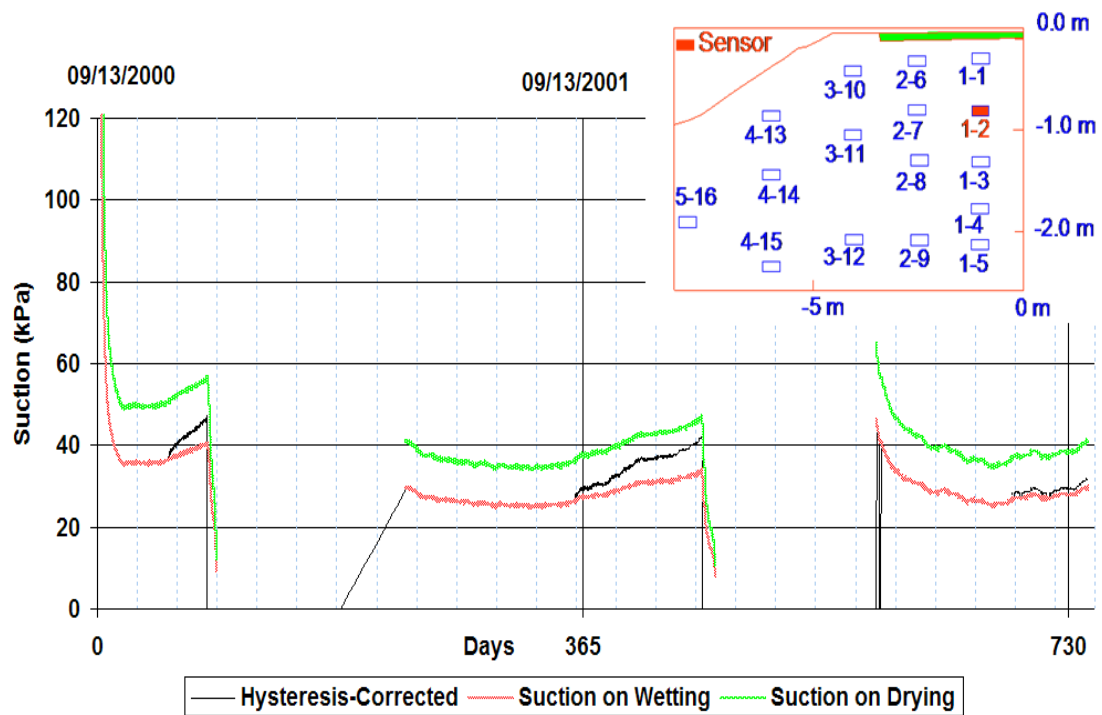


Figure B.14 Suctions with and without hysteresis correction at Sensor B1-2

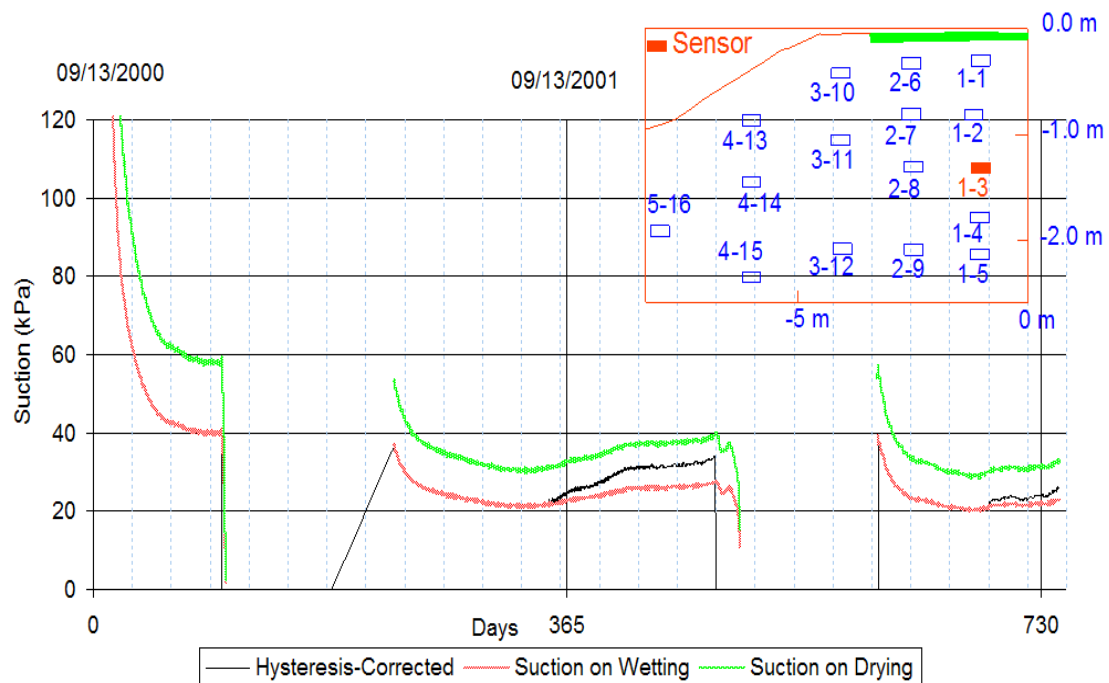


Figure B.15 Suctions with and without hysteresis correction at Sensor B1-3

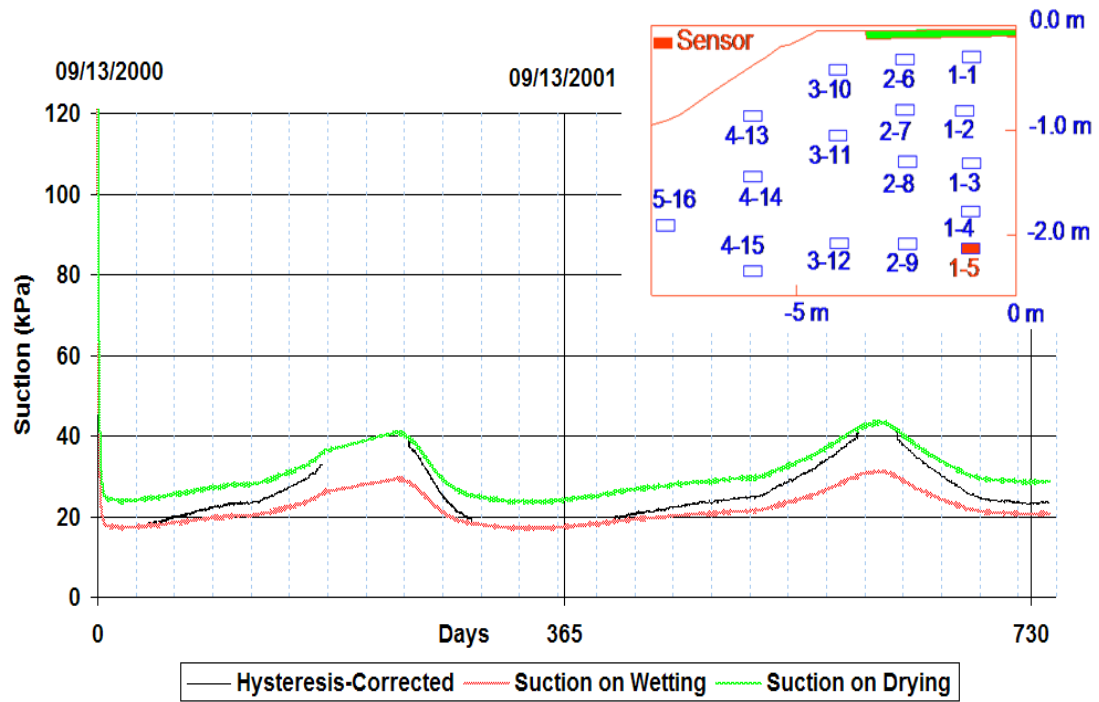


Figure B.16 Suctions with and without hysteresis correction at Sensor B1-5

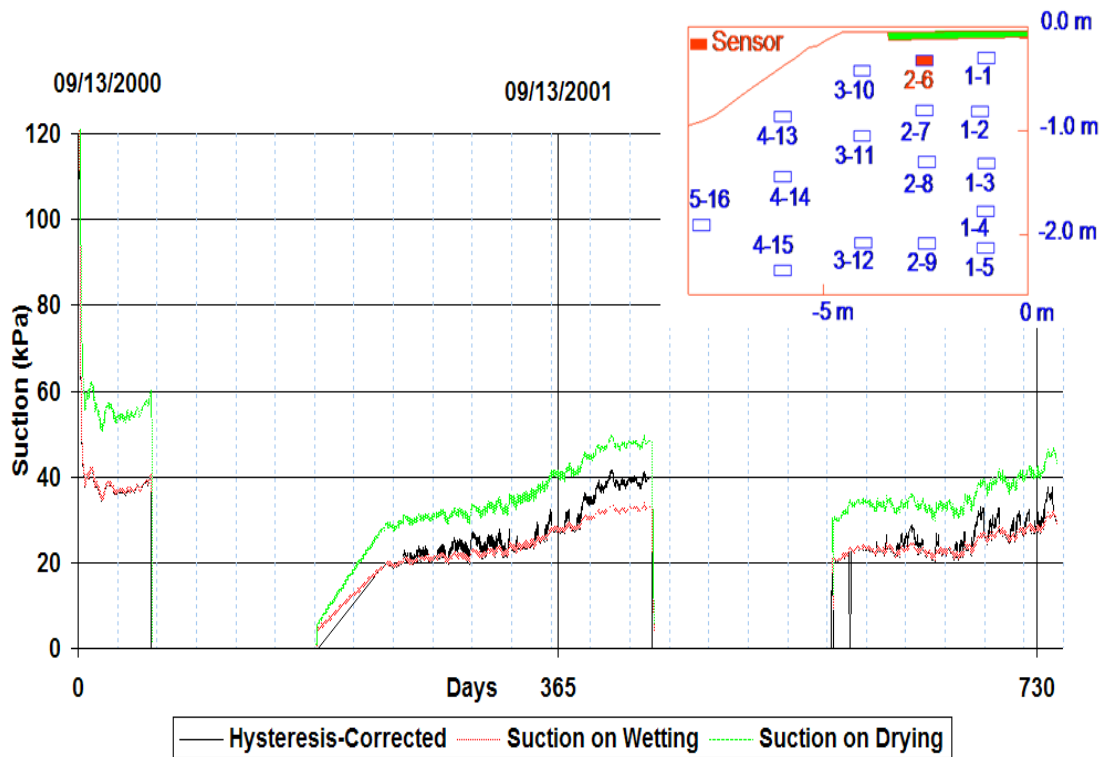


Figure B.17 Suctions with and without hysteresis correction at Sensor B2-6

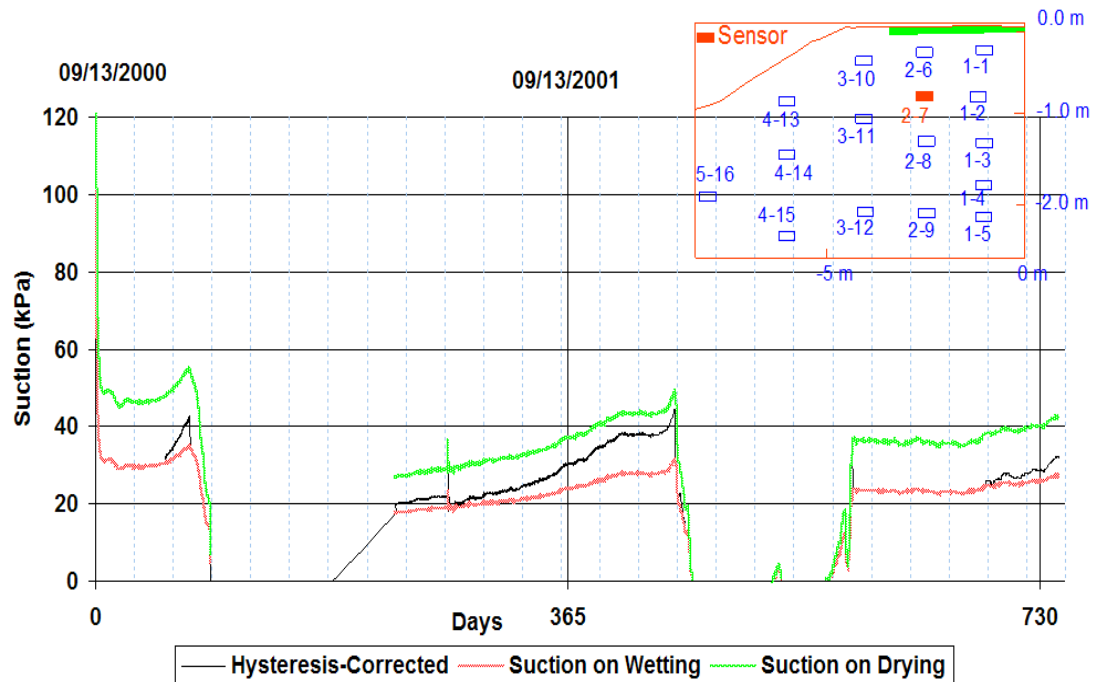


Figure B.18 Suctions with and without hysteresis correction at Sensor B2-7

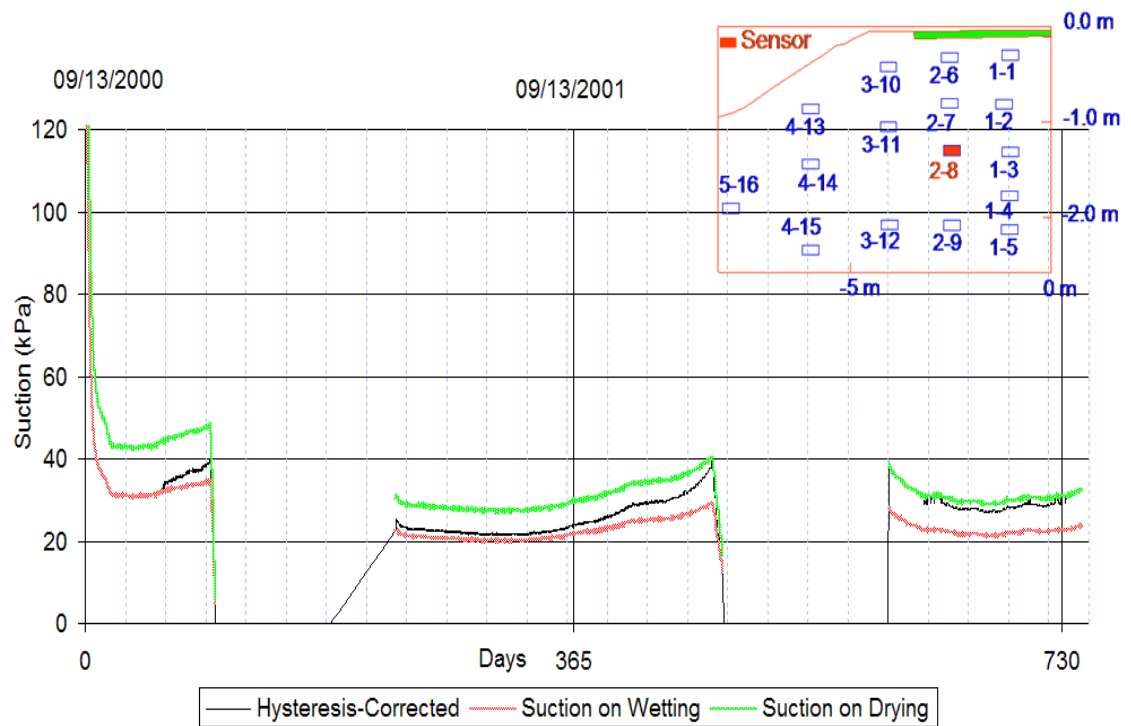


Figure B.19 Suctions with and without hysteresis correction at Sensor B2-8

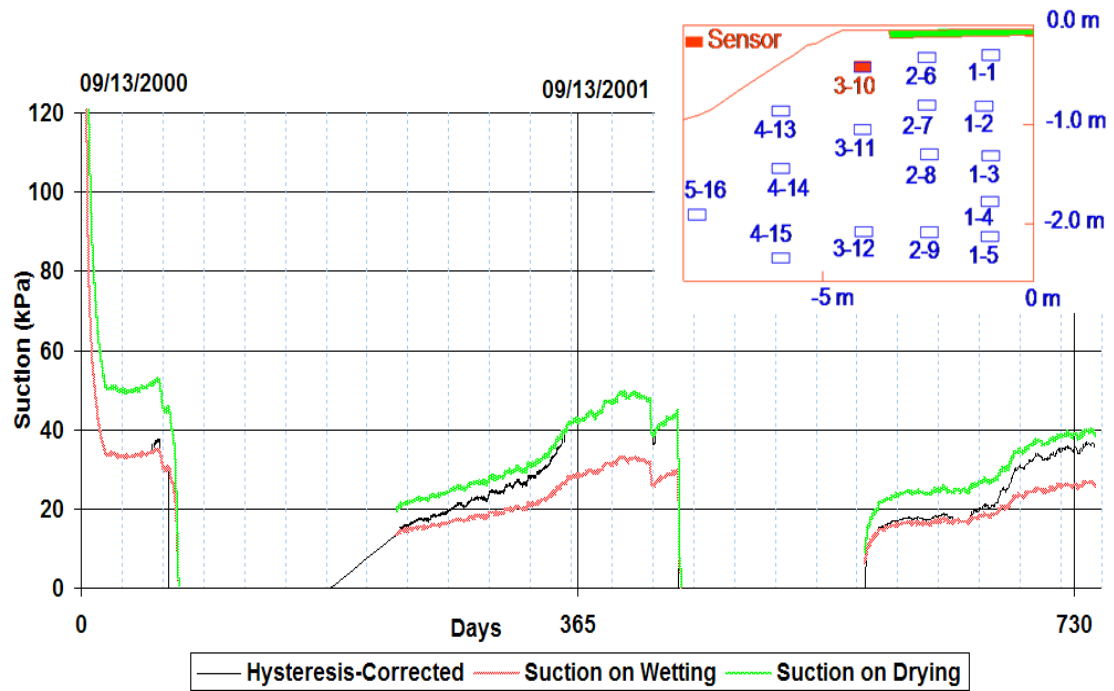


Figure B.20 Suctions with and without hysteresis correction at Sensor B3-10

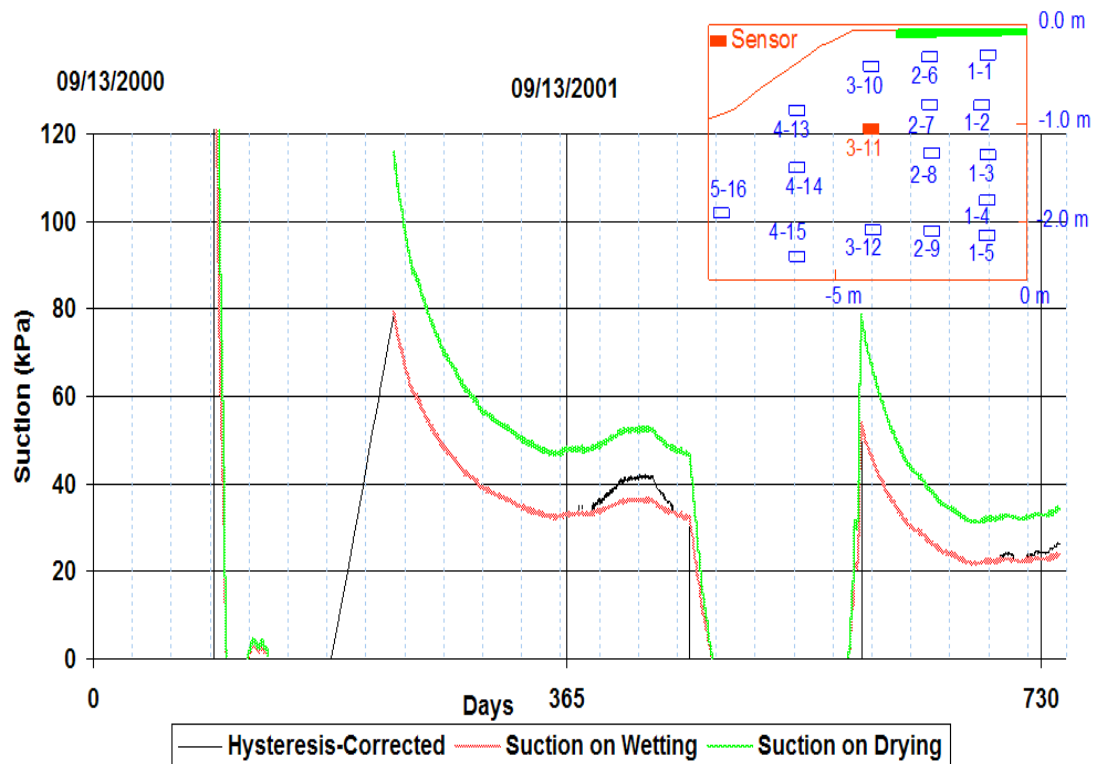


Figure B.21 Suctions with and without hysteresis correction at Sensor B3-11

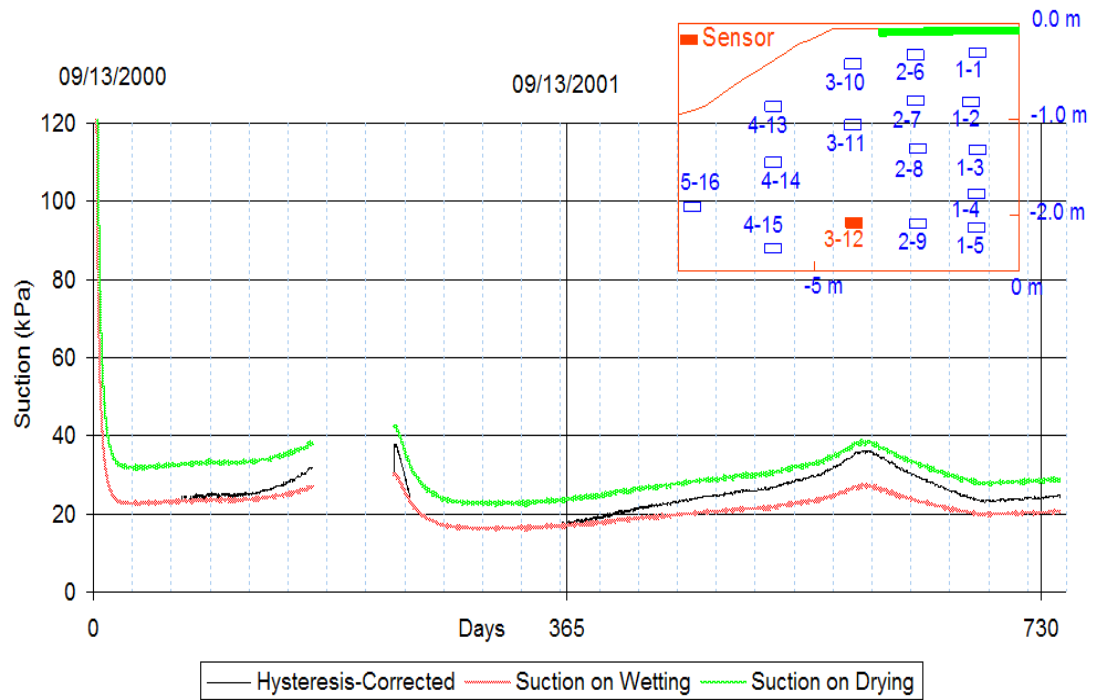


Figure B.22 Suctions with and without hysteresis correction at Sensor B3-12

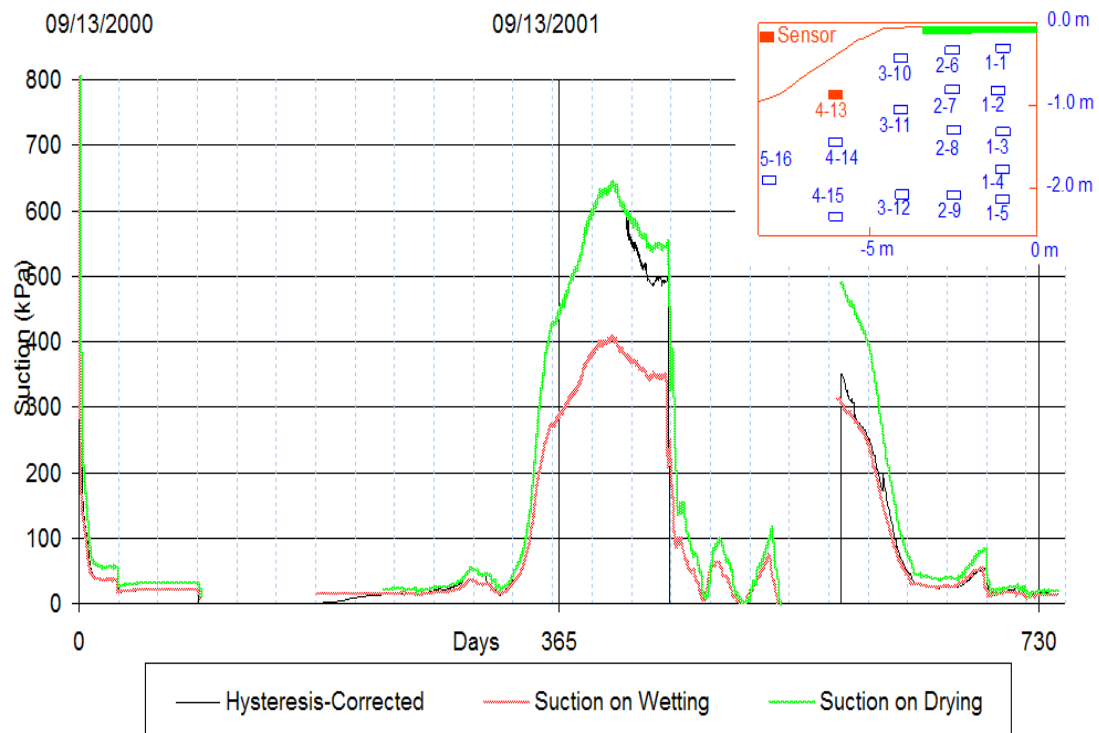


Figure B.23 Suctions with and without hysteresis correction at Sensor B4-13

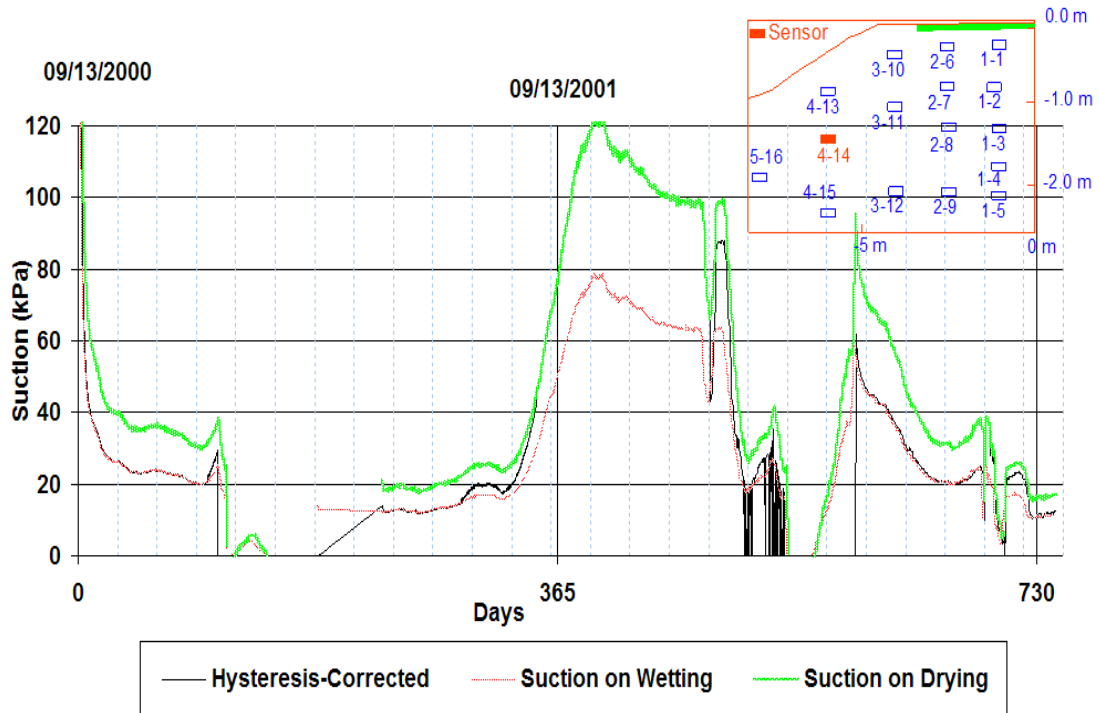


Figure B.24 Suctions with and without hysteresis correction at Sensor B4-14

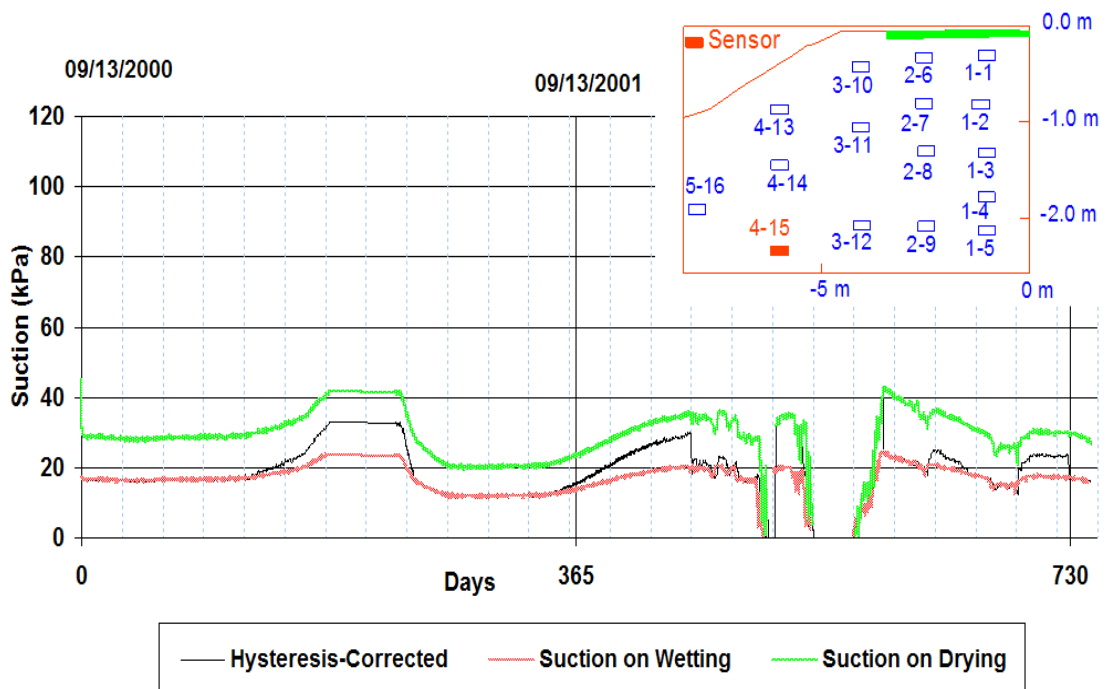


Figure B.25 Suctions with and without hysteresis correction at Sensor B4-15

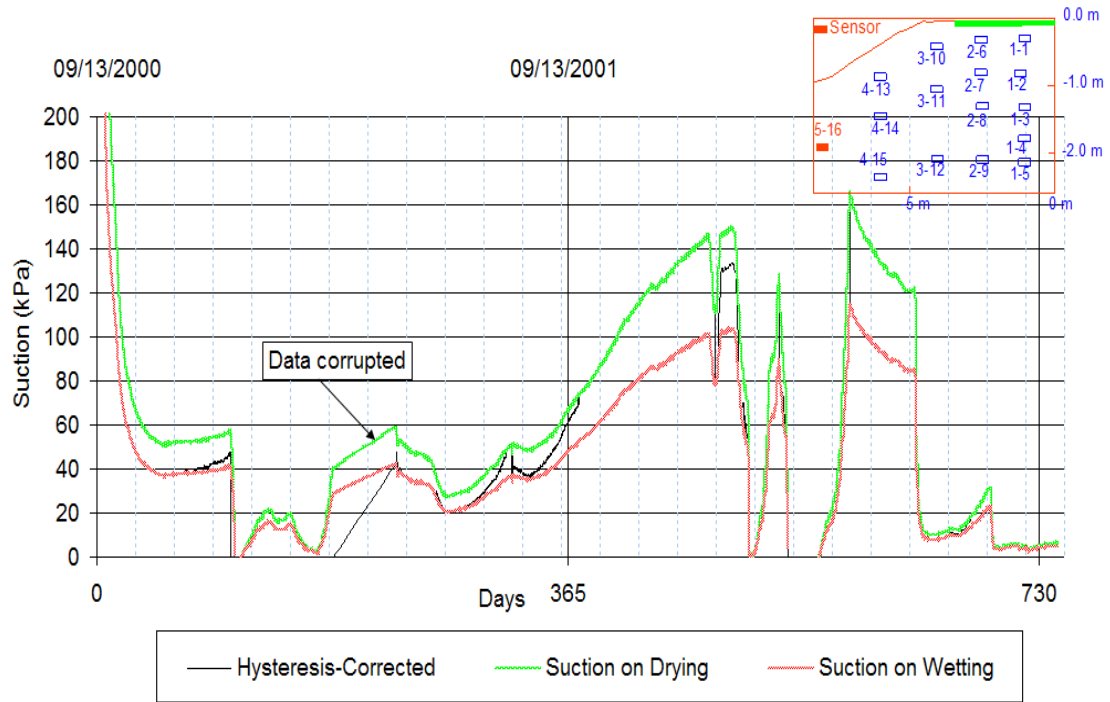


Figure B.25 Suctions with and without hysteresis correction at Sensor B5-16

B.3 Contour maps of matric suctions

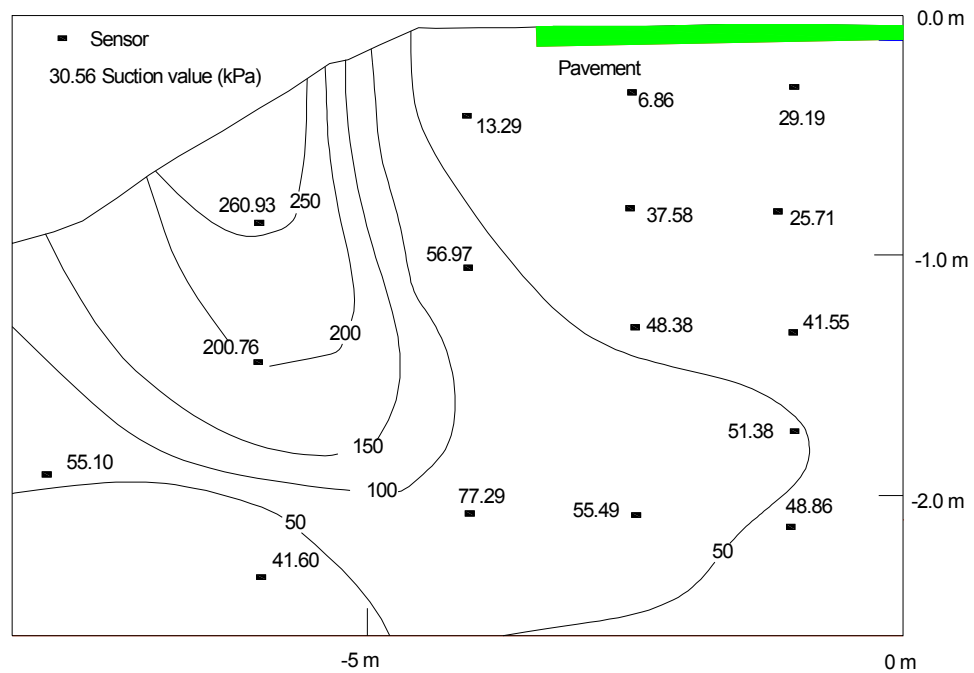


Figure B.26 Contour map of matric suctions in May at Torquay

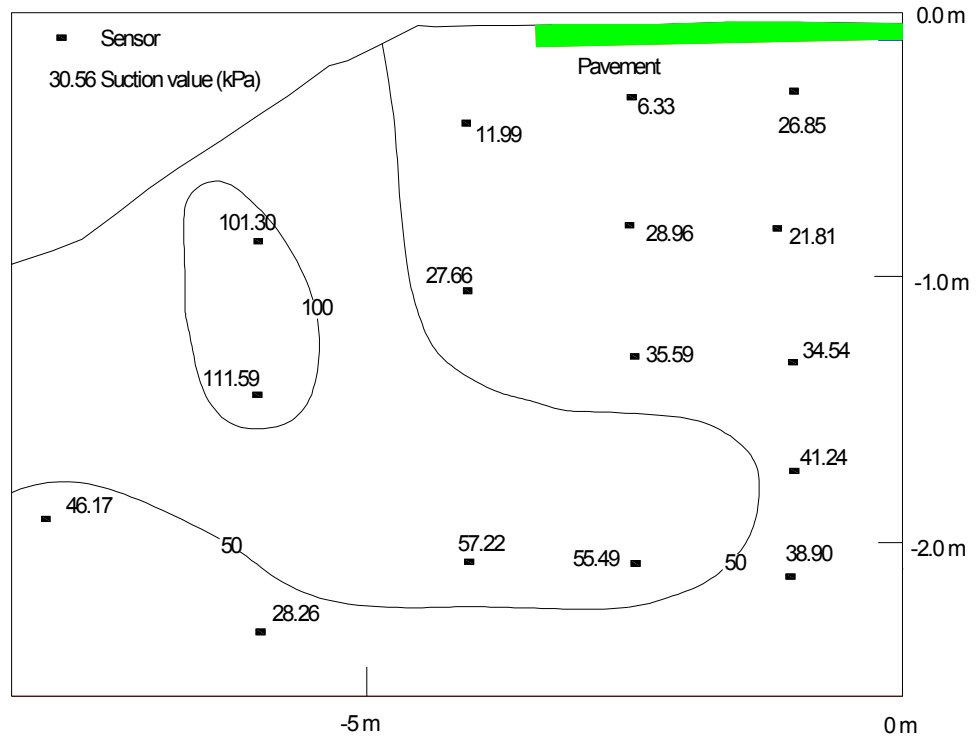


Figure B.27 Contour map of matric suctions in June at Torquay

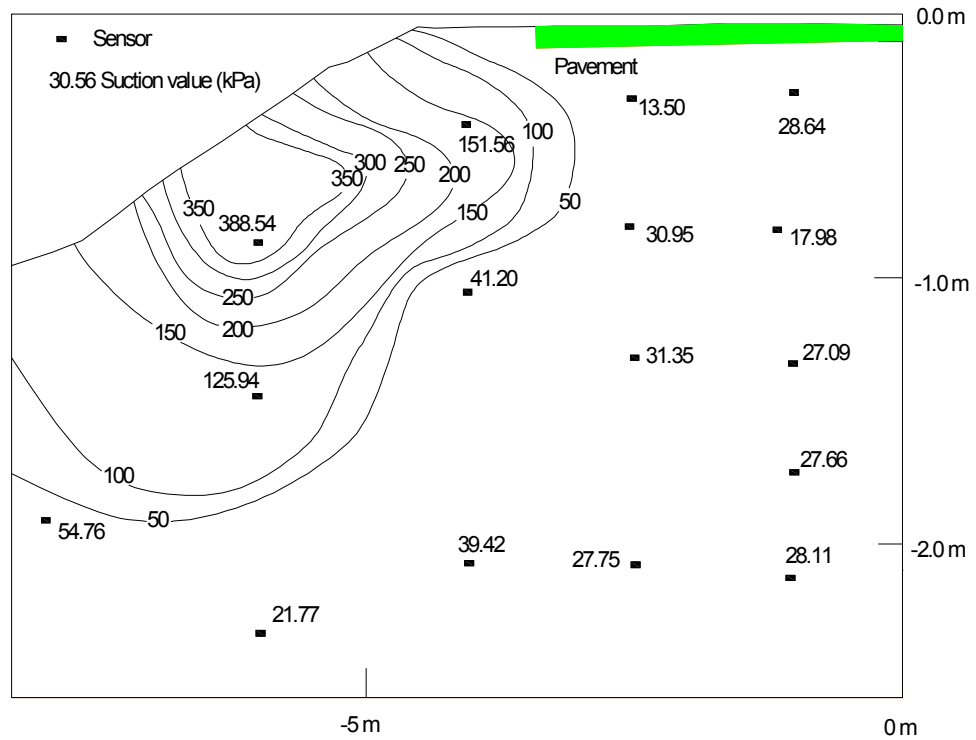


Figure B.28 Contour map of matric suctions in August at Torquay

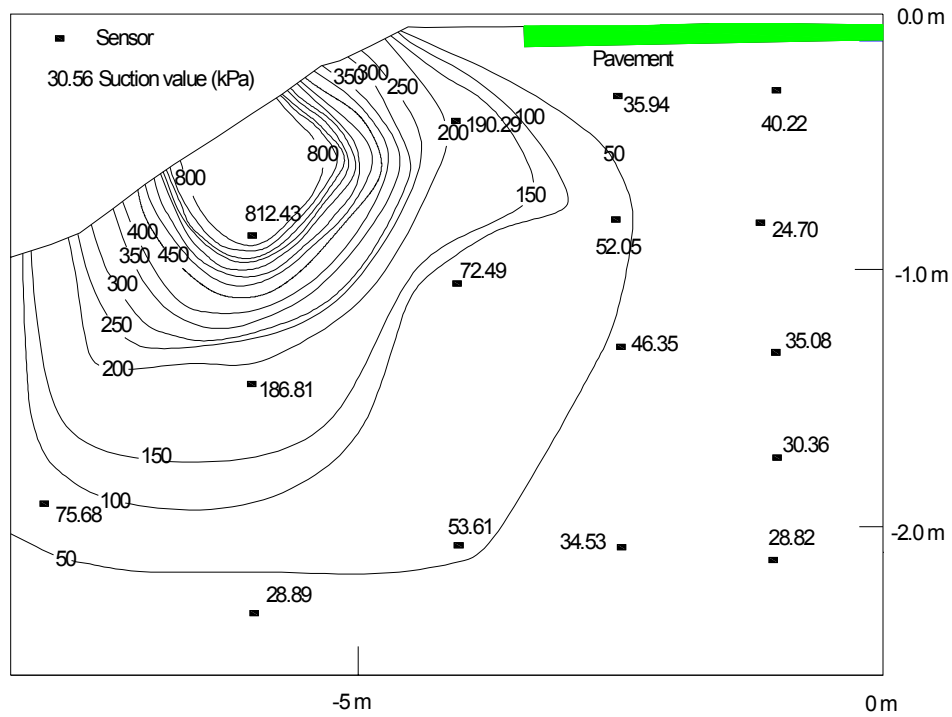


Figure B.29 Contour map of matric suctions in October at Torquay

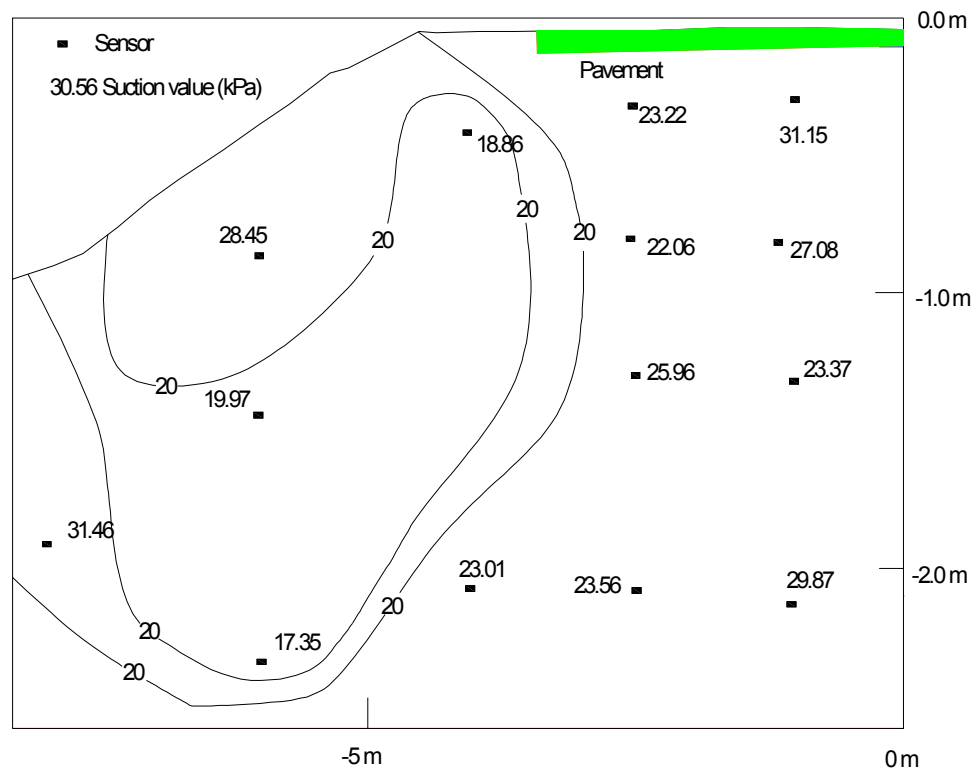


Figure B.30 Contour map of matric suctions in June at Bethune

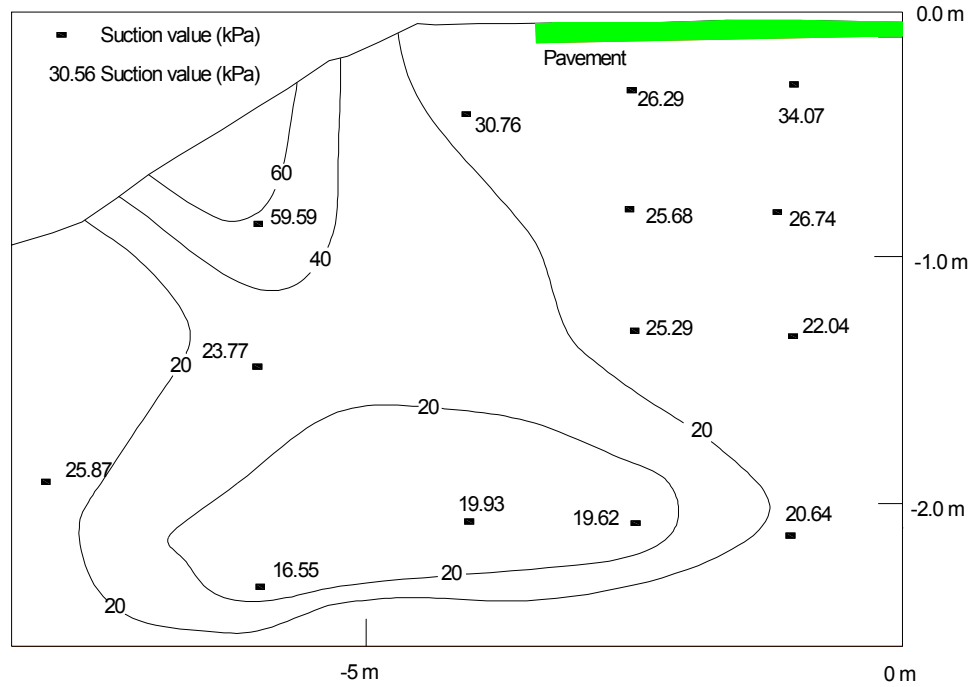


Figure B.31 Contour map of matric suctions in August at Bethune

B.4 Suctions along vertical and horizontal grid-lines at Torquay

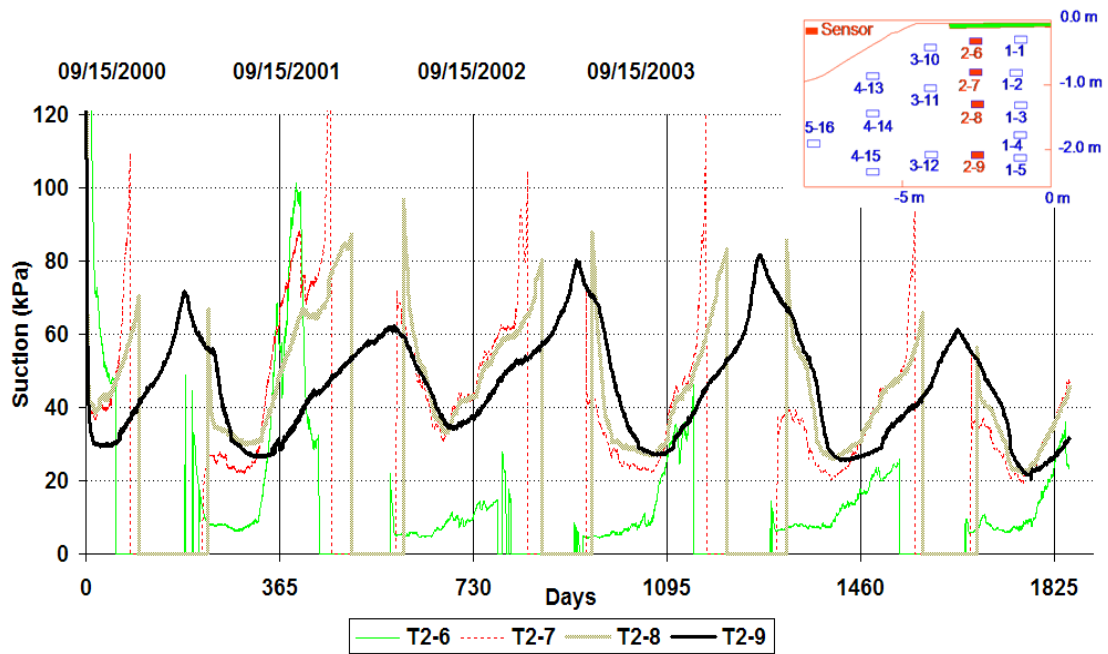


Figure B.32 Suctions along outer vertical grid-line under driving lane at Torquay

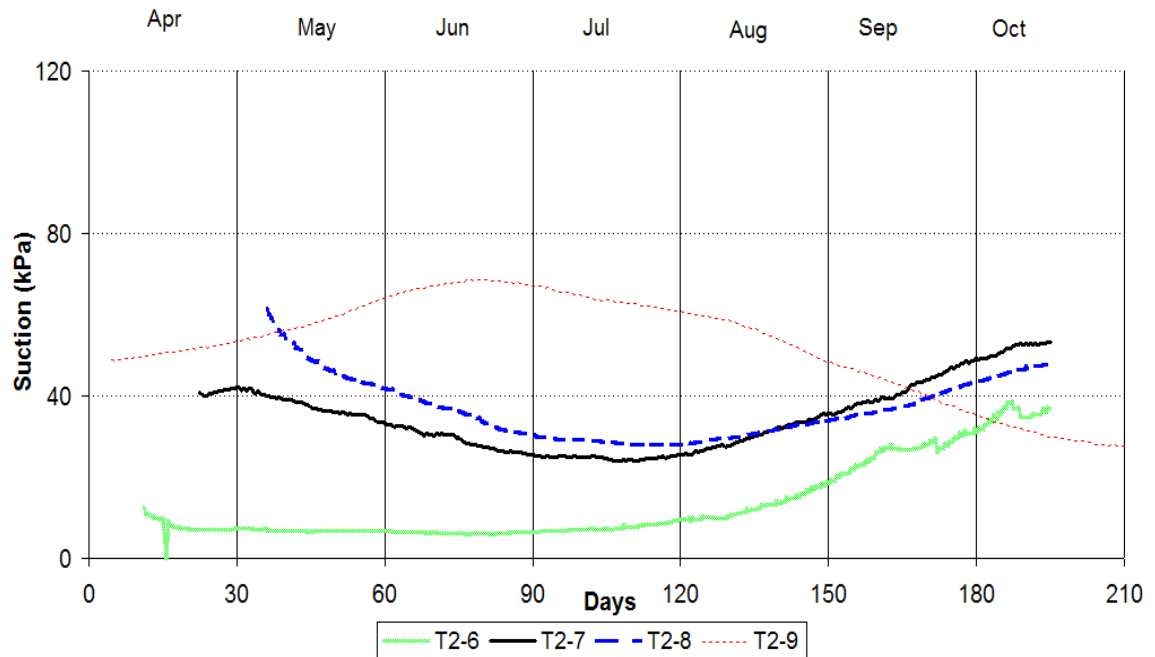


Figure B.33 Five-year average suctions along outer vertical grid-line under driving lane at Torquay

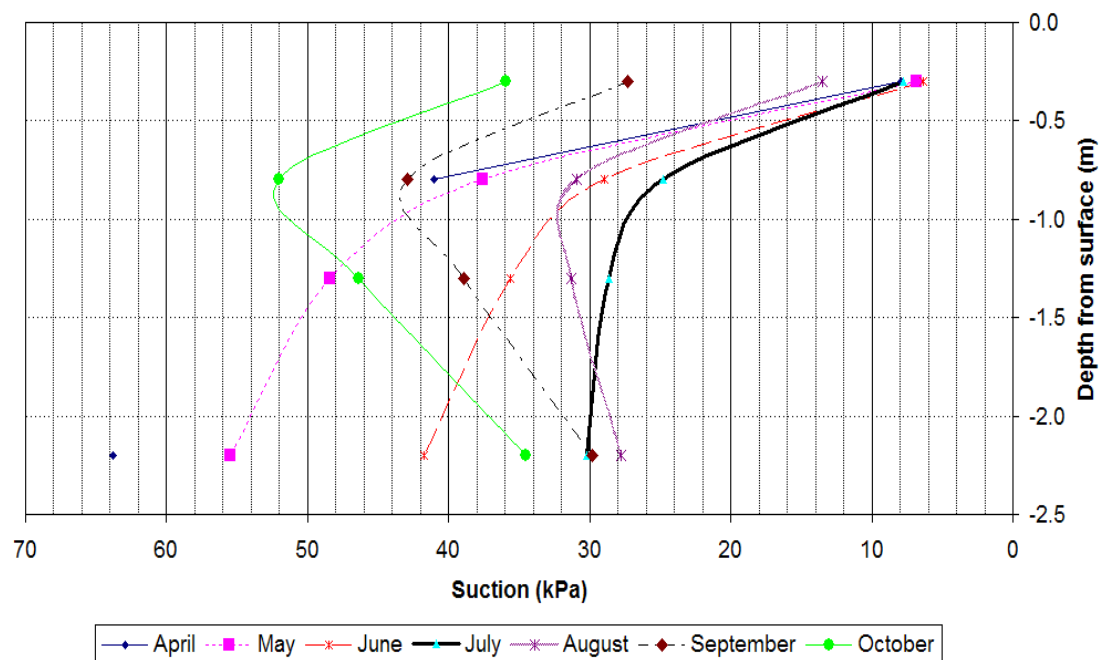


Figure B.34 Five-year average suctions versus depth along outer vertical grid-line under driving lane at Torquay

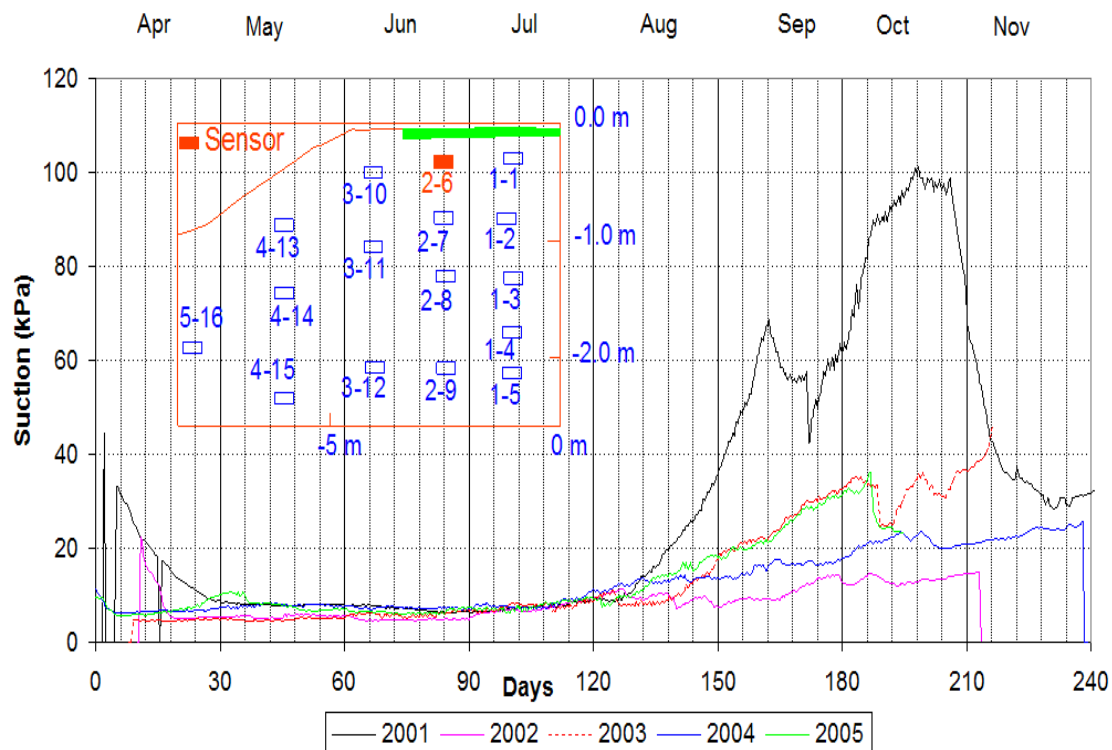


Figure B.35 Suctions at Sensor T2-6 for years 2001 to 2005 at Torquay

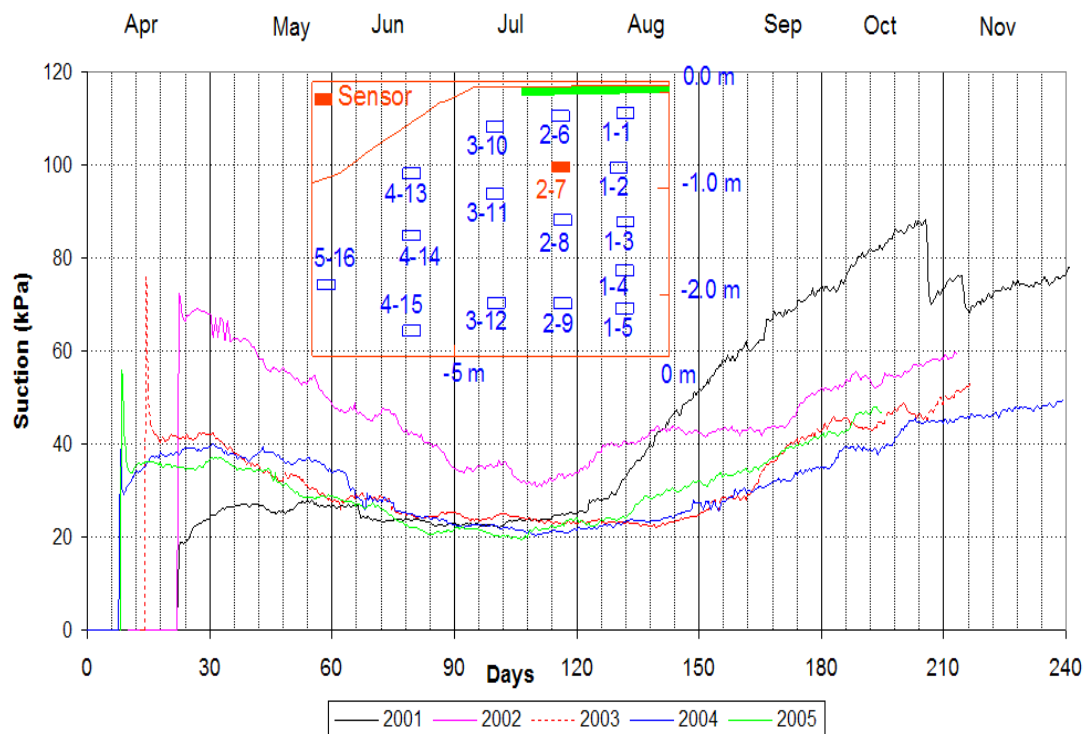


Figure B.36 Suctions at Sensor T2-7 for years 2001 to 2005 at Torquay

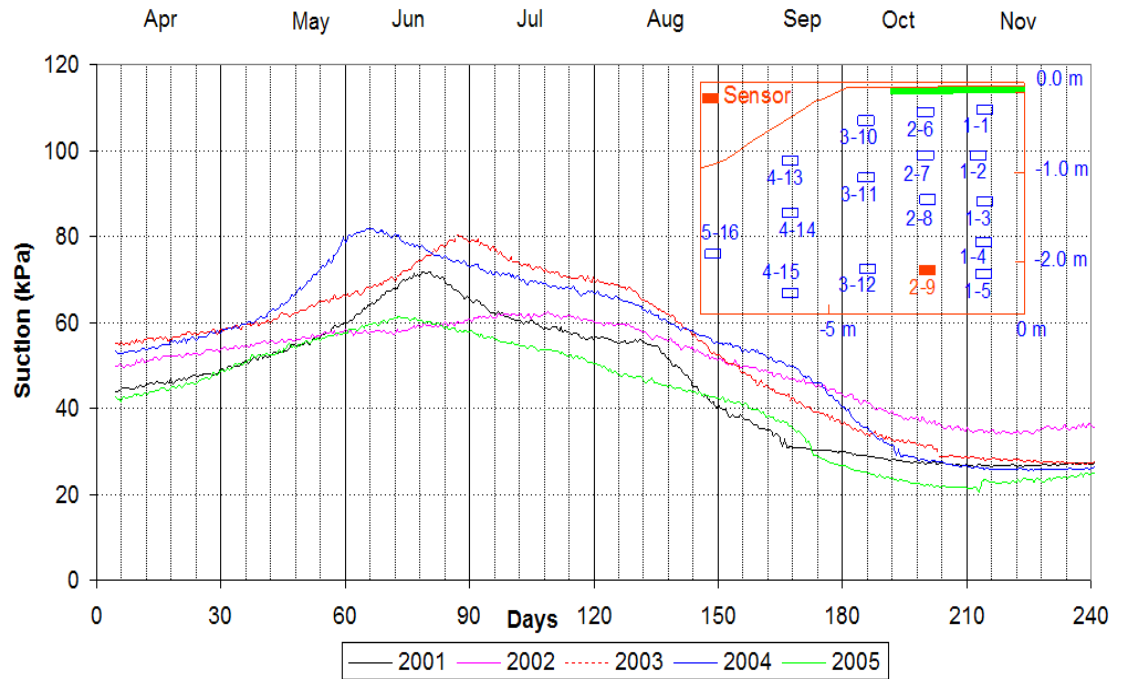


Figure B.37 Suctions at Sensor T2-9 for years 2001 to 2005 at Torquay

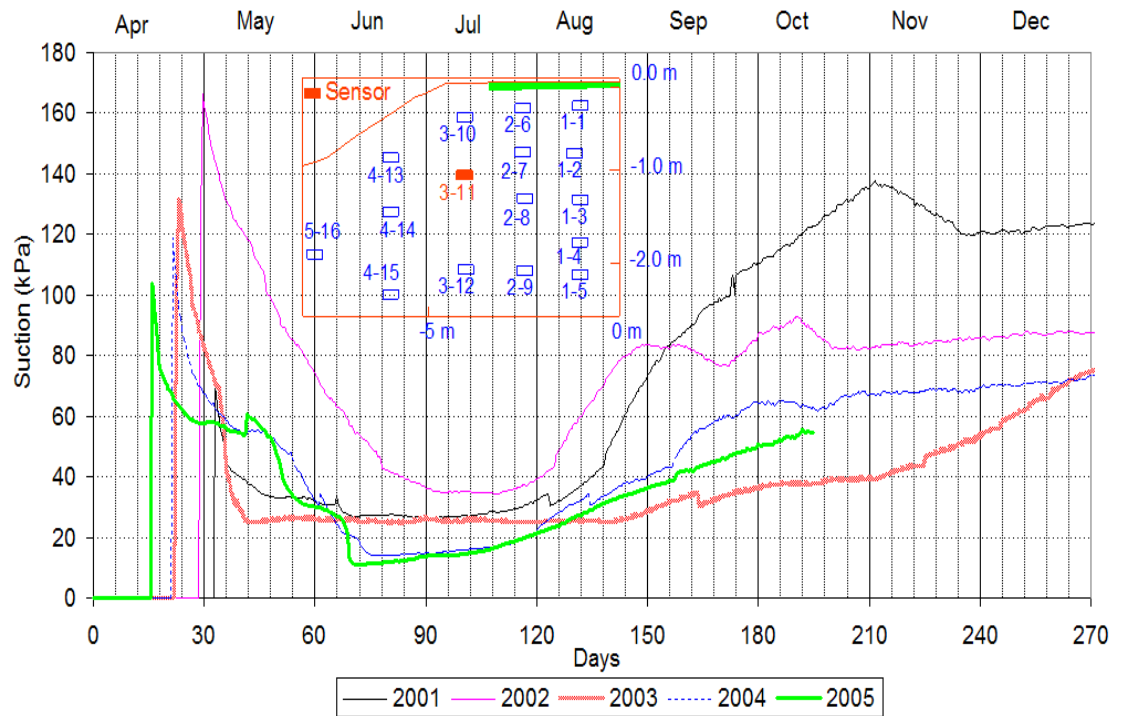


Figure B.38 Suctions at Sensor T3-11 for years 2001 to 2005 at Torquay

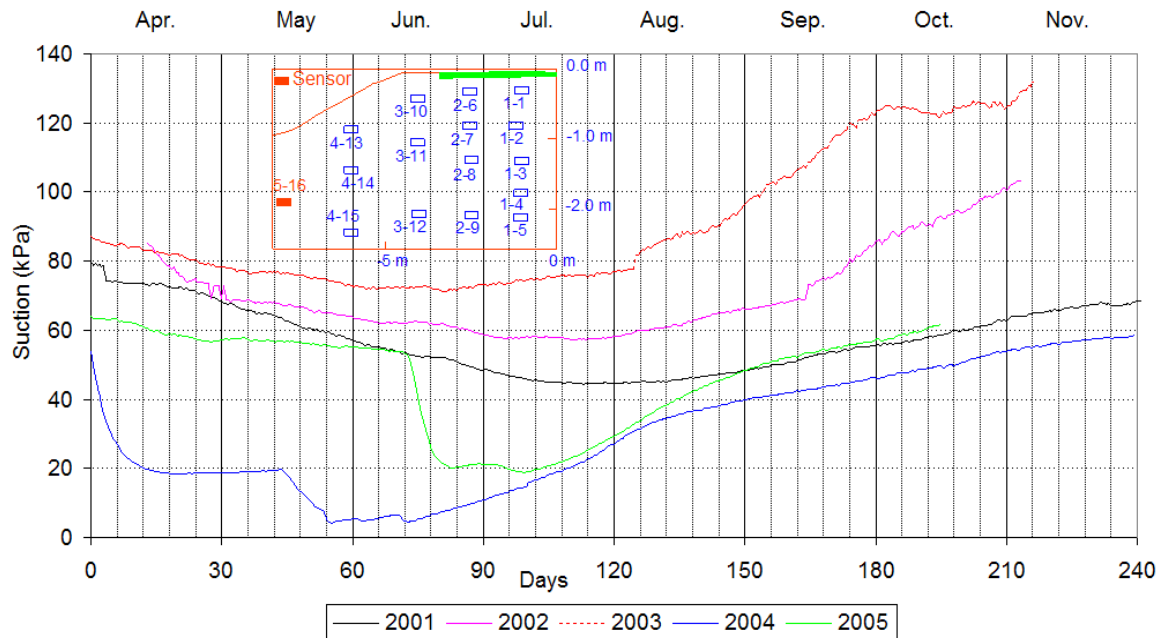


Figure B.39 Suctions at Sensor T5-16 for years 2001 to 2005 at Torquay

B.5 Suctions along vertical and horizontal grid-lines at Bethune

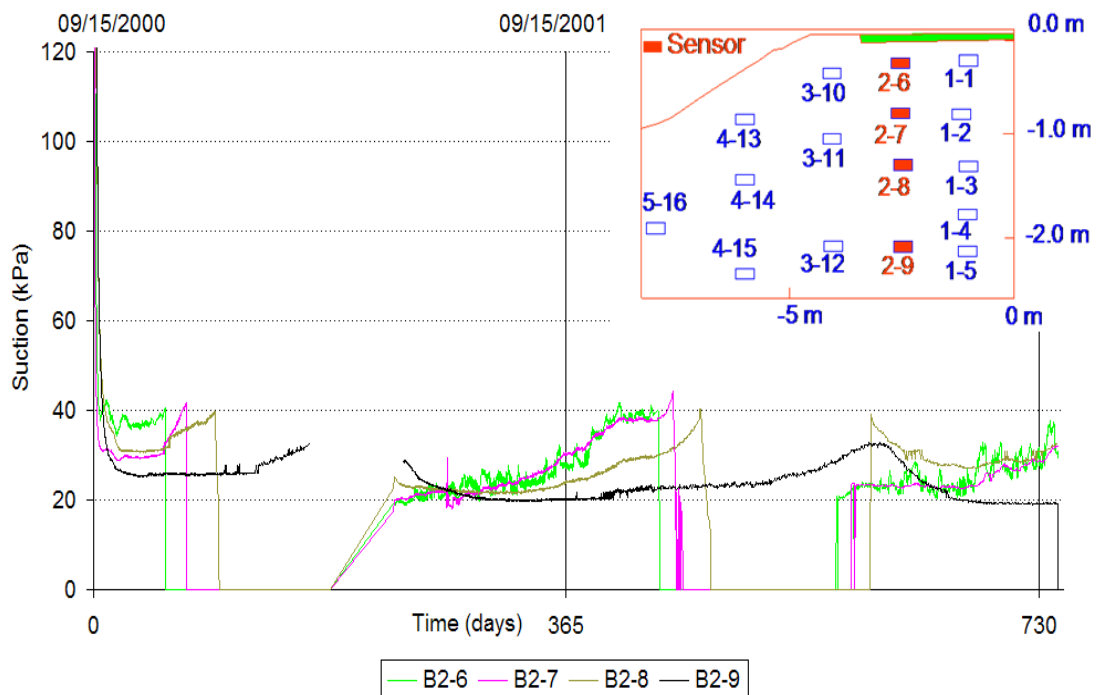


Figure B.40 Suctions along outer vertical grid-line under driving-lane at Bethune

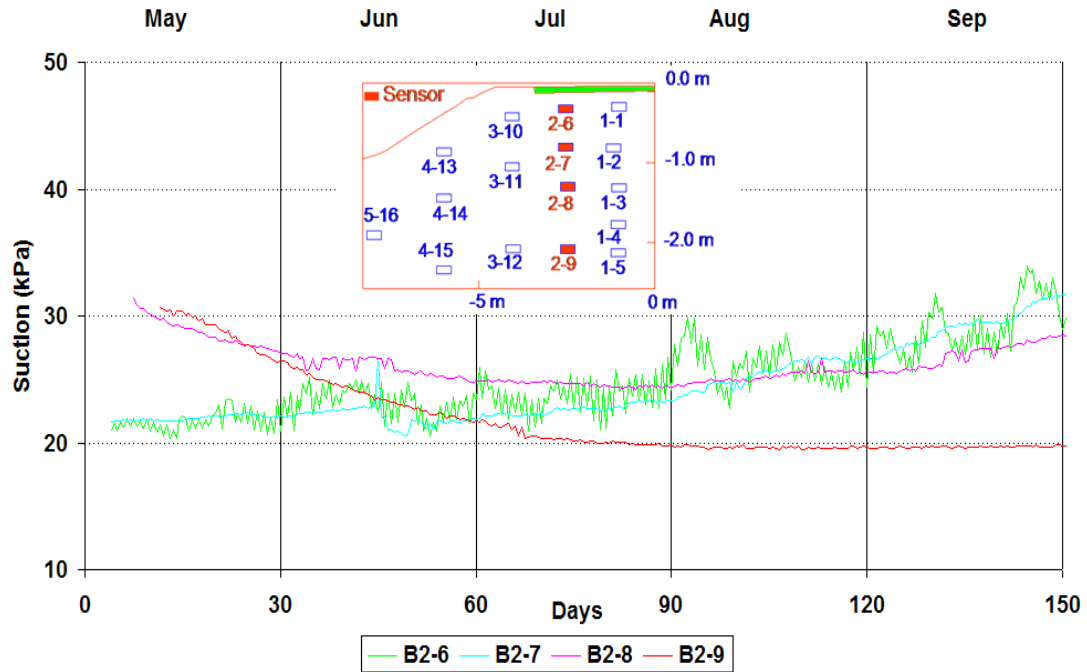


Figure B.41 Two-year average suctions along outer vertical grid-line under driving-lane at Bethune

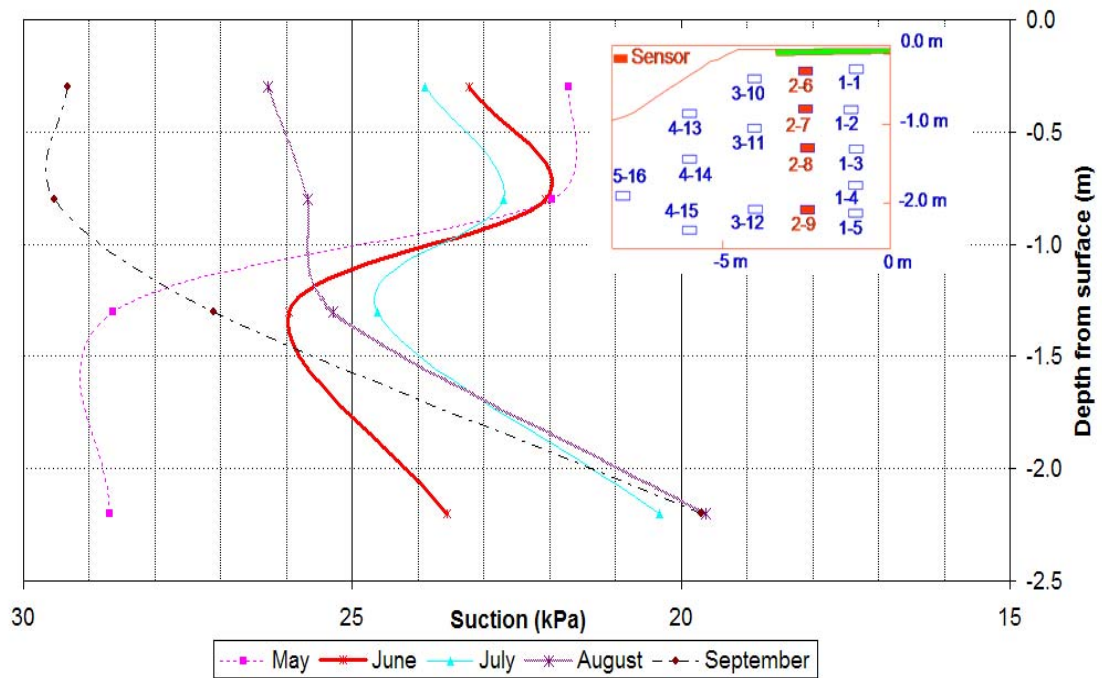


Figure B.42 Two-year average suctions versus depth along outer vertical grid-line under driving-lane at Bethune

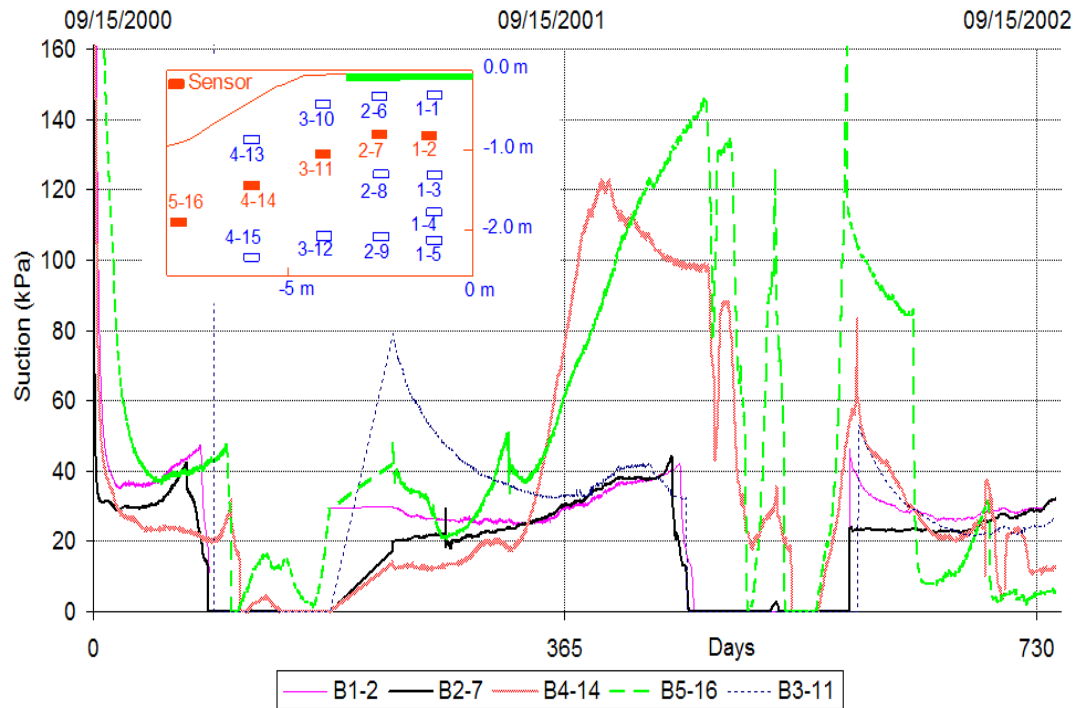


Figure B.43 Suctions along horizontal middle-depth sensors at Bethune

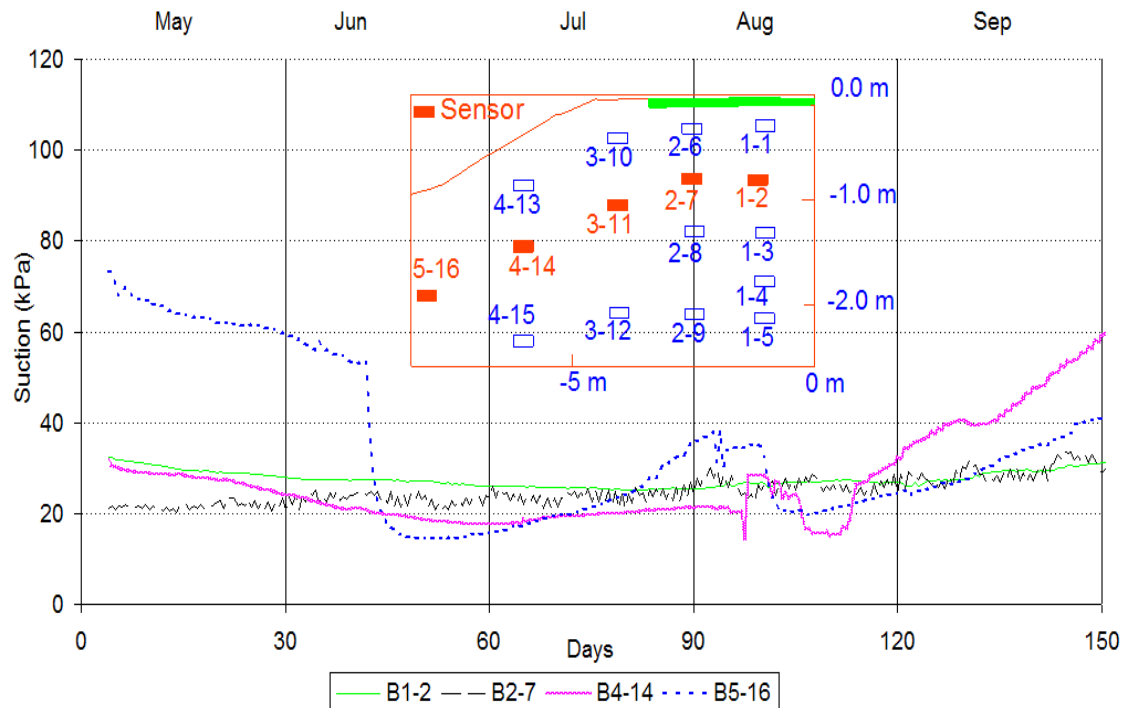


Figure B.44 Two-year average suctions along horizontal middle-depth sensors at Bethune

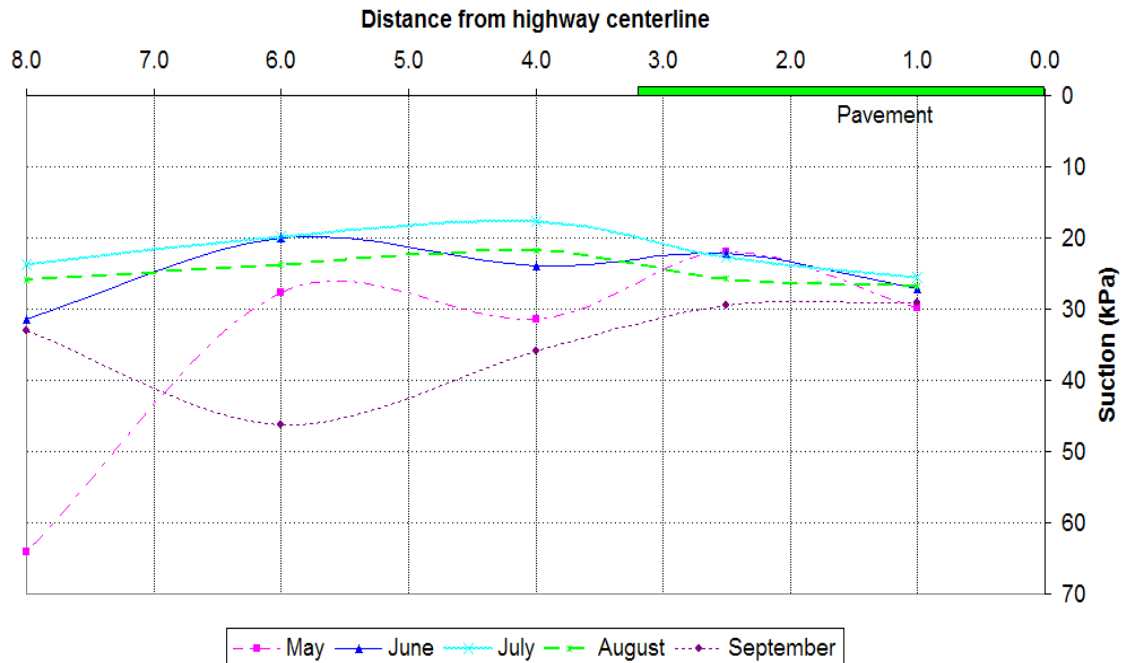


Figure B.45 Two-year average suctions versus distance from the highway centerline along horizontal middle-depth sensors at Bethune

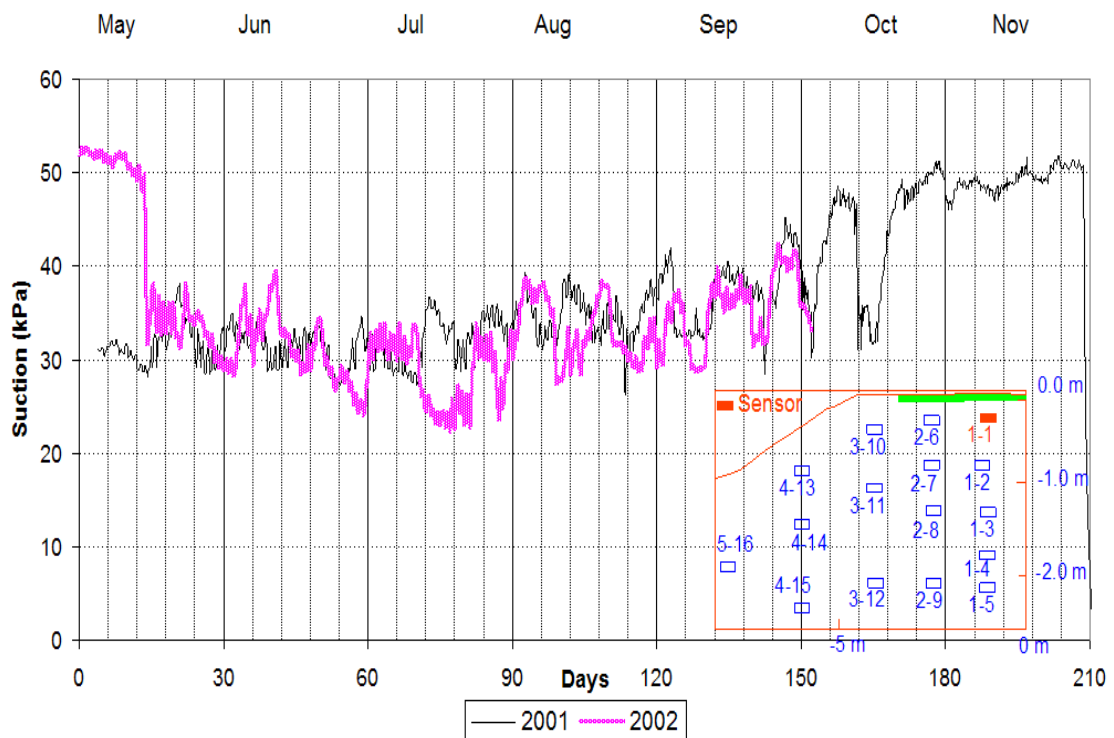


Figure B.46 Suctions at Sensor B1-1 for years 2001 to 2022 at Bethune

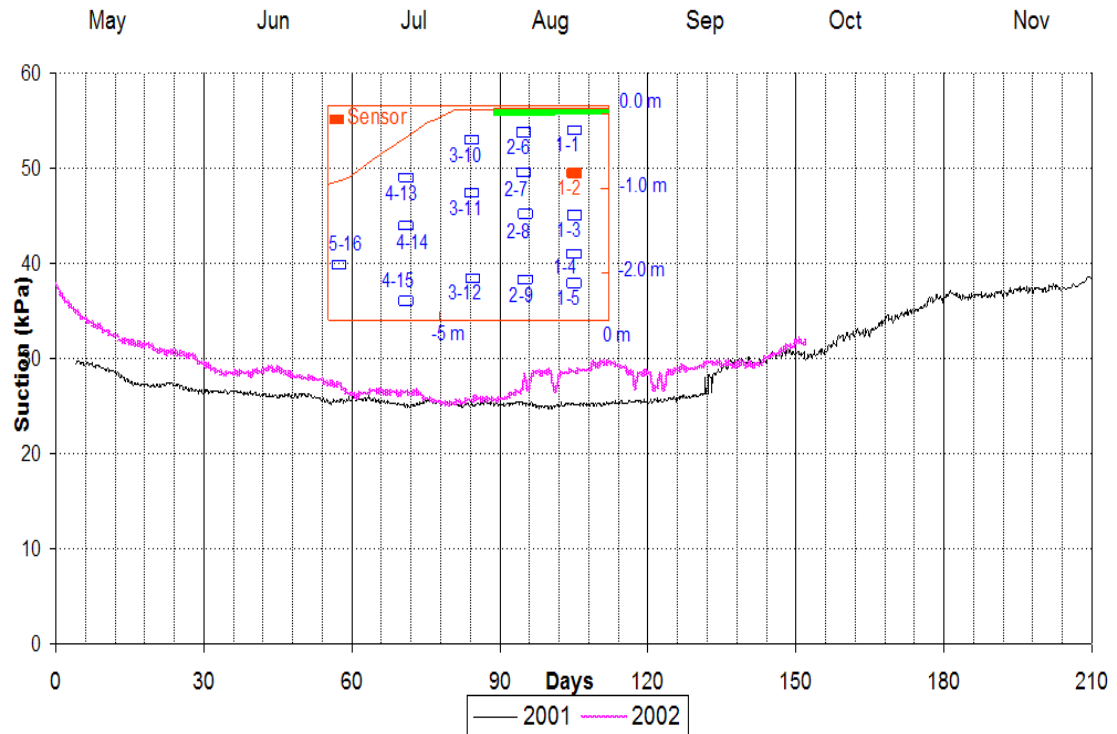


Figure B.47 Suctions at Sensor B1-2 for years 2001 to 2002 at Bethune

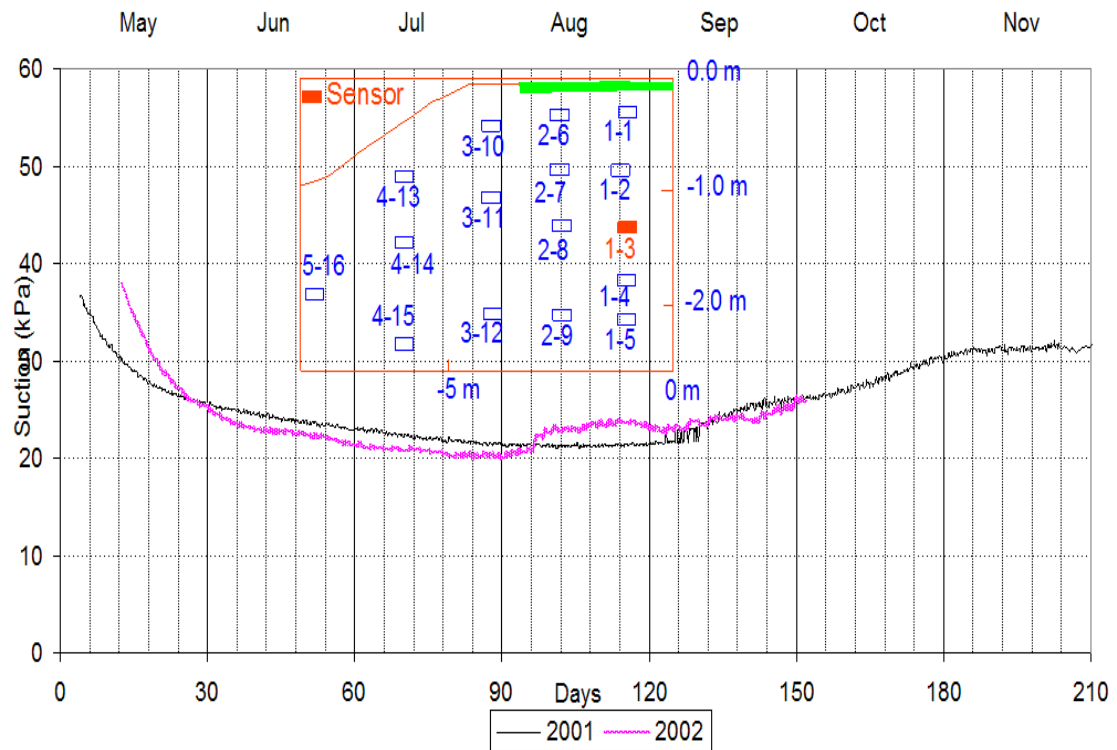
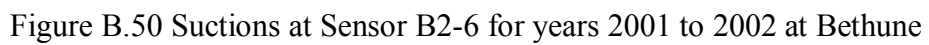
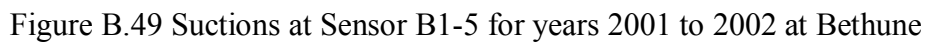


Figure B.48 Suctions at Sensor B1-3 for years 2001 to 2002 at Bethune



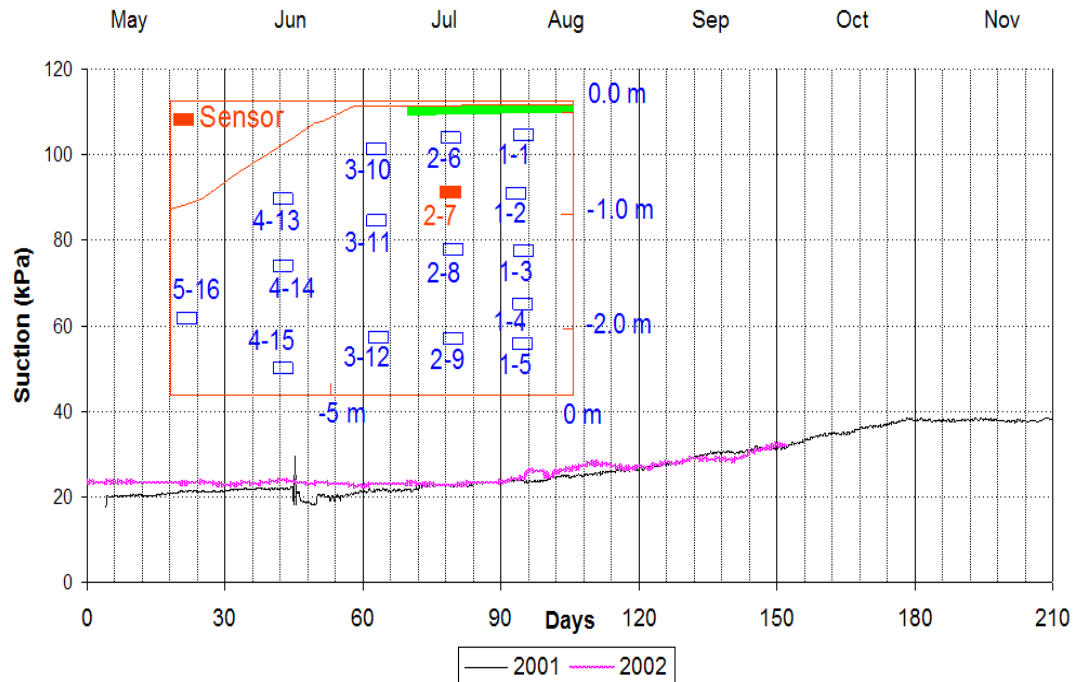


Figure B.51 Suctions at Sensor B2-7 for years 2001 to 2002 at Bethune

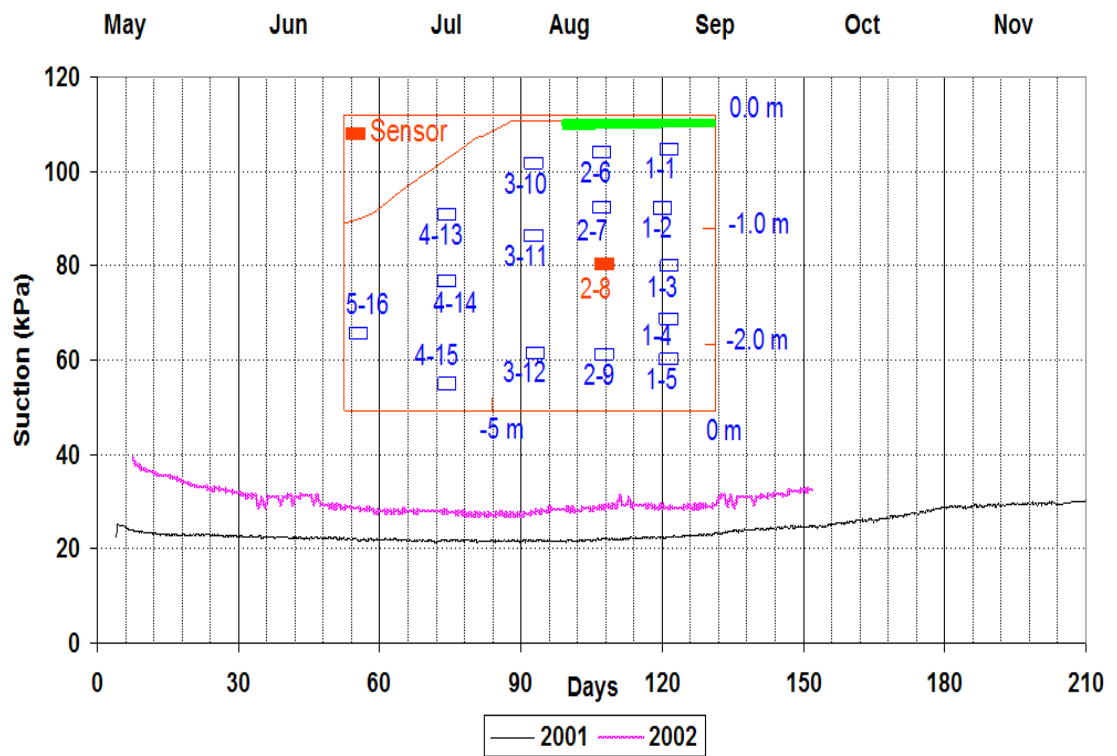


Figure B.52 Suctions at Sensor B2-8 for years 2001 to 2002 at Bethune

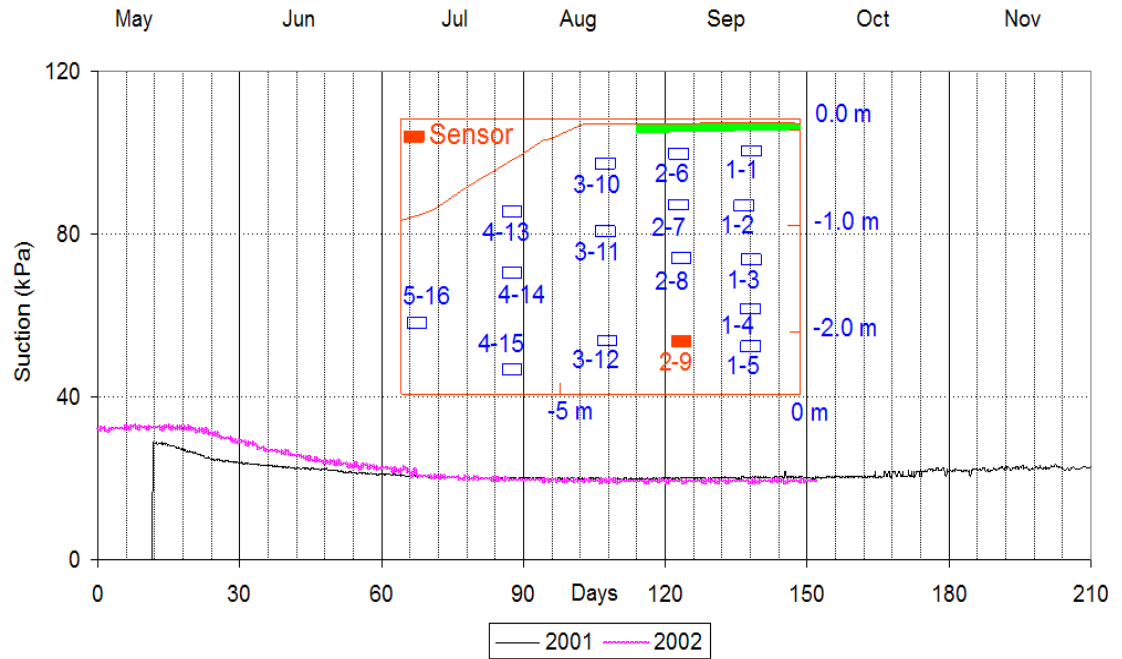


Figure B.53 Suctions at Sensor B2-9 for years 2001 to 2002 at Bethune

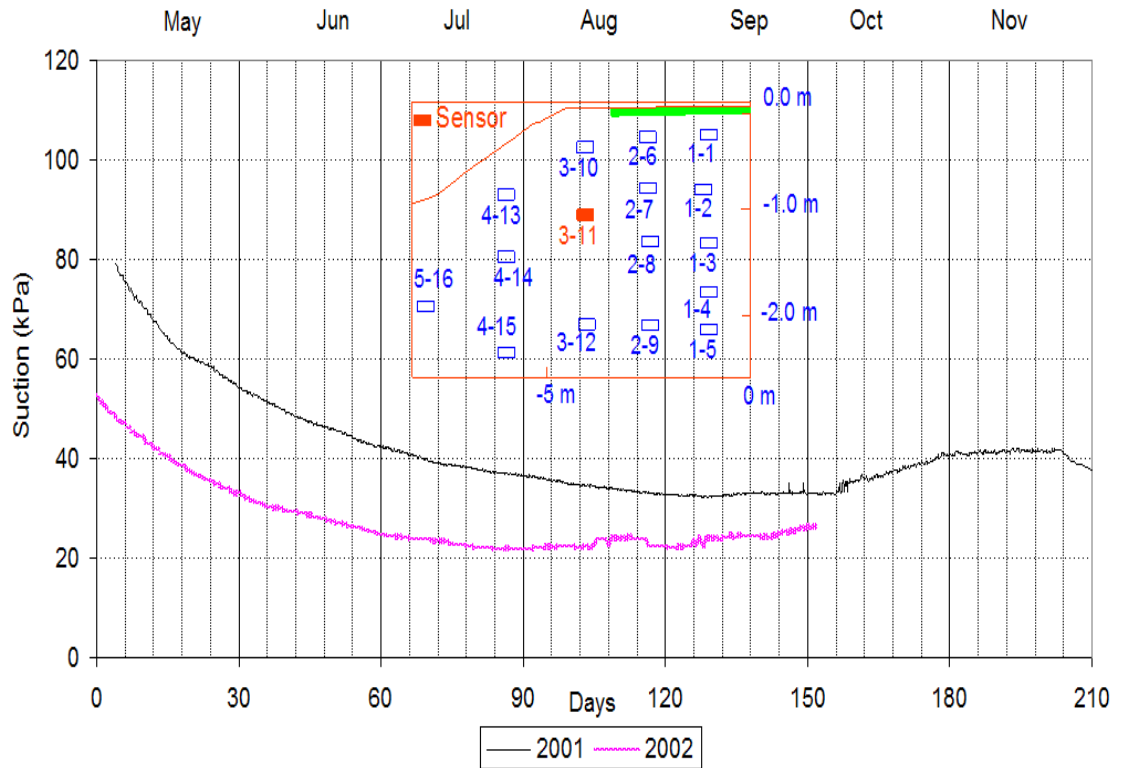


Figure B.54 Suctions at Sensor B3-11 for years 2001 to 2002 at Bethune

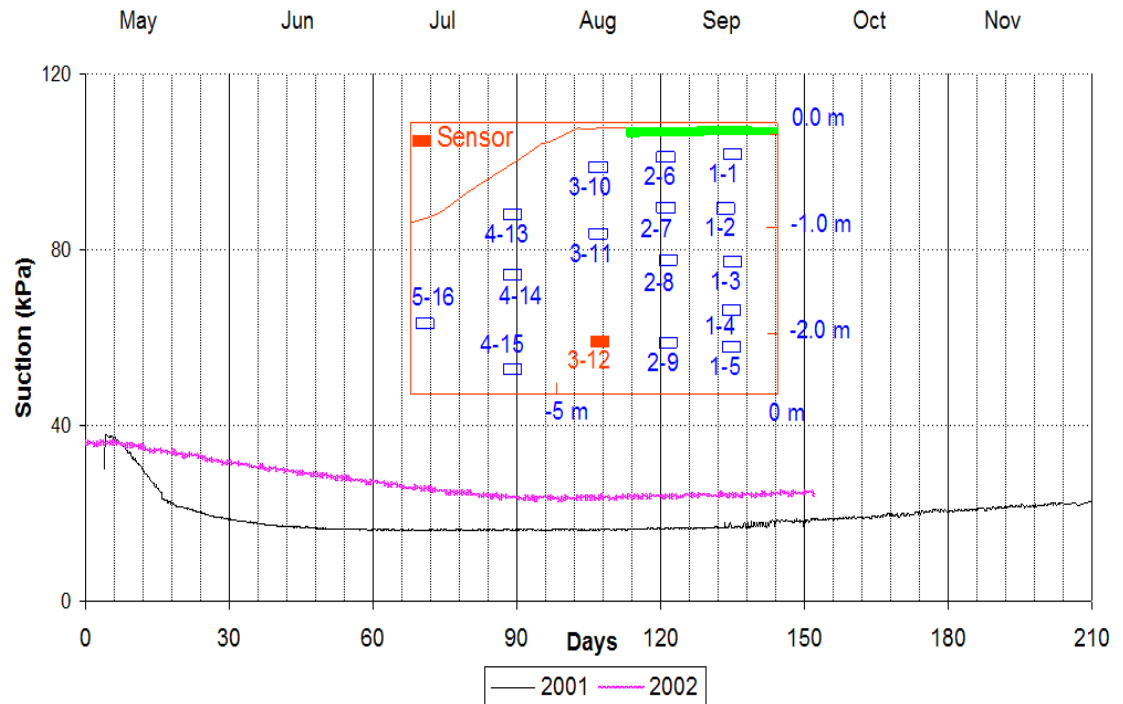


Figure B.55 Suctions at Sensor B3-12 for years 2001 to 2002 at Bethune

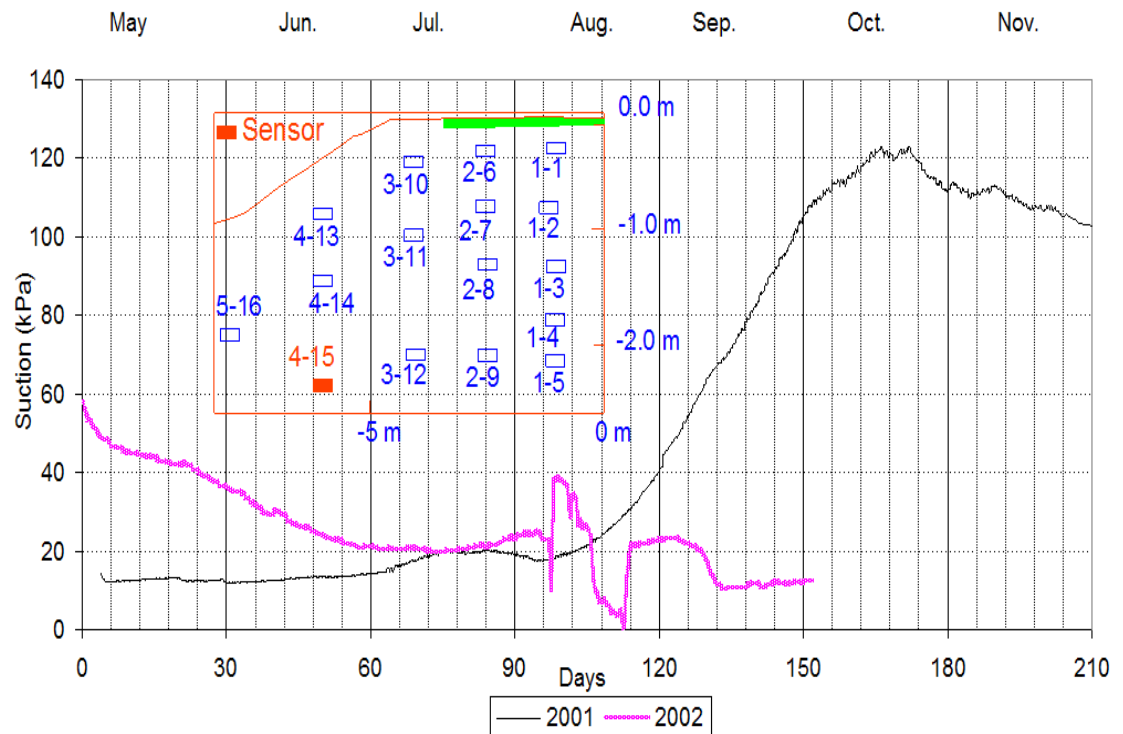


Figure B.56 Suctions at Sensor B4-15 for years 2001 to 2002 at Bethune

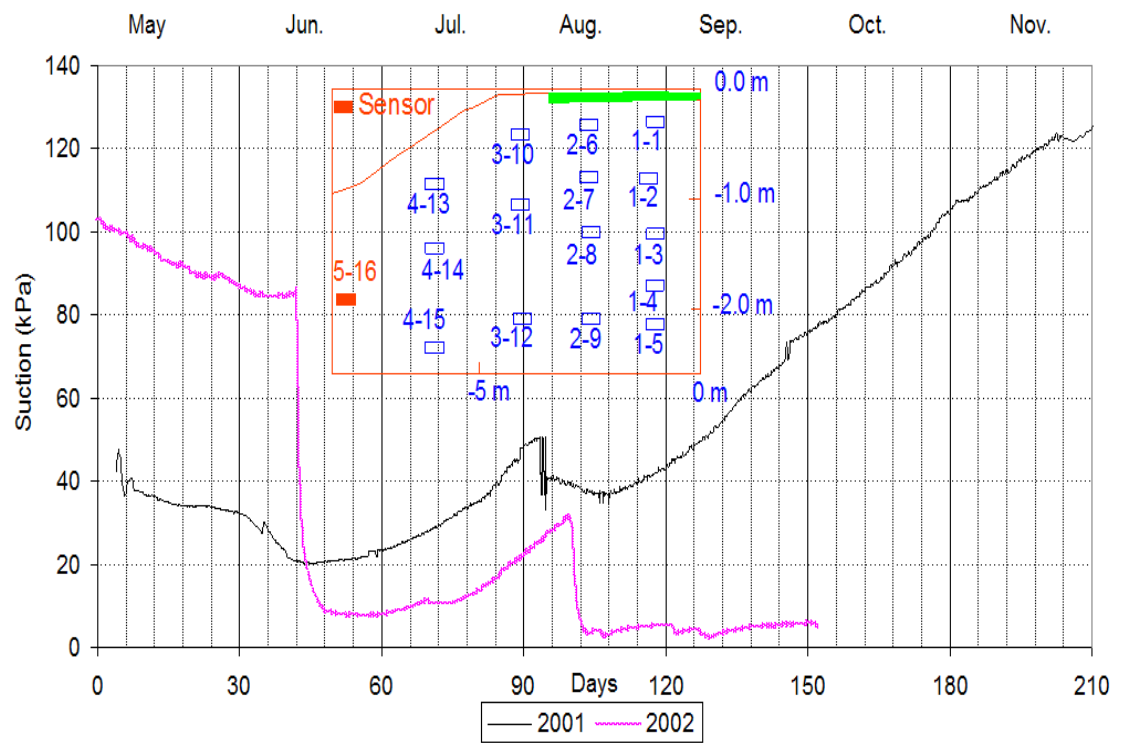


Figure B.57 Suctions at Sensor B5-16 for years 2001 to 2002 at Bethune

APPENDIX C

SITE INVESTIGATION AND LABORATORY TEST RESULTS

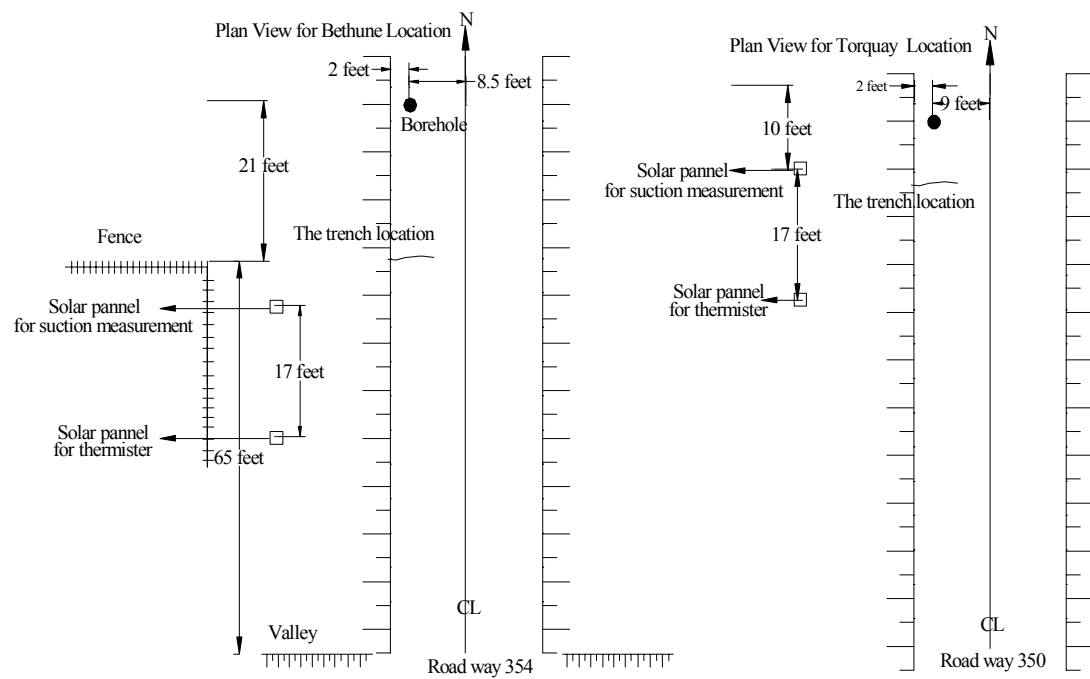


Figure C.1 Plan for site investigation at the Bethune site and Torquay site

Borehole Log								
Borehole No: B5			Location: Bethune					
Commenced: Sept 13/2004			Total depth (cm): 326					
Finished: Sept 13/2004			Driller: Saskatchewan Highways and Transportation					
Descriptor: Quan Nguyen			Drill rig: Mobile Truck Mounting					
Layer #	Soil description	Legend	Depth (cm)	Sample (cm)		Drilling run (cm)	Recovery (cm)	Note
				UD	W/C			
1	0-10cm: Asphalt				10-18	0-18	0	
2	10-38cm: Sandy Clay Till hard, grey in color		20	18-38	18-38	18-38	15	
3	38-53cm: some Top Soil		40	38-53	38-53	38-53	12	
4	53-83cm: Sandy Clay Till hard, grey in color		60	53-68	53-68	53-68	15	
5	83-98cm: Dense Sand and Stone		80	68-83	68-83	68-83	15	
6	98-128cm: Sandy Clay Till hard, grey in color		100	83-98	83-98	83-98	10	
7	128-133cm: Stone		120	98-113	98-113	98-113	15	
8	133-148cm: Sandy Clay Till hard, grey in color		140	113-128	113-128	113-128	13.5	
9	148-193cm: Sandy top soil		160			128-133	0	Stone
			180	133-148	133-148	133-148	12	
			200	148-163	148-163	148-163	12	
			220	163-178	163-178	163-178	12	
			240	178-193	178-193	178-193	8	Stone
10	193-201cm: Stones encountered		260			193-201	0	Stone
11	201-326cm: Sandy Clay Till with Stones (Glacial origin) Hard, Brown-Grey Mottled End of borehole at 326cm		280	201-216	201-216	201-216	12	
			300	216-231	216-231	216-231	13	
			320	231-246	231-246	231-246	14	
			340	246-261	246-261	246-261	15	
			360	261-276	261-276	261-276	10	
			380	276-281	276-281	276-281	0	Stone
			400	281-296	281-296	281-296	14	
			420	296-326		296-326	29	



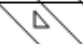


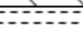
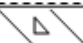
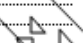
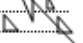
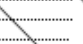


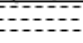
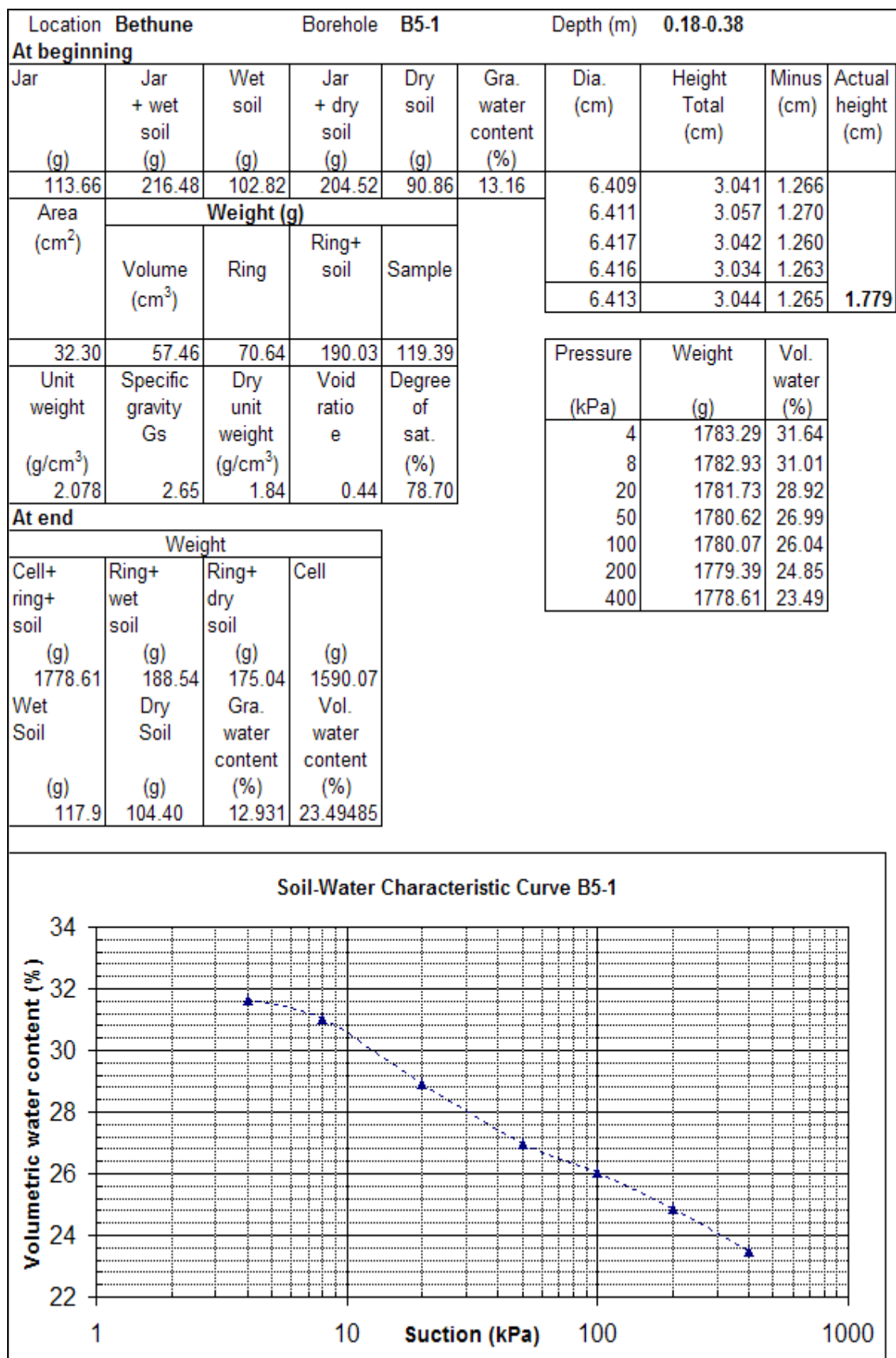
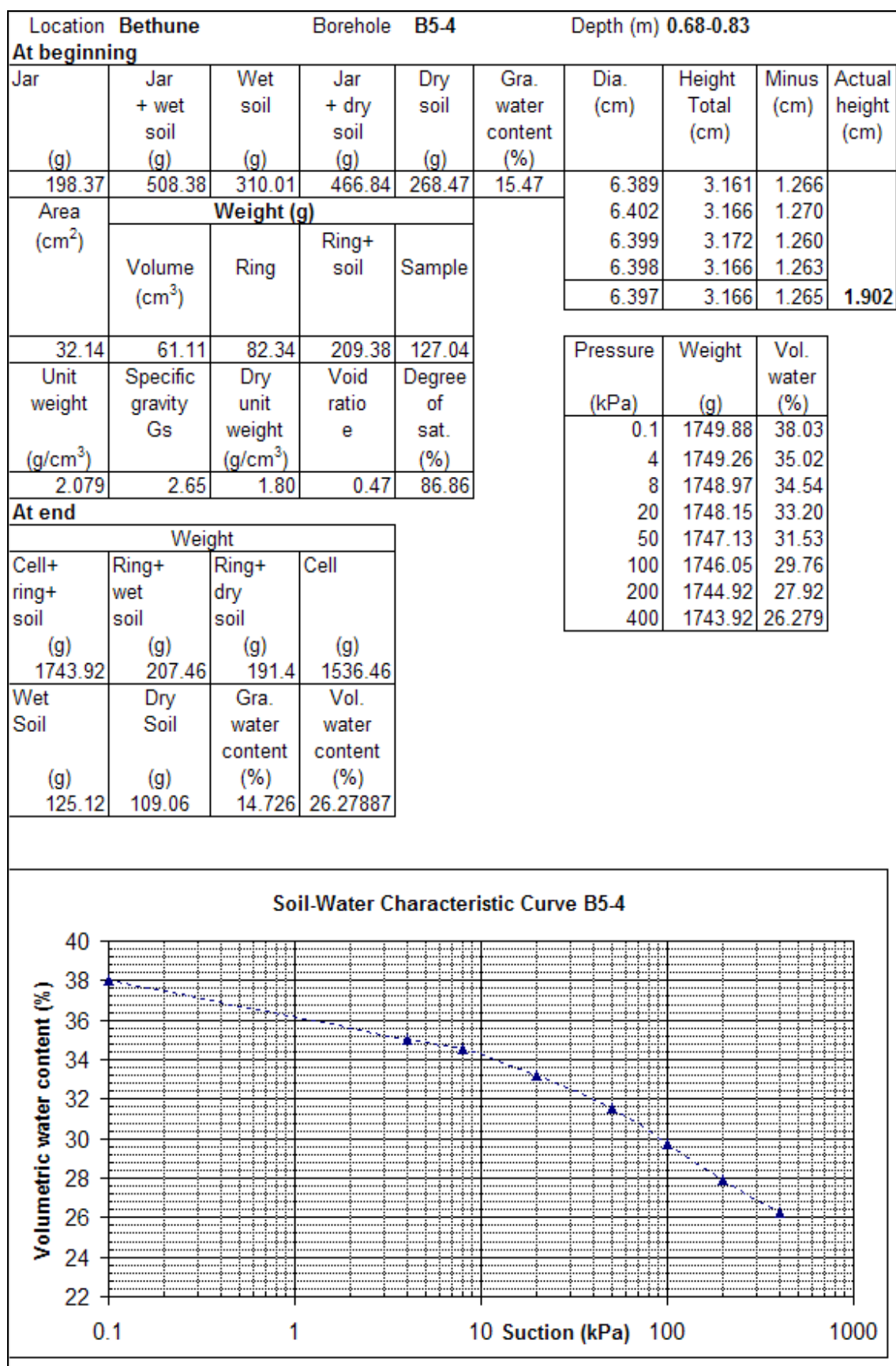
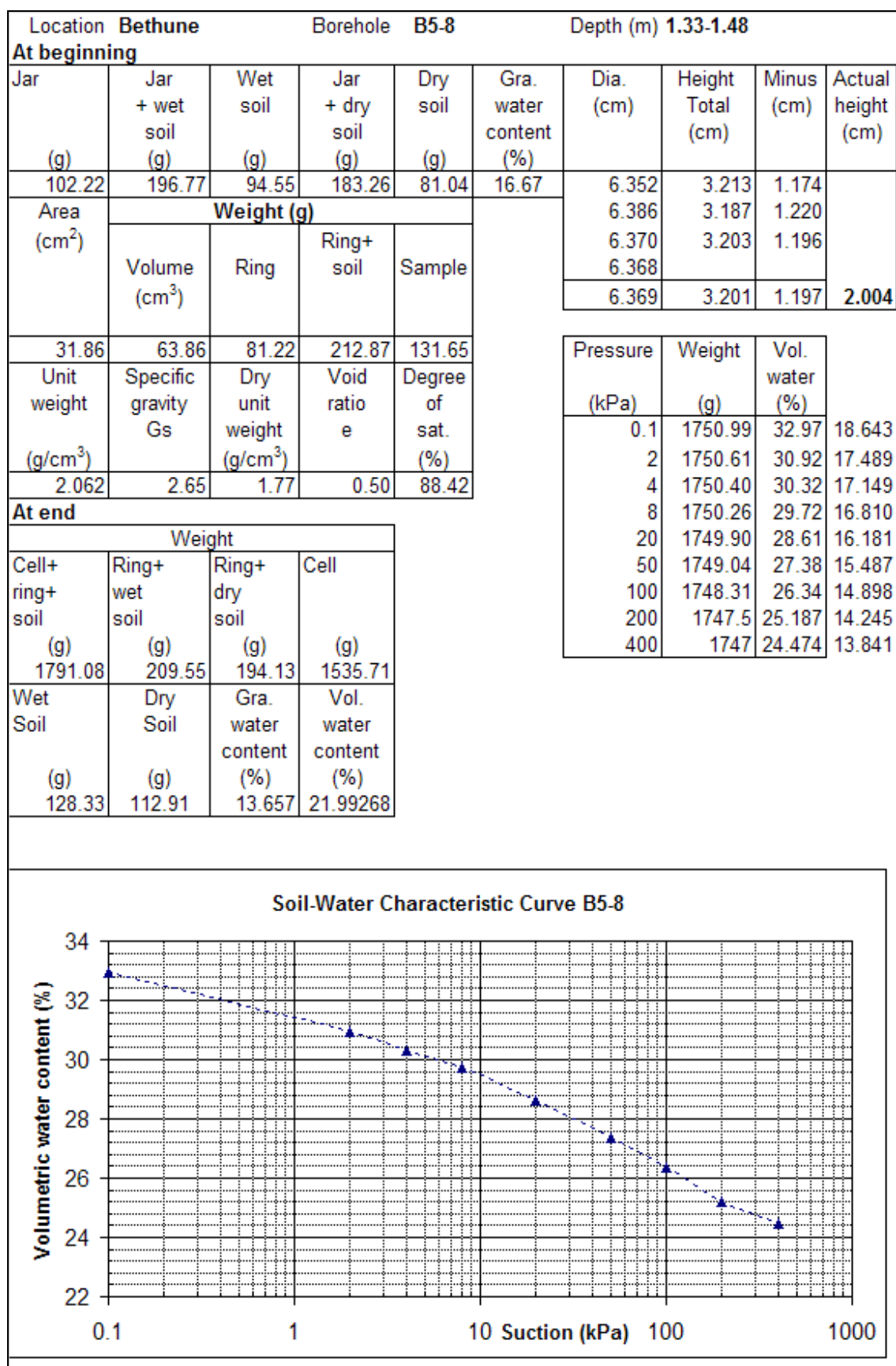
Borehole Log								
Borehole No: T5			Location: Torquay					
Commenced: Sept 13/2004			Total depth (cm): 340					
Finished: Sept 14/2004			Driller: Saskatchewan Highways and Transportation					
Descriptor: Quan Nguyen			Drill rig: Mobile Truck Mounting					
Layer #	Soil description	Legend	Depth (cm)	Sample (cm)		Drilling run (cm)	Recovery (cm)	Note
				UD	W/C			
1	0-8cm: Asphalt					0-10	0	
2	10-25cm: Fill with some organics		20	10-25	10-25	10-25	15	
3	25-100cm: Sandy Clay Till Brown - Mottled with Rust 55-70cm: Encountered stones 5-7cm indiameter 85-100cm: Encountered stones 5-7cm indiameter	 	40	25-40	25-40	25-40	15	
				40-55	40-55	40-55	15	
			60	55-70	55-70	55-70	14	Stone
			80	70-85	70-85	70-85	13.5	
				85-100	85-100	85-100	14	Stone
			100					
4	100-115cm: Sandy Silt, Brown			100-115	100-115	100-115	13	
5	115-145cm: Core loss, very disturbed: Sandy silt		120	115-145	115-145	115-145	26	2 nd Attempt
			140					
6	145-175cm: Glacial Sandy Clay Till Brown-Red Mottled, Hard,		160	145-160	145-160	145-160	13	
				160-175	160-175	160-175	13	
7	175-235cm: Sandy Clay Till with many lenses of Sand Rock encountered at depth 190 cm	  	180	175-190	175-190	175-190	13	
			200	190-205	190-205	190-205	12	
			220	205-235	205-235	205-235	24	
8	235-310cm: Glacial Sandy Clay Till with some lenses of Sand	 	240	235-250	235-250	235-250	15	
			260	250-265	250-265	250-265	12	
			280	265-295	265-295	265-295	26	
			300	295-310	295-310	295-310	15	
9	320-340: Sandy Silt End of borehole at 340cm		320	310-340		310-340	27	
			340					

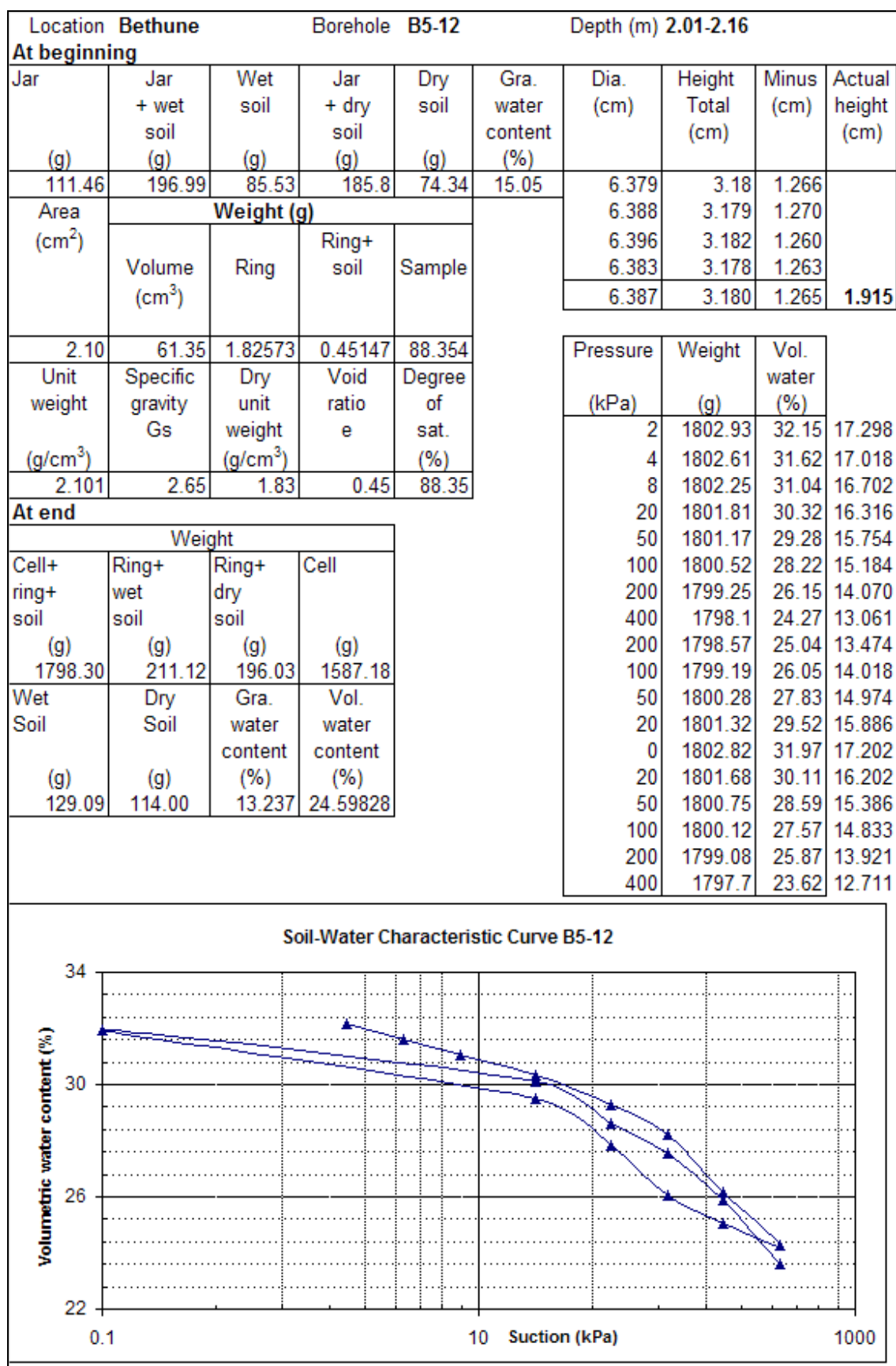
Table C.1 Field tests - water content as of 13th and 14th/September 2004

Bethune			Torquay		
No	Depth (cm)	Water content (%)	No	Depth (cm)	Water content (%)
1	10-18	10.80	1	10-25	14.60
2	18-38	11.99	2	25-40	13.88
3	38-53	14.19	3	40-55	13.23
4	53-68	13.75	4	55-70	13.37
5	68-83	12.74	5	70-85	14.56
6	83-98	10.00	6	85-100	14.97
7	98-113	12.00	7	100-115	13.48
8	113-128	13.61	8	115-145	15.94
9	133-148	14.29	9	145-160	14.88
10	148-163	19.19	10	160-175	16.21
11	163-178	15.78	11	175-190	15.36
12	178-193	14.57	12	190-205	11.25
13	201-216	13.08	13	205-235	15.80
14	216-231	12.46	14	235-250	14.61
15	231-246	12.52	15	250-265	11.75
16	246-261	12.60	16	265-295	14.62
17	261-278	12.45	17	295-310	16.57
18	281-296	11.02			







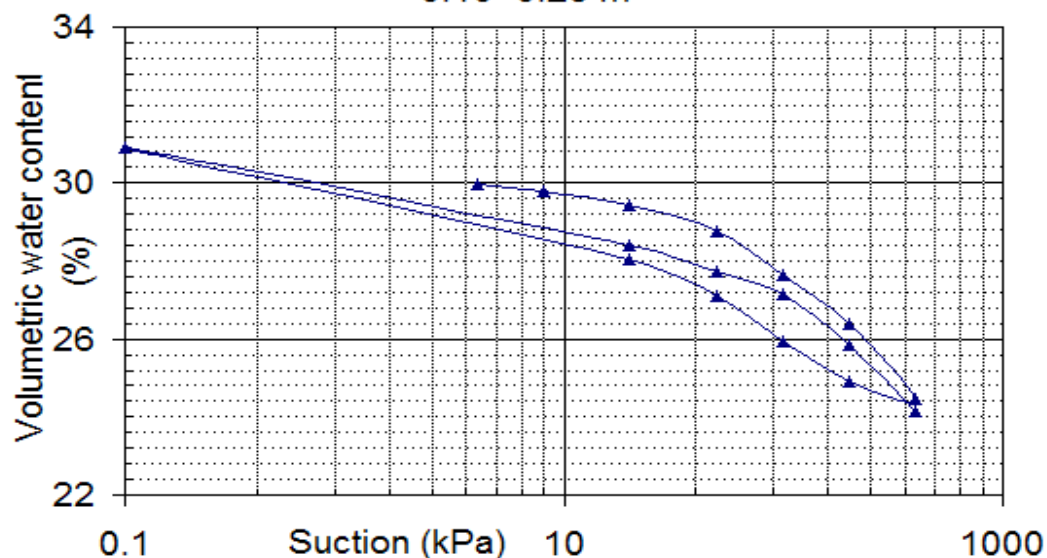


Soil-Water Characteristic Curve B5-18

Suction (kPa)	Volumetric water content (%)
0.1	36.2
0.2	36.0
0.5	35.5
1.0	35.0
2.0	34.5
5.0	33.8
10.0	32.8
20.0	31.0
50.0	29.5
100.0	28.2
200.0	26.5
400.0	25.2

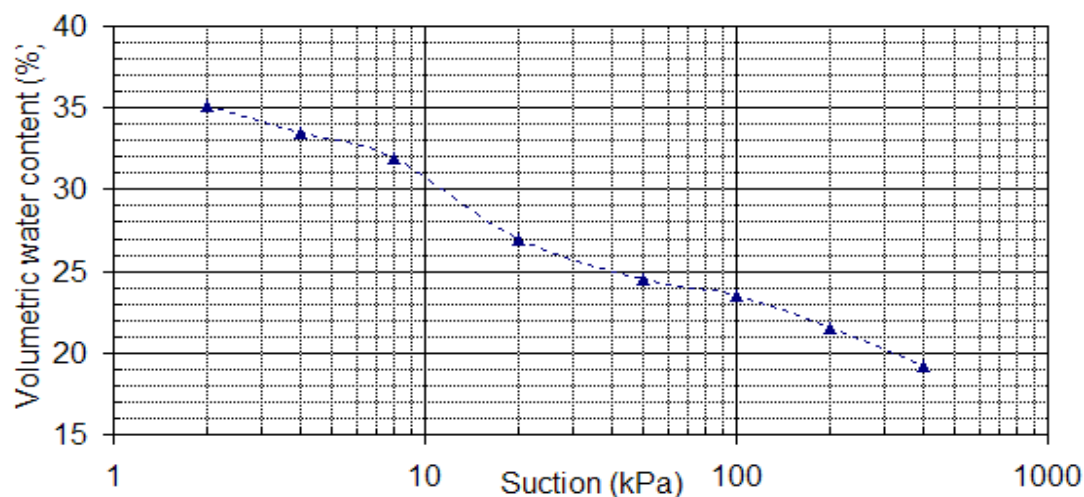
Location Torquay		Borehole T5-1				Depth (m) 0.10-0.25			
At beginning									
Jar	Jar + wet soil	Wet soil	Jar + dry soil	Dry soil	Gra. water content	Dia. (cm)	Height Total (cm)	Minus (cm)	Actual height (cm)
(g)	(g)	(g)	(g)	(g)	(%)				
118.24	209.66	91.42	200.25	82.01	11.47	6.397	3.151	1.266	
Area (cm ²)	Weight (g)					6.397	3.17	1.270	
	Volume (cm ³)	Ring	Ring+ soil	Sample		6.388	3.178	1.260	
						6.394	3.154	1.263	
						6.394	3.163	1.265	1.899
32.11	60.96	79.03	210.22	131.19					
Unit weight	Specific gravity	Dry unit weight	Void ratio	Degree of sat.		Pressure	Weight	Vol. water	
(g/cm ³)	Gs	(g/cm ³)	e	(%)		(kPa)	(g)	(%)	
2.152	2.65	1.93	0.37	81.59		4	1793.94	29.99	15.882
At end						8	1793.82	29.79	15.778
						20	1793.61	29.45	15.595
						50	1793.20	28.77	15.239
						100	1792.51	27.64	14.639
						200	1791.74	26.38	13.970
						400	1790.58	24.48	12.963
						200	1790.85	24.92	13.197
						100	1791.47	25.93	13.736
						50	1792.17	27.08	14.344
						20	1792.76	28.05	14.857
						0	1794.5	30.91	16.368
						20	1792.97	28.40	15.039
						50	1792.57	27.74	14.692
						100	1792.21	27.15	14.379
						200	1791.42	25.85	13.692
						400	1790.39	24.16	12.798

Soil-Water Characteristic Curve T5-1 at depth from 0.10 -0.25 m



Location Torquay			Borehole T5-5		Depth (m) 0.70-0.85				
At beginning									
Jar	Jar + wet soil	Wet soil	Jar + dry soil	Dry soil	Gra. water content	Dia. (cm)	Height Total (cm)	Minus (cm)	Actual height (cm)
(g)	(g)	(g)	(g)	(g)	(%)				
102.55	201.35	98.8	190.12	87.57	12.82	6.404	3.137	1.266	1.878
Area (cm ²)	Weight (g)					6.387	3.148	1.270	
	Volume (cm ³)	Ring	Ring+ soil	Sample		6.391	3.141	1.260	
						6.397	3.144	1.263	
						6.395	3.143	1.265	
32.12	60.31	78.08	197.85	119.77					
Unit weight	Specific gravity	Dry unit weight	Void ratio	Degree of sat.		Pressure	Weight	Vol. water	
(g/cm ³)	Gs	(g/cm ³)	e	(%)		(kPa)	(g)	(%)	
1.986	2.65	1.76	0.51	67.23		2	1829.22	35.09	19.842
At end						4	1828.83	33.44	18.911
						8	1827.90	31.90	18.039
						20	1824.94	26.99	15.263
						50	1823.46	24.54	13.876
						100	1822.86	23.55	13.313
						200	1821.64	21.52	12.170
						400	1820.24	19.20	10.857
Weight									
Cell+ ring+ soil	Ring+ wet soil	Ring+ dry soil	Cell						
(g)	(g)	(g)	(g)						
1820.24	196.32	184.74	1623.92						
Wet Soil	Dry Soil	Gra. water content	Vol. water content						
(g)	(g)	(%)	(%)						
118.24	106.66	10.86	19.20						

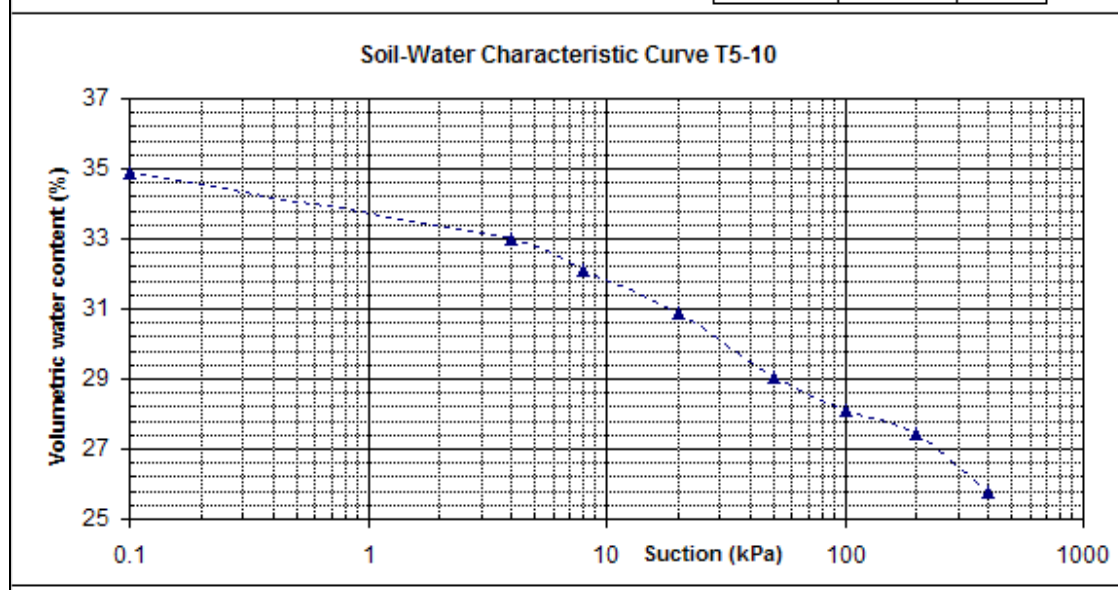
Soil-Water Characteristic Curve T5-5 at depth 0.70 - 0.85 m

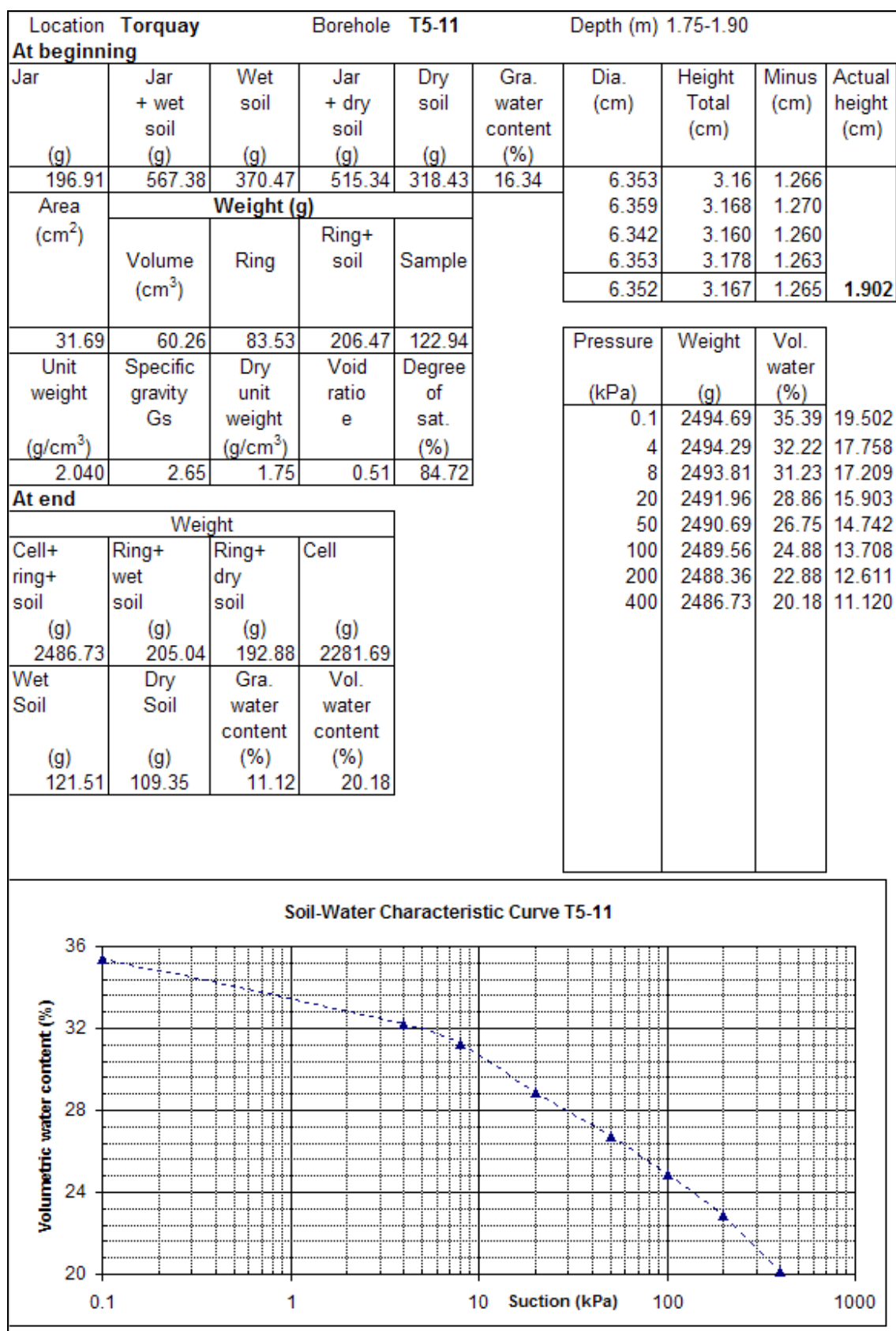


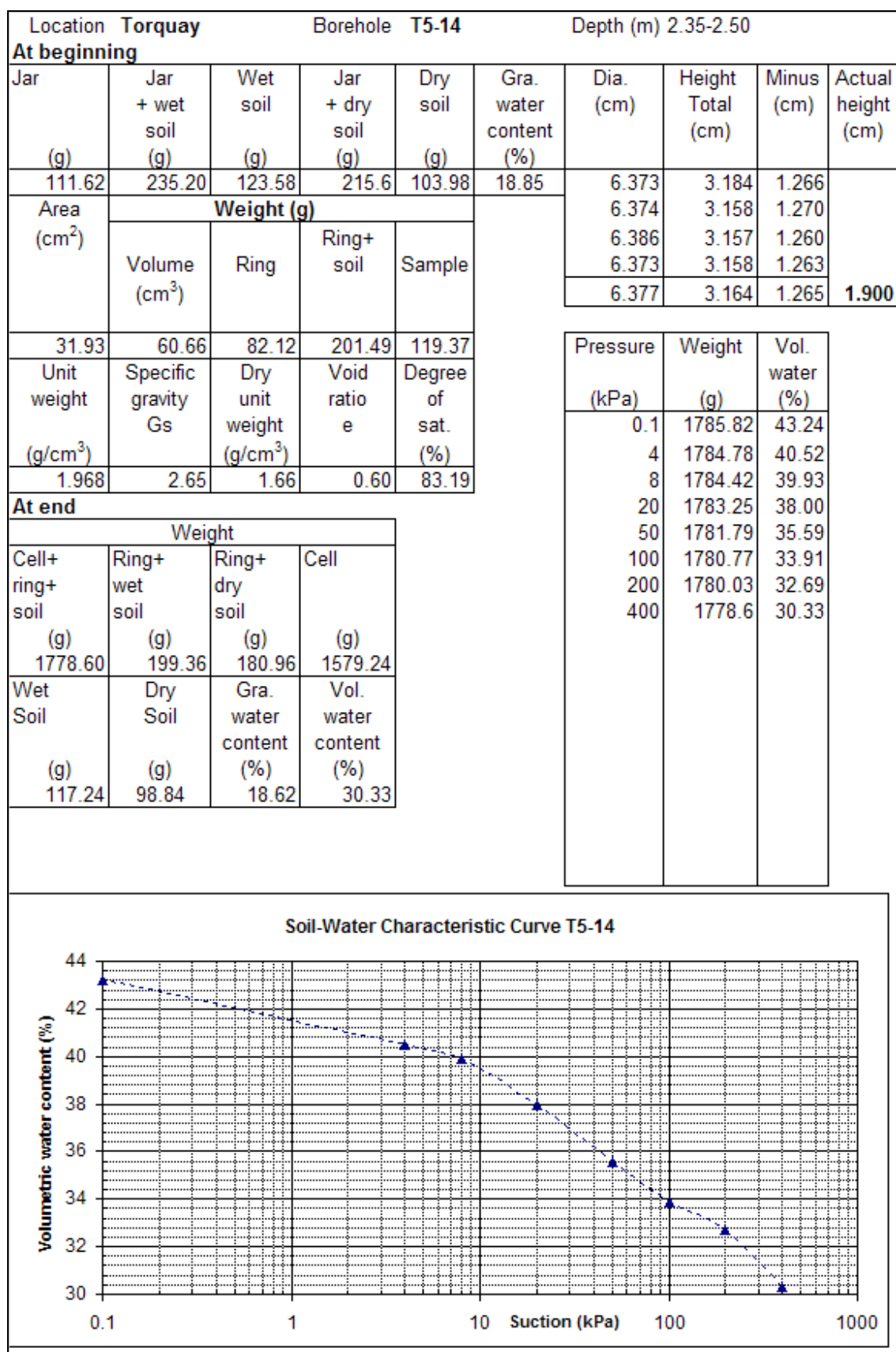
Soil-Water Characteristic Curve T5-6

Suction (kPa)	Volumetric water content (%)
0.1	40.5
0.2	40.0
0.5	39.5
1.0	39.0
2.0	38.5
5.0	37.0
10.0	36.5
20.0	34.0
50.0	31.5
100.0	30.0
200.0	28.0
400.0	26.0

Location Torquay		Borehole T5-10			Depth (m) 1.60-1.75				
At beginning									
Jar	Jar + wet soil	Wet soil	Jar + dry soil	Dry soil	Gra. water content	Dia. (cm)	Height Total (cm)	Minus (cm)	Actual height (cm)
(g)	(g)	(g)	(g)	(g)	(%)				
111.55	181.59	70.04	171.75	60.2	16.35	6.354	3.149	1.266	
Area (cm ²)	Weight (g)					6.354	3.141	1.270	
	Volume (cm ³)	Ring	Ring+ soil	Sample		6.344	3.140	1.260	
						6.362	3.141	1.263	
						6.354	3.143	1.265	1.878
31.70	59.54	88.53	215.4	126.87					
Unit weight	Specific gravity	Dry unit weight	Void ratio	Degree of sat.		Pressure	Weight	Vol. water	
(g/cm ³)	Gs	(g/cm ³)	e	(%)		(kPa)	(g)	(%)	
2.040	2.65	1.75	0.51	84.72		0.1	1755.28	34.88	18.860
						4	1754.75	32.99	17.838
						8	1754.46	32.10	17.359
						20	1754.10	30.89	16.707
						50	1752.42	29.07	15.722
						100	1751.84	28.10	15.195
						200	1751.46	27.46	14.850
						400	1750.45	25.76	13.933
At end									
Weight									
Cell+ ring+ soil	Ring+ wet soil	Ring+ dry soil	Cell						
(g)	(g)	(g)	(g)						
1750.45	213.97	198.63	1536.48						
Wet Soil	Dry Soil	Gra. water content	Vol. water content						
(g)	(g)	(%)	(%)						
125.44	110.10	13.93	25.76						



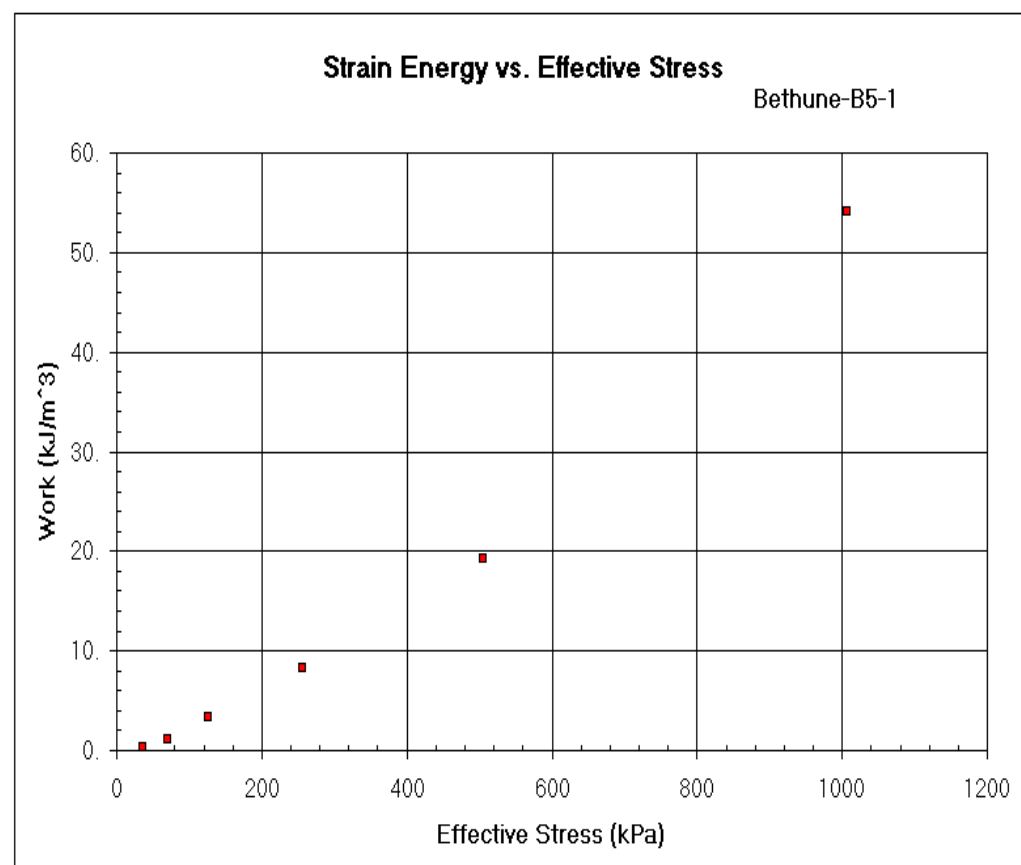
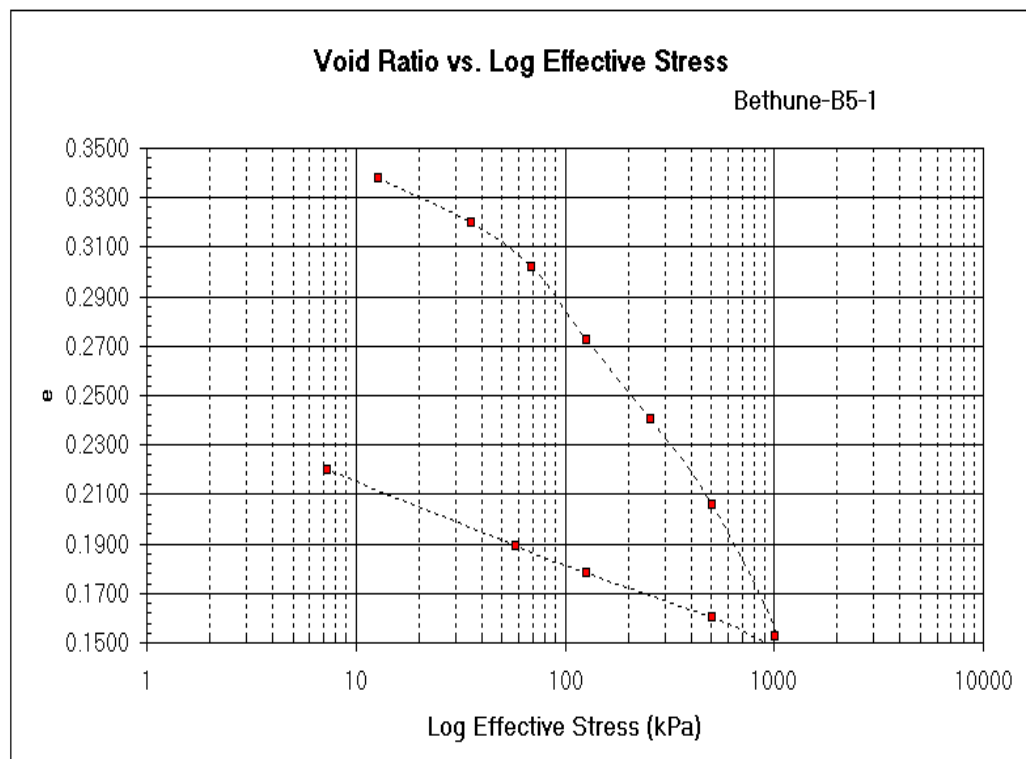




Site: Bethune Sample: B5-1 Date: July, 2 2005 Depth(m): 0.18-0.38 Hole: B5 Technician: Q. Nguyen			
W.C. Determination	Beginning of test	End of test	
Ting & Glass Plate #	2	2	
WT. Wet sample & Tare	260.67	254.98	
WT. Dry sample and tare	241.63	241.63	
Tare	80.29	80.29	
Weight of water	19.04	13.35	
Weight of soil	161.34	161.34	
Water content %	11.80	8.27	
Diam. Test Ring (cm)			6.381
Area of test ring (cm ²)		a	31.979
Height sample beginning of test (cm)		h ₁	2.547
Specific gravity solids		G	2.650
WT. Dry sample		W _s	161.340
Reduced height of solids	$h_s = W_s/aG$	h _s	1.904
Change in height of sample begin to end test		dh	0.224
Height of sample at end of test	$h_2 = h_1 - dh$	h ₂	2.322
Height of water at begin of test	$h_{w1} = W_{w1}/a$	h _{w1}	0.595
Height of water at end of test	$h_{w2} = W_{w2}/a$	h _{w2}	0.417
Sat. degree at begin of test	$S_{w1} = h_{w1}/h_1 - h_s$	S ₁	0.926
Sat. degree at end of test	$S_{w2} = h_{w2}/h_2 - h_s$	S ₂	0.998
Void ratio	$e_1 = (h_1 - h_s)/h_s$	e ₁	0.338
$e = e_1 - \text{Defl.}/H_s$	$e = w * G$	e	0.313

B5-1												
Pressure (kPa)	Dial 1 (cm)	Defl. (cm)	Defl/Hs	e	Pavg	H	dDefl.	Strain	Inc.Strain Energy	Strain Energy		
12.9	0.7604	0.0000	0.0000	0.3376		2.5465						
35.6	0.7265	0.0339	0.0178	0.3198	24.25	2.5126	0.0339	0.0135	0.3272	0.		
69.6	0.6925	0.0679	0.0357	0.3019	52.60	2.4786	0.0340	0.0137	0.7216	1.		
126.3	0.6358	0.1246	0.0654	0.2721	97.97	2.4219	0.0567	0.0234	2.2936	3.		
256.0	0.5755	0.1849	0.0971	0.2404	191.16	2.3616	0.0603	0.0255	4.8810	8.		
506.1	0.5091	0.2513	0.1320	0.2056	381.06	2.2952	0.0664	0.0289	11.0241	19.		
1006.5	0.4081	0.3523	0.1850	0.1525	756.31	2.1942	0.1010	0.0460	34.8131	54.		
506.1	0.4233	0.3371	0.1771	0.1605	756.31	2.2094	-0.0152	-0.0069	-5.2032	49.		
126.3	0.4571	0.3033	0.1593	0.1783	316.24	2.2432	-0.0338	-0.0151	-2.8224	46.		
58.2	0.4773	0.2831	0.1487	0.1889	92.29	2.2634	-0.0202	-0.0089	-3.1398	43.		
7.3	0.5361	0.2243	0.1178	0.2197	66.80	2.3222	-0.0790	-0.0340	-2.2725	44.		

* Dial 50- Dial reading for 50% consolidation at pressure 2												
** Time 50-Time required to reach 50% consolidation at pressure 2												
Pressure 1 (kPa)	Pressure 2 (kPa)	P avg (kPa)	Dial 100 (cm)	Dial 50* (cm)	Time 50** (min)	H (cm)	Cv (sq cm/sec)	Av (1/kPa)	Mv (1/kPa)	K (m/sec)	Cv (sq m/year)	
12.90	35.61	24.25	0.7265	0.7343	5	2.52035	0.001042814	0.000784076	0.000586197	5.99496E-08	3.289	0.942
35.61	69.60	52.60	0.6925	0.7018	17	2.48785	0.000298851	0.000525452	0.000398142	1.16689E-08	2.556	1.043
69.60	126.34	97.97	0.6358	0.6479	6	2.434	0.000810485	0.000524829	0.000403125	3.20421E-08	1.389	1.061
126.34	255.98	191.16	0.5755	0.5888	14	2.37485	0.000330673	0.000244316	0.000192054	6.22816E-09	1.389	1.061
255.98	506.14	381.06	0.5091	0.5301	10	2.31615	0.00044034	0.000139417	0.000112393	4.8536E-09	1.061	3.157
506.14	1006.47	756.31	0.4081	0.4316	12	2.21765	0.000336403	0.000106033	8.79525E-05	2.90164E-09	3.157	0.810
1006.47	506.14	756.31	0.4233	0.4226	4	2.20865	0.001001034	1.59574E-05	1.38457E-05	1.35925E-09	0.810	0.220
506.14	126.34	316.24	0.4571	0.4516	16	2.23765	0.000256874	4.67445E-05	4.02796E-05	1.01471E-09	0.220	0.114
126.34	58.25	92.29	0.4773	0.4712	60	2.2573	6.97079E-05	0.000155812	0.00013224	9.04027E-10	0.114	0.000
58.25	7.26	32.75	0.5361	0.5161	120	2.3022	3.62543E-05	0.000605724	0.000509498	1.8115E-09	0.000	
7.26												



Site: Bethune Sample: B5-4 Date: July, 11 2005 Depth(m): 0.68-0.83 Hole: B5 Technician: Q. Nguyen			
W.C. Determination	Beginning of test	End of test	
Ting & Glass Plate #	2	2	
WT. Wet sample & Tare	257.76	256.03	
WT. Dry sample and tare	241.67	241.67	
Tare	85.03	85.03	
Weight of water	16.09	14.36	
Weight of soil	156.64	156.64	
Water content %	10.27	9.17	
Diam. Test Ring (cm)			6.385
Area of test ring (cm ²)		a	32.017
Height sample beginning of test (cm)		h_1	2.406
Specific gravity solids		G	2.700
WT. Dry sample		W_s	156.640
Reduced height of solids	$h_s = W_s / aG$	h_s	1.812
Change in height of sample begin to end test		dh	0.142
Height of sample at end of test	$h_2 = h_1 - dh$	h_2	2.264
Height of water at begin of test	$h_{w1} = W_{w1} / a$	h_{w1}	0.503
Height of water at end of test	$h_{w2} = W_{w2} / a$	h_{w2}	0.449
Sat. degree at begin of test	$S_{w1} = h_{w1} / h_1 - h_s$	S_1	0.846
Sat. degree at end of test	$S_{w2} = h_{w2} / h_2 - h_s$	S_2	0.991
Void ratio	$e_1 = (h_1 - h_s) / h_s$	e_1	0.328
$e = e_1 - \text{Defl.} / H_s$	$e = w * G$	e	0.277

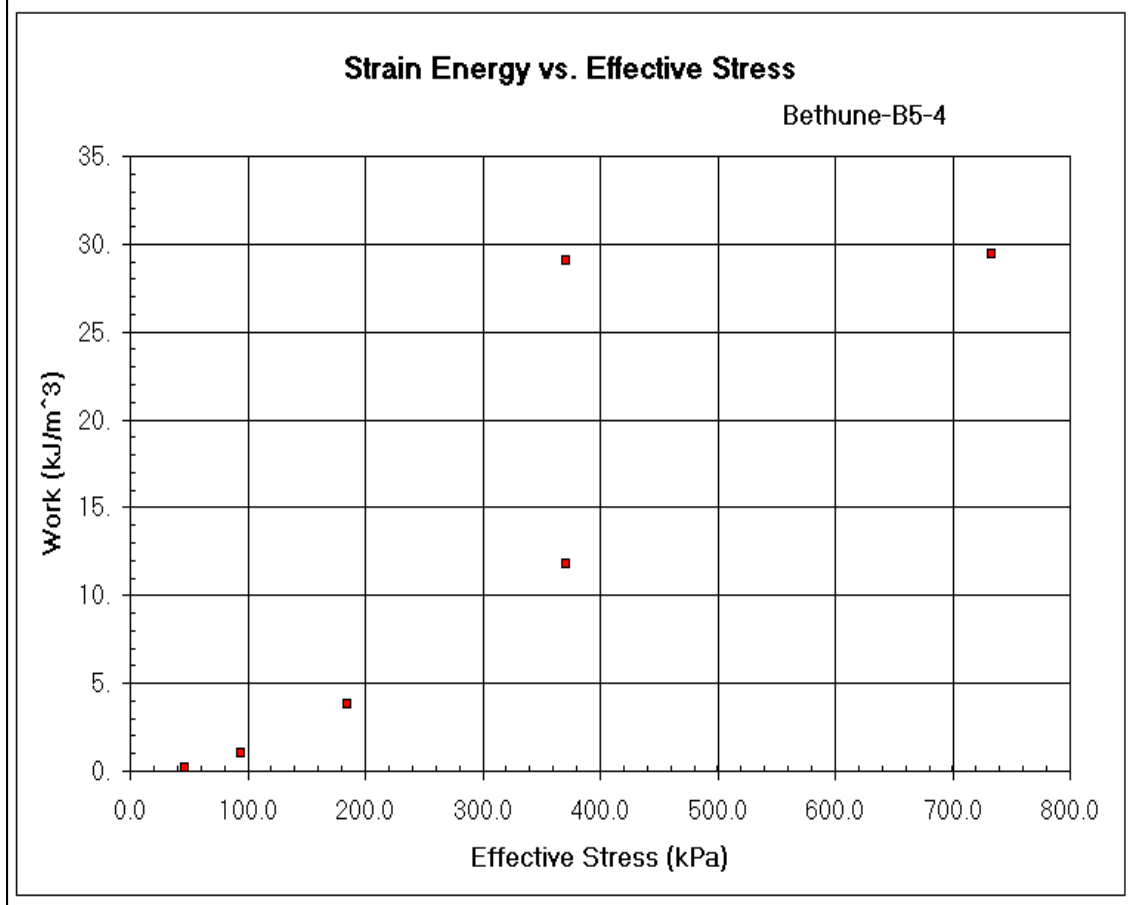
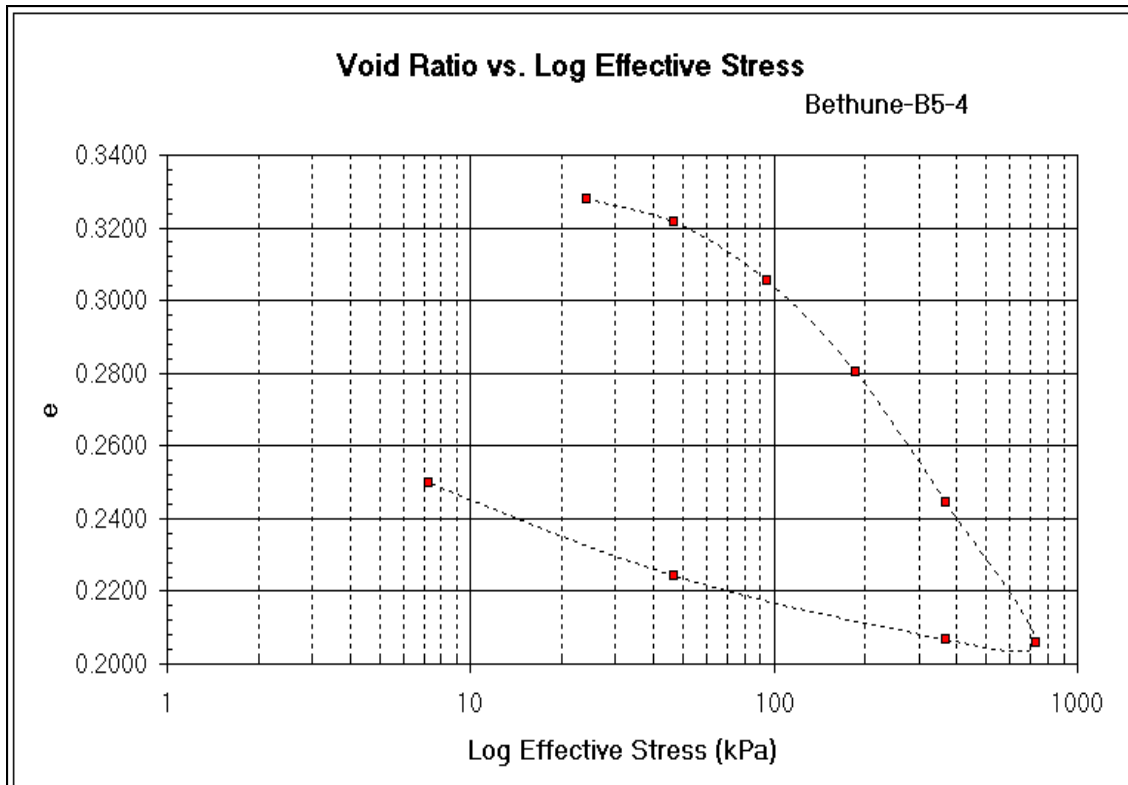
B5-4

[illegible]

* Dial 50- Dial reading for 50% consolidation at pressure 2

** Time 50-Time required to reach 50% consolidation at pressure 2

[illegible]



Site: Bethune Sample: B5-16 Date: June, 13 2005 Depth(m): 2.61-2.76 Hole: B5 Technician: Q. Nguyen			
W.C. Determination	Beginning of test	End of test	
Ting & Glass Plate #	2	2	
WT. Wet sample & Tare	239.89	235.42	
WT. Dry sample and tare	219.13	219.13	
Tare	75.14	75.14	
Weight of water	20.76	16.29	
Weight of soil	143.99	143.99	
Water content %	14.42	11.31	
Diam. Test Ring (cm)			6.405
Area of test ring (cm ²)		a	32.220
Height sample beginning of test (cm)		h_1	2.416
Specific gravity solids		G	2.700
WT. Dry sample		W_s	143.990
Reduced height of solids	$h_s = W_s / aG$	h_s	1.655
Change in height of sample begin to end test		dh	0.254
Height of sample at end of test	$h_2 = h_1 - dh$	h_2	2.163
Height of water at begin of test	$h_{w1} = W_{w1} / a$	h_{w1}	0.644
Height of water at end of test	$h_{w2} = W_{w2} / a$	h_{w2}	0.506
Sat. degree at begin of test	$S_{w1} = h_{w1} / h_1 - h_s$	S_1	0.847
Sat. degree at end of test	$S_{w2} = h_{w2} / h_2 - h_s$	S_2	0.996
Void ratio	$e_1 = (h_1 - h_s) / h_s$	e_1	0.460
$e = e_1 - \text{Defl.} / H_s$	$e = w * G$	e	0.389

B5-16

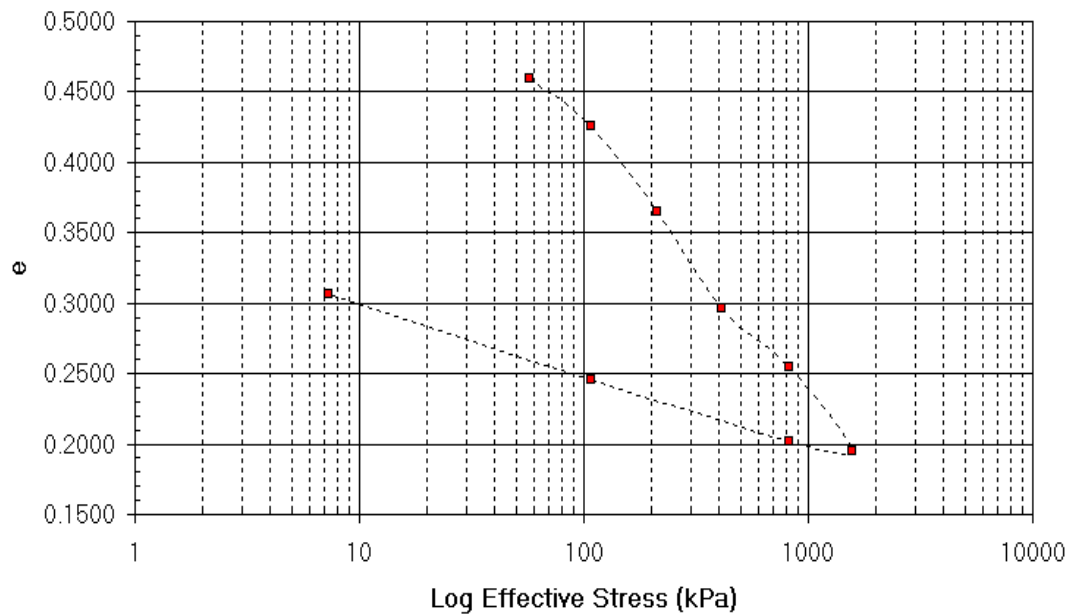
* Dial 50- Dial reading for 50% consolidation at pressure 2

**** Time 50-Time required to reach 50% consolidation at pressure 2**

[illegible]

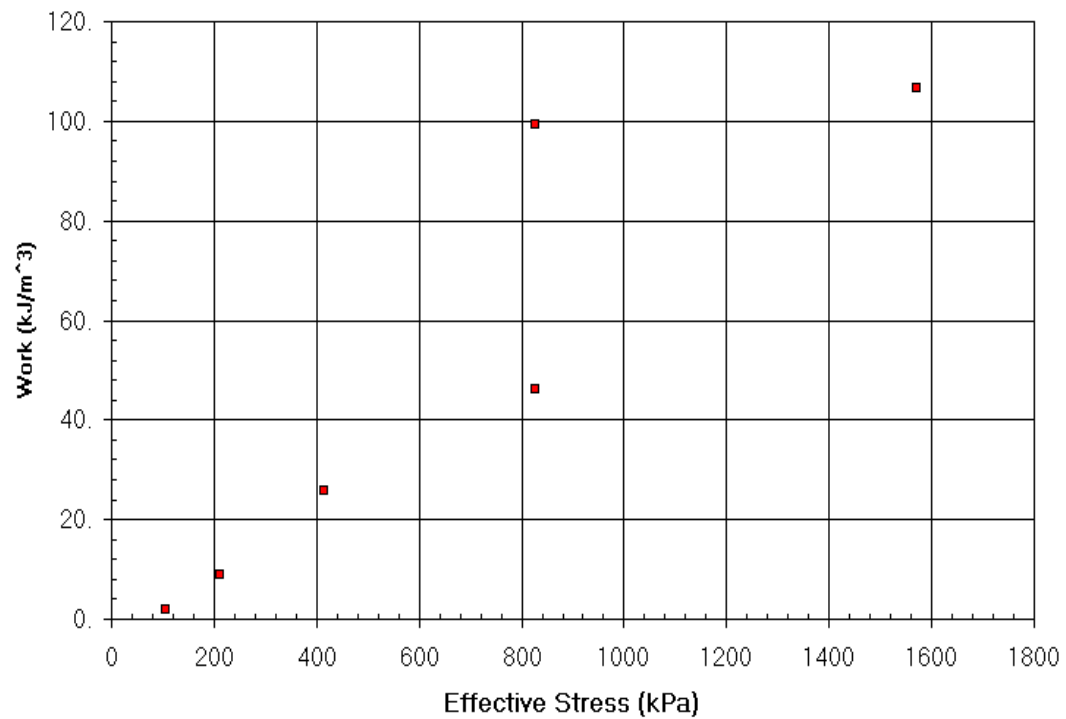
Void Ratio vs. Log Effective Stress

Bethune-B5-16



Strain Energy vs. Effective Stress

Bethune-B5-16

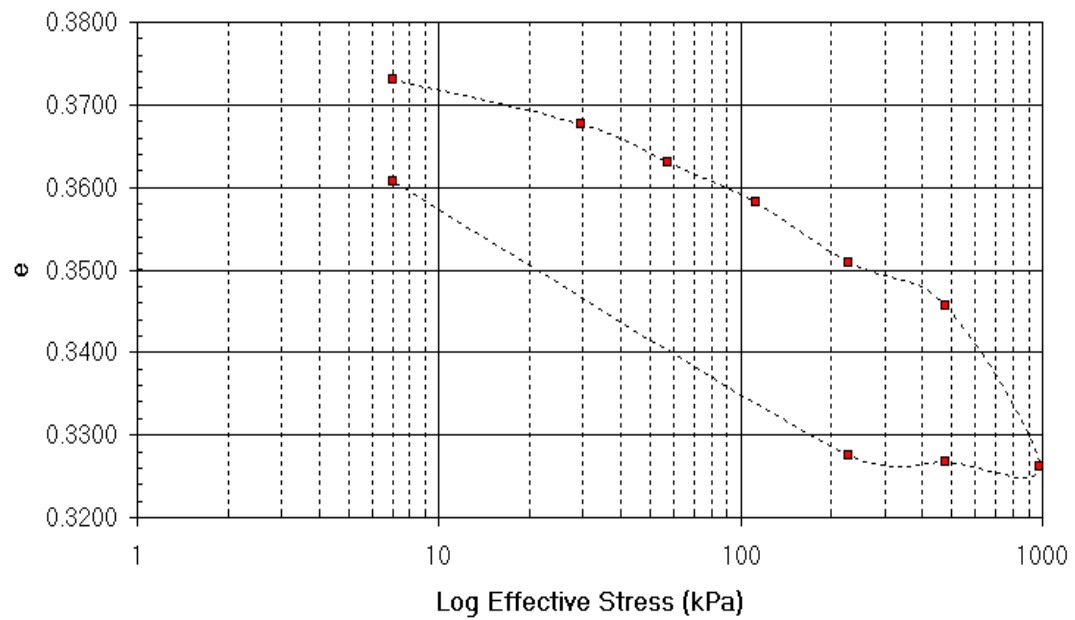


Site: Bethune Sample: T5-1 Date: June, 13 2005 Depth(m): 0.10-0.25 Hole: T5 Technician: Q. Nguyen			
W.C. Determination	Beginning of test	End of test	
Ting & Glass Plate #	2	2	
WT. Wet sample & Tare	197.99	199.89	
WT. Dry sample and tare	185.37	185.37	
Tare	76.66	76.66	
Weight of water	12.62	14.52	
Weight of soil	108.71	108.71	
Water content %	11.61	13.36	
Diam. Test Ring (cm)			6.389
Area of test ring (cm ²)		a	32.054
Height sample beginning of test (cm)		h_1	1.757
Specific gravity solids		G	2.650
WT. Dry sample		W_s	108.710
Reduced height of solids	$h_s = W_s/aG$	h_s	1.280
Change in height of sample begin to end test		dh	0.016
Height of sample at end of test	$h_2 = h_1 - dh$	h_2	1.741
Height of water at begin of test	$h_{w1} = W_{w1}/a$	h_{w1}	0.394
Height of water at end of test	$h_{w2} = W_{w2}/a$	h_{w2}	0.453
Sat. degree at begin of test	$S_{w1} = h_{w1}/h_1 - h_s$	S_1	0.825
Sat. degree at end of test	$S_{w2} = h_{w2}/h_2 - h_s$	S_2	0.981
Void ratio	$e_1 = (h_1 - h_s)/h_s$	e_1	0.373
$e = e_1 - \text{Defl.}/H_s$	$e = w * G$	e	0.308

T5-1												
Pressure (kPa)	Dial 1 (cm)	Defl. (cm)	Defl/Hs	e	Pavg	H	dDefl.	Strain	Inc. Strain Energy	Strain Energy		
7.1	0.1000	0.0000	0.0000	0.3731		1.7573						
29.7	0.0931	0.0069	0.0054	0.3677	18.38	1.7504	0.0069	0.0039	0.0724	0.		
57.2	0.0872	0.0128	0.0100	0.3631	43.45	1.7445	0.0059	0.0034	0.1470	0.		
112.8	0.0810	0.0190	0.0148	0.3582	85.00	1.7383	0.0062	0.0036	0.3032	1.		
228.5	0.0715	0.0285	0.0223	0.3508	170.65	1.7288	0.0095	0.0055	0.9378	1.		
478.1	0.0650	0.0350	0.0273	0.3457	353.30	1.7223	0.0065	0.0038	1.3334	3.		
977.2	0.0399	0.0601	0.0470	0.3261	727.66	1.6972	0.0251	0.0148	10.7617	14.		
478.1	0.0408	0.0592	0.0463	0.3268	727.66	1.6981	-0.0009	-0.0005	-0.3857	13.		
228.5	0.0416	0.0584	0.0456	0.3275	353.30	1.6989	-0.0008	-0.0005	-0.1664	13.		
7.1	0.0841	0.0159	0.0124	0.3607	117.79	1.7414	-0.0425	-0.0244	-2.8747	10.		
* Dial 50- Dial reading for 50% consolidation at pressure 2												
** Time 50-Time required to reach 50% consolidation at pressure 2												
Pressure 1 (kPa)	Pressure 2 (kPa)	P avg (kPa)	Dial 100 (cm)	Dial 50* (cm)	Time 50** (min)	H (cm)	Cv (sq cm/sec)	Av (1/kPa)	Mv (1/kPa)	K (m/sec)	Cv (sq m/year)	
7.06	29.69	18.38	0.0931	0.0956	8	1.7528	0.000315232	0.000238229	0.000173499	5.36368E-09	0.994	1.128
29.69	57.21	43.45	0.0872	0.0894	7	1.7466	0.000357721	0.000167554	0.000122508	4.2978E-09	0.712	0.596
57.21	112.79	85.00	0.081	0.0828	11	1.74	0.000225923	8.71632E-05	6.39456E-05	1.4168E-09	0.103	1.507
112.79	228.51	170.65	0.0715	0.0735	13	1.73075	0.000189139	6.4147E-05	4.72281E-05	8.76025E-10	1.864	14.938
228.51	478.09	353.30	0.065	0.0675	75	1.72475	3.25571E-05	2.03505E-05	1.50653E-05	4.81018E-11	108.493	0.000
478.09	977.24	727.66	0.0399	0.0490	5	1.7062	0.000477909	3.92921E-05	2.91975E-05	1.36844E-09		
977.24	478.09	727.66	0.0408	0.0400	4	1.6972	0.0005911	1.40888E-06	1.0624E-06	6.15867E-11		
478.09	228.51	353.30	0.0416	0.0414	0.5	1.69865	0.004736884	2.50468E-06	1.88772E-06	8.76933E-10		
228.51	7.06	117.79	0.0841	0.3900	0.1	2.04725	0.034403034	0.000149962	0.00011297	3.8115E-07		

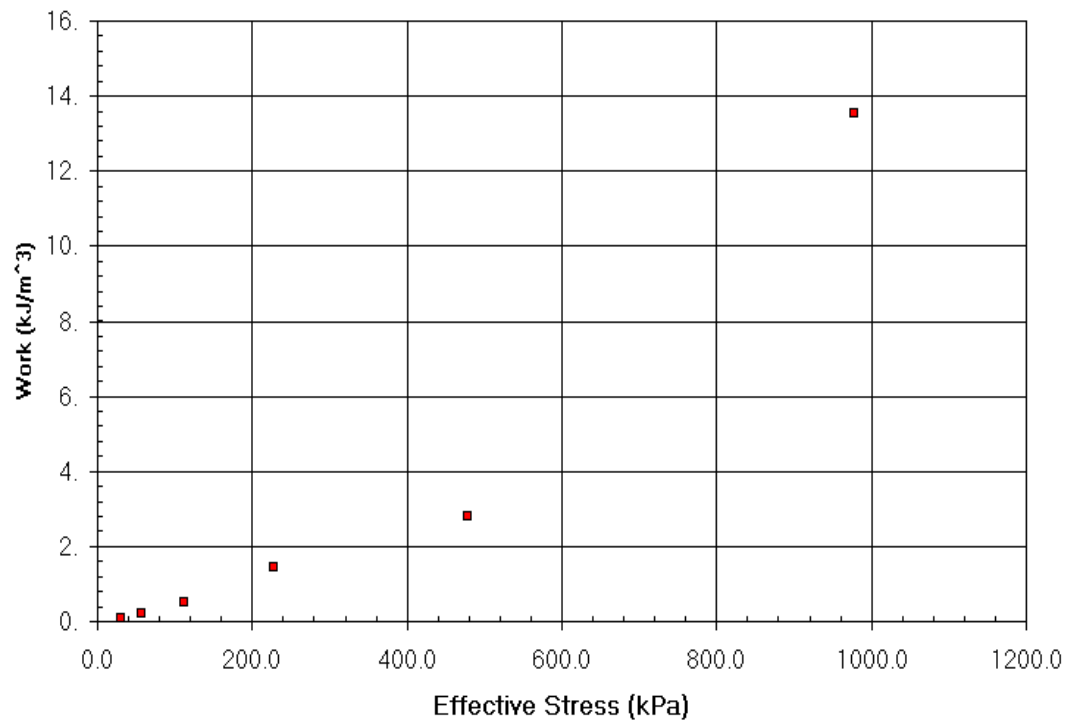
Void Ratio vs. Log Effective Stress

Torquay-T5-1



Strain Energy vs. Effective Stress

Torquay-T5-1



Site: Bethune Sample: T5-2 Date: March, 17 2005 Depth(m): 0.25-0.40 Hole: T5 Technician: Q. Nguyen			
W.C. Determination	Beginning of test	End of test	
Ting & Glass Plate #	2	2	
WT. Wet sample & Tare	240.5	240.6	
WT. Dry sample and tare	222.21	222.21	
Tare	75.13	75.13	
Weight of water	18.29	18.39	
Weight of soil	147.08	147.08	
Water content %	12.44	12.50	
Diam. Test Ring (cm)			6.396
Area of test ring (cm ²)		a	32.126
Height sample beginning of test (cm)		h_1	2.297
Specific gravity solids		G	2.700
WT. Dry sample		W_s	147.080
Reduced height of solids	$h_s = W_s / aG$	h_s	1.696
Change in height of sample begin to end test		dh	0.026
Height of sample at end of test	$h_2 = h_1 - dh$	h_2	2.271
Height of water at begin of test	$h_{w1} = W_{w1} / a$	h_{w1}	0.569
Height of water at end of test	$h_{w2} = W_{w2} / a$	h_{w2}	0.572
Sat. degree at begin of test	$S_{w1} = h_{w1} / (h_1 - h_s)$	S_1	0.946
Sat. degree at end of test	$S_{w2} = h_{w2} / (h_2 - h_s)$	S_2	0.995
Void ratio	$e_1 = (h_1 - h_s) / h_s$	e_1	0.355
$e = e_1 \cdot \text{Defl.} / H_s$	$e = w \cdot G$	e	0.336

T5-2

Pressure (kPa)	Dial 1 (cm)	Defl. (cm)	Defl/Hs	e	Pavg	H	dDefl.	Strain	Inc.Strain Energy	Strain Energy
24.1	0.1885	0.0000	0.0000	0.3549		2.2973				
46.8	0.1785	0.0100	0.0059	0.3490	35.41	2.2873	0.0100	0.0044	0.1548	0.
91.4	0.1671	0.0214	0.0126	0.3422	69.10	2.2759	0.0114	0.0050	0.3461	1.
183.4	0.1365	0.0520	0.0307	0.3242	137.42	2.2453	0.0306	0.0136	1.8729	2.
360.3	0.0935	0.0950	0.0560	0.2988	271.85	2.2023	0.0430	0.0195	5.3079	8.
688.6	0.0400	0.1485	0.0876	0.2673	524.42	2.1488	0.0535	0.0249	13.0567	21.
1186.6	-0.0140	0.2025	0.1194	0.2354	937.58	2.0948	0.0540	0.0258	24.1686	45.
688.6	-0.0068	0.1953	0.1152	0.2397	937.58	2.1020	-0.0072	-0.0034	-3.2114	42.
360.3	0.0045	0.1840	0.1085	0.2463	524.44	2.1133	-0.0113	-0.0053	-2.8042	39.
183.4	0.0217	0.1668	0.0984	0.2565	271.88	2.1305	-0.0172	-0.0081	-2.1949	37.
46.8	0.0580	0.1305	0.0770	0.2779	115.12	2.1668	-0.0363	-0.0168	-1.9286	35.
1.6	0.1621	0.0264	0.0156	0.3393	24.19	2.2709	-0.1041	-0.0458	-1.1091	34.

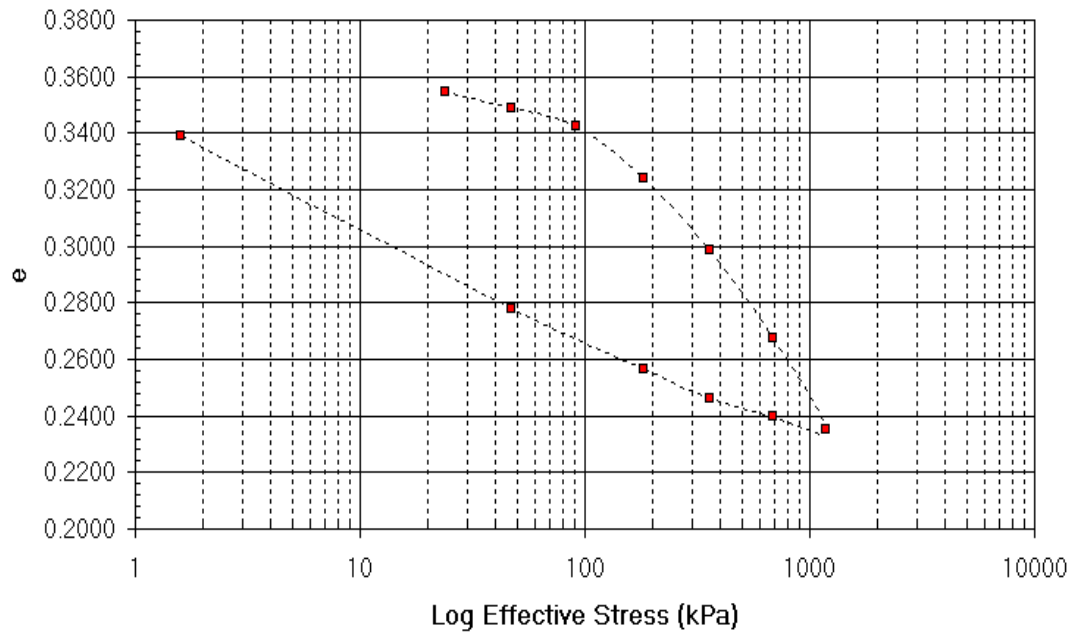
* Dial 50- Dial reading for 50% consolidation at pressure 2

** Time 50- Time required to reach 50% consolidation at pressure 2

Pressure 1 (kPa)	Pressure 2 (kPa)	P avg (kPa)	Dial 100 (cm)	Dial 50* (cm)	Time 50** (min)	H (cm)	Cv (sq cm/sec)	Av (1/kPa)	Mv (1/kPa)	K (m/sec)	Cv (sq m/year)
24.05	46.77	35.41	0.1785	0.1800	4	2.28883	0.001075037	0.000259574	0.000191587	2.01988E-08	3.390
46.77	91.42	69.10	0.1671	0.1703	10	2.27913	0.000426378	0.000150571	0.000111619	4.66735E-09	1.345
91.42	183.42	137.42	0.1365	0.1460	30	2.25483	0.000139111	0.00019616	0.000146143	1.99378E-09	0.439
183.42	360.28	271.85	0.0935	0.1073	10	2.21608	0.000403113	0.000143387	0.000108283	4.28077E-09	1.271
360.28	688.56	524.42	0.04	0.0568	12	2.16558	0.000320792	9.61131E-05	7.39994E-05	2.32803E-09	0.722
688.56	1186.60	937.58	-0.014	0.0042	16	2.11308	0.00022907	6.39451E-05	5.04583E-05	1.13354E-09	0.024
1186.60	688.56	937.58	-0.0068	-0.0079	480	2.10093	7.54811E-06	8.52601E-06	6.9012E-06	5.10857E-12	0.330
688.56	360.31	524.44	0.0045	0.0023	35	2.11108	0.00010452	2.03021E-05	1.63768E-05	1.67866E-10	0.355
360.31	183.45	271.88	0.0217	0.0184	33	2.12718	0.000112551	5.73549E-05	4.60184E-05	5.07947E-10	0.160
183.45	46.80	115.12	0.058	0.0445	75	2.15333	5.07477E-05	0.000156663	0.000124683	6.20526E-10	88.994
46.80	1.59	24.19	0.1621	0.1621	0.15	2.27088	0.028219764	0.001358046	0.001062716	2.94108E-06	0.000
1.59											

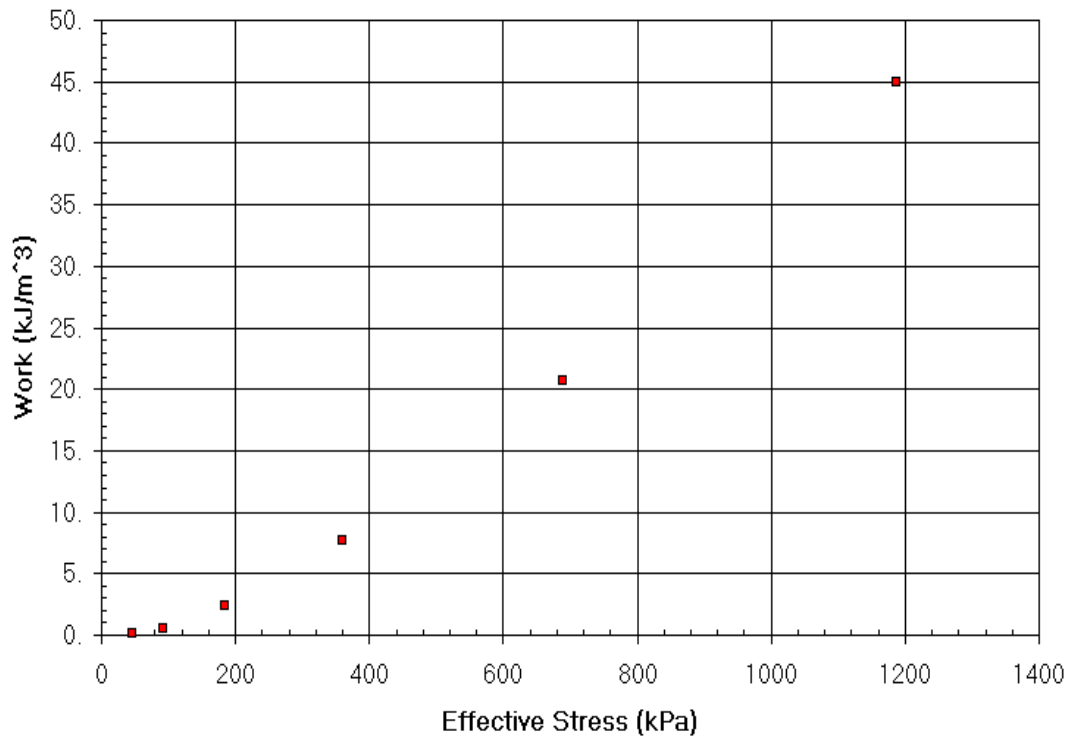
Void Ratio vs. Log Effective Stress

Torquay-T5-2



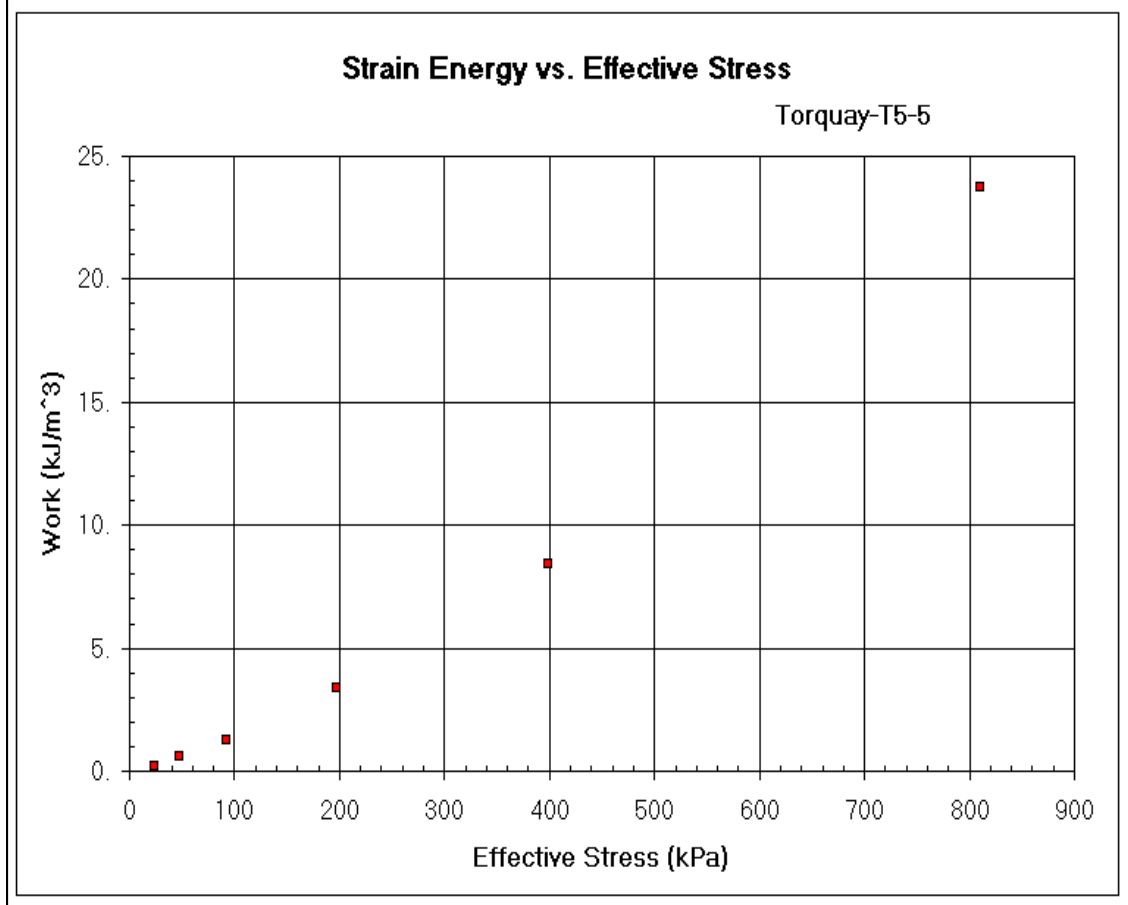
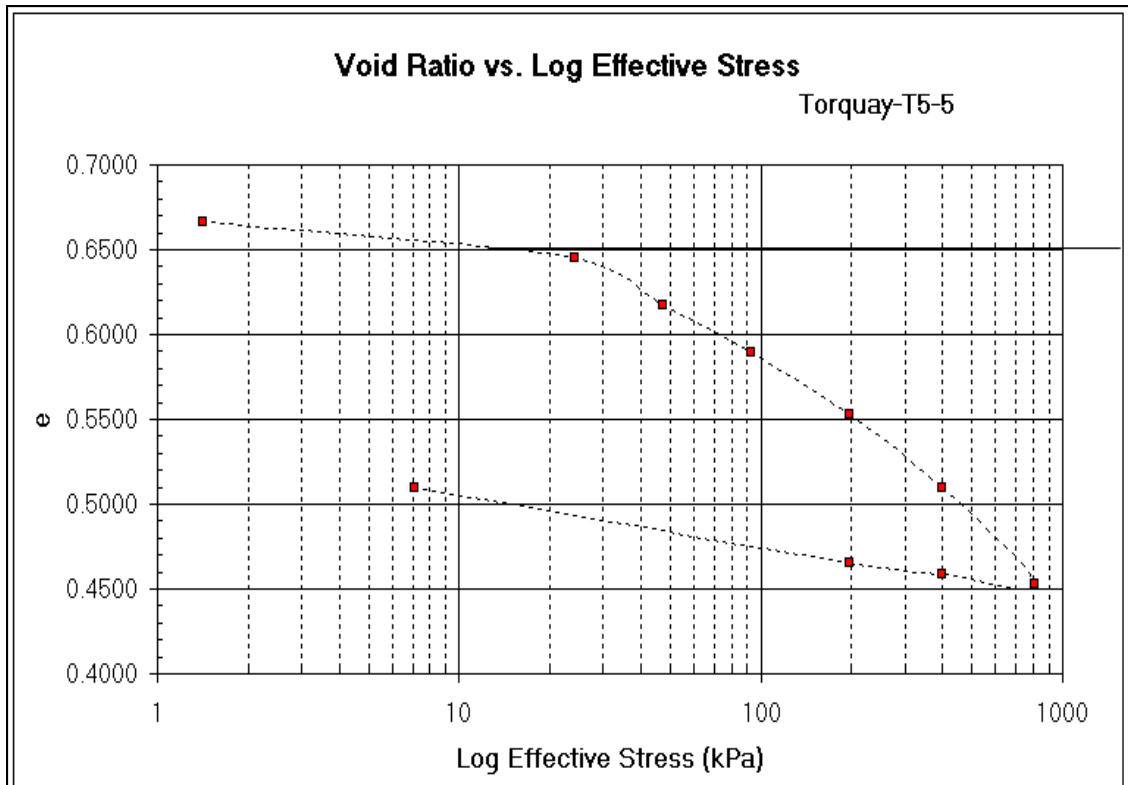
Strain Energy vs. Effective Stress

Torquay-T5-2



Site: Bethune Sample: T5-5 Date: June, 7 2005 Depth(m): 0.70-0.85 Hole: T5 Technician: Q. Nguyen			
W.C. Determination	Beginning of test	End of test	
Ting & Glass Plate #	2	2	
WT. Wet sample & Tare	233.74	236.26	
WT. Dry sample and tare	212.23	212.23	
Tare	83.53	83.53	
Weight of water	21.51	24.03	
Weight of soil	128.7	128.7	
Water content %	16.71	18.67	
Diam. Test Ring (cm)			6.389
Area of test ring (cm ²)		a	31.750
Height sample beginning of test (cm)		h ₁	2.540
Specific gravity solids		G	2.660
WT. Dry sample		W _s	128.700
Reduced height of solids	$h_s = W_s / aG$	h _s	1.524
Change in height of sample begin to end test		dh	0.240
Height of sample at end of test	$h_2 = h_1 - dh$	h ₂	2.300
Height of water at begin of test	$h_{w1} = W_{w1} / a$	h _{w1}	0.677
Height of water at end of test	$h_{w2} = W_{w2} / a$	h _{w2}	0.757
Sat. degree at begin of test	$S_{w1} = h_{w1} / h_1 - h_s$	S ₁	0.667
Sat. degree at end of test	$S_{w2} = h_{w2} / h_2 - h_s$	S ₂	0.975
Void ratio	$e_1 = (h_1 - h_s) / h_s$	e ₁	0.667
$e = e_1 - \text{Defl.} / H_s$	$e = w * G$	e	0.445

T5-5												
Pressure (kPa)	Dial 1 (cm)	Defl. (cm)	Defl/Hs	e	Pavg	H	dDefl.	Strain	Inc. Strain Energy	Strain Energy		
1.4	0.4945	0.0000	0.0000	0.6668		2.5400						
24.3	0.4615	0.0330	0.0217	0.6451	12.85	2.5070	0.0330	0.0132	0.1692	0.		
47.2	0.4198	0.0747	0.0490	0.6178	35.73	2.4653	0.0417	0.0169	0.6043	1.		
92.9	0.3760	0.1185	0.0778	0.5890	70.02	2.4215	0.0438	0.0181	1.2665	1.		
197.3	0.3205	0.1740	0.1142	0.5526	145.10	2.3660	0.0555	0.0235	3.4038	3.		
399.1	0.2555	0.2390	0.1568	0.5100	298.20	2.3010	0.0650	0.0282	8.4236	8.		
810.9	0.1687	0.3258	0.2138	0.4530	604.97	2.2142	0.0868	0.0392	23.7158	24.		
399.1	0.1770	0.3175	0.2083	0.4584	604.97	2.2225	-0.0083	-0.0037	-2.2593	-2.		
197.3	0.1869	0.3076	0.2019	0.4649	298.20	2.2324	-0.0099	-0.0044	-1.3224	-1.		
7.1	0.2545	0.2400	0.1575	0.5093	102.22	2.3000	-0.0676	-0.0294	-3.0045	-3.		
* Dial 50- Dial reading for 50% consolidation at pressure 2												
** Time 50-Time required to reach 50% consolidation at pressure 2												
Pressure 1 (kPa)	Pressure 2 (kPa)	P avg (kPa)	Dial 100 (cm)	Dial 50* (cm)	Time 50** (min)	H (cm)	Cv (sq cm/sec)	Av (1/kPa)	Mv (1/kPa)	K (m/sec)	Cv (sq m/year)	
1.42	24.29	12.85	0.4615	0.4680	15	2.5135	0.000345718	0.000946684	0.000567969	1.92567E-08	1.090	
24.29	47.16	35.73	0.4198	0.4297	7	2.47515	0.00071839	0.001196647	0.000727386	5.12461E-08	2.266	
47.16	92.88	70.02	0.376	0.3855	5	2.431	0.000970186	0.000628673	0.000388605	3.69742E-08	3.060	
92.88	197.33	145.10	0.3205	0.3318	2	2.37725	0.002319395	0.000348678	0.000219428	4.99118E-08	7.314	
197.33	399.06	298.20	0.2555	0.2713	5	2.31675	0.000881137	0.000211439	0.000136183	1.1768E-08	2.779	
399.06	810.88	604.97	0.1687	0.1909	5	2.23635	0.00082104	0.000138313	9.16006E-05	7.37563E-09	51.122	
810.88	399.06	604.97	0.177	0.1765	0.25	2.222	0.016210749	1.32257E-05	9.10242E-06	1.44709E-08	0.586	
399.06	197.33	298.20	0.1869	0.1857	22	2.2312	0.000185742	3.22038E-05	2.2081E-05	4.02221E-10	2.239	
197.33	7.12	102.22	0.2545	0.2324	6	2.27785	0.000709829	0.000233214	0.000159197	1.10822E-08	0.000	
7.12												



Site: Bethune Sample: T5-12 Date: July, 3 2005 Depth(m): 1.90-2.05 Hole: T5 Technician: Q. Nguyen			
W.C. Determination	Beginning of test	End of test	
Ting & Glass Plate #	2	2	
WT. Wet sample & Tare	251.68	248.6	
WT. Dry sample and tare	228.14	228.14	
Tare	77.81	77.81	
Weight of water	23.54	20.46	
Weight of soil	150.33	150.33	
Water content %	15.66	13.61	
Diam. Test Ring (cm)			6.389
Area of test ring (cm ²)		a	32.054
Height sample beginning of test (cm)		h_1	2.478
Specific gravity solids		G	2.700
WT. Dry sample		W_s	150.330
Reduced height of solids	$h_s = W_s / aG$	h_s	1.737
Change in height of sample begin to end test		dh	0.099
Height of sample at end of test	$h_2 = h_1 - dh$	h_2	2.379
Height of water at begin of test	$h_{w1} = W_{w1} / a$	h_{w1}	0.734
Height of water at end of test	$h_{w2} = W_{w2} / a$	h_{w2}	0.638
Sat. degree at begin of test	$S_{w1} = h_{w1} / h_1 - h_s$	S_1	0.992
Sat. degree at end of test	$S_{w2} = h_{w2} / h_2 - h_s$	S_2	0.995
Void ratio	$e_1 = (h_1 - h_s) / h_s$	e_1	0.426
$e = e_1 - \text{Defl.} / H_s$	$e = w * G$	e	0.423

T5-12

Pressure (kPa)	Dial 1 (cm)	Defl. (cm)	Defl/Hs	e	Pavg	H	dDefl.	Strain	Inc.Strain Energy	Strain Energy
35.4	0.6480	0.0000	0.0000	0.4263		2.4775				
57.9	0.6313	0.0167	0.0096	0.4167	46.65	2.4608	0.0167	0.0068	0.3166	0.
107.8	0.6035	0.0445	0.0256	0.4007	82.89	2.4330	0.0278	0.0114	0.9471	1.
215.6	0.5630	0.0850	0.0489	0.3774	161.70	2.3925	0.0405	0.0169	2.7372	4.
419.1	0.5124	0.1356	0.0781	0.3483	317.32	2.3419	0.0506	0.0216	6.8560	11.
834.6	0.4508	0.1972	0.1135	0.3128	626.82	2.2803	0.0616	0.0270	16.9329	28.
419.1	0.4579	0.1901	0.1094	0.3169	626.82	2.2874	-0.0071	-0.0031	-1.9456	26.
57.9	0.5013	0.1467	0.0845	0.3419	238.51	2.3308	-0.0434	-0.0186	-4.4411	21.
7.0	0.5492	0.0988	0.0569	0.3694	32.50	2.3787	-0.0479	-0.0201	0.0000	21.

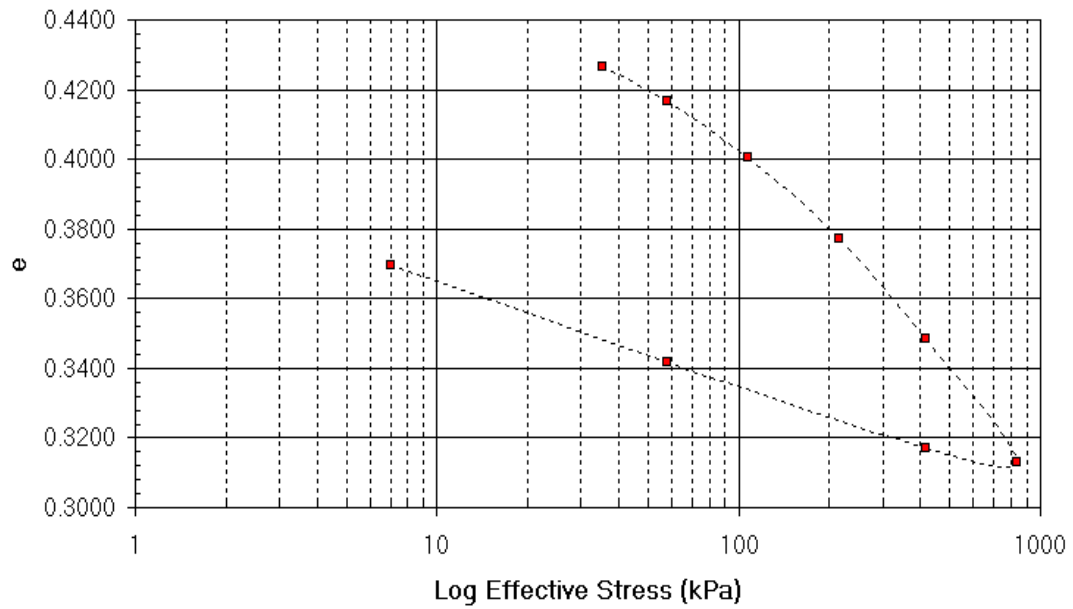
* Dial 50- Dial reading for 50% consolidation at pressure 2

** Time 50- Time required to reach 50% consolidation at pressure 2

Pressure 1 (kPa)	Pressure 2 (kPa)	P avg (kPa)	Dial 100 (cm)	Dial 50* (cm)	Time 50** (min)	H (cm)	Cv (sq cm/sec)	Av (1/kPa)	Mv (1/kPa)	K (m/sec)	Cv (sq m/year)
35.37	57.94	46.65	0.6313	0.6357	5	2.46515	0.000997635	0.00042589	0.000298592	2.92136E-08	3.146
57.94	107.84	82.89	0.6035	0.6113	4	2.44075	0.00122248	0.000320753	0.000226406	2.71435E-08	3.855
107.84	215.56	161.70	0.563	0.5730	6	2.4025	0.000789643	0.000216456	0.000154533	1.19671E-08	2.490
215.56	419.07	317.32	0.5124	0.5280	5	2.35745	0.000912368	0.000143139	0.00010392	9.29837E-09	2.877
419.07	834.57	626.82	0.4508	0.4699	8	2.2994	0.000542493	8.53537E-05	6.33065E-05	3.36805E-09	1.711
834.57	419.07	626.82	0.4579	0.4566	5	2.28605	0.000857939	9.83784E-06	7.4938E-06	6.30514E-10	2.706
419.07	57.94	238.51	0.5013	0.4892	12	2.31865	0.000367743	6.91877E-05	5.25389E-05	6.30514E-10	1.160
57.94	7.05	32.50	0.5492	0.5285	0.5	2.358	0.009127936	0.000541874	0.00040382	1.89479E-09	28.786
7.05										3.6149E-07	0.000

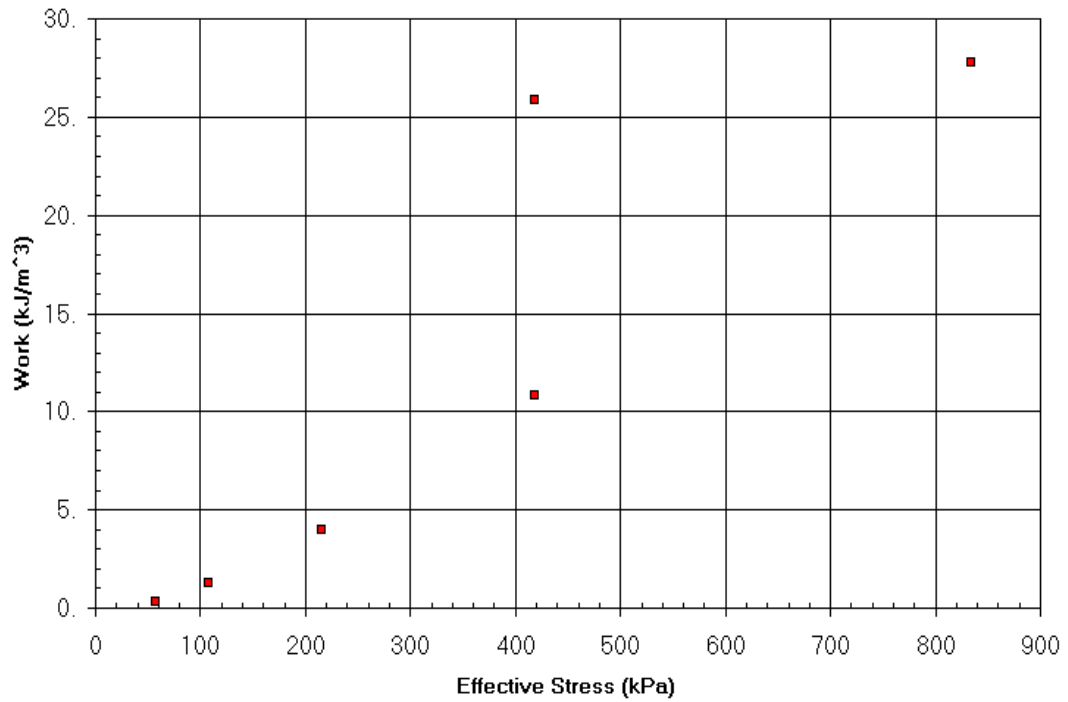
Void Ratio vs. Log Effective Stress

Torquay-T5-12



Strain Energy vs. Effective Stress

Torquay-T5-12



Site: Bethune Sample: T5-14 Date: June, 20 2005 Depth(m): 2.35-2.50 Hole: T5 Technician: Q. Nguyen			
W.C. Determination	Beginning of test	End of test	
Ting & Glass Plate #	2	2	
WT. Wet sample & Tare	211.89	204.13	
WT. Dry sample and tare	190.3	190.3	
Tare	69.72	69.72	
Weight of water	21.59	13.83	
Weight of soil	120.58	120.58	
Water content %	17.91	11.47	
Diam. Test Ring (cm)			6.401
Area of test ring (cm ²)		a	32.182
Height sample beginning of test (cm)		h_1	2.234
Specific gravity solids		G	2.700
WT. Dry sample		W_s	120.580
Reduced height of solids	$h_s = W_s/aG$	h_s	1.388
Change in height of sample begin to end test		dh	0.408
Height of sample at end of test	$h_2 = h_1 - dh$	h_2	1.826
Height of water at begin of test	$h_{w1} = W_{w1}/a$	h_{w1}	0.671
Height of water at end of test	$h_{w2} = W_{w2}/a$	h_{w2}	0.430
Sat. degree at begin of test	$S_{w1} = h_{w1}/h_1 - h_s$	S_1	0.793
Sat. degree at end of test	$S_{w2} = h_{w2}/h_2 - h_s$	S_2	0.980
Void ratio	$e_1 = (h_1 - h_s)/h_s$	e_1	0.610
$e = e_1 - \text{Defl.}/H_s$	$e = w * G$	e	0.483

T5-14

Pressure (kPa)	Dial 1 (cm)	Defl. (cm)	Defl/Hs	e	Pavg	H	dDefl.	Strain	Inc.Strain Energy	Strain Energy
7.1	0.8600	0.0000	0.0000	0.6100		2.2342				
29.1	0.7931	0.0669	0.0482	0.5618	18.10	2.1673	0.0669	0.0309	0.5586	1.
57.3	0.7146	0.1454	0.1048	0.5052	43.17	2.0888	0.0785	0.0376	1.6225	2.
112.6	0.6348	0.2252	0.1623	0.4477	84.93	2.0090	0.0798	0.0397	3.3737	6.
227.9	0.5485	0.3115	0.2245	0.3855	170.24	1.9227	0.0863	0.0449	7.6413	13.
476.5	0.4662	0.3938	0.2838	0.3262	352.16	1.8404	0.0823	0.0447	15.7484	29.
973.6	0.3950	0.4650	0.3351	0.2749	725.03	1.7692	0.0712	0.0402	29.1790	58.
476.5	0.3953	0.4647	0.3349	0.2751	725.03	1.7695	-0.0003	-0.0002	-0.1229	58.
191.7	0.4013	0.4587	0.3305	0.2794	334.10	1.7755	-0.0060	-0.0034	-1.1290	57.
57.3	0.4181	0.4419	0.3184	0.2915	124.50	1.7923	-0.0168	-0.0094	-1.1670	56.
7.2	0.4519	0.4081	0.2941	0.3159	99.48	1.8261	-0.0506	-0.0277	-2.7567	54.

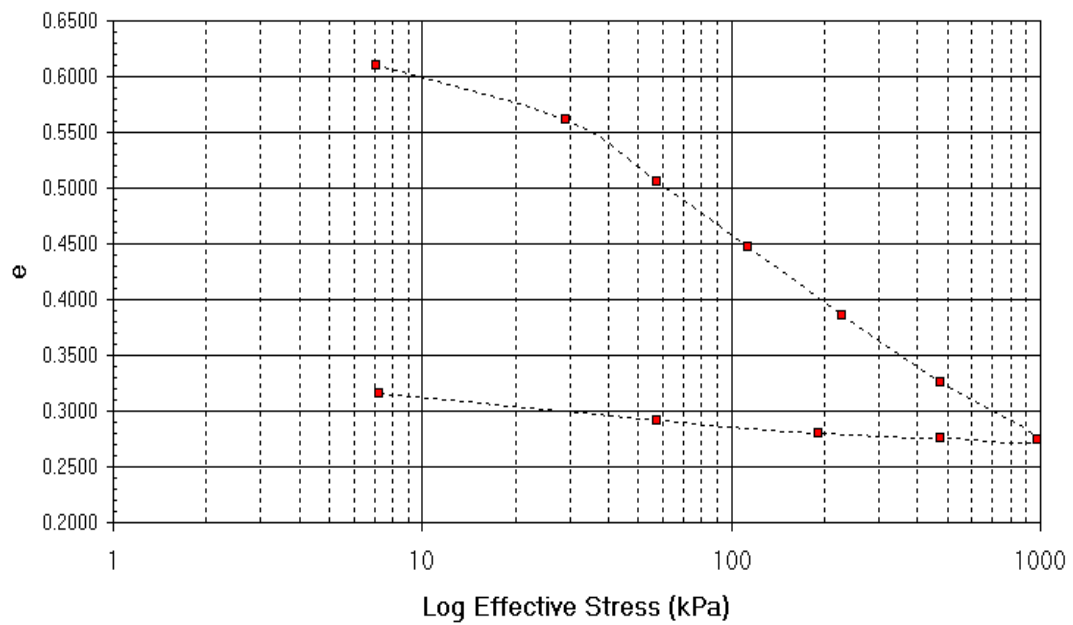
* Dial 50- Dial reading for 50% consolidation at pressure 2

** Time 50- Time required to reach 50% consolidation at pressure 2

Pressure 1 (kPa)	Pressure 2 (kPa)	P avg (kPa)	Dial 100 (cm)	Dial 50* (cm)	Time 50** (min)	H (cm)	Cv (sq cm/sec)	Av (1/kPa)	Mv (1/kPa)	K (m/sec)	Cv (sq m/year)
7.10	29.09	18.10	0.7931	0.8111	5	2.18522	0.000783924	0.002192898	0.001362056	1.04714E-07	2.472
29.09	57.26	43.17	0.7146	0.1703	2.2	1.54447	0.000889999	0.002008206	0.001285843	1.12231E-07	2.807
57.26	112.61	84.93	0.6348	0.6579	3	2.03207	0.001129821	0.001038921	0.000690215	7.64769E-08	3.563
112.61	227.87	170.24	0.5485	0.5733	4.3	1.94742	0.000723943	0.000539559	0.000372699	2.64606E-08	2.283
227.87	476.45	352.16	0.4662	0.4891	8	1.86327	0.000356217	0.000238582	0.000172197	6.01557E-09	1.123
476.45	973.62	725.03	0.395	0.4175	9	1.79167	0.00029277	0.000103202	7.78171E-05	2.23428E-09	0.923
973.62	476.45	725.03	0.3953	0.3952	8	1.76937	0.000321219	4.34839E-07	3.41077E-07	2.34428E-09	1.013
476.45	191.74	334.10	0.4013	0.3992	5	1.77337	0.000516276	1.51865E-05	1.19099E-05	1.07446E-11	1.628
191.74	57.26	124.50	0.4181	0.4116	18	1.78577	0.000145423	9.00208E-05	7.03595E-05	6.03012E-10	0.459
57.26	7.22	32.24	0.4519	0.4347	30	1.80887	8.95255E-05	0.00048682	0.000376928	1.00344E-09	0.282
7.22										3.30934E-09	0.000

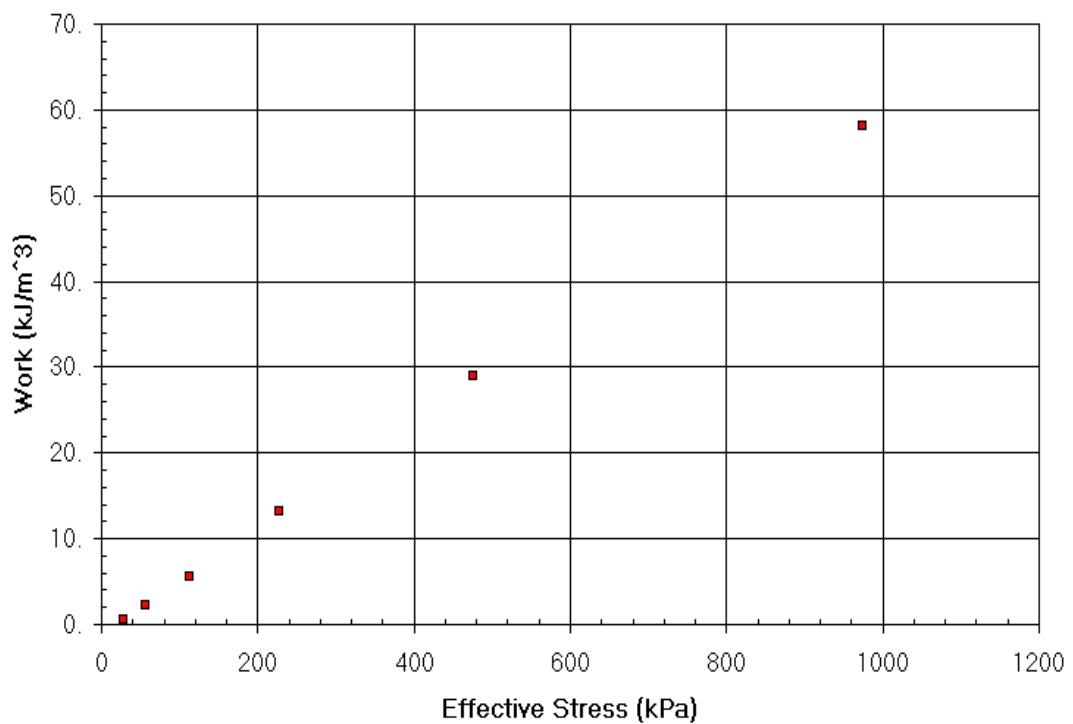
Void Ratio vs. Log Effective Stress

Torquay-T5-14



Strain Energy vs. Effective Stress

Torquay-T5-14



Site: Bethune Sample: T5-17 Date: June, 26 2005 Depth(m): 2.95-3.10 Hole: T5 Technician: Q. Nguyen			
W.C. Determination	Beginning of test	End of test	
Ting & Glass Plate #	2	2	
WT. Wet sample & Tare	338.11	337.67	
WT. Dry sample and tare	315.09	315.09	
Tare	172.36	172.36	
Weight of water	23.02	22.58	
Weight of soil	142.73	142.73	
Water content %	16.13	15.82	
Diam. Test Ring (cm)			6.338
Area of test ring (cm ²)		a	31.545
Height sample beginning of test (cm)		h ₁	2.496
Specific gravity solids		G	2.650
WT. Dry sample		W _s	142.730
Reduced height of solids	$h_s = W_s / aG$	h _s	1.707
Change in height of sample begin to end test		dh	0.065
Height of sample at end of test	$h_2 = h_1 - dh$	h ₂	2.431
Height of water at begin of test	$h_{w1} = W_{w1} / a$	h _{w1}	0.730
Height of water at end of test	$h_{w2} = W_{w2} / a$	h _{w2}	0.716
Sat. degree at begin of test	$S_{w1} = h_{w1} / (h_1 - h_s)$	S ₁	0.925
Sat. degree at end of test	$S_{w2} = h_{w2} / (h_2 - h_s)$	S ₂	0.989
Void ratio	$e_1 = (h_1 - h_s) / h_s$	e ₁	0.462
$e = e_1 - \text{Defl.} / H_s$	$e = w * G$	e	0.427

T5-17

Pressure (kPa)	Dial 1 (cm)	Defl. (cm)	Defl/Hs	e	Pavg	H	dDefl.	Strain	Inc.Strain Energy	Strain Energy
24.6	0.8000	0.0000	0.0000	0.4621		2.4964				
47.6	0.7830	0.0170	0.0100	0.4521	36.13	2.4794	0.0170	0.0069	0.2477	0.
92.4	0.7584	0.0416	0.0244	0.4377	70.00	2.4548	0.0246	0.0100	0.7015	1.
184.6	0.7192	0.0808	0.0473	0.4148	138.50	2.4156	0.0392	0.0162	2.2475	3.
364.0	0.6658	0.1342	0.0786	0.3835	274.31	2.3622	0.0534	0.0226	6.2009	9.
698.1	0.5918	0.2082	0.1219	0.3402	531.03	2.2882	0.0740	0.0323	17.1733	27.
1205.3	0.5240	0.2760	0.1616	0.3004	951.68	2.2204	0.0678	0.0305	29.0593	56.
698.1	0.5271	0.2729	0.1598	0.3023	951.68	2.2235	-0.0031	-0.0014	-1.3268	54.
364.0	0.5419	0.2581	0.1512	0.3109	531.03	2.2383	-0.0148	-0.0066	-3.5112	51.
184.6	0.5625	0.2375	0.1391	0.3230	274.31	2.2589	-0.0206	-0.0091	-2.5015	48.
24.6	0.6345	0.1655	0.0969	0.3652	104.62	2.3309	-0.0720	-0.0309	-3.2317	45.
1.6	0.7350	0.0650	0.0381	0.4240	13.12	2.4314	-0.1005	-0.0413	-0.5424	45.

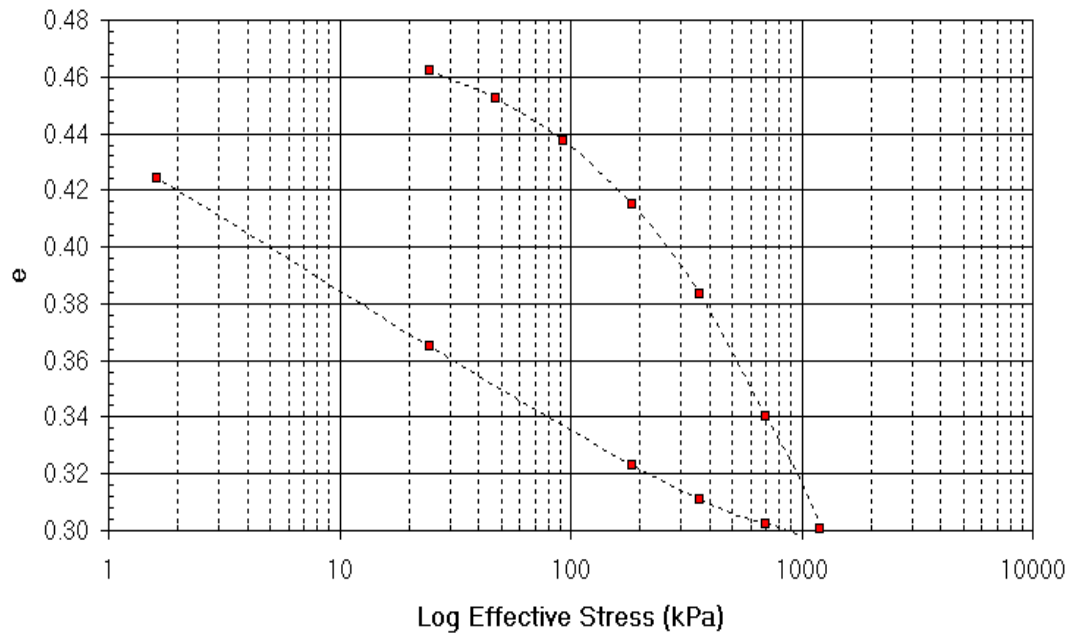
* Dial 50- Dial reading for 50% consolidation at pressure 2

** Time 50- Time required to reach 50% consolidation at pressure 2

Pressure 1 (kPa)	Pressure 2 (kPa)	P avg (kPa)	Dial 100 (cm)	Dial 50* (cm)	Time 50** (min)	H (cm)	Cv (sq cm/sec)	Av (1/kPa)	Mv (1/kPa)	K (m/sec)	Cv (sq m/year)
24.63	47.63	36.13	0.783	0.7875	15	2.48392	0.000337627	0.000432937	0.000296109	9.8045E-09	1.065
47.63	92.37	70.00	0.7584	0.7653	11	2.46172	0.000452208	0.000322007	0.000221748	9.83407E-09	1.426
92.37	184.62	138.50	0.7192	0.7306	15	2.42702	0.000322336	0.000248864	0.000173096	5.47182E-09	1.017
184.62	363.99	274.31	0.6658	0.6819	10	2.37832	0.000464295	0.000174363	0.000123245	5.61178E-09	1.464
363.99	698.07	531.03	0.5918	0.6165	9	2.31292	0.000487902	0.00012973	9.37698E-05	4.48675E-09	1.539
698.07	1205.29	951.68	0.524	0.5512	11	2.24757	0.000376953	7.82874E-05	5.84169E-05	2.15954E-09	1.189
1205.29	698.07	951.68	0.5271	0.5257	8	2.22212	0.000506639	3.57951E-06	2.75254E-06	1.36763E-10	1.598
698.07	363.99	531.03	0.5419	0.5378	15	2.23422	0.000273158	2.59459E-05	1.99238E-05	5.33732E-10	0.861
363.99	24.62	194.31	0.6345	0.6043	50	2.30067	8.68945E-05	0.000159808	0.000121905	1.03884E-09	0.274
24.62	1.62	13.12	0.735	0.7215	65	2.41792	7.38285E-05	0.002558774	0.001874341	1.35709E-08	0.233
1.62											0.000

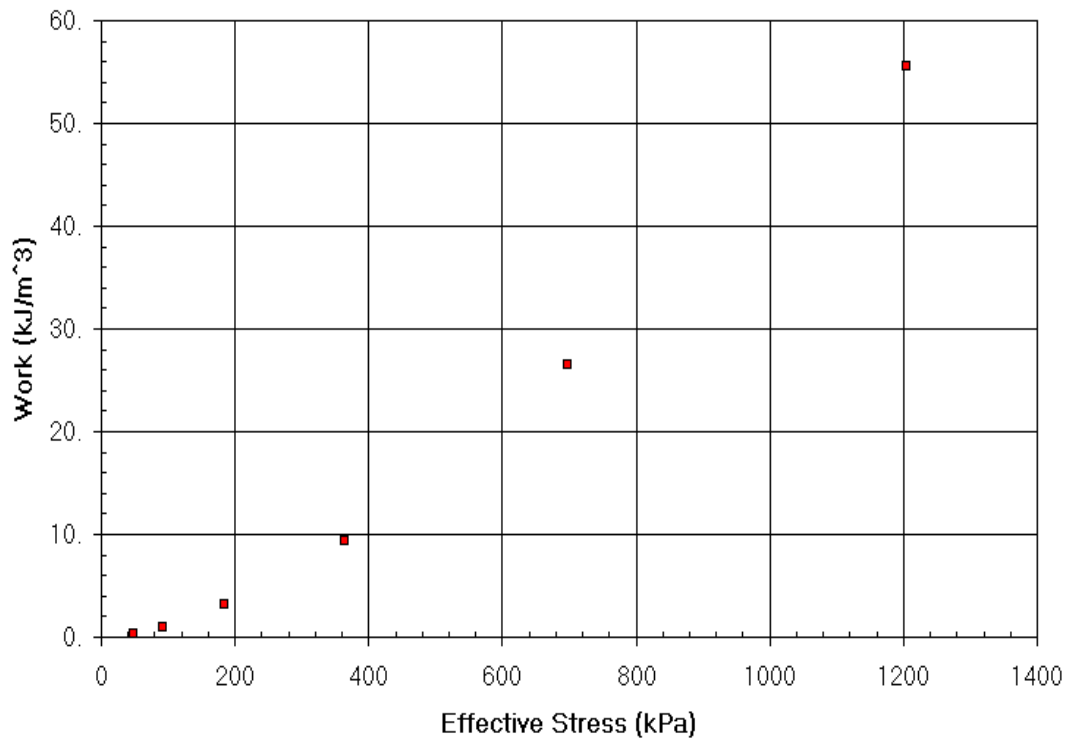
Void Ratio vs. Log Effective Stress

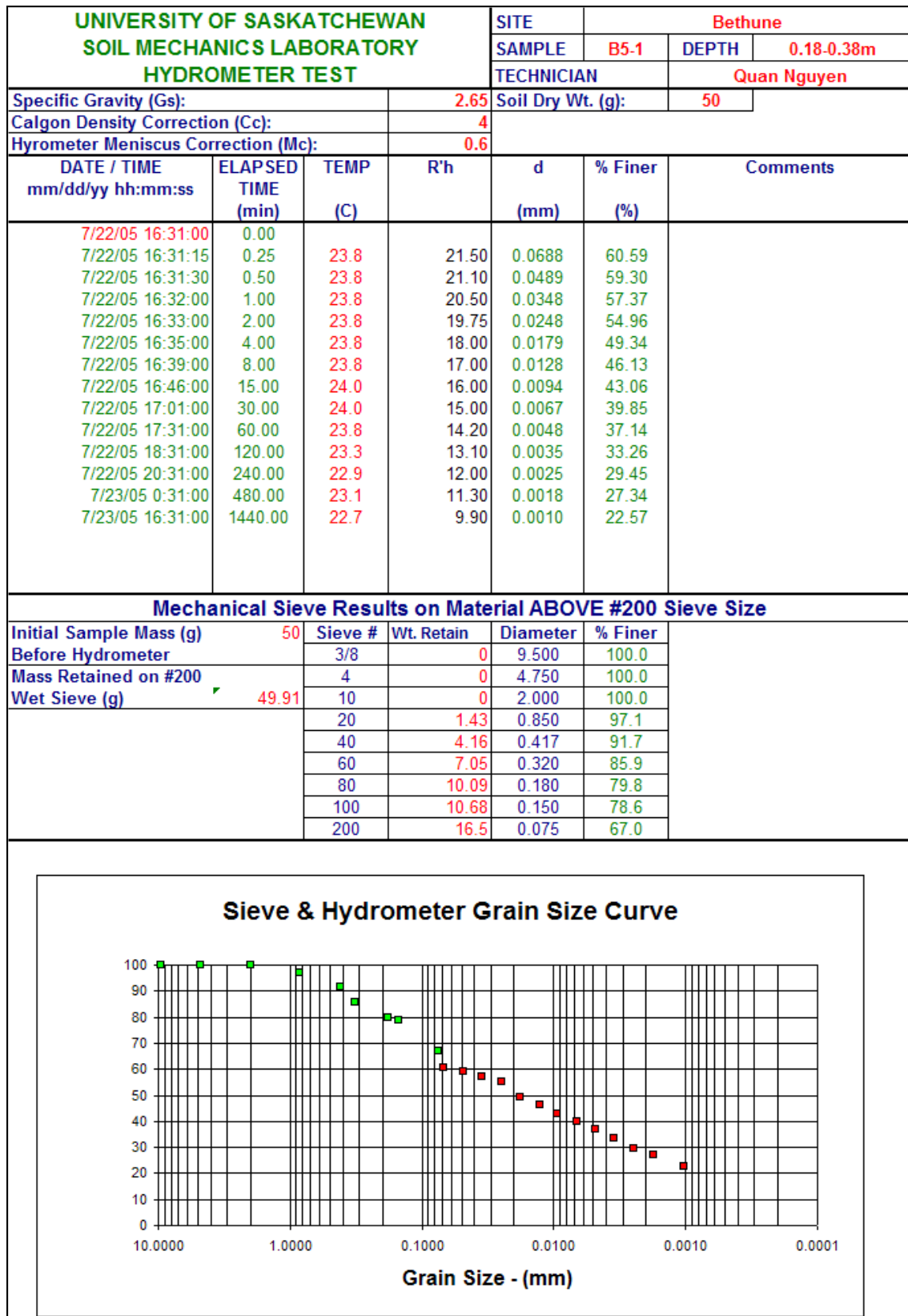
Torquay-T5-17



Strain Energy vs. Effective Stress

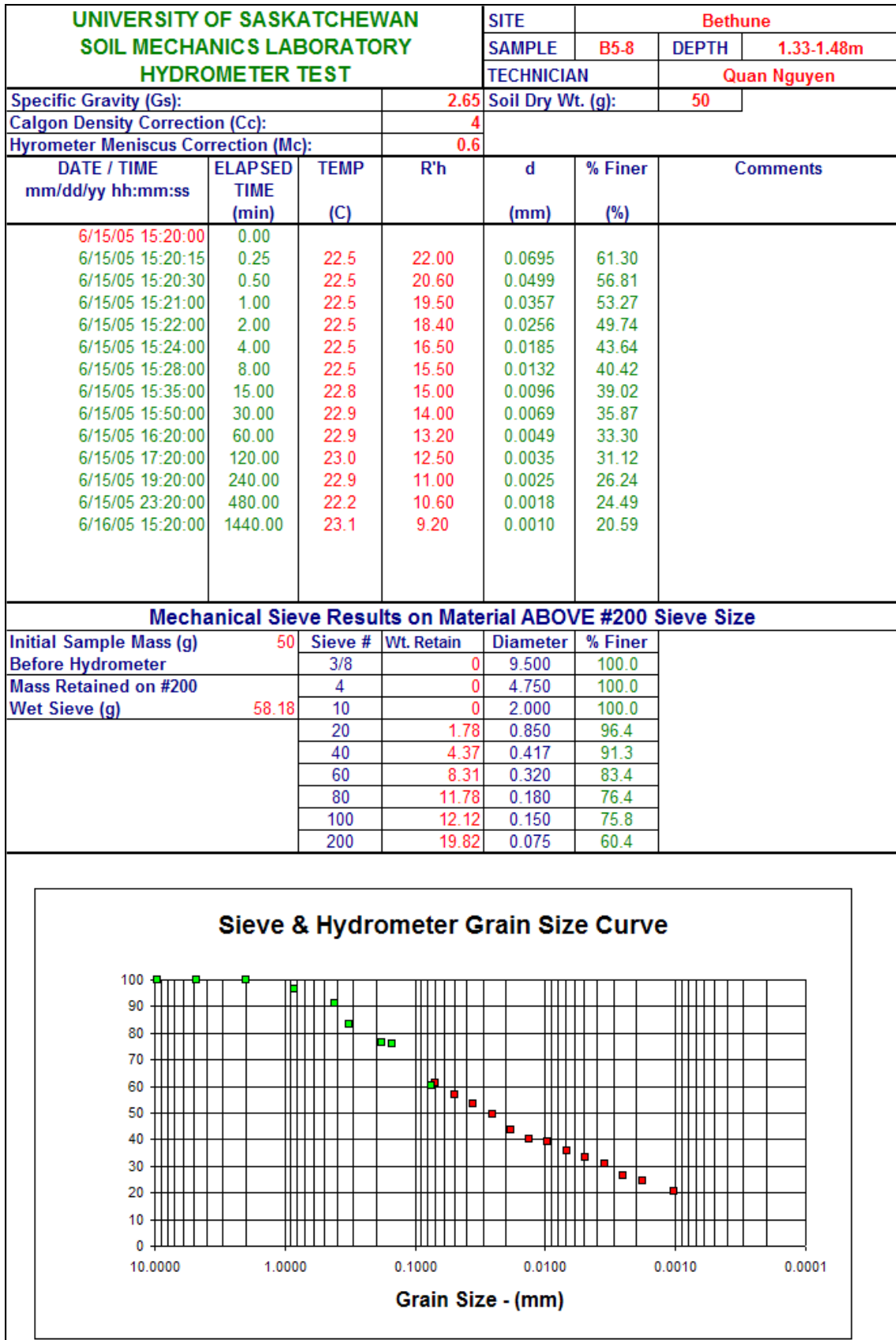
Torquay-T5-17

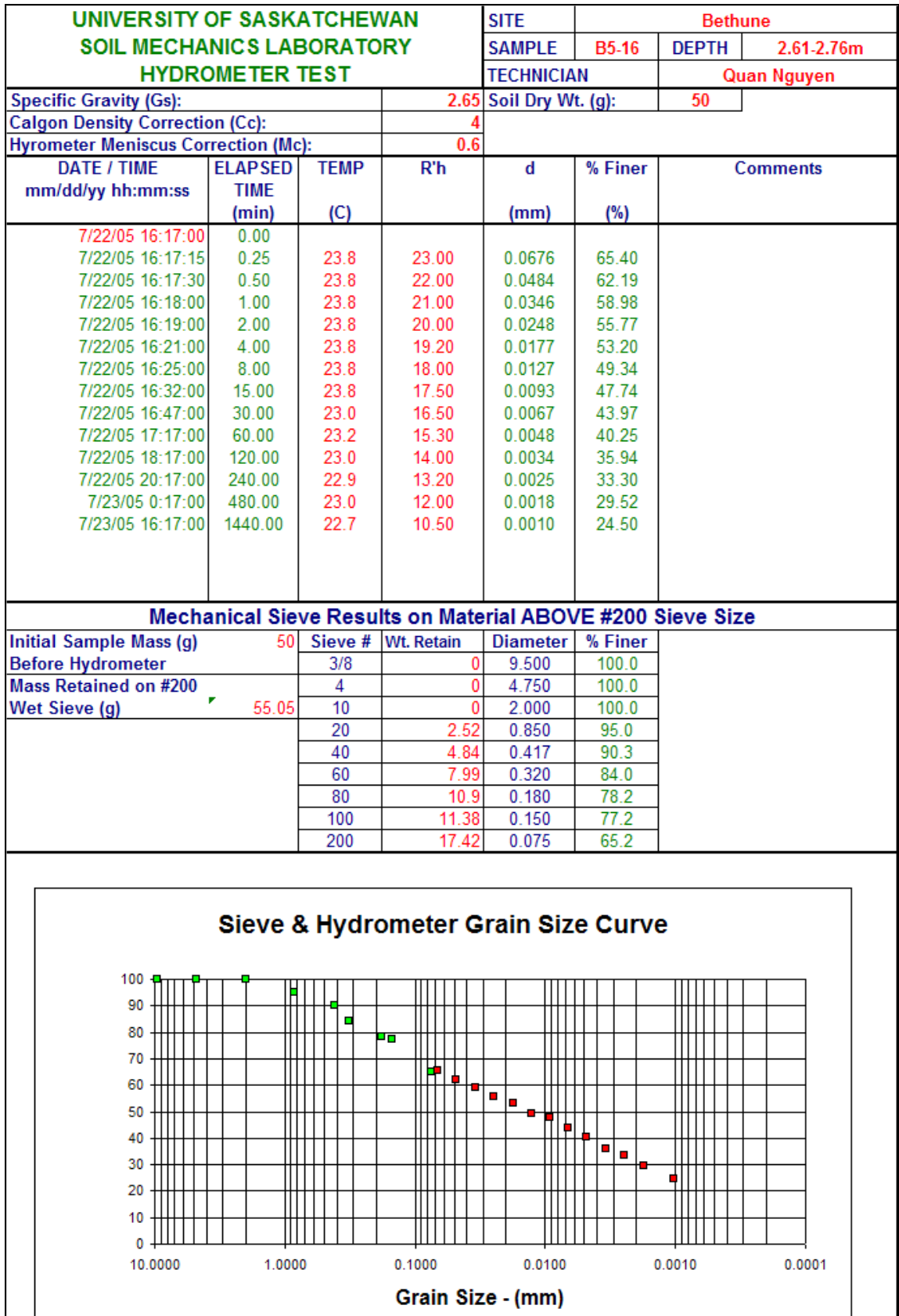


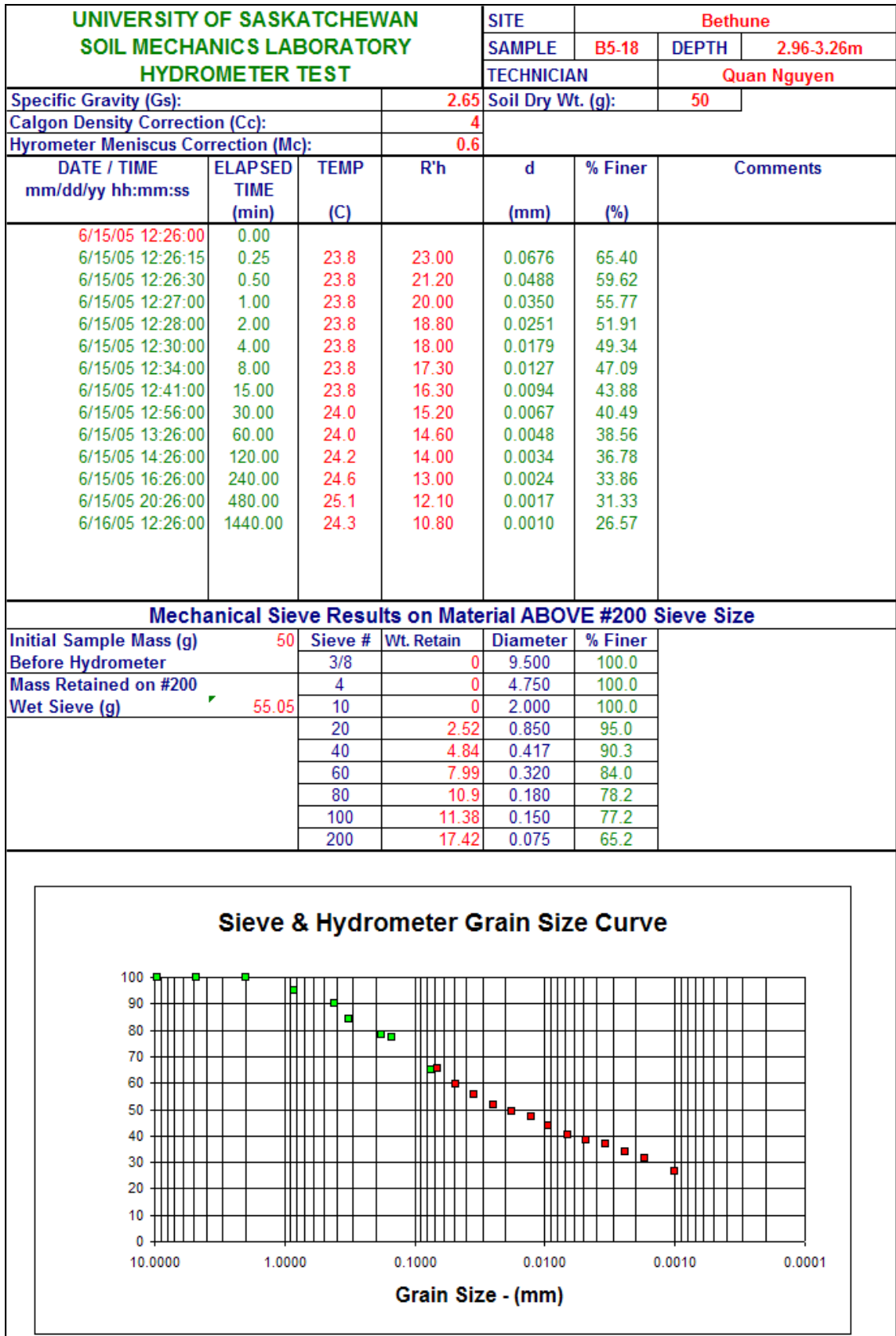


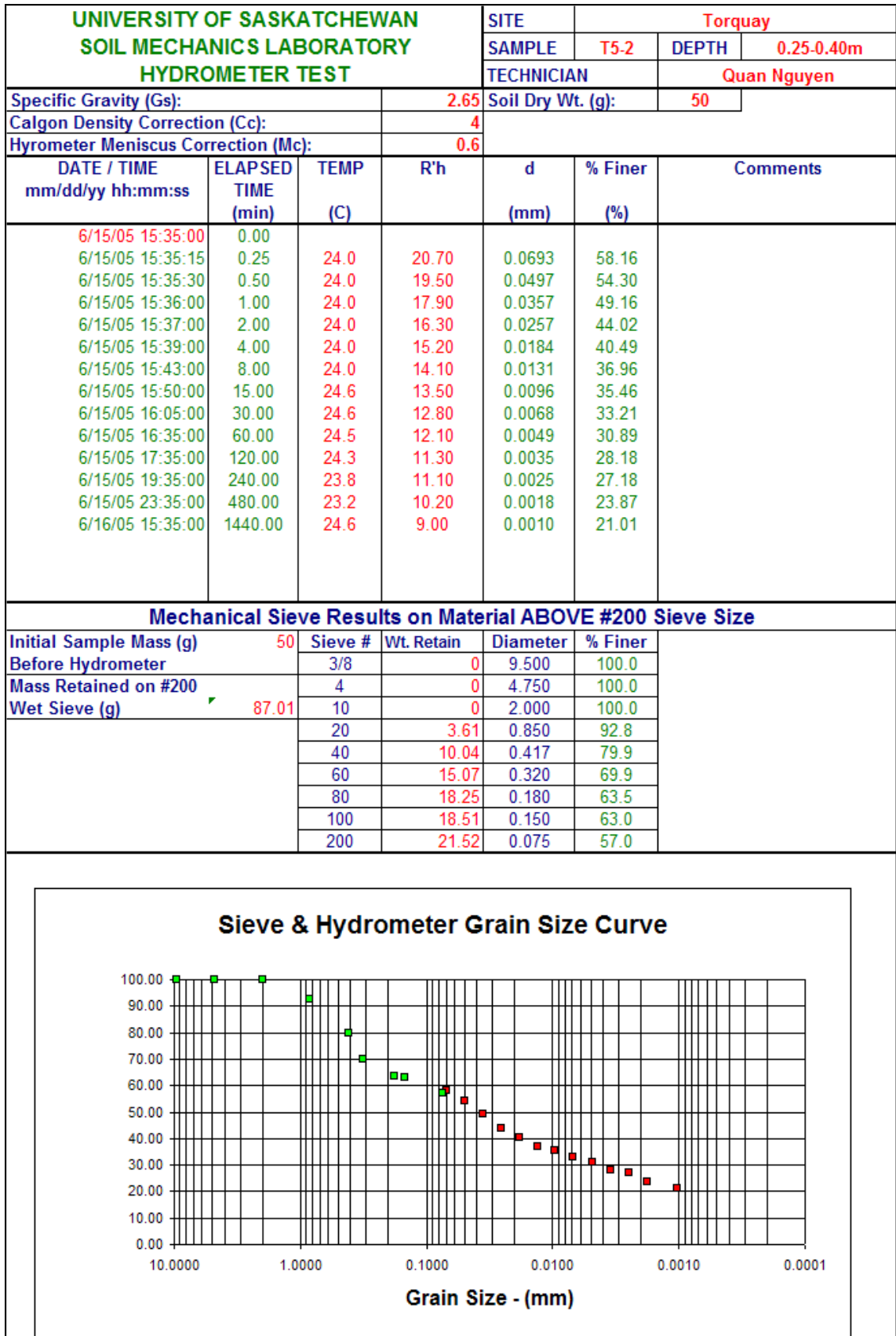
UNIVERSITY OF SASKATCHEWAN SOIL MECHANICS LABORATORY HYDROMETER TEST				SITE		Bethune	
				SAMPLE	B5-4	DEPTH	0.68-0.83m
				TECHNICIAN		Quan Nguyen	
Specific Gravity (Gs):			2.65	Soil Dry Wt. (g):		50	
Calgon Density Correction (Cc):			4				
Hyrometer Meniscus Correction (Mc):			0.6				
DATE / TIME mm/dd/yy hh:mm:ss	ELAPSED TIME (min)	TEMP (C)	R'h	d (mm)	% Finer (%)	Comments	
7/4/05 16:31:00	0.00						
7/4/05 16:31:15	0.25	23.8	21.50	0.0688	60.59		
7/4/05 16:31:30	0.50	23.8	21.10	0.0489	59.30		
7/4/05 16:32:00	1.00	23.8	20.50	0.0348	57.37		
7/4/05 16:33:00	2.00	23.8	19.75	0.0248	54.96		
7/4/05 16:35:00	4.00	23.8	18.00	0.0179	49.34		
7/4/05 16:39:00	8.00	23.5	17.00	0.0128	45.92		
7/4/05 16:46:00	15.00	23.8	16.00	0.0094	42.92		
7/4/05 17:01:00	30.00	23.5	15.00	0.0068	39.50		
7/4/05 17:31:00	60.00	23.3	14.20	0.0048	36.79		
7/4/05 18:31:00	120.00	23.1	13.10	0.0035	33.12		
7/4/05 20:31:00	240.00	22.9	12.00	0.0025	29.45		
7/5/05 0:31:00	480.00	22.9	11.30	0.0018	27.20		
7/5/05 16:31:00	1440.00	22.8	9.90	0.0010	22.64		
Mechanical Sieve Results on Material ABOVE #200 Sieve Size							
Initial Sample Mass (g)	50	Sieve #	Wt. Retain	Diameter	% Finer		
Before Hydrometer		3/8	0	9.500	100.0		
Mass Retained on #200		4	0	4.750	100.0		
Wet Sieve (g)	0	10	0	2.000	100.0		
		20	1.6	0.850	96.8		
		40	3.93	0.417	92.1		
		60	7.48	0.320	85.0		
		80	10.6	0.180	78.8		
		100	10.9	0.150	78.2		
		200	17.83	0.075	64.3		
<p style="text-align: center;">Sieve & Hydrometer Grain Size Curve</p> <p style="text-align: center;">Grain Size - (mm)</p>							

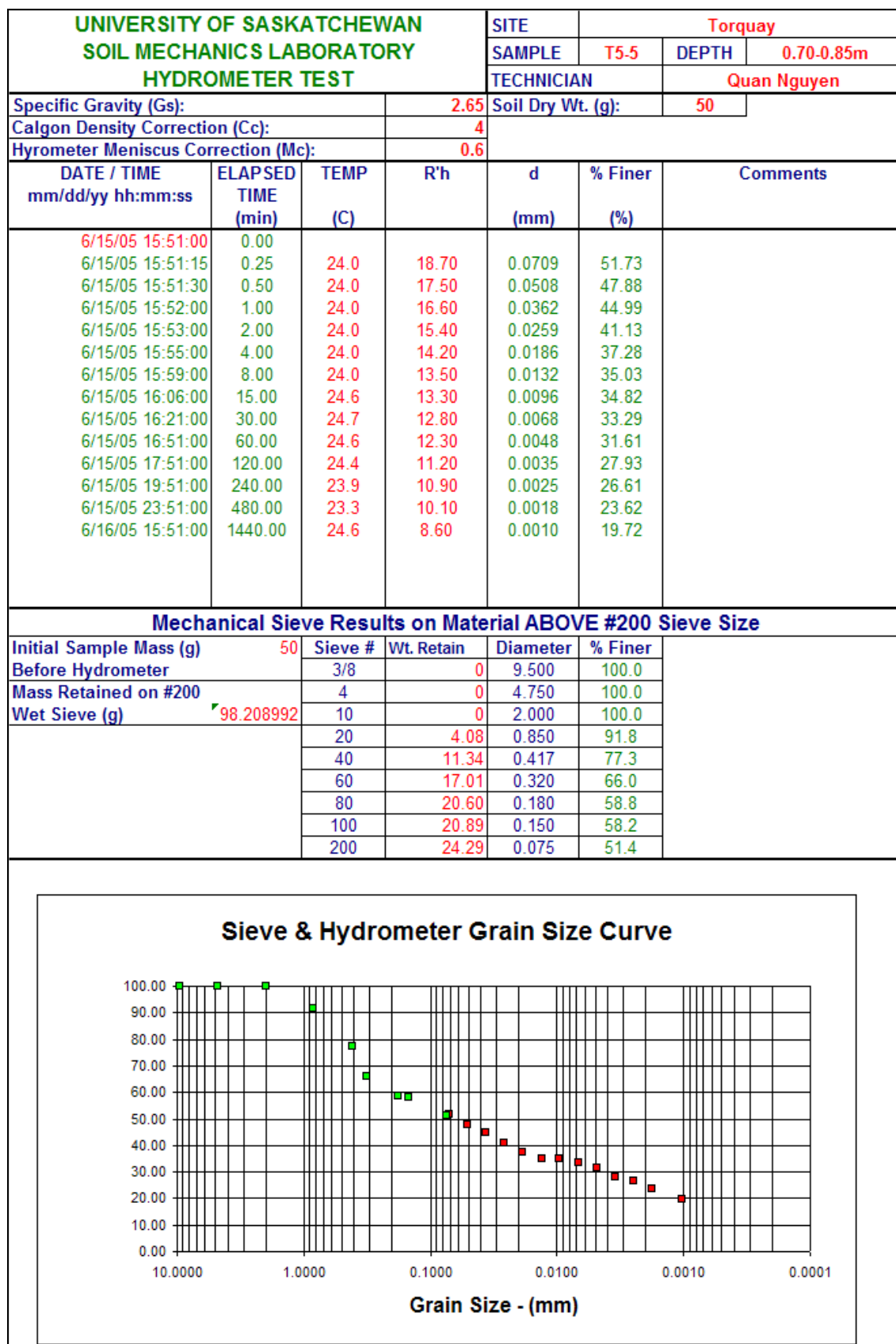
UNIVERSITY OF SASKATCHEWAN SOIL MECHANICS LABORATORY HYDROMETER TEST				SITE		Bethune	
				SAMPLE	B5-7	DEPTH	1.13-1.28m
				TECHNICIAN		Quan Nguyen	
Specific Gravity (Gs):			2.65	Soil Dry Wt. (g):		50	
Calgon Density Correction (Cc):			4				
Hyrometer Meniscus Correction (Mc):			0.6				
DATE / TIME mm/dd/yy hh:mm:ss	ELAPSED TIME (min)	TEMP (C)	R'h	d (mm)	% Finer (%)	Comments	
6/15/05 12:37:00	0.00						
6/15/05 12:37:15	0.25	23.8	23.00	0.0676	65.40		
6/15/05 12:37:30	0.50	23.8	22.10	0.0483	62.51		
6/15/05 12:38:00	1.00	23.8	21.10	0.0346	59.30		
6/15/05 12:39:00	2.00	23.8	20.10	0.0247	56.09		
6/15/05 12:41:00	4.00	23.8	18.20	0.0179	49.99		
6/15/05 12:45:00	8.00	23.5	17.80	0.0127	48.49		
6/15/05 12:52:00	15.00	23.8	17.20	0.0093	46.77		
6/15/05 13:07:00	30.00	23.6	16.50	0.0067	44.38		
6/15/05 13:37:00	60.00	24.0	15.60	0.0047	41.78		
6/15/05 14:37:00	120.00	24.0	14.40	0.0034	37.92		
6/15/05 16:37:00	240.00	24.6	13.20	0.0024	34.50		
6/15/05 20:37:00	480.00	25.2	12.20	0.0017	31.73		
6/16/05 12:37:00	1440.00	24.3	10.50	0.0010	25.61		
Mechanical Sieve Results on Material ABOVE #200 Sieve Size							
Initial Sample Mass (g)	50	Sieve #	Wt. Retain	Diameter	% Finer		
Before Hydrometer		3/8	0	9.500	100.0		
Mass Retained on #200		4	0	4.750	100.0		
Wet Sieve (g)	53.54	10	0	2.000	100.0		
		20	1.64	0.850	96.7		
		40	4.02	0.417	92.0		
		60	7.65	0.320	84.7		
		80	10.84	0.180	78.3		
		100	11.15	0.150	77.7		
		200	18.24	0.075	63.5		
<p align="center">Sieve & Hydrometer Grain Size Curve</p> <p align="center">Grain Size - (mm)</p>							

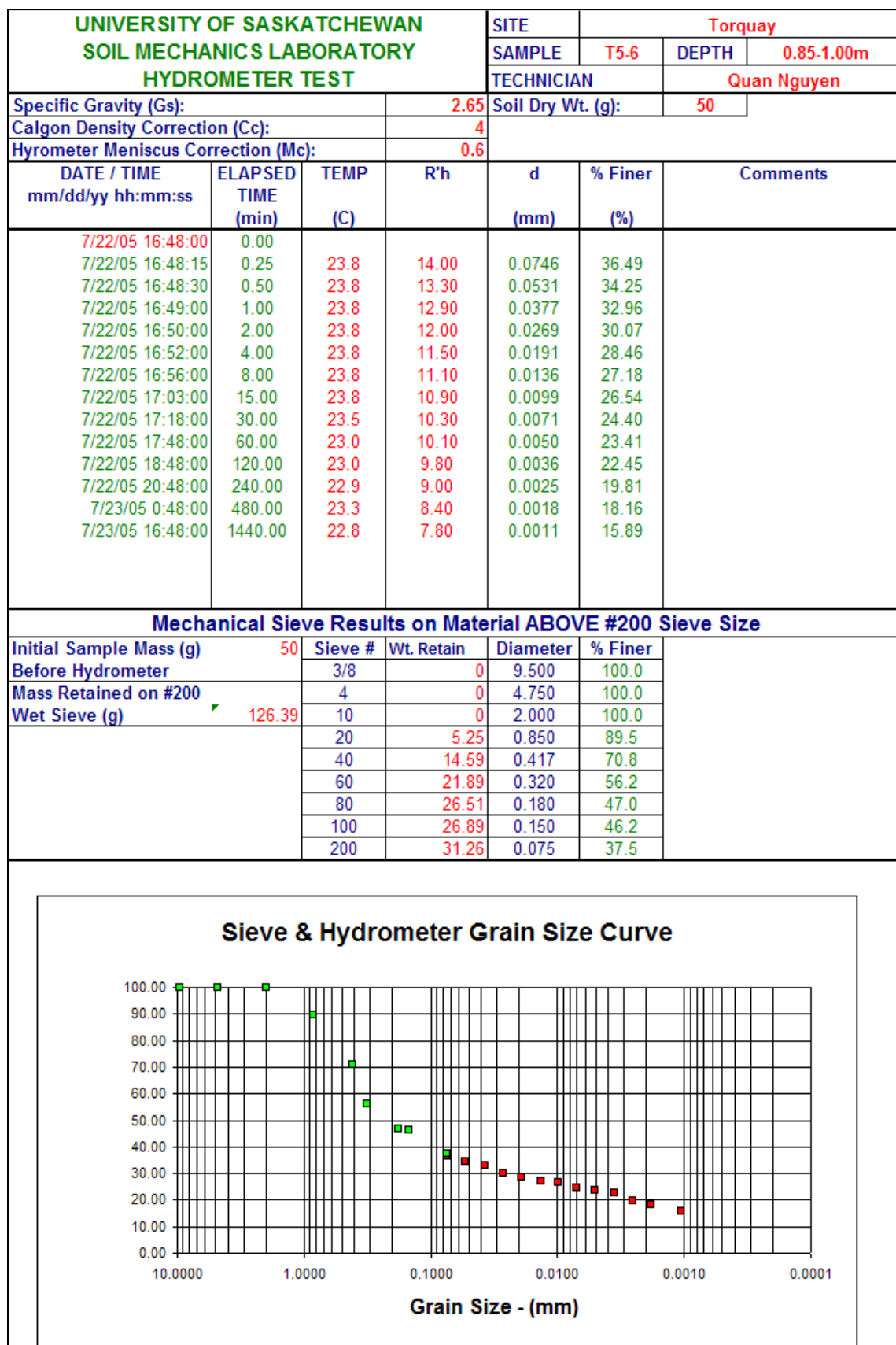


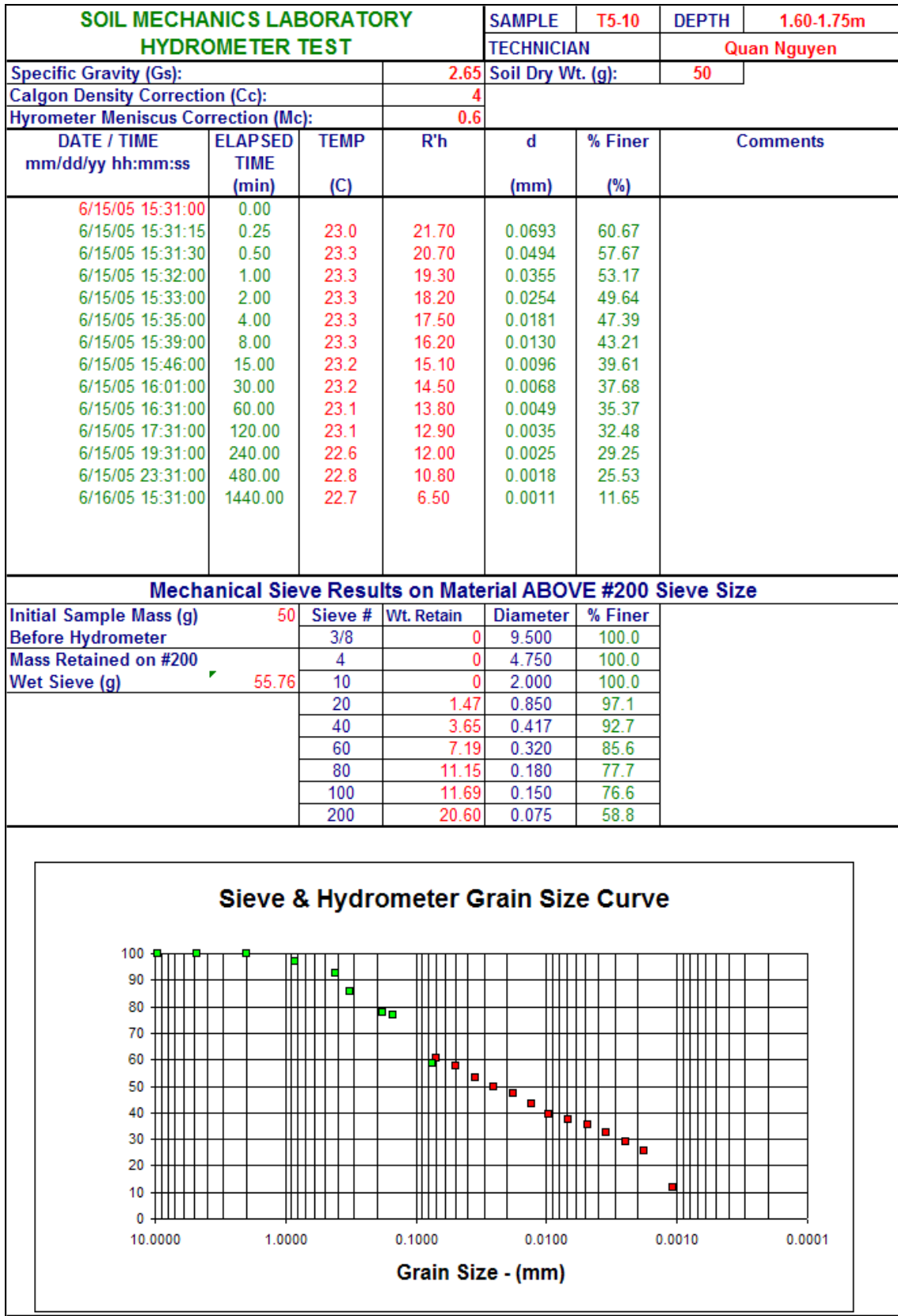


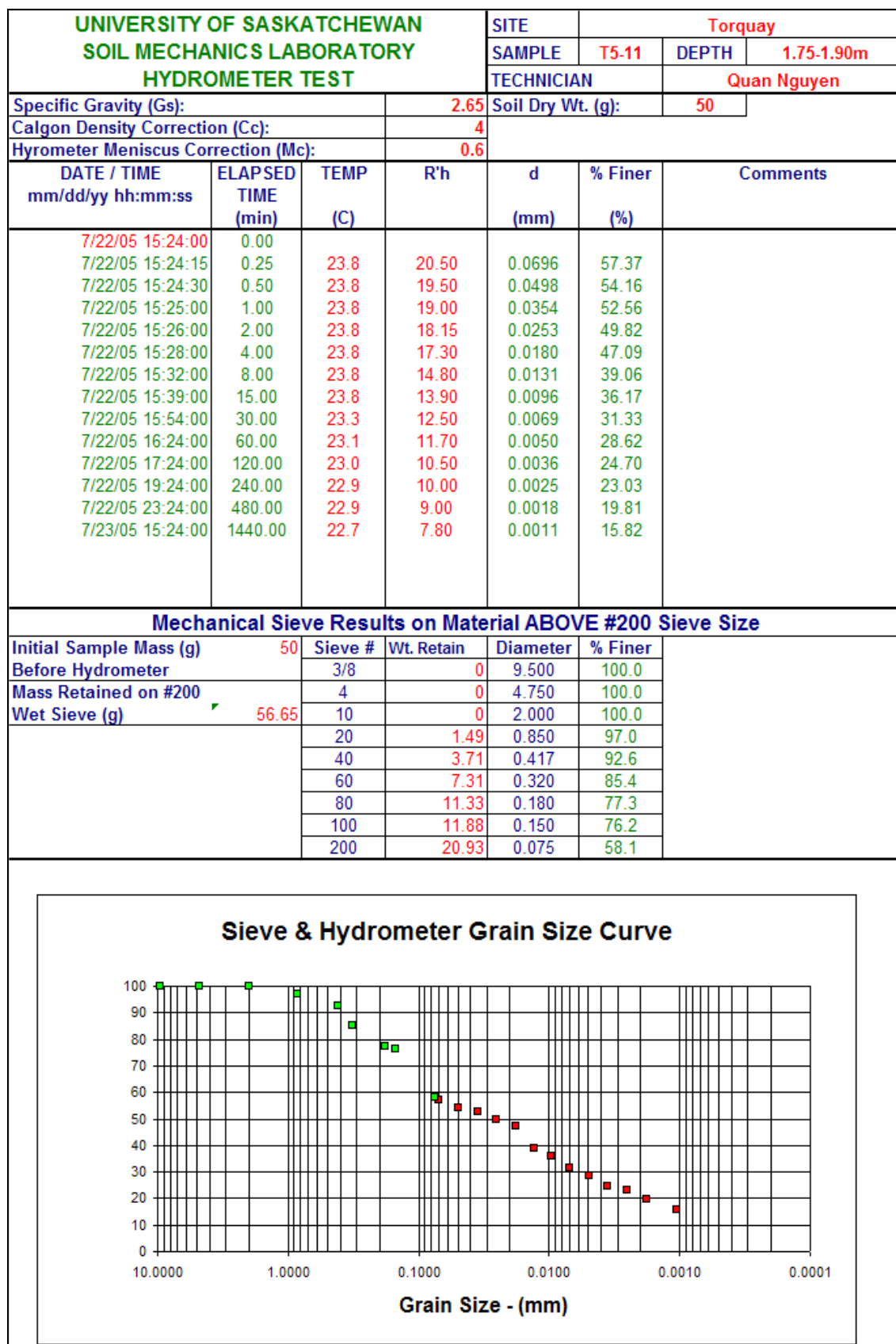


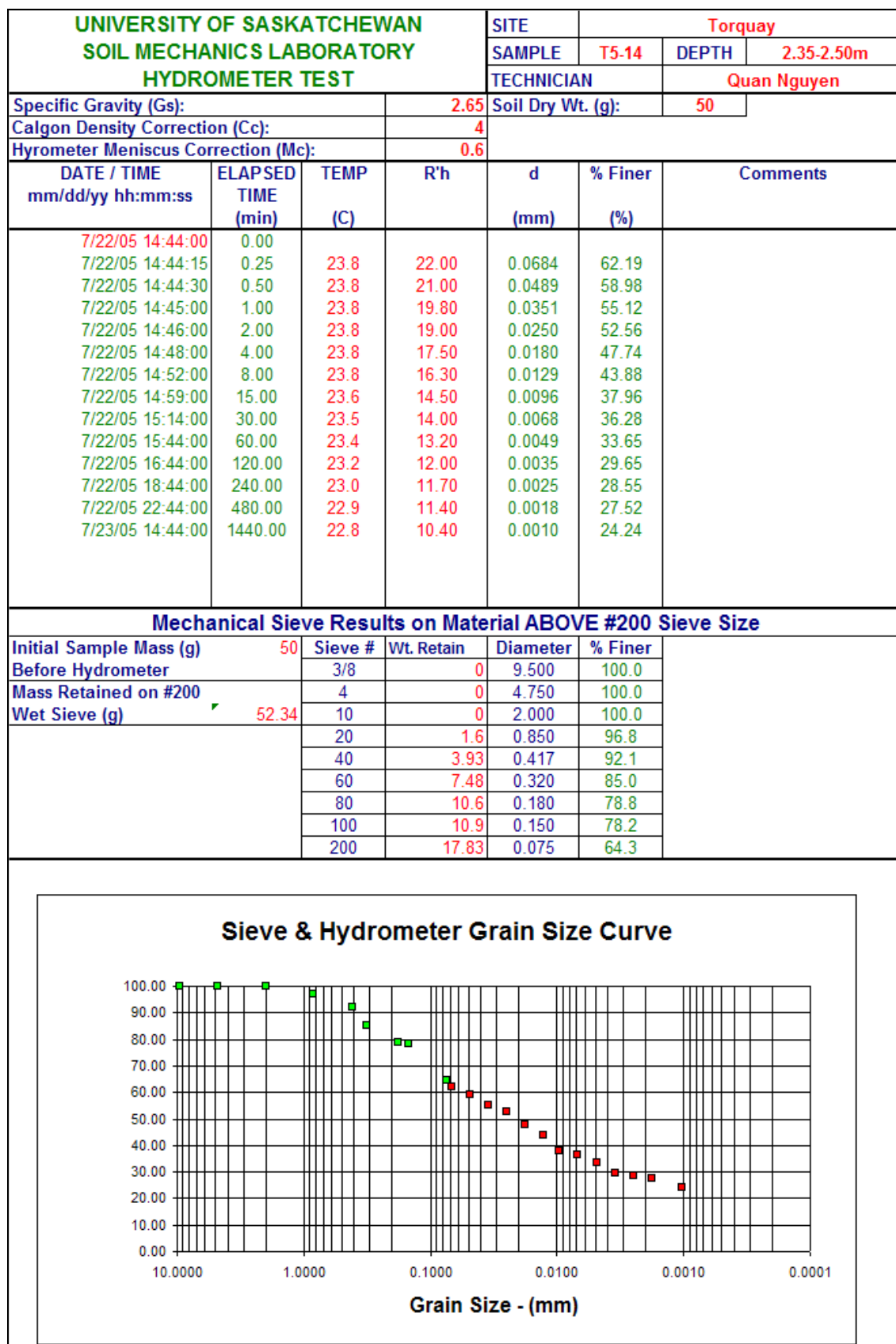


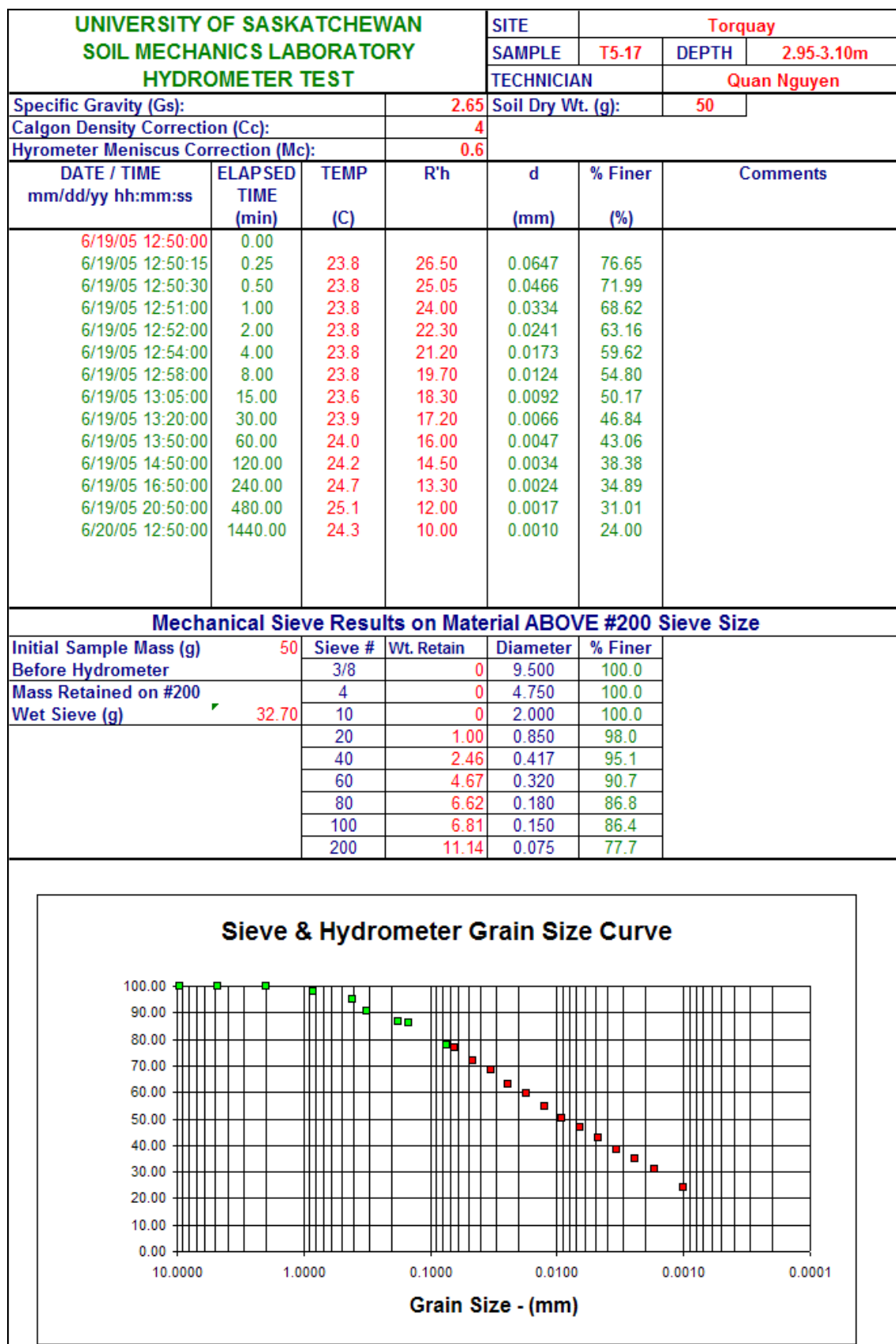












Summary of Atterberg Limit Tests										
1	Sample:	B5-1	Location:	Bethune	Depth (m):	0.18-0.38	W _L (%)	29.0	W _P (%)	13.2
2	Sample:	B5-7	Location:	Bethune	Depth (m):	1.13-1.28	W _L (%)	31.5	W _P (%)	15.0
3	Sample:	B5-16	Location:	Bethune	Depth (m):	2.61-2.76	W _L (%)	34.8	W _P (%)	16.9
4	Sample:	B5-18	Location:	Bethune	Depth (m):	2.96-3.26	W _L (%)	32.8	W _P (%)	16.1
5	Sample:	T5-2	Location:	Torquay	Depth (m):	0.25-0.4	W _L (%)	31.6	W _P (%)	13.7
6	Sample:	T5-5	Location:	Torquay	Depth (m):	0.70-0.85	W _L (%)	34.0	W _P (%)	19.2
7	Sample:	T5-6	Location:	Torquay	Depth (m):	0.85-1.00	W _L (%)	33.0	W _P (%)	16.2
8	Sample:	T5-10	Location:	Torquay	Depth (m):	1.60-1.75	W _L (%)	37.0	W _P (%)	19.1
9	Sample:	T5-11	Location:	Torquay	Depth (m):	1.75-1.90	W _L (%)	32.0	W _P (%)	16.1
10	Sample:	T5-14	Location:	Torquay	Depth (m):	2.35-2.50	W _L (%)	36.8	W _P (%)	17.4
11	Sample:	T5-17	Location:	Torquay	Depth (m):	2.96-3.26	W _L (%)	49.0	W _P (%)	17.7